Ordered mesoporous metal oxides for solid oxide fuel cells and gas sensors

Laura Almar Liante

ADVERTIMENT. La consulta d'aquesta tesi queda condicionada a l'acceptació de les següents condicions d'ús: La difusió d'aquesta tesi per mitjà del servei TDX (**www.tdx.cat**) i a través del Dipòsit Digital de la UB (**diposit.ub.edu**) ha estat autoritzada pels titulars dels drets de propietat intel·lectual únicament per a usos privats emmarcats en activitats d'investigació i docència. No s'autoritza la seva reproducció amb finalitats de lucre ni la seva difusió i posada a disposició des d'un lloc aliè al servei TDX ni al Dipòsit Digital de la UB. No s'autoritza la presentació del seu contingut en una finestra o marc aliè a TDX o al Dipòsit Digital de la UB (framing). Aquesta reserva de drets afecta tant al resum de presentació de la tesi com als seus continguts. En la utilització o cita de parts de la tesi és obligat indicar el nom de la persona autora.

ADVERTENCIA. La consulta de esta tesis queda condicionada a la aceptación de las siguientes condiciones de uso: La difusión de esta tesis por medio del servicio TDR (**www.tdx.cat**) y a través del Repositorio Digital de la UB (**diposit.ub.edu**) ha sido autorizada por los titulares de los derechos de propiedad intelectual únicamente para usos privados enmarcados en actividades de investigación y docencia. No se autoriza su reproducción con finalidades de lucro ni su difusión y puesta a disposición desde un sitio ajeno al servicio TDR o al Repositorio Digital de la UB. No se autoriza la presentación de su contenido en una ventana o marco ajeno a TDR o al Repositorio Digital de la UB (framing). Esta reserva de derechos afecta tanto al resumen de presentación de la tesis como a sus contenidos. En la utilización o cita de partes de la tesis es obligado indicar el nombre de la persona autora.

WARNING. On having consulted this thesis you're accepting the following use conditions: Spreading this thesis by the TDX (**www.tdx.cat**) service and by the UB Digital Repository (**diposit.ub.edu**) has been authorized by the titular of the intellectual property rights only for private uses placed in investigation and teaching activities. Reproduction with lucrative aims is not authorized nor its spreading and availability from a site foreign to the TDX service or to the UB Digital Repository. Introducing its content in a window or frame foreign to the TDX service or to the UB Digital Repository is not authorized (framing). Those rights affect to the presentation summary of the thesis as well as to its contents. In the using or citation of parts of the thesis it's obliged to indicate the name of the author.

Ordered mesoporous metal oxides for solid oxide fuel cells and gas sensors

Laura Almar Liante
Dr. Albert Tarancón Rubio
Dra. Teresa Andreu Arbella

Ordered mesoporous metal oxides for solid oxide fuel cells and gas sensors

Laura Almar Liante

Thesis submitted to apply for the degree of Doctor, in the Nanoscience Program of the University of Barcelona.

Departament d'electrònica, Facultat de Fisica

Supervisors:
Dr. Albert Tarancón Rubio
Dra. Teresa Andreu Arbella

Tutor:
Dr. Joan Ramón Morante Lleonart

June 2014

Universitat de Barcelona

Institut de Recerca en Energia de Catalunya
Catalonia Institute for Energy Research

El Dr. Albert Tarancón Rubio y la Dra. Teresa Andreu Arbella, investigadores del Institut de Recerca en Energia de Catalunya (IREC), CERTIFICAN:

Que la memoria titulada **Ordered Mesoporous Metal Oxides for Solid Oxide Fuel Cells and Gas Sensors** presentada por Laura Almar Liante para optar al grado de Doctor en el Programa de Nanociencias de la Universitat de Barcelona ha sido realizada bajo su dirección en el Institut de Recerca en Energia de Catalunya (IREC).

Barcelona, Junio de 2014

Dr. Albert Tarancón Rubio

Dra. Teresa Andreu Arbella

Nobody ever figures out what life is all about,
and it doesn't matter. Explore the world.
Nearly everything is really interesting
if you go into it deeply enough

— Richard P. Feynman

Abstract

Nanomaterials have received increasing attention during the last decades in the solid state field since they play a major role as catalyst and catalyst supports for many applications including fuel cells or gas sensors. The interest is mainly due to their high specific surface area, which leads to an increase of performance and a cost-effective solution for expensive or rare materials. However, many studies have reported the collapse of nanostructures at high temperature as one of the main drawbacks for their implementation in real devices and therefore, routes to thermally stabilize these materials must be explored.

In this thesis, the unique features of ordered mesoporous materials fabricated by nanocasting are exploited to create quasi-universal thermal stabilization methodologies, allowing implementing and evaluating them in high temperature energy applications e.g. solid oxide fuel cells.

The work developed is divided into seven parts. The first chapter introduces the basics of mesoporous materials, solid oxide fuel cells, catalysis and gas sensors. The second chapter focuses on the experimental procedures and the characterization tools employed. In the third chapter, a novel route to thermally stabilize 3-D open mesoporous structures is presented. The next three chapters, show the fabrication and evaluation of thermal stable mesoporous materials as electrodes for solid oxide fuel cells. Finally, chapter seven presents the suitability of mesoporous ceramic oxides as functional materials in humidity sensors.

Resumen

Los nano-materiales han recibido especial atención durante estas últimas décadas en el campo del estado sólido dado el importante papel que desempeñan como catalizadores y/o soportes catalíticos en diversas aplicaciones, tales como las pilas de combustible o los sensores de gas. Este interés se debe principalmente a su elevada área específica, que da lugar a una mejora del rendimiento y es una solución efectiva para aquellas aplicaciones que requieran materiales de elevado coste. Sin embargo tal y como señalan muchos estudios, el colapso de estas nano-estructuras a elevadas temperaturas es uno de los mayores inconvenientes para su implementación en dispositivos reales, siendo por tanto necesario explorar nuevas rutas que consigan estabilizar estos materiales térmicamente.

El objetivo de la presente tesis es desarrollar metodologías cuasi-universales de estabilización térmica, mediante la explotación de las características exclusivas que poseen los materiales mesoporosos ordenados fabricados a partir de un template. Lo cual nos permite implementarlos y evaluarlos en aplicaciones energéticas que operan a elevada temperatura p.ej. pilas de combustible de óxido sólido.

El trabajo desarrollado se divide en siete partes. El primer capítulo introduce los fundamentos de los materiales mesoporosos, las pilas de combustible de óxido sólido, la catálisis y los sensores de gas. En el segundo capítulo se detallan los procedimientos experimentales y las técnicas de caracterización empleados. El tercer capítulo presenta una nueva metodología para estabilizar térmicamente los materiales mesoporosos de estructura 3-D abierta. Los siguientes tres capítulos, muestran la fabricación y el comportamiento electroquímico de materiales mesoporosos térmicamente estables trabajando como electrodos de pilas de combustible de óxido sólido. Por último, en el capítulo siete se demuestra la viabilidad de los óxidos cerámicos mesoporosos como materiales funcionales en sensores de humedad.

Acknowledgments

Es mi turno, el barco parece que está llegando a su puerto y aunque cuando estás dentro navegando muchas veces da la sensación de marejada y perdonarme pero en estos momentos siento los sesos un poco derretidos (será que soy de la Mancha), estoy segura que una vez plante los pies sobre tierra firme, recordaré esta etapa con *una sonrisa y una lagrimilla* como una de las mejores vividas. Ahora toca echar la vista atrás y cual abuelo sabio recordar todas las personas que me han acompañado y que han hecho posible que esta historia finalice con este grato desenlace.

En primer lugar agradecer a mis directores de tesis, me siento muy afortunada de que me eligieseis, de haberos tenido como supervisores y de que siempre que lo he necesitado haya podido contar con vuestra ayuda y vuestros consejos. Albert Tarancón una y mil veces gracias, que esta tesis esté llegando a buen puerto no es sino señal de la energía y el esfuerzo que siempre has mostrado. Gracias, por haber luchado porque aprenda todos y cada uno de los campos que abarca el hacer un doctorado y por saber transmitir ese optimismo que se hace contagioso, cuando se sabe que el trabajo está bien hecho. A Teresa, la otra pieza que encajaba perfectamente en el puzle, muchas gracias por el aporte de empatía y serenidad que has tenido durante todos estos años hacia mí. Por darme tantas ideas en la parte de la química que tanto costaba durante los primeros años. Un barco dirigido por Joan Ramón Morante, gracias por haberme dado la oportunidad de realizar este proyecto dentro de su equipo.

Cuando comencé esta aventura allá por el 2010, el grupo de Nanoiónica lo formábamos tan sólo Albert, Alex, Manex y yo. Muchas gracias Alex por haber estado siempre al pie del cañón, aportando nuevas ideas y ayudando allá donde se te requiriese. Al poco tiempo llegaron mis *nanoionic girls* con las que he compartido tantas risas, diversas experiencias y momentos: Dolors al final llegó el principio de tu fin! mil gracias por todos los sabios consejos, Bibiana *moltes mercés* por echarme una mano siempre que te la he pedido y Saranya *keep it up it is almost there!* Y poco a poco fueron llegando muchos más miembros al grupo, gracias Marc, Roberto e Iñigo por haber sobrellevado mis dudas este último año. A todos los demás

miembros de nanoiónica (Paula, Gerard, Pepín, Eulalia, Marcus, Verónica) es un placer ver como el equipo se está haciendo grande con gente tan maja.

Por supuesto también tengo que agradecer a muchos otros miembros de IREC y de la UB, a los que tuve la suerte de poder conocer un poquito más aquel primer año que compartimos laboratorio en la UB. Andrés gracias por haber sido un súper apoyo y un buen amigo todos estos años. A Doris, Raquel, María, Alex, Marcel, Cristian, Cristina mil gracias por vuestra ayuda y todos los buenos momentos compartidos. A compañeros del máster y de la UB Oriol, Jordi, Roberto, Alba, Román, Erik,… un placer y mucha suerte. Gracias a David y Marco por tener siempre mi querido BET a punto. A Lluís, Sonia y Paqui por todos los TEM-EELS buscando el mesoporoso infiltrado. Gracias a Yang (y a su estancia) y a Guilhem por todas las ideas y aportaciones que han hecho más rico este trabajo. Y al resto de personas y nuevas incorporaciones de IREC Alberto, Javi, Erdem, Mariano y Silvia por haber amenizado tantos raticos. A los que ya marcharon pero dejaron su huella y aportaron un granico de arena que hace que yo esté acabando este trabajo; gracias Marta, Eleonora, Javi R. y Fran.

Last year I had the great chance and experience of going to Georgia Tech (Atlanta). Thank you Prof. Meilin Liu for giving me the opportunity of working within your professional team during six months. Special thanks to Dr. Minyang Gong and Dr. Dong Ding who were working hard along with me and taught me so many techniques about the fabrication of IT-SOFCs. Thanks to Dr. JP Lee, Dr. Yan Li, X. Li and all the others members for making enjoyable my stay in the United States.

A mis amigos (Viti, Kike, Xavi, Dodi, Paola, Delfín, Ana, Ele y Lau) un placer haberos vuelto encontrar o haberos conocido en Barcelona "la Valencia adulta", gracias por haber hecho posible que desconectase y relativizase las cosas.

A mi tío Virgilio que lleva cuatro años intentando entender que es eso de las pilas. A mi hermanica una persona de la que nunca dejaré de aprender cosas nuevas y nunca dejará de sorprenderme (gratamente). Y por último permitirme dedicar esta tesis a mis padres, lo más bonico y lo que más quiero, gracias por habernos animado siempre a perseguir nuestros ideales.

Barcelona a 31 de Mayo de 2014.

Index

1. INTRODUCTION 1
1.1. Frame of the Thesis 5
1.2. Nanostructured Materials 7
1.2.1. A brief introduction to nanotechnology 7
1.2.2. Nanoporous materials 8
1.3. Mesoporous Materials 9
1.3.1. Soft-templating method 10
1.3.2. Hard-templating method 11
1.3.3. Thermal stability 13
1.4. High Temperature Applications 15
1.4.1. Solid Oxide Fuel Cells 15
1.4.1.1. Brief history of the fuel cells 15
1.4.1.2. Basic operation principle 16
1.4.1.3. Lowering the operation temperature (IT - SOFC) 19
1.4.2. Catalysis 21
1.4.3. Sensors 22
1.5. Scope of the Research 25
References 27

2. EXPERIMENTAL METHODS 31
2.1. Overview of the Chapter 35
2.2. Synthesis of Powder of the Mesoporous Materials 36
2.2.1. Synthesis of powder of the KIT-6 hard template 36
2.2.2. Synthesis of powder of the mesoporous metal oxide replicas 39
2.2.2.1. Procedures and materials 39
2.2.2.2. Silicon content after template removal 41
2.2.3. Impregnation of mesoporous metal oxides powder 41
2.3. Fabrication of Electrochemical Devices 43
2.3.1. Shaping methods 43
2.3.1.1. Pulsed Laser Deposition (PLD) 43
2.3.1.2. Air brushing technique 44
2.3.1.3. Tape casting 45
2.3.1.3.1. Synthesis procedure 46
2.3.1.3.2. Volume shrinkage 47
2.3.1.4. Drop coating technique 49
2.3.2. Fabrication of Solid Oxide Fuel Cells (IT-SOFCs) 49
2.3.2.1. Fabrication of symmetrical cells 49
2.3.2.1.1. Symmetrical cells of mesoporous cermets 49
2.3.2.1.2. Symmetrical cells of MIEC infiltrated in mesoporous scaffolds 50
2.3.2.2. Fabrication of electrolyte-supported cells 51
2.3.2.3. Fabrication of anode-supported IT-SOFCs 53
2.3.3. Fabrication of humidity sensors 54

2.4. Structural Characterization Techniques 55
2.4.1. X-Ray Diffraction (XRD) 55
2.4.2. In-situ high temperature XRD 56
2.4.3. Small Angle X-ray Scattering (SAXS) 57
2.4.4. Nitrogen physisorption measurements (BET) 57
2.4.5. Scanning Electron Microscopy (SEM) 58
2.4.6. Transmission Electron Microscopy (TEM) and Electron Energy Loss Spectroscopy (EELS) 59
2.4.7. Temperature Programmed Reduction (TPR) 60
2.4.8. Thermogravimetric Analysis (TGA) and Oxygen Storage Capacity Experiments (OSC) 61
2.4.9. Inductively Coupled Plasma Optical Emission Spectroscopy (ICP-OES) 61
2.4.10. Raman spectroscopy 62
2.5. Electrical Characterization Techniques 62
2.5.1. Experimental setup SOFCs 63
2.5.2. Experimental set-up sensors 64
2.5.3. Impedance spectroscopy measurements 65
2.5.4. Potentiostatic and galvanostatic measurements 68
References 69

3. SYNTHESIS AND THERMAL STABILIZATION OF MESOPOROUS METAL OXIDES. A CASE STUDY ON CGO 71
3.1. Interest of CGO for High Temperature Applications and Self-limited Grain Growth Regime 75
3.2. Synthesis and Characterization of the CGO Mesoporous Oxide 78
3.3. Thermal Treatment and Stability of the Ordered Mesoporous Structure 82
3.3.1. Structural evolution with temperature 82
3.3.2. Validity of the self-limited grain growth for nanocasting of mesoporous 87
3.4. Functionality of the Long-term Stable Mesoporous CGO 91
3.5. Conclusions 94
References 95

4. CERAMIC-METAL MESOPOROUS COMPOSITES AS ANODE FOR SOFCS 97
4.1. Anode requirements for SOFC applications 101
4.2. Structural Characterization of Powder of Mesoporous Composites of NiO-CGO 105
4.2.1. NiO matrix 105
4.2.2. CGO infiltrated matrix 108
4.3. Electrochemical Performance and Stability of Ni-CGO Mesoporous Anodes 113
4.3.1. Morphological characterization 113
4.3.2. Electrochemical performance 116
4.3.3. Stability 118
4.4. Fuel Cell Performance of Ni-CGO Mesoporous Anodes 119
4.4.1. Electrolyte supported cells 119
4.4.2. Anode supported cells 122
4.5. Conclusions 124
References 126

5. INFILTRATED MESOPOROUS COMPOSITES AS A CATHODE FOR IT-SOFCS 129
5.1. Cathode requirements and advantages of infiltrated microstructures 133
5.2. Structural Characterization of $Sm_{0.5}Sr_{0.5}CoO_{3-\delta}$ infiltrated Mesoporous Scaffolds of $Ce_{0.8}Sm_{0.2}O_{1.9}$ 138
5.2.1. Mesoporous samarium-doped ceria (SDC) powder 138
5.2.2. Mesoporous SDC ceramic scaffold infiltrated with SSC 140
5.3. Electrochemical Performance and Stability of $Sm_{0.5}Sr_{0.5}CoO_{3-\delta}$ infiltrated Mesoporous $Ce_{0.8}Sm_{0.2}O_{1.9}$ Cathodes 144
5.3.1. Optimization of attachment temperature and electrochemical characterization of symmetrical cells 144
5.3.2. Equivalent circuit for MIEC electrodes 147
5.3.3. Long-term stability 149
5.4. Conclusions 158
References 159

6. PERFORMANCE AND STABILITY OF FULLY MESOPOROUS ELECTRODES FUEL CELLS 161
6.1. Nano-structured Electrodes for IT-SOFCs. Performance and Stability Concerns. 165
6.2. Fabrication and Structural Characterization of a SOFC with Fully Mesoporous Electrodes 167
6.3. Fuel Cell Performance 170
6.4. Long-term Stability Test 172
6.5. Post-Test Cell Characterization 177
6.6. Conclusions 181
References 183

7. MESOPOROUS CERAMIC OXIDES FOR HUMIDITY SENSORS 185
7.1. Requirements of Humidity Sensors and Advantages of using Ceramic Mesoporous Materials 189
7.2. Characterization of CGO Mesoporous Humidity Sensors 190
7.2.1. Structural characterization 190
7.2.2. Humidity sensing capabilities of a mesoporous CGO film 191
7.2.3. Mechanism of humidity sensing 195
7.2.4. Effect of temperature 198
7.2.5. Effect of the thickness of the sensing layer 200
7.2.6. Effect of the pore size 201
7.3. Conclusions 202
References 204

8. CONCLUSIONS 205

APPENDIXES **211**

A. COMPOSITIONAL OPTIMIZATION OF MESOPOROUS NICKEL BASED CERMETS FOR SOFCS **213**
A.1. Structural characterization of symmetrical cells of Ni-CGO mesoporous cermets with different nickel content **217**
A.2. Electrochemical performance of Ni-CGO mesoporous anodes **219**
References **221**

B. LOWERING THE SINTERING TEMPERATURE OF BI-LAYER ELECTROLYTES FOR ANODE-SUPPORTED IT-SOFCS **223**

B.1. Requirements and fabrication concerns of anode-supported cells **227**
B.2. Fabrication and structural characterization of bi-layer electrolytes for anode-supported IT-SOFCs **228**
B.2.1. Particle size distribution *228*
B.2.2. Sintering aid *229*
B.3. Fuel cells performance **233**
B.4. Conclusions **234**
References **235**

C. TRANSMISSION LINES BASED EQUIVALENT CIRCUIT ANALOGOUS TO ADLER-LANE-STEELE MODEL FOR MIECS **237**

1
Introduction

Porous materials are like music:
the gaps are as important as the filled-in bits
- G.Q. Lu and X.S. Zhao

1. Introduction

1.1. Frame of the Thesis 5

1.2. Nanostructured Materials 7

1.2.1. A brief introduction to nanotechnology 7

1.2.2. Nanoporous materials 8

1.3. Mesoporous Materials 9

1.3.1. Soft-templating method 10

1.3.2. Hard-templating method 11

1.3.3. Thermal stability 13

1.4. High Temperature Applications 15

1.4.1. Solid Oxide Fuel Cells 15

1.4.1.1. Brief history of the fuel cells 15

1.4.1.2. Basic operation principle 16

1.4.1.3. Lowering the operation temperature (IT - SOFC) 19

1.4.2. Catalysis 21

1.4.3. Sensors 22

1.5. Scope of the Research 25

References 27

1. Introduction

1.1. Frame of the Thesis

The increase of the energy demand together with the higher cost of fossil fuels and the environmental concerns have received considerable attention during the last decades. There are global policies focused into the reduction of the CO_2 emissions (carbon tax) and the replacement of our existing energy system, based on fossil fuels, by renewable energies, which do not produce harmful emissions. The research plays a key role in the search of alternatives offering possible solutions to supply energy preserving our environment.

Among the available technologies towards a *clean* energy future, fuel cells offer an interesting alternative as they are unique in terms of efficiency and low emissions. Although important advances have been reached during the last years in this field, fuel cells seemed to be couple with the idea of the *hydrogen economy* and thus, their implementation has been postpone as a future solution. However, Solid Oxide fuel cells (SOFCs) can run with a wide range of fuels from hydrogen to hydrocarbons, allowing their use in our existing hydrocarbon based energy system providing the required reduction in CO_2 emissions [1].

On the other hand, the emerging field of nanotechnology allows nowadays the fabrication of a broad range of materials in the nano-scale. Nanomaterials have shown unique features and advantages compared to bulk materials, particularly those associated to their high surface area. In the field of energy, the interest of using them have increased during the last decades, since they play a major role as catalyst and catalyst support for many applications including fuel cells [2,3]. This interest is mainly due to their high specific surface area that results in an increase of performance and a cost-effective solution for expensive or rare materials.

However, the use of the nanomaterials in many applications where high temperatures are involved (such as SOFCs) brings many associated issues since nanomaterials tend to exponentially grow with temperature, forming coarse particles, decreasing the number of reaction active sites and therefore, decreasing the performance with the time. Therefore, routes to thermally stabilize these materials in the nanoscale must be explored to take benefit of their implementation in temperature applications like the above mentioned electrochemical devices.

All these reasons justify and constitute the frame of this thesis (**Figure 1.1**), which is devoted to exploit the unique features of ordered mesoporous metal oxides, focusing on exploring universal thermal stabilization methodologies, which allow implementing them in high temperature energy applications.

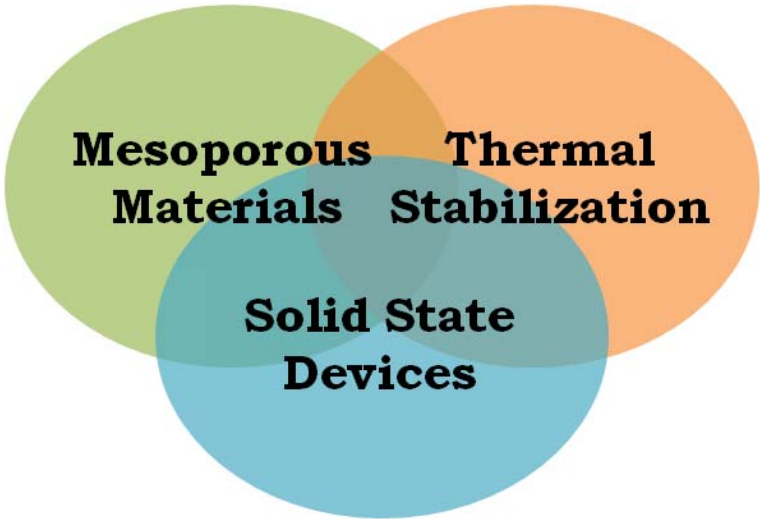

Figure 1.1. Frame of this thesis.

1.2. Nanostructured Materials

1.2.1. A brief introduction to nanotechnology

Nanotechnology is an interdisciplinary field, defined as "the creation of functional materials, devices and systems through the control of matter on the nanometer scale (1-100 nm) and the exploitation of the novel phenomena and properties (physical, chemical, biological) at this length" (*NASA*) [4].

Although the application of nanomaterials has been raised recently, the concept has its roots in 1959 in the famous talk given by Richard P. Feynman, entitled *There is Plenty of Room at the Bottom*. The physicist speculated that materials could be arranged and manufactured from individual atoms in the way one wants [5]. However, it was not until the 1980s when the born of the Scanning Tunneling Microscopy (STM) and the discovery of fullerene emerged the field (**Figure 1.2)** [6,7].

Today, nanomaterials have been expanded to a wide number of structural and functional applications. Nanomaterials are based on metal, ceramic, polymeric materials or composites. The possibility of tuning the size and study their properties in the nanometer scale (by the developed characterization tools) allowed discovering unique features that generate billions of dollars everyday *e.g.* tailoring high surface to volume ratio of the materials improved the control of the reactivity and thus the performance of many catalysts [8].

The advantages of these nanomaterials already reached the market, more than 1600 commercial products such as cosmetics, food packaging or automobiles, are already identified as nanotechnology-based [9].

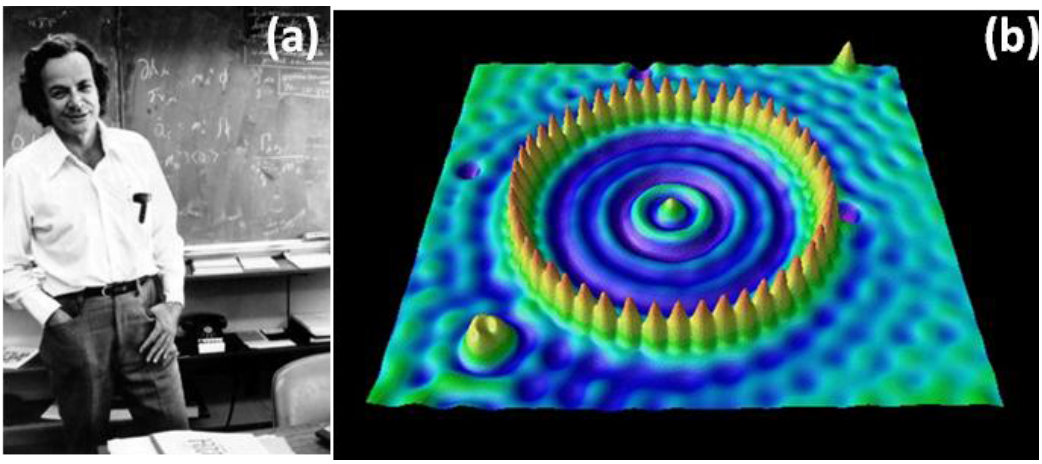

Figure 1.2. (a) Richard Feynman during one of his lectures; (b) Quantum corral. Ring of atoms are shown in light shade of green, in which the ripples (colored in blue) are wave patterns of some of the electrons trapped in the corral. (*extracted from IBM Almaden Research Center, San Jose, CA* [10]).

1.2.2. Nanoporous materials

The study and applicability of materials with controllable pore dimensions has been important in many fields ranging from chemistry to physics, biology, medicine or engineering. According to the IUPAC, solid materials can be classified into three categories according to their pore size: pores with a diameter below 2 nm are called microporous, between 2-50 nm are mesoporous and above 50 nm are macroporous.

Zeolites are microporous (pore size of ~15 Å) aluminosilicates, that were synthesized in an early work of Barrer [11] and became the most widely used catalyst in the industry due to their high surface area and the possibility of controlling their adsorption capacity and tailoring the active sites. However, the use of zeolites as molecular sieves is limited to relatively small molecules and became inadequate when the reactants to catalyze exceeded the size of the pores. In this case, the strategy is to keep the ordered porous structure, making materials with larger pores therefore moving to the mesoporous region [12].

1.3. Mesoporous Materials

In 1992 Mobil Oil researchers developed the first family of ordered mesoporous materials, the so-called M41S materials [13,14]. The most representative silica solids of this family are represented in **Figure 1.3**; the MCM-41 (hexagonal, space group *p6mm*), MCM-48 (cubic, space group *Ia3d*) and the MCM-50 (laminar, space group *p2*) [15].

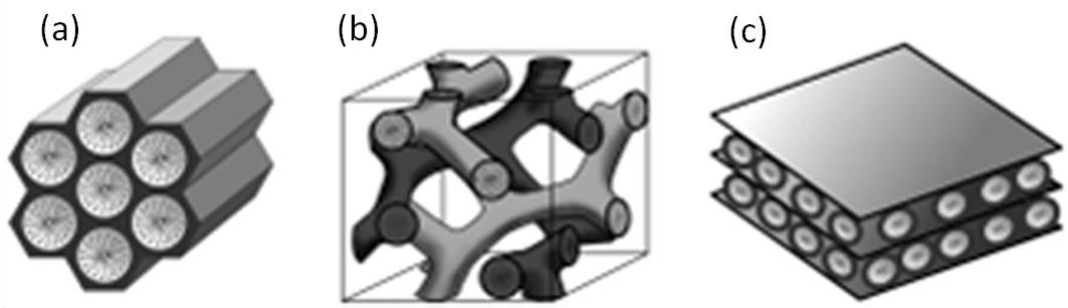

Figure 1.3. Scheme of the structures of mesoporous M41S materials (a) MCM-41 (2D hexagonal, space group *p6mm*), b) MCM-48 (cubic, space group *Ia3d*), and c) MCM-50 (lamellar, space group *p*2) (*extracted from ref* [15]).

First mesoporous materials were silica-based synthesized by hydrolysis and condensation of the silica precursors (sol-gel process) in the presence of surfactant crystal micelles. To fabricate the mesoporous silica, the silica source is usually tetraethylorthosilicate (TEOS, $Si(OC_2H_5)_4$) together with long chain ammonium salts, amines or triblock-copolymers used as templating agents. The mesoporous silica is obtained after the removal of the surfactants, commonly by calcination.

From nineties hundreds of papers appeared in the literature, reporting new methodologies of synthesis, different geometries, materials and strategies to fabricate them also tuning their pore sizes [16–18]. Among the most representative family series of mesoporous materials are SBA (Santa Barbara University) [19], MSU (Michigan State University) [20], KIT (Korean Institute of Technology) [21] and FDU (Fudan University) [22].

The potential advantages of the synthesis of non-siliceous mesoporous structures was first suggested by Stucky *et al.* [23] and successfully applied by Ying *et al.* [24] in 1995. In that case the aqueous synthesis route limited the range of compositions. Further new synthesis methodologies such induced self assembly (EISA) [25] and nanocasting [26] quickly expanded the range of materials fabricated.

Among the non-siliceous mesoporous materials, metal oxides have a great interest because the number of applications and the functionality properties are very broad. A high number of families of mesoporous metal oxides with ordered geometries have been prepared using various inorganic precursors and a wide variety of soft templates (cationic, anionic, block copolymer), hard templates (mesoporous-SiO_2, mesoporous Carbon) or a combination of both in a recently reported referred as CASH ("combined assembly by soft and hard") [26–37]. An excellent review of Schüth *et al.* about the synthesis of the non-siliceous mesoporous oxides including discussion of the structures and the constituting elements has been recently published [35].

In the following section the traditional and most used synthesis routes to fabricate mesoporous metal oxides are discussed, the soft-templating (surfactant/block copolymer) method and the hard-templating (nanocasting) method.

1.3.1. Soft-templating method

Soft-templates methods are adapted directly from the silica mesoporous synthesis route and therefore, are based on the self-organization of amphiphilic materials (surfactant or block copolymers) as templates **Figure 1.4**.

Two main routes have been adapted aqueous solution and evaporation-induced self-assembly (EISA) processes. In the aqueous based synthesis, the cooperative assembly between the inorganic precursors with the surfactant and the simultaneous hydrolysis-condensation process is the key issue, leading to the desired mesoporous oxides after the removal of the surfactants [23]. Four different synthesis routes depending on the charge interaction between the surfactant "S" and the inorganic species "I" have been reported: S^+I^-, S^-I^+, $S^+X^-I^+$, $S^-X^+I^-$ ("X" representing a mediator).

In the EISA synthesis the use of volatile solvents slows the hydrolysis and condensation rate of the metal species. After evaporation of the solvent, the surfactants became highly concentrated, leading to ordered mesoporous composites. The surfactants are usually removed by calcination [38].

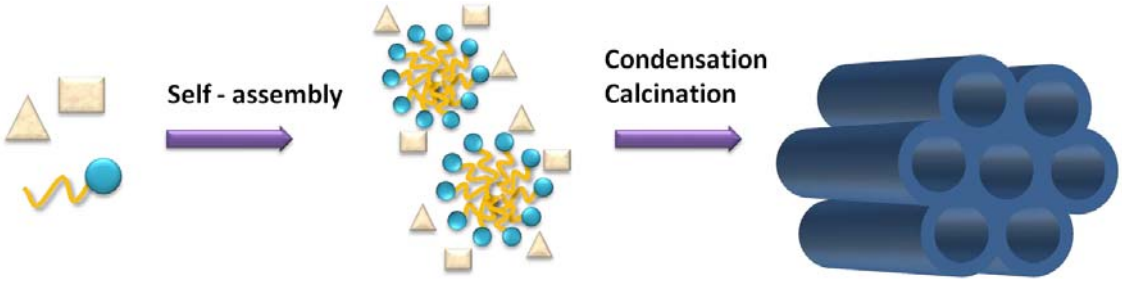

Figure 1.4. Representation of the different steps of the soft-templating route, carried out to obtain mesoporous metal oxides.

The main drawback of the soft-templating methods are the amorphous walls and the low thermal stability. The non-siliceous mesoporous oxides synthesized only have amorphous or semi-amorphous crystalline frameworks, because the ordered mesoporous structures collapse during the thermal crystallization process [39].

1.3.2. Hard-templating method

Hard-templating methods or nanocasting processes are based on the use of molds to replicate the mesoporous structure. They opened a wider range of non-siliceous mesoporous materials, which were not possible to synthesize by soft-templating processes [40].

Typically the process involves fours steps (see a sketch of the method in **Figure 1.5**):

1) Template fabrication: mesoporous silica is an ideal candidate due to its highly ordered and uniform structure. If the pores are connected in the template, organized 3-D structures as the original can be obtained. Moreover, the obtained replica can be further infiltrated and used again as template [41,42].
2) Impregnation of precursors inside the template pores: the most commonly used is wet impregnation, where the precursors are dissolved in a solvent and introduced in the template by capillarity.
3) Calcination to obtain the desired crystalline phase.
4) Template removal: templates should be removed without affecting the replica, silica templates are usually removed by a solution of NaOH or HF depending on the stability of the fabricated mesoporous replica.

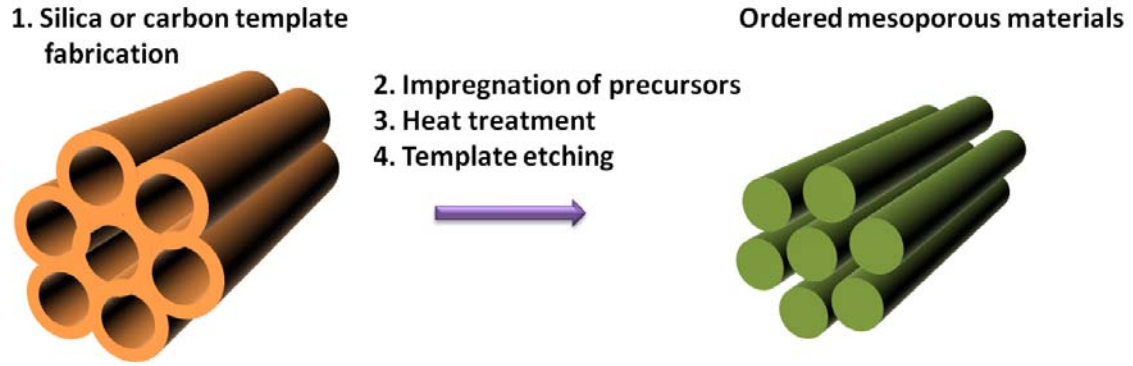

Figure 1.5. Basic scheme of the hard-templating method for obtaining mesoporous metal oxides.

The main advantages of the hard-templating methods are the possibility to obtain a wide variety of materials with high surface area and uniform pore sizes, different meso-structures (only by changing the template) and higher thermal stability [43].

1.3.3. Thermal stability

After more than two decades of intense research in the mesoporous field, their thermal stability is still a major challenge. Most of the mesoporous materials require a further high-temperature molding step for making them thermally stable and feasible for real applications.

A clear example are mesoporous metal oxides which are potential materials for many high temperature energy applications such as fuel cells, electrolysis cells, gas separation membranes, photovoltaic cells, high temperature catalysis or gas sensing.

The thermal stability of different mesoporous silica templates was studied in detail by Cassiers *et al.* [44] and found to be related with the wall thickness. Thicker pore walls lead to a higher thermal stability and with the concentration of silica species on the pore walls (silica precursor used in the synthesis). For instance temperature stability above 850 ºC was found for the SBA-15.

For mesoporous metal oxides the thermal stability is usually lower and the mesoporous structures tend to collapse at temperatures of ~600 ºC in air [45]. The thermal stability is related with two characteristic temperatures of each material, the glass-transition temperature (T_g) or the crystallization temperature.

In a glass-transition state the material flows to form a melt which will tend to merge to lower the specific surface energy and therefore, the meso-structure would collapse (e.g. the T_g of silica materials is 1200 ºC).

For soft-templating methods, if a material starts to crystallize the meso-structure will collapse when the particle size grows above a larger size than the wall thickness of the mesopores (~ 2-10 nm). Hydrothermal treatment was demonstrated to be an effective approach to improve the thermal stability, due to a uniformization of the particle size during the treatment [46,47].

On the other hand, if a material is synthesized inside a hard template support and has crystallized to a certain extent, its thermal stability will largely be decided by the dependence of the crystal size with the temperature. Metal oxides with larger crystal sizes

than the pore-wall thickness of the silica template were obtained while keeping the meso-structure, e.g. Mesoporous Co_3O_4 is obtained from a nanocasting approach with an average particle size of 20 nm [48]. Therefore, obviously the thermal stability of the mesoporous metal oxides obtained from hard-templates is higher than for the replicas obtained from soft-templating techniques.

Apart from that, several smart approaches have been developed in order to improve the thermal stability of the synthesized mesoporous metal oxides at intermediate temperatures (T ~ 600-750 ºC). Crepaldi *et al.* obtained mesoporous nanocrystalline yttria-zirconia and ceria-zirconia by an EISA derived method at temperatures as high as 700 ºC [49]. Li *et al.* developed a strategy to synthesize self-ordered mesoporous nanocomposites, combining the surfactant template self-assembly, with *in-situ* crystallization of glass-based nanocomposites, in which nanocrystals precipitate within the amorphous matrix [50]. Lee *et al.* developed the combined assembly by soft and hard methods (CASH), in which an *in-situ* formed carbon acts as rigid support for the synthesis of highly crystalline mesoporous oxides [51]. Adding a crystallization inhibitor (e.g. phosphate radicals) which decreases the crystallization rate [45] or adding a dopant or additive [52] are another common approaches.

Although several approaches have been presented, they usually involved very tedious methodologies. Due to the potential of the mesoporous materials in high temperature energy applications, the development of novel stabilization methods would lead to a deep impact in the field.

Moreover, there is a lack of real tests demonstrating the thermal stability of the synthesized mesoporous materials in the proposed electrochemical devices (e.g. fuel/electrolysis cells) working under real continuous operational conditions.

1.4. High Temperature Applications

1.4.1. Solid Oxide Fuel Cells

1.4.1.1. Brief history of the fuel cells

In 1838, C. F. Schönbein identified for the first time the electrolysis-effect [53]. One year later, W. R. Grove introduced the concept of the fuel-cell, *i.e.* producing electricity by combining the constituents of water, hydrogen and oxygen [54]. The first fuel cell arrangement was presented by him a couple of years later, based on a diluted solution of sulfuric acid as electrolyte to oxidize the hydrogen. The generated current was used to split the water in the upper part vessel into its constituents (**Figure 1.6**) [55,56].

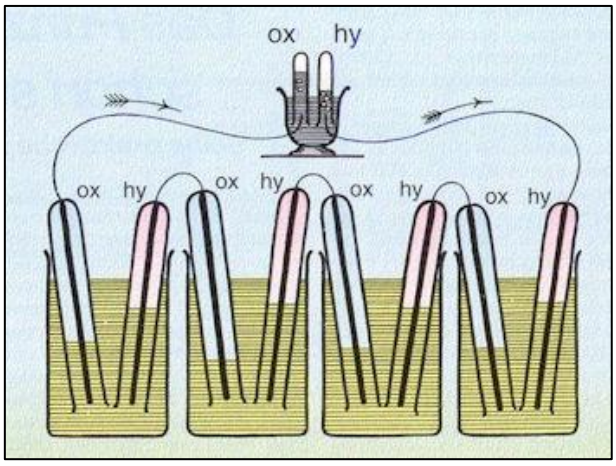

Figure 1.6. Scheme of the first fuel cell arrangement by W. R. Grove.

The basics of the ceramic fuel cells have their roots on the discovery of W. H. Nernst in 1899, who used yttrium-doped-zirconia to replace the carbon filaments in incandesce lamps [57]. In 1937, E. Bauer and H. Preiss presented the first ceramic fuel cell operating at a temperature of 1000 ºC based on a doped zirconia electrolyte, Fe_3O_4 as cathode and Fe or carbon as anode [58].

By the 1960s, ceramic fuel cells (SOFCs) started to develop for practical applications [59–64]. The original choice of yttrium-doped-zirconia as electrolyte has been extended until today. For the further years, the research was focused in making full-dense, thinner electrolytes and optimizing the different configurations and interconnectors.

The first SOFCs had platinum electrodes and interconnectors [63], which were replaced in the 1970s by Ni/ZrO_2 ceramic-metal (*cermet*) materials as anode [65,66], doped In_2O_3 as cathode [67], and doped $CoCr_2O_4$ as interconnect [68]. At the present, the conductors $La_{1-x}Sr_xMnO_3$ and $La_{1-x}Sr_xCoO_3$ are the most common cathodes, Ni-YSZ as an anode and $LaCrO_3$ is the usual choice as interconnect at high temperatures [69,70].

1.4.1.2. Basic operation principle

A fuel cell is an electrochemical device that converts the chemical energy of the reactants directly into electrical energy. As electrochemical converters their efficiency overcomes the limitations of heat engines (Carnot cycle).

Among the different types, Solid Oxide Fuel Cells (SOFCs) is the usual choice working at high temperatures (600-1000 ºC). The main advantages compared to other types of cells are a higher global efficiency ($\eta_{GLOBAL} \sim$ 45-85 %), the flexibility of fuels that can be used, the mechanical stability of the solid electrolyte and the higher tolerance to impurities such as CO or sulfur in the fuel.

A SOFC consists of a solid ceramic electrolyte and two electrodes, *i.e.* a cathode and an anode. The electrolytes are ionically conducting oxides. At the cathode side oxygen (O_2) (usually from air) is reduced and the oxide ions (O^{2-}) are transported through the electrolyte to the anode where they react with the gaseous fuel, yielding heat, water and releasing electrons (e^-) to the external circuit. **Figure 1.7** shows a basic scheme and the simplified partial reactions that take place in the electrodes (if hydrogen gas is used as fuel).

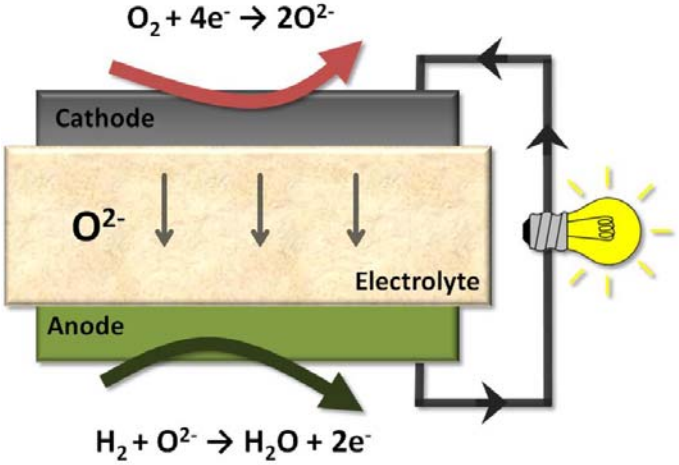

Figure 1.7. Scheme and basic principle of a SOFC working with hydrogen as fuel.

The overall reaction is therefore,

$$H_2 + \frac{1}{2} O_2 \rightarrow H_2O \qquad \textbf{(1.1)}$$

The **Nernst equation (1.2)**, defines the thermodynamic potential (E_r) of the cell for the reaction (1.1) at a temperature (T). This expression defines the potential without current flowing through the device (ideal open circuit voltage, OCV). The measured voltage (V) will be lower due to the different polarizations; ohmic or resistance polarization (IR), activation or charge polarization (η_{act}) and concentration or diffusion polarization (η_{conc}) **(1.3)** (**Figure 1.8**),

$$E_r = E_0 + \frac{RT}{2F} ln \frac{p_{O_2}^{1/2} p_{H_2}}{P_{H_2O}} \qquad \textbf{(1.2)}$$

$$V = E_r - IR - \eta_{act} - \eta_{conc} \qquad \textbf{(1.3)}$$

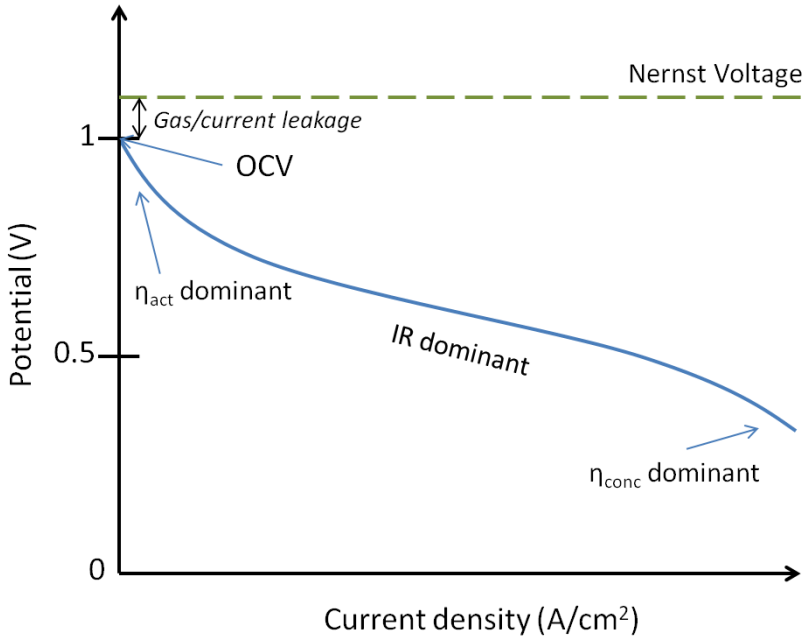

Figure 1.8. Ideal and measured Current –Voltage curve (IV) for a SOFC with the corresponding polarization losses dominant in each region (activation polarization (η_{act}), ohmic polarization (IR) and concentration polarization (η_{conc})).

High fuel flexibility is one of the main advantages of the SOFCs. Apart from hydrogen, hydrocarbons (e.g. CH_4), carbons (e.g. C, CO) or coal syngas mixtures (i.e. CO_2-H_2 mixtures) can be used as fuels due to the high temperature and thus, the high electrode kinetics. Therefore, hydrocarbons could be used even without the need of an external reformer reducing the costs and complexity of the systems [71]. Moreover, the exhausted gases of the SOFCs running with hydrocarbons are mainly H_2O and CO_2, thus contributing to reduce the emissions responsible of the climate change.

The active site where the electrons, the gas and the oxide ions meet and the reaction take place is the so-called **Triple-Phase-Boundary** (TPB). The use of pure electronic conductors as electrodes limits the TPB to the interface of the electrodes with the electrolyte. The increase of TPB or number of active reaction sites increases the performance of the SOFCs. Common strategies to increase the TPB are the use of (i) a mixture of pure electronic and pure ionic powders (cermets) and/or (ii) mixed ionic electronic conductors (MIECs) (**Figure 1.9**).

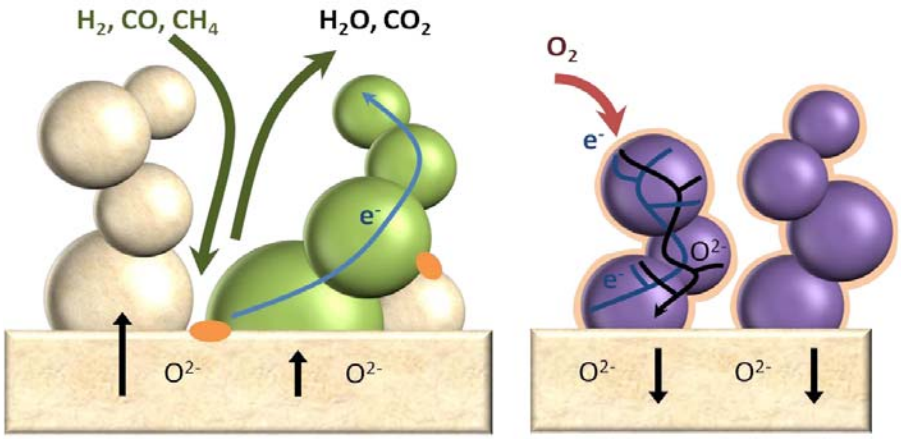

Figure 1.9. Common strategies to increase the Triple-Phase-Boundary (TPB) shown in orange in SOFCs. Cermet mixture as anode (right), MIEC as cathode (left).

1.4.1.3. Lowering the operation temperature (Intermediate Temperature - SOFC)

The major technical issue that has limited the development and commercialization of this technology is its high operating temperature (T ~ 1000 ºC). The high operating temperatures put numerous requirements related to materials compatibility that result in higher costs, degradation problems, slow start-up and thermal mismatch between the cell components. On the other hand, in contrast to the efficiency of the heat engines dependent on the Carnot cycle, the decrease of temperature of the fuel cells theoretically increases the efficiency. Therefore, over the past decade, a lot of efforts have been devoted to lower the operating temperature to the intermediate range (IT = 600-800 ºC) [72].

Unfortunately, the lower is the operational temperature; the higher are the resistive losses across the electrolyte and the overpotentials at the air and fuel electrodes. The strategies followed during the last decades lowering the SOFCs operating temperature involve the use of (i) thinner solid electrolytes, (ii) alternative solid electrolytes with higher conductivities (iii) improved electrode materials.

The fabrication of **thinner electrolytes** is one of the most used approaches to decrease the operation temperature of the SOFCs [71,72]. **Figure 1.10** shows the ionic

conductivity of different materials used as SOFC electrolytes versus the temperature and the relationship between these parameters and the maximum electrolyte thickness, in order to obtain the target area specific resistance (a suitable power density) of the cell [73,74]. The vast majority of cells use yttria-doped-zirconia (YSZ) as electrolyte and as it is observed in the figure, a thickness below 15 μm is required to give a considered suitable power density of 0.5 W/cm^2, in the intermediate temperature range (T < 800 ºC). This fact explains why the SOFC community has moved from electrolyte-supported to anode-supported configurations.

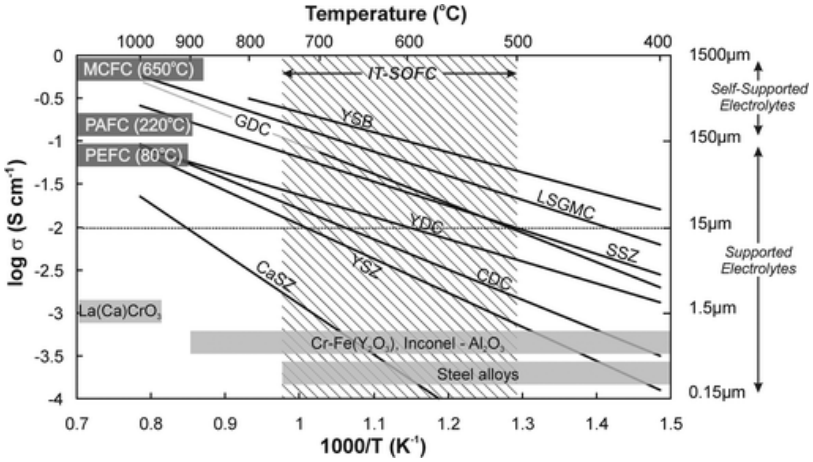

Figure 1.10. Specific ionic conductivity of different SOFC electrolytes and interconnect materials as function of the reciprocal temperature. Conductivity data from K. Wincewicz *et al.* and ref. therein [75]. YSB $[(Bi_2O_3)_{0.75}(Y_2O_3)_{0.25}]$; LSGMC $(La_xSr_{1-x}Ga_yMg_{1-y-z}Co_zO_3$; $x \approx 0.8$, $y \approx 0.8$, $z \approx 0.085)$; CGO $(Ce_{0.9}Gd_{0.1}O_{1.95})$; SSZ $[(ZrO_2)_{0.8}(Sc_2O_3)_{0.2}]$; YDC $(Ce_{0.8}Y_{0.2}O_{1.96})$; CDC $(Ce_{0.9}Ca_{0.1}O_{1.8})$; YSZ $[(ZrO_2)_{0.92}(Y_2O_3)_{0.08}]$; CaSZ $(Zr_{0.85}Ca_{0.15}O_{1.85})$. The conductivity range of electrolytes used in MCFC, PAFC and PEFC are included for comparison (*taken from ref.* [76]).

On the other hand, as it can be extracted from **Figure 1.10**, it is possible to use **alternative electrolyte materials** with higher conductivities in the IT range. Doped-ceria materials are the common choice since apart from the superior ionic conductivity, present a better catalytic activity for reforming hydrocarbons. Unfortunately, ceria-doped materials become electronically conductive under reducing atmospheres, leading to a lower open-circuit-voltage (OCV) thus decreasing the efficiency.

Significant increases in power density and reduction in the operating temperature have been attained by optimizing the thicknesses of bi-layered electrolytes. For instance, Wachsman and Lee recently proposed a ceria/bismuth oxide bi-layered electrolyte giving an exceptionally power output of 2 W/cm^2 at 650 ºC [77].

According to the figure, scandia-stabilized zirconia (SSZ) is a good candidate and has become a common choice due its higher ionic conductivity in the intermediate temperature range compared to YSZ, allowing using them even in electrolyte-supported fuel cell configurations.

Enginnering the microstructure of the electrodes by using nanostructures would lead to an increase of the active reaction sites (TPB) and lower activation polarization. Infiltration techniques of nanostructure catalysts demonstrated to have lower polarization resistance compared to conventionally fabricated electrodes [78].

1.4.2. Catalysis

Catalysis has a tremendous impact on many processes of the chemical industry, such as processing and production of fuels, chemicals or consumer products and environmental protection and remediation [79]. Indeed, a market intelligence company which provides business research reports and consulting services, the Transparency Market Research, estimates that the catalysts demand in 2012 was worth USD 19.2 billion and is forecast to reach USD 24.1 billion by the end of 2018 [80]. A catalyst lowers the activation energy of a reaction, leading to a higher reaction rate, reducing the costs and improving the selectivity. It is not consumed and remains unchanged at the end of the reaction.

Heterogeneous catalysts act in a different phase than the reactants; the active phase is generally a solid supported and dispersed on a second (also solid) material. The support prevent the agglomeration or sintering of the usually small active catalyst particles, enhancing the effectiveness, the specific activity per gram and thus, reducing the costs. Supports are porous materials with a high surface area and may or not interact with the catalyst particles.

Zeolites (microporous) and mesoporous materials have been chosen as catalysts in industry for decades due to their specific and unique features (see **section 1.2.2 and 1.3**) [12]. They have interest from the point of view of acid, base, and redox catalysis. They are also excellent supports of active phases e.g. high dispersion of Pt, Pd, Pt-Re and Ni-Mo generates hydrogenation and reforming catalysts. Moreover, their pore size can be modified and their surface can be functionalized to anchor specific metal particles or complex molecules. Some excellent reviews can be found in the literature [81,82].

The thermal stability of nanostructure catalysts is always reported as one of the major issues. Several important industrial processes such as CO oxidation, partial oxidation, cracking of hydrocarbons and combustion reactions are carried out at temperatures above 300 ºC and therefore, stable catalysts at the high reaction temperatures are in high demand [83]. For instance, **high temperature catalysis** involves the steam reforming of natural gas taking place at temperatures as high as 800 ºC. In the dry reforming both green house gases CO_2 and CH_4 react producing synthetic gas (syngas), a mixture of H_2/CO. Syngas is further used in the industry to produce hydrocarbons (Fischer-Tropsch) and other valuable oxygenated chemicals.

1.4.3. Sensors

Automated systems controlling health and environmental issues are also among the top priorities of the technological developments today. Both industrial and domestic fields require sensors monitoring the concentration of certain substances. Typical applications are the control and supervision of certain parameters *e.g.* humidity; the detection of a compound for safety issues *e.g.* explosive or toxic substance in an industrial process; or the control of gas emissions in automobiles. The demand of more reliable and robust devices is still increasing and therefore, the research and development plays an important key role.

Regardless the different sensing mechanism, most of the sensors involve the interaction of a molecule on a solid surface. This fact explains why materials with large pore to volume ratio are desirable. In particular, mesoporous materials possess high pore

volume with open ordered and regular pores. Moreover, the size of their pores offer advantages compared with micro-pore (*e.g.* zeolites) or macro-pore materials, combining high gas accessibility with high surface area, and can be tuned for selectively detecting the target molecules.

Gas sensors are among the most studied devices due to the large number of processes and substances to be monitor in the industry, the public safety and the environmental concerns. Up to now, a large number of mesoporous materials specially silica (with or without functionalized pores) and metal oxides have been already tested as gas sensors showing an enhanced performance and are extensively reviewed in the literature [84,85].

Due to the broad sensing field, in this thesis we centered the fabrication of robust and reliable **humidity sensors**. Humidity control is crucial for many manufacturing industries such as textiles, food storing/processing, paper, semiconductor and petrochemical [86,87]. The first commercial humidity sensors were developed in Japan at the end of the 1970s [88–90].

The materials commercially developed for humidity sensors can be classified into two groups, organic and ceramic oxides. Organic polymers have shown a lot of challenges due to their poor mechanical and chemical stability, presenting hysteresis, slow response time, long-term drift and degradation over the time [91].

In contrast, ceramic oxides possess higher mechanical strength, better thermal stability and faster response to humidity changes. The main problem of the ceramic humidity sensors is related to the need of a periodical heat treatment to recover the initial properties; a drift in the resistance of the ceramic sensor is reported after long exposures under humid environments, due to the formation of hydroxyl ions on the surface. However, the hydroxyl groups can be removed and the humidity sensor recovers the initial state by heating to temperatures above 400 ºC [92].

Porous ceramics form a common group of materials to sense humidity. The adsorption mechanism of the water molecules on the surface of the ceramic oxides is well known (**Figure 1.11**). First, a chemisorbed layer is formed on the available sites of the oxide surface, causing dissociation of water molecules to surface hydroxyls. After the

first layer of water is formed, subsequent layers are physisorbed. The molecules in the first physisorbed layer are bounded through double hydrogen bonds and cannot move. At higher humidity levels, water molecules are singly bounded and form a liquid-like network. Thus, the water molecules from the second layer can move or rotate freely (like in bulk liquid water) and the Grotthuss mechanism or the protons transport become dominant [93].

From the surface adsorption mechanism, it is clear that large pore volumes are desirable in order to get high sensitive humidity sensors. Moreover, the response and recovery times of the ceramic sensors can be controlled by the pore size. The detection limit can be set very low by decreasing the pore size [91,93].

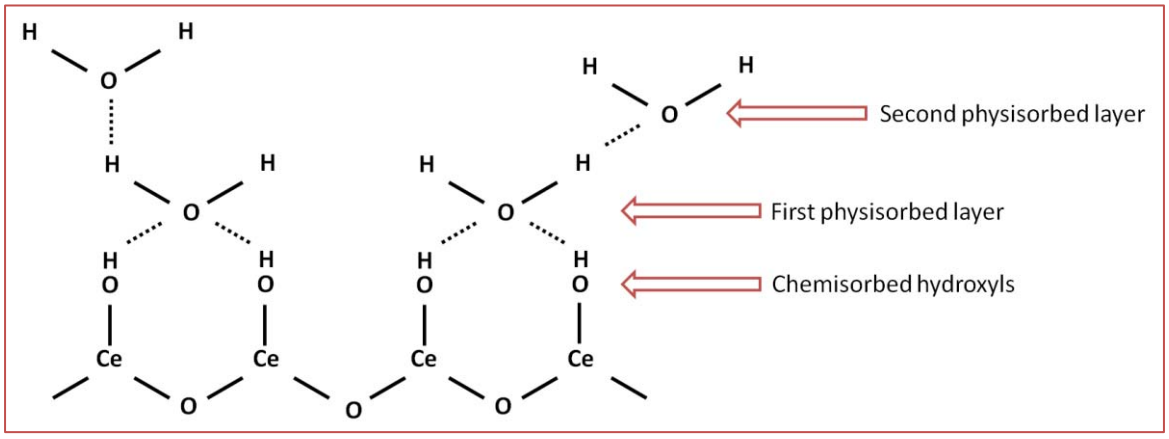

Figure 1.11. Multi-layer adsorption of condensed water on the surface of the ceramic oxide CeO_2.

1.5. Scope of the Research

This thesis is devoted to the synthesis and characterization of thermally stable mesoporous metal oxides as high performance materials in diverse electrochemical devices *i.e.* IT-SOFCs, gas sensors and catalysts supports. The work developed intends first, to take advantage of the known unique features of the ordered mesoporous metal oxides replicas synthesized by a nanocasting methodology (high surface area and pore volume). Second, investigate different novel routes to thermally stabilize those mesoporous metal oxides. Finally, implement the mesoporous materials in real electrochemical devices and study its performance and the expected long-term stability.

In addition, it is expected that the synthesis procedures, the fabrication techniques and the experimental set-ups used and optimized in this work, will serve as background and inspiration for the future generations of the "Nanoionics and Fuel Cells group", in the Advanced Materials Department at IREC which started running, along with this thesis, four years ago.

The thesis is organized as described in the following,

- **Chapter 2** shows the experimental methods used in this work. A detailed explanation of the procedure followed to synthesize mesoporous powder and to fabricate the electrochemical cells and humidity sensors is presented. Moreover, the main structural and electrical characterization techniques employed during this thesis are introduced.
- **Chapter 3** describes a route to thermally stabilize 3D-open mesoporous structures. The functionality of the stabilized mesoporous replica as a catalyst support is further presented.

The next three chapters are devoted to explain the synthesis and characterization of mesoporous materials as electrodes for IT-SOFCs,

- **Chapter 4** firstly describes an approach to thermally stabilize mesoporous composites by forming a close compact unit. Ceramic-metal mesoporous materials are fabricated by this approach and characterized and tested as anodes for IT-SOFCs.
- **Chapter 5** presents infiltrated mesoporous composites. Mesoporous ceramic scaffolds are fabricated according to the stabilization route presented in the Chapter 3 and further infiltrated with a catalyst. Electrochemical cells fabricated with this architecture are characterized and tested as cathodes for IT-SOFCs.
- **Chapter 6** shows the fuel cell performance and long-term stability of an IT-SOFC fabricated using fully mesoporous electrodes.

After that, a dedicated chapter is devoted to the implementation of mesoporous materials in gas sensing applications:

- **Chapter 7** presents a humidity sensor based on mesoporous ceramic oxides. The properties and mechanism of sensing are shown together with an analysis of the response and detection limits of the device.

The conclusions of this thesis are finally summarized in the **Chapter 8.**

Three appendixes are added at the end of the manuscript. **Appendix A** describes the compositional optimization of the mesoporous nickel based cermets. **Appendix B** explains a study performed to lower the sintering temperature of bi-layer electrolytes in anode supported IT-SOFCs. **Appendix C** presents the transmission lines equivalent circuit used to fit the impedance spectra of Chapter 5, and its analogy to the Adler-Lane Steele model for MIECs.

References

[1] E.D. Wachsman, K.T. Lee, Science 334 (2011) 935.

[2] Z.Y. Zhou, N. Tian, J.T. Li, I. Broadwell, S.G. Sun, Chem. Soc. Rev. 40 (2011) 4167.

[3] C. Sun, H. Li, L. Chen, Energy Environ. Sci. 5 (2012) 8475.

[4] T. Harper, Nanotechnology 14 (2003).

[5] R.P. Feynman, (Transcript Talk Http//www.zyvex.com/nanotech/feynman.html) (1959).

[6] G. Binnig, H. Rohrer, Patent US4343993 A. Scanning Tunneling Microscope, 1982.

[7] H.W. Kroto, J.R. Heath, S.C. O'Brien, R.F. Curl, R.E. Smalley, Nature 318 (1985) 162.

[8] http://www.nano.gov, Natl. Nanotechnol. Iniative.

[9] http://www.nanotechproject.org/cpi, Consum. Prod. Invent. (2014).

[10] http://www.almaden.ibm.com/vis/stm/images/stm_small.gif.

[11] R.M. Barrer, Zeolites 1 (1981) 130.

[12] A. Corma, Chem. Rev. 97 (1997) 2373.

[13] C.T. Kresge, M.E. Leonowicz, W.J. Roth, J.C. Vartuli, J.S. Beck, Nature 359 (1992) 710.

[14] J.S. Beck, J.C. Vartuli, W.J. Roth, M.E. Leonowicz, C.T. Kresge, K.D. Schmitt, C.T.W. Chu, D.H. Olson, E.W. Sheppard, J. Am. Chem. Soc. 114 (1992) 10834.

[15] F. Hoffmann, M. Cornelius, J. Morell, M. Fröba, Angew. Chem. Int. Ed. Engl. 45 (2006) 3216.

[16] C.T. Kresge, J.C. Vartuli, W.J. Roth, M.E. Leonowicz, 08801 (2004).

[17] A. Corma, Q. Kan, M.T. Navarro, J. Pérez-Pariente, F. Rey, Chem. Mater. 9 (1997) 2123.

[18] P. Van Der Voort, C. Vercaemst, D. Schaubroeck, F. Verpoort, Phys. Chem. Chem. Phys. 10 (2008) 347.

[19] D. Zhao, Science 279 (1998) 548.

[20] S.A. Bagshaw, E. Prouzet, T.J. Pinnavaia, Science 269 (1995) 1242.

[21] R. Ryoo, J.M. Kim, C.H. Ko, C.H. Shin, J. Phys. Chem. 100 (1996) 17718.

[22] C. Yu, Y. Yu, D. Zhao, Chem. Commun. (2000) 575.

[23] Q. Huo, D.I. Margolese, U. Ciesla, P. Feng, T.E. Gier, P. Sieger, R. Leon, P.M. Petroff, F. Schüth, G.D. Stucky, Nature 368 (1994) 317.

[24] D.M. Antonelli, J.Y. Ying, Angew. Chemie Int. Ed. English 34 (1995) 2014.

[25] Y. Lu, R. Ganguli, C.A. Drewien, M.T. Anderson, C.J. Brinker, W. Gong, Y. Guo, H. Soyez, B. Dunn, M.H. Huang, J.I. Zink, Nature 389 (1997) 364.

[26] R. Ryoo, S.H. Joo, S. Jun, J. Phys. Chem. B 103 (1999) 7743.

[27] P. Yang, D. Zhao, D.I. Margolese, B.F. Chmelka, G.D. Stucky, Chem. Mater. 11 (1999) 2813.

[28] M.J. MacLachlan, N. Coombs, G.A. Ozin, Nature 397 (1999) 681.

[29] U. Ciesla, S. Schacht, G.D. Stucky, K.K. Unger, F. Schüth, Angew. Chemie 108 (1996) 597.

[30] U. Ciesla, S. Schacht, G.D. Stucky, K.K. Unger, F. Schüth, Angew. Chemie Int. Ed. English 35 (1996) 541.

[31] J. Lee, S. Yoon, T. Hyeon, S.M. Oh, K.B. Kim, Chem. Commun. (1999) 2177.

[32] E. Rossinyol, A. Prim, E. Pellicer, J. Rodriguez, F. Peiro, A. Cornet, J. Morante, B. Tian, T. Bo, D. Zhao, Sensors Actuators B Chem. 126 (2007) 18.

[33] A. Prim, E. Pellicer, E. Rossinyol, F. Peiró, A. Cornet, J.R. Morante, Adv. Funct. Mater. 17 (2007) 2957.

[34] E. Rossinyol, A. Prim, E. Pellicer, J. Arbiol, F. Hernández-Ramírez, F. Peiró, A. Cornet, J.R. Morante, L.A. Solovyov, B. Tian, T. Bo, D. Zhao, Adv. Funct. Mater. 17 (2007) 1801.

[35] D. Gu, F. Schuth, F. Schüth, Chem. Soc. Rev. 43 (2013) 313.

[36] Y. Ren, Z. Ma, P.G. Bruce, Chem. Soc. Rev. 41 (2012) 4909.

[37] Y. Ye, C. Jo, I. Jeong, J. Lee, Nanoscale 5 (2013) 4584.

[38] D. Grosso, F. Cagnol, G.J. de A.A. Soler-Illia, E.L. Crepaldi, H. Amenitsch, A. Brunet-Bruneau, A. Bourgeois, C. Sanchez, Adv. Funct. Mater. 14 (2004) 309.

[39] Y. Shi, Y. Wan, D. Zhao, Chem. Soc. Rev. 40 (2011) 3854.

[40] F. Schüth, Chem. Mater. 13 (2001) 3184.

[41] A.H. Lu, W. Schmidt, A. Taguchi, B. Spliethoff, B. Tesche, F. Schüth, Angew. Chem. Int. Ed. Engl. 41 (2002) 3489.

[42] M. Kang, S.H. Yi, H.I. Lee, J.E. Yie, J.M. Kim, Chem. Commun. (2002) 1944.

[43] H. Yang, D. Zhao, J. Mater. Chem. 15 (2005) 1217.

[44] K. Cassiers, T. Linssen, M. Mathieu, M. Benjelloun, K. Schrijnemakers, P. Van Der Voort, P. Cool, E.F. Vansant, Chem. Mater. 14 (2002) 2317.

[45] D. Zhao, Y. Wan, W. Zhou, Ordered Mesoporous Materials, Wiley-VCH Verlag & Co, Weinheim, Germany, 2013.

[46] S. Fujihara, T. Maeda, H. Ohgi, E. Hosono, H. Imai, S.-H. Kim, Langmuir 20 (2004) 6476.

[47] D.S. Kim, S.Y. Kwak, Appl. Catal. A Gen. 323 (2007) 110.

[48] Y. Wang, C.M. Yang, W. Schmidt, B. Spliethoff, E. Bill, F. Schüth, Adv. Mater. 17 (2005) 53.

[49] E.L. Crepaldi, G.J. de A. A. Soler Illia, A. Bouchara, D. Grosso, D. Durand, C. Sanchez, Angew. Chemie 115 (2003) 361.

[50] D. Li, H. Zhou, I. Honma, Nat. Mater. 3 (2003) 65.

[51] J. Lee, M.C. Orilall, S.C. Warren, M. Kamperman, F.J. DiSalvo, U. Wiesner, Nat. Mater. 7 (2008) 222.

[52] P. Periyat, K.V. Baiju, P. Mukundan, P.K. Pillai, K.G.K. Warrier, Appl. Catal. A Gen. 349 (2008) 13.

[53] C.F. Schöenbein, Phil. Mag. 14 (1839) 43.

[54] W.R. Grove, Phil. Mag. 14 (1839) 127.

[55] W.R. Grove, Phyl. Trans. (1843) 91.
[56] W.R. Grove, Phyl. Trans. (1845) 351.
[57] W. Nernst, Z. Elektrochemie 4 (1899) 41.
[58] E. Bauer, H. Preiss, Z. Elektrochemie 43 (1937) 727.
[59] W.E. Tragert, R.L. Fullman, R.E. Carter, Patent US 3138490, 1964.
[60] W. Oser, Patent US 3281273, 1966.
[61] R.J. Ruka, J. Weissbart, Patent US 3400054, 1968.
[62] D.T. Bray, L.D. Lagrange, U. Merten, C.D. Park, Patent US 3300344, 1967.
[63] D.H. Archer, E.F. Sverdrup, W.A. English, W.G. Carlson, Tech. Doc. Rept. ASD-TDR-63-448 (1963).
[64] J. Weissbart, J. Ruka, J. Electrochem. Soc. 109 (1962) 723.
[65] Westinghouse Electr. Corp., Final Report, Proj. Fuel Cell Rep. No 57 (1970).
[66] H.S. Spacil, Patent US 3503809, 1970.
[67] E.F. Sverdrup, A.D. Glasser, D.H. Archer, Patent US 3558360, 1971.
[68] D.B. Meadowcroft, J. Phys. D Appl. Phys. 2 (1969) 1225.
[69] D.D. Button, D.H. Archer, American Ceramic Society 68th Annual Meeting, 1966.
[70] F.J. Rohr, Patent G 2614728.4, 1976.
[71] E.D. Wachsman, K.T. Lee, Science 334 (2011) 935.
[72] A. Tarancón, Energies 2 (2009) 1130.
[73] B.C.H. Steele, J. Mater. Sci. 36 (2001) 1053.
[74] B. Steele, Solid State Ionics 75 (1995) 157.
[75] K. Wincewicz, J. Cooper, J. Power Sources 140 (2005) 280.
[76] D.J.L. Brett, A. Atkinson, N.P. Brandon, S.J. Skinner, Chem. Soc. Rev. 37 (2008) 1568.
[77] J.S. Ahn, D. Pergolesi, M.A. Camaratta, H. Yoon, B.W. Lee, K.T. Lee, D.W. Jung, E. Traversa, E.D. Wachsman, Electrochem. Commun. 11 (2009) 1504.
[78] D. Ding, X. Li, S.Y. Lai, K. Gerdes, M. Liu, Energy Environ. Sci. 7 (2014) 552.
[79] J.Y. Ying, AIChE J. 46 (2000) 1902.
[80] http://www.transparencymarketresearch.com/global-Refinery-Catalyst-Market.html.
[81] A. Taguchi, F. Schüth, Ordered Mesoporous Materials in Catalysis, 2005.
[82] C. Perego, R. Millini, Chem. Soc. Rev. 42 (2013) 3956.
[83] S.H. Joo, J.Y. Park, C.-K. Tsung, Y. Yamada, P. Yang, G.A. Somorjai, Nat. Mater. 8 (2009) 126.
[84] T. Wagner, S. Haffer, C. Weinberger, D. Klaus, M. Tiemann, Chem. Soc. Rev. 42 (2013) 4036.
[85] B.J. Melde, B.J. Johnson, P.T. Charles, Sensors 8 (2008) 5202.
[86] N. Yamazoe, Y. Shimizu, Sensors and Actuators 10 (1986) 379.
[87] B.M. Kulwicki, J. Am. Ceram. Soc. 74 (1991) 697.
[88] T. Ishida, T. Kobayashi, K. Kuwahara, H. Hatanaka, Nat. Tech. Rep. 24 (1978) 436.

[89] K. Otsuka, S. Kinoki, T. Usui, Denshi-Zairyo 19 (1980) 68.

[90] Y. Sudo, Denshi-Zairyo 19 (1980) 74.

[91] E. Traversa, Sensors Actuators B Chem. 23 (1995) 135.

[92] T. Morimoto, M. Nagao, F. Tokuda, J. Phys. Chem. 73 (1969) 243.

[93] G. Korotcenkov, Handbook of Gas Sensor Materials, Springer, 2013.

2
Experimental methods

A scientist in his laboratory is not a mere technician:
he is also a child confronting natural phenomena
that impress him as though they were fairy tails
- Marie Curie

2. Experimental Methods

2.1. Overview of the Chapter 35

2.2. Synthesis of Powder of the Mesoporous Materials 36

2.2.1. Synthesis of powder of the KIT-6 hard template 36

2.2.2. Synthesis of powder of the mesoporous metal oxide replicas 39

2.2.2.1. Procedures and materials 39

2.2.2.2. Silicon content after template removal 41

2.2.3. Impregnation of mesoporous metal oxides powder 41

2.3. Fabrication of Electrochemical Devices *43*

2.3.1. Shaping methods 43

2.3.1.1. Pulsed Laser Deposition (PLD) 43

2.3.1.2. Air brushing technique 44

2.3.1.3. Tape casting 45

2.3.1.3.1. Synthesis procedure 46

2.3.1.3.2. Volume shrinkage 47

2.3.1.4. Drop coating technique 49

2.3.2. Fabrication of Solid Oxide Fuel Cells (IT-SOFCs) 49

2.3.2.1. Fabrication of symmetrical cells 49

2.3.2.1.1. Symmetrical cells of mesoporous cermets 49

2.3.2.1.2. Symmetrical cells of MIEC infiltrated in mesoporous scaffolds 50

2.3.2.2. Fabrication of electrolyte-supported cells 51

2.3.2.3. Fabrication of anode-supported IT-SOFCs 53

2.3.3. Fabrication of humidity sensors 54

2.4. Structural Characterization Techniques 55

2.4.1. X-Ray Diffraction (XRD) 55

2.4.2. In-situ high temperature XRD 56

2.4.3. Small Angle X-ray Scattering (SAXS) 57

2.4.4. Nitrogen physisorption measurements (BET) 57

2.4.5. Scanning Electron Microscopy (SEM) 58

2.4.6. Transmission Electron Microscopy (TEM) and Electron Energy Loss Spectroscopy (EELS) *59*
2.4.7. Temperature Programmed Reduction (TPR) *60*
2.4.8. Thermogravimetric Analysis (TGA) and Oxygen Storage Capacity Experiments (OSC) *61*
2.4.9. Inductively Coupled Plasma Optical Emission Spectroscopy (ICP-OES) *61*
2.4.10. Raman spectroscopy *62*

2.5. Electrical Characterization Techniques 62

2.5.1. Experimental setup SOFCs *63*
2.5.2. Experimental setup sensors *64*
2.5.3. Impedance spectroscopy measurements *65*
2.5.4. Potentiostatic and galvanostatic measurements *68*

References 69

2. Experimental Methods

2.1. Overview of the Chapter

The **aim of this chapter** is to give a general overview of the experimental methods and tools employed in this thesis emphasizing their main interest for the following chapters. The work developed can be divided into two main experimental parts: (i) synthesis and fabrication (ii) characterization techniques.

The **section 2.2.1** presents the details of the **synthesis** route used to make the mesoporous powder from a hard silica template. A KIT-6 mesoporous silica is chosen as the template, due to its symmetry and versatility to fabricate replicas with different pore sizes. A brief explanation of the synthesis of the template powder from the precursors and the conditions used to make different replicas are detailed. Moreover, a brief structural characterization of the synthesized KIT-6 powder under different conditions is presented. The synthesis of the mesoporous KIT-6 is considered a tool for the further fabrication of the mesoporous oxides replicas, therefore is included in the experimental methods.

The different conditions used to make the mesoporous metal oxides replica are described in **section 2.2.2.** The KIT-6 with the desired geometry (single or double gyroid) and pore size is chosen accordingly for the further desired functionalization.

After that, the different **deposition techniques** used to **fabricate the electrochemical cells** are described in **section 2.3**.

Symmetrical cells with the synthesized mesoporous materials were fabricated, to study their conductivity and for optimization of critical parameters like the thickness of the layer, the attachment temperature to the electrolyte or the influence of the current collector. Once the cell with the mesoporous material was optimized, it was tested as an electrode for IT-SOFC.

In this thesis, both common cell configurations (electrolyte and anode supported cells) have been fabricated and electrochemically tested. Electrolyte-supported cells were fabricated because this configuration allows a more straightforward implementation and

characterization of electrode materials. In addition, since anode-supported cells are the ideal fuel cell configuration lowering the operating temperature, this type of cells based on mesoporous materials were fabricated and tested for cell optimization purposes.

Sensors based on the mesoporous replica powders were also fabricated in order to discuss the humidity sensing mechanism of the synthesized materials.

Characterization techniques are fundamental tools in material science to study the structure and the properties of the materials and understand their behavior. The different structural techniques routinely used to characterize the powder and the fabricated devices are described in the **section 2.4**. Moreover, the electrical and electrochemical properties were studied by common AC and DC methods. A general background of them and the specific setups employed are given in the **section 2.5**.

2.2. Synthesis of Powder of the Mesoporous Materials

2.2.1. Synthesis of powder of the KIT-6 hard template

A mesoporous silica KIT-6 with three-dimensional *Ia3d* symmetry, prepared by aqueous-based sol-gel route under acidic conditions is used as hard template in the whole thesis [1].

For the preparation of powder of KIT-6, a 1:1 (wt %) aqueous mixture of Pluronic® P123 triblock copolymer ($EO_{20}PO_{70}EO_{20}$, EO: ethylene oxide and PO: propylene oxide) and 1-butanol (BuOH), with a 0.5 M HCl concentration were mixed at 36 ºC in a thermal bath. Tetraethyl orthosilicate (TEOS) was added as silicon precursor in a mole ratio of TEOS:P123:HCl:H_2O:BuOH = 1:0.017:1.83:195:1.31.

Once all the components were dissolved, a hydrothermal treatment was performed at either 36 ºC or 90 ºC for 24 h and the resulting template will be denoted as **KIT-6-36** and **KIT-6-90**, respectively. Samples were then filtered, cleaned with water and dried in an oven at 60 ºC. Finally the powder was calcined at 550 ºC for 4 h to burn all the surfactants.

The structure of the synthesized KIT-6 mesoporous silica templates was studied by low angle XRD diffraction and nitrogen physisorption measurements. **Figure2.1a** shows the low angle X-ray pattern of the synthesized KIT-6. The characteristic XRD peaks confirm the formation of an ordered mesoporous structure with cubic *Ia3d* symmetry. The characteristic peak corresponding to the plane (211), which indicates the formation of the cubic *Ia3d* phase was observed after 24 hours of reaction, from a hydrothermal treatment temperature of 36 °C, in agreement with Kleitz *et al.* [1]. The position of the (211) reflection of the mesoporous structure, allows determining the periodicity of the ordered structure. A lattice constant (*b*) of 21.6 and 22.7 nm is obtained for the KIT-6-36 and KIT-6-90, respectively (see **Table 2.1**).

Figure 2.1b shows a typical TEM image of the cubic *Ia3d* KIT-6 silica recorded along the [111] direction where the ordered domains of the 3-D bicontinuous meso-structure are clearly observed.

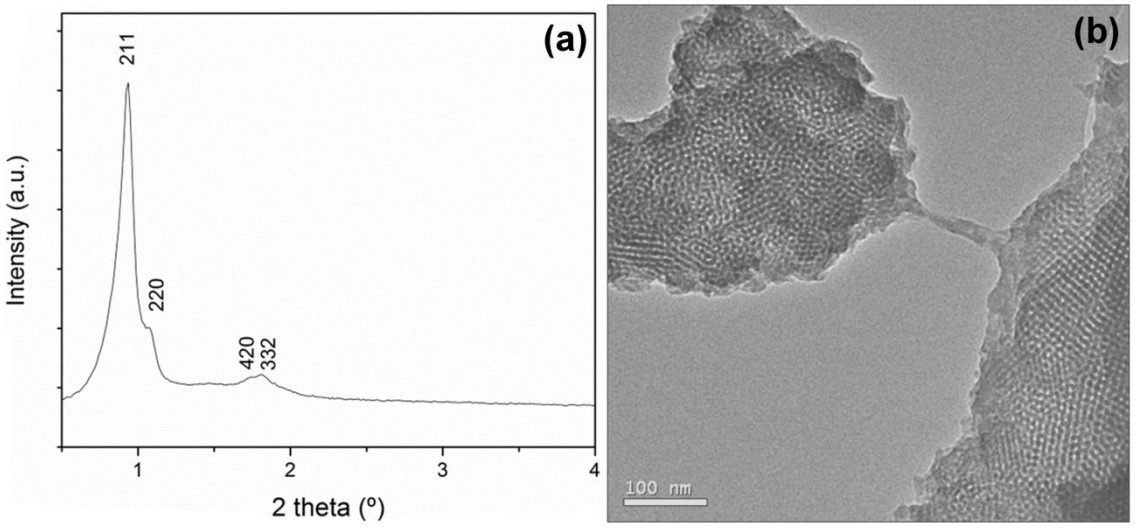

Figure 2.1. a) Low angle XRD pattern and b) TEM image along the [111] direction characteristics of the KIT-6 mesoporous silica template with *Ia3d* cubic structure.

The nitrogen adsorption–desorption isotherms obtained for the KIT-6-36 and KIT-6-90 mesoporous silica templates are shown in **Figure 2.2a**. The isotherms for both silica templates can be classified as type IV, typical of mesoporous materials which present

pore condensation with a H1 hysteresis loop, which is characteristic of channel pores with narrow size. The rest of the structural parameters obtained from the nitrogen physisorption measurements for the KIT-6 hydrothermal synthesized at 36 and 90 ºC are shown in **Table 2.1.** BET areas of 700 and 786 m^2/g and pore volumes of 0.620 and 0.829 cm^3/g were obtained for the KIT-6-36 and KIT-6-90 silica templates, respectively. The mean pore size was calculated using the BJH model (d_{BJH}) and the adsorption isotherm data is 5.6 nm for the KIT-6-36 and 8.6 nm for the KIT-6-90.

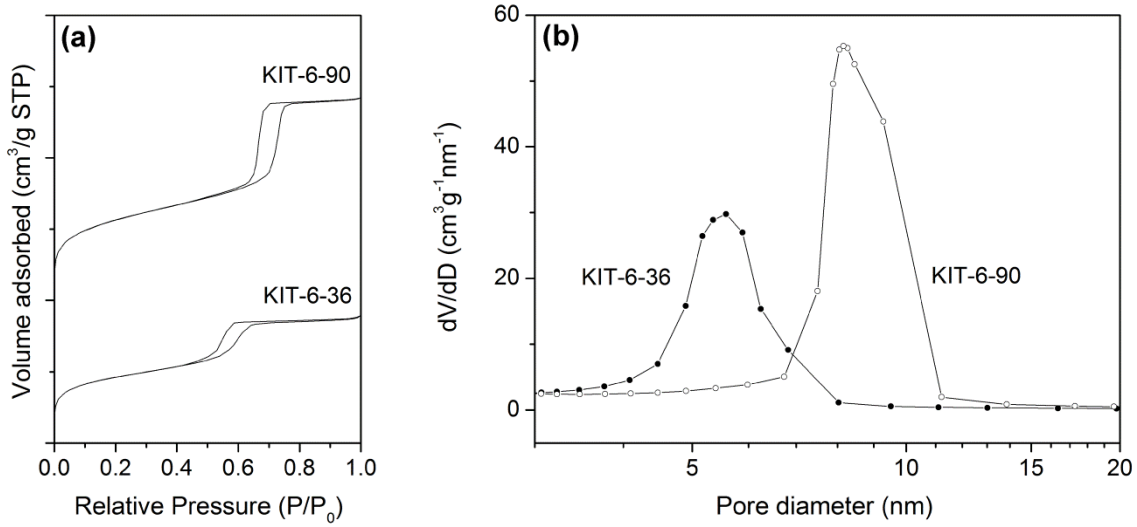

Figure 2.2. a) N_2 adsorption–desorption isotherms and b) Pore size distributions of the KIT-6 with hydrothermal treatments performed at different temperatures: 36 and 100 °C (KIT-6-36 and KIT-6-90, respectively).

It should be pointed out that in agreement with the literature [1], different hydrothermal temperatures permit to tune the pore size of the silica hard template. **In this thesis,** the mesoporous of the KIT-6 is always used as silica template. The synthesis parameters to obtain either KIT-6-36 or KIT-6-90 are chosen depending on the final application of the mesoporous replica, as explains below, in order to optimize the performance.

Table 2.1. Structural Parameters obtained by Analysis of XRD Patterns and Nitrogen Adsorption-Desorption Measurement.

	b (nm)	**BET (m^2/g)**	**Pore volume (cm^3/g)**	**d_{BJH}* (nm)**
KIT-6-36	21.6(1)	700 (7)	0.620	5.6 ± 0.7
KIT-6-90	22.7(1)	786 (2)	0.829	8.6 ± 0.9

* The uncertainty corresponds to the standard deviations of the Gaussian pore size distributions

2.2.2. Synthesis of powder of the mesoporous metal oxide replicas

2.2.2.1. Procedures and materials

Mesoporous metal oxides are synthesized as replica of silica KIT-6 hard template by wet impregnation method and subsequent calcination. In general, a stoichiometric amount of metal nitrates is dissolved in ethanol. Once dissolved, the silica template KIT-6 is added, keeping the ratio 1.5 mmol of metal ions per 0.15 g KIT-6.

The resulting mixture is stirred for 1 h, dried at 60 ºC and the resulting powders were subjected to a final calcination step (in general at a temperature of 600 ºC for 5 h) for achieving the desired single phase.

Remaining silica template is removed with hot 2 M NaOH at 70 ºC and the solid phase is separated by centrifugation, washed several times with deionized water and dried. A scheme of the synthesis procedure followed to obtain mesoporous replicas from KIT-6-36 and KIT-6-90 is shown in **Figure 2.3**.

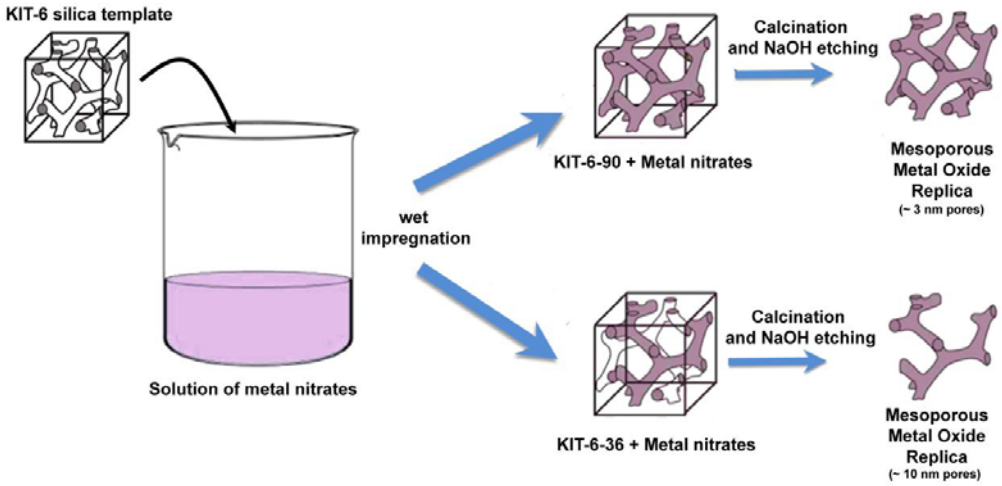

Figure 2.3. Scheme of the synthesis of powder of mesoporous metal oxide replicas by wet impregnation of the silica template KIT-6.

Different materials were fabricated by employing slight different procedures. **Table 2.2** summarizes the materials synthesized as mesoporous replicas and their acronyms. The impregnation approach, type of KIT-6 (hydrothermal synthesized either at 36 or 90 ºC), the precursors and the calcination conditions used are shown. Moreover, the chapters showing the results of the structural characterization and the further functionalization of the mesoporous powder are indicated.

Table 2.2. Synthesis details of the Powder of the Mesoporous Metal Oxide Replicas.

	Acronym	Impregnation Approach	KIT-6	Precursors	Calcination	Chapter
Ceria doped gadolinium ($Ce_{0.8}Gd_{0.2}O_{1.9}$)	CGO CGO-600	multistep	KIT-6-90	$Ce(NO_3)_3 \cdot 6H_2O$ $Gd(NO_3)_3 \cdot 6H_2O$ $\frac{[Gd^{3+}]}{[Gd^{3+}]+[Ce^{3+}]} = 2$	350 ºC, 4 h 600 ºC, 5 h	**3**
Nickel oxide (NiO)	NiO	single	KIT-6-90	$Ni(NO_3)_2 \cdot 6H_2O$	600 ºC, 5 h	**4**
Ceria doped samarium ($Ce_{0.8}Sm_{0.2}O_{1.9}$)	SDC	single	KIT-6-36	$Ce(NO_3)_3 \cdot 6H_2O$ $Sm(NO_3)_3 \cdot 6H_2O$ $\frac{[Sm^{3+}]}{[Sm^{3+}]+[Ce^{3+}]} = 2$	600 ºC, 5 h	**5**

2.2.2.2. Silicon content after template removal

Due to the well-known negative effect of SiO_2 segregation impurities along the grain boundaries and surface on ionic conductivity and catalysis performance [2–5], an analysis of the silica content after template removal have been carried out by Inductively Coupled Plasma and Energy Dispersive X-Ray (EDX).

An iterative washing methodology was implemented in the methodology. Increasing the number of times where the mesoporous material is washed with the NaOH hot solution, the silica content remaining in the replica decreases (1 wash ~3.51 % Si, 2 washes ~1.6 % Si, 4 washes ~1.3 % Si). It was also found better to wash the replica several times with deionized water (1.16 % Si) than with a solution of H_2O:EtOH (50 % wt) (1.5 % Si).

Although these values are over the typical levels of silicon impurities that affect the metal oxide properties (low-grade metal oxide powders typically contain silica impurities < 100 ppm), it is believed that keeping the high surface area contribute to minimize the portion of surface blocked by the impurity in the mesoporous case of study. Despite this, an iterative process of template removal is recommended.

2.2.3. Impregnation of mesoporous metal oxides powder

Ceramic-Metal (cermet) mesoporous powders were synthesized by a subsequent impregnation step. The metallic phase mesoporous replica (obtained as explained in the **previous section**), was further impregnated with an ethanol solution of the stoichiometric amount of the corresponding ceramic nitrate salts, stirred for 1 h and dried. Finally, the ceramic crystallized inside the metallic phase template by a thermal treatment at 900 - 1100 ºC for 3 h (**Figure 2.4**). In general, powder with two different weight ratios of metallic phase – ceramic phase (50:50 % wt and 65:35 % wt) were prepared.

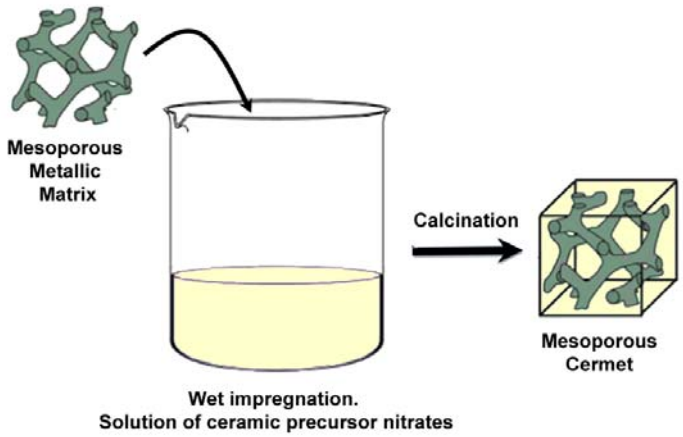

Figure 2.4. Scheme of the synthesis of the impregnation of mesoporous metal oxide powder.

By the described approach, several common cermets used as anodes in IT-SOFCs were synthesized. The composition of the cermet, metallic matrix, ceramic precursors and calcination conditions are described in the **Table 2.3**. A complete structural characterization of the resulting cermets is shown in **Chapter 4**. Moreover, the performance of cells with mesoporous cermets was measured in the indicated chapters. The **Appendix A** is devoted to optimize the composition of the nickel based cermets.

Table 2.3. Synthesis details of the Impregnation of Mesoporous Metal Oxides.

Cermet	Acronym	Mesoporous Metallic Matrix	Ceramic Precursors	Calcination	Chapter
NiO - $Ce_{0.8}Gd_{0.2}O_{1.9}$	NiO - CGO	NiO	$Ce(NO_3)_3 \cdot 6H_2O$ $Gd(NO_3)_3 \cdot 6H_2O$	900 – 1100 ºC, 3 h	**4**
NiO – 92 ZrO_2·8 Y_2O_3	NiO - YSZ	NiO	$Zr(NO_3)_2 \cdot xH_2O$ $Y(NO_3)_3 \cdot 6H_2O$	900 ºC, 3 h	**4**
NiO - $Ce_{0.8}Sm_{0.2}O_{1.9}$	NiO - SDC	NiO	$Ce(NO_3)_3 \cdot 6H_2O$ $Sm(NO_3)_3 \cdot 6H_2O$	1100 ºC, 3 h	**6**

2.3. *Fabrication of Electrochemical Devices*

In this section the deposition techniques used to fabricate the electrochemical devices are introduced. Firstly, a general description of the different shaping methods and the usefulness in the thesis is presented.

In the second part of the section the fabrication of the electrochemical devices are described: (i) Symmetrical cells, (ii) Electrolyte-supported IT-SOFCs, (iii) Anode-supported IT-SOFCs and (iv) Sensors.

2.3.1. Shaping methods

2.3.1.1. Pulsed Laser Deposition (PLD)

Pulsed laser deposition (PLD) is a thin film deposition technique which uses high power laser pulses to melt, evaporate and ionize a target material. The ablation of the target produces a plasma plume that deposits perpendicularly onto a substrate where it condenses and the thin film grows (**Figure 2.5**).

The non-equilibrium nature of the PLD ablation process, due to absorption of high laser energy densities by a small volume of material on the target, allows growing films with similar stoichiometry than the one of the target material. It is then possible growing crystalline films at temperatures much lower than the typical crystallization temperatures required for most complex oxides (usually higher than 1000 ºC).

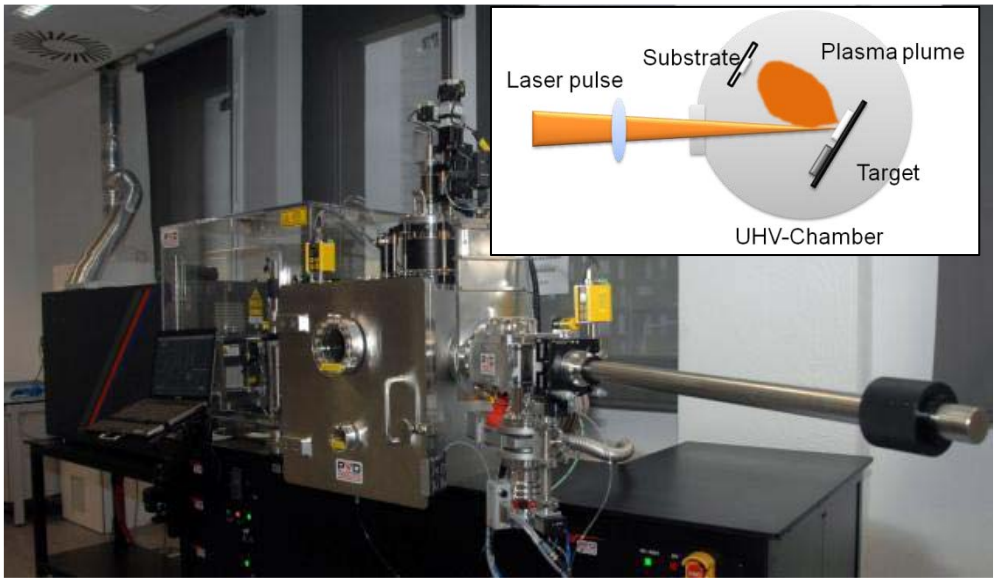

Figure 2.5. PLD equipment used in this work to deposit thin films of dense CGO (located at IREC). The inset shows a schematic diagram of a typical laser deposition setup.

In this thesis, PLD was used to fabricate dense diffusion barrier layers of CGO onto one side of the tape castings for the electrolyte-supported IT-SOFCs. Dense thin film layers fabricated with PLD, were demonstrated to be an efficient method to prevent the migration of ions from the cathode towards the electrolyte and minimize the CGO-YSZ inter-diffusion, additionally presenting low resistance. In the PLD chamber, the CGO target was irradiated with a 20 ns pulse from a KrF excimer laser with a characteristic 248 nm wavelength and laser energy density of 0.8 J/cm^2. The substrate was located at a distance of 9 cm from the target. The deposition rate was 0.38 nm/s. This procedure results in a CGO dense layer of thickness ~ 1-2 μm.

2.3.1.2. Air brushing technique

Ethanol-inks based of commercial or mesoporous powders were prepared to be airbrushed. A 1 % wt of dispersant PVP (polyvinylpyrrolidone) is added to the mixture and stirred for more than 24 h. For air-brushing the variable parameters: pressure of

nitrogen, distance to the target substrate and number of times to pull the trigger button were optimized and fixed, to achieve reproducible layers of ~ 20 μm thickness.

In this thesis, air brushing was routinely used to fabricate porous layers as electrodes for IT-SOFCs, due to its simplicity and the possibility to easily obtain reproducible thicknesses.

2.3.1.3. Tape casting

Tape casting is a ceramic forming technology, developed by the industry as the demand of larger and thinner (reproducible) substrates increased [6]. In this technique, a slurry is spread over a planar surface, controlling the thickness by carefully chosen the height of the doctor blade (**Figure 2.6**). The uniformity and viscosity of the slurry is crucial to fabricate a proper and consolidated *green body*. The slurry is made by grinding the ceramic powder in an organic vehicle. The use of organic additives is essential since each of them plays a different role [7,8].

In the first step of the milling process, the powder is mixed with the dispersant and the solvent; the mixture is grinded to break agglomerates and obtain a homogeneous slurry with low viscosity. In a second step, a binder and a plasticizier are added to prepare the slurry with the proper viscosity for casting. After degasification of the slurry, it is extended uniformly over a planar surface covered by a sheet of paper or plastic, with a thickness controlled by selecting the height of the doctor blade. The so-extended tape needs to be dried to evaporate the solvents. After that, the obtained *green body* is ready to be cut to the desired geometry and sintered to produce a dense ceramic layer.

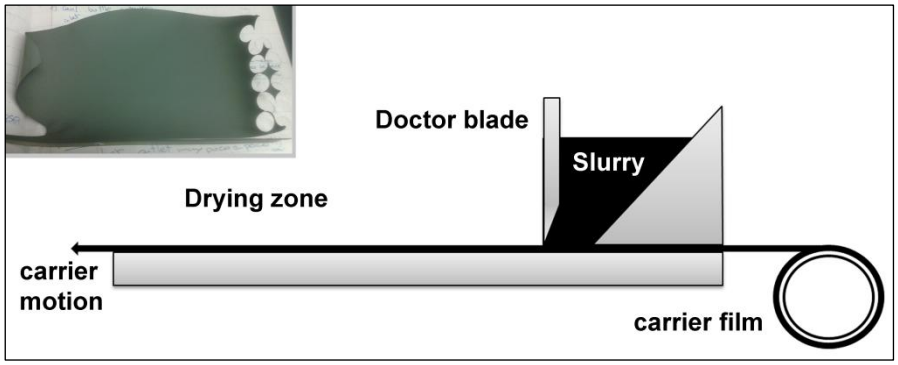

Figure 2.6. Scheme of a laboratory tape-casting setup. The inset image shows the fabricated *green* mesoporous NiO-YSZ tape casting (*University of Georgia Tech*).

In this thesis, tape castings of NiO-YSZ from both commercial and mesoporous powders were prepared to constitute the substrate of anode-supported IT-SOFCs. Details of the synthesis procedure and a study of the volume shrinkage of the fabricated tapes are presented below.

2.3.1.3.1. Synthesis procedure

All tape cast slurries are prepared using a two-stage milling process. The initial slurry contained the NiO-YSZ powder (55 - 45 % wt), graphite and starch (added as pore formers), the solvents (ethanol and xylene) and the dispersant (Menhaden Fish Oil, Richard E. Mistler). This non-viscous slurry is ball-milled for 24 h prior to addition of the other constituents.

After that, a common binder (Polyvinyl Butyral, PVB) and plasticizers (Polyalkylene Glycol, PAG and Butyl Benzyl Phthalate, BBP) are added and the mixture is ball-milled for another 24 h to obtain uniform and stable slurry, which is then degassed at room temperature under vacuum before cast. The height of the doctor blade is chosen to obtain a *green tape* with the desired thickness. The tape dried overnight before punched into ~ 10.7 – 12.7 cm diameter pieces.

2.3.1.3.2. Volume shrinkage

The porous anode substrate can greatly enhance the electrolyte-layer densification during the co-firing, by loss of pore volume from the anode self-shrinkage. Shrinkage measurements of the different anode tape castings prepared were done, pre-sintering the tapes from 25 to 1150 ºC.

The volumetric shrinkage of each type of anode is measured with a caliber, after sintering in the same furnace at each temperature for 2 hours, and calculated in comparison to green state as,

$$\Delta S = \frac{V_{sintered}}{V_{green}} - 1 \qquad \textbf{(2.1)}$$

Figure 2.7 shows the volumetric shrinkage curves measured for the different types of the anode supports fabricated with commercial and mesoporous powder. Tapes of commercial powder were fabricated by two approaches: in the first the fabricated tape as-cast and dried gave a thickness of ~ 700 μm, a second approach was done by pressing two laminated thinner anode tapes (of ~ 300 μm thickness each) under a pressure of 100 MPa. On the other hand, mesoporous tapes were fabricated; the tapes as-cast and dried had a thickness of ~ 600 μm.

For the anode tapes made with regular NiO-YSZ powders the sintering shrinkage can be separated into three stages. The early volumetric shrinkage of 3 - 4 % observed for sintering below 750 ºC, can be attributed to the carbon burn-out and initial particle growth within the anode body. At the second stage between 750 - 950 ºC, the anodes further shrink by 3 - 6 %, which is possibly due to the begin of sintering for NiO particle in the anode at around 900 ºC [9]. For the first two stages, un-pressed and pressed anode tapes rather exhibited similar sintering shrinkage as they had the same powder, composition and amount of pore former.

Significantly larger shrinkage occurred for pressed-tape in comparison to un-pressed tape at temperature above 1000 ºC, when sintering of the YSZ particles in anode can be

also expected to begin. Even though, anode substrates in this experiment are rather free-sintered without the constraint effects from co-sintering with electrolyte, the results verify that introduction of compaction pressure of 100 MPa clearly enhanced the anode substrates shrinkage, which greatly improves the SSZ-SDC electrolyte densification at relatively low co-sintering temperature.

On the other hand, the anode tape castings made with mesoporous NiO-YSZ powders showed no apparent shrinkage until temperature above 900 ºC and the sintered anode substrate was very weak, even for performing the size measurement. This is because the multi-step synthesis of mesoporous NiO-YSZ powder involves pre-calcination of the particles at 900 ºC, which increases the structure stability while reducing the sintering of the anode during subsequent processing at low temperature.

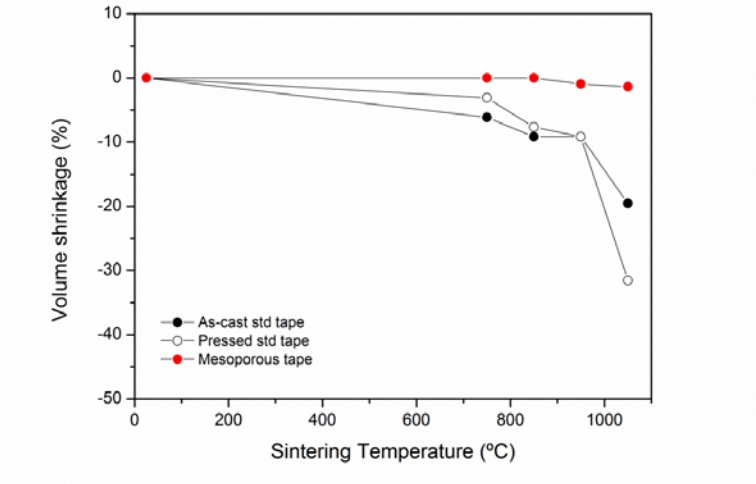

Figure 2.7. Volumetric shrinkage curves versus the sintered temperature carried out on the different tape-casting prepared.

Based on the previous discussion green tape-castings made from commercial NiO-YSZ powder were subjected to pre-sintering step at 850 °C for 2 h, while temperatures up of 1100 ºC for 2 h were required for the fabricated mesoporous green tapes to get enough mechanical stability and volume shrinkage, to further fabricate on the top a dense electrolyte layer.

2.3.1.4. Drop coating technique

Wet process techniques are considered cost effective, although they are not fully optimized to fabricate dense layers [10]. The cost-efficient and industrially robust fabrication of high-performance SOFCs is very important to promote their energy-competiveness for large-scale applications.

Several physical and chemical techniques have been employed to fabricate high quality and dense thin electrolyte films. However, these vapor deposition techniques (*e.g.* chemical vapor deposition (CVD), physical vapor deposition (PVD), electrochemical vapor deposition (EVD), pulsed laser deposition (PLD), plasma spray,…) are in general more expensive.

In this thesis, fabrication of dense electrolyte layers was deposited on the pre-sintered tape casting by a drop coating process and further tested as anode supported cells. More details about the deposition procedure and the materials used can be found in the **section 2.3.1.3**. Moreover, a study performed to reduce the firing temperature of the deposited electrolyte is shown in **Appendix B**.

2.3.2. Fabrication of Solid Oxide Fuel Cells (IT-SOFCs)

2.3.2.1. Fabrication of symmetrical cells

Two different approaches for fabricating electrodes of symmetrical cells are done, using different materials: (i) mesoporous cermets as anodes, (ii) infiltration of MIEC catalyst in mesoporous ceramic scaffolds as cathodes. Ceria based pellets are used as electrolytes.

2.3.2.1.1. Symmetrical cells of mesoporous cermets

Symmetrical cells based on CGO pellets working as electrolytes and mesoporous nickel-ceria cermets (Ni-CGO) as electrodes are fabricated. Full-dense pellets of CGO

($\delta \sim 99$ %) are prepared by uniaxial-pressing of commercial powder of CGO (CeO_2 - 10 mol% Gd_2O_3, Fuel Cell Materials) and sintered at 1425 ºC. In order to improve the attachment of the electrodes, a very thin layer of CGO is airbrushed on both sides and heat treated at 1350 ºC for 3 h.

To deposit the electrodes, mesoporous nickel/gadolinium-doped ceria ink based on ethanol is airbrushed onto both sides of the ceria pellets. Single and double layer electrodes are deposited. A study performed to optimize the composition of the cermets is shown in **Appendix A**. The single layer electrode is composed by NiO:CGO with 65:35 % wt, while the double layer is based on a functional layer of NiO-CGO with 50:50 % wt placed close to the electrolyte and a layer of NiO-CGO 65:35 % wt closer to the current collector. The layers are attached at a time at T_{att} = 1200 ºC for 3 h. A scheme is shown in **Figure 2.8**. The morphology and electrochemical performance of the so-fabricated mesoporous cermets as anodes of IT-SOFCs are presented in **Chapter 4**.

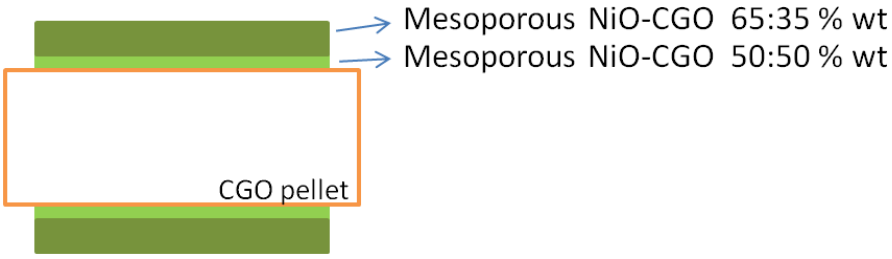

Figure 2.8. Basic scheme of the symmetrical cells fabricated with a double layer of mesoporous cermets.

2.3.2.1.2. Symmetrical cells of MIEC infiltrated in mesoporous scaffolds

Symmetrical cells based on samaria-doped ceria (SDC) pellets are fabricated. Full dense SDC pellets produced by uniaxial pressure from SDC commercial powder (Samaria doped ceria 20 % - Fuel Cell Materials) and sintered at 1425 ºC.

To fabricate the ceramic scaffold, an ink based on ethanol is fabricate with the SDC mesoporous powder and airbrushed onto both sides of the ceria pellets. The layer is sintered at different temperatures, in order to optimize the attachment temperature

(T_{att} = 1000, 1050, 1100 ºC). The thickness of the deposited porous layer is ~ 10 µm and the electrode active area 0.7 cm^2.

The catalyst MIEC $Sm_{0.5}Sr_{0.5}CoO_{3-\delta}$ (SSC) is introduced into the as-sintered mesoporous scaffold by a solution infiltration [11]. Stoichiometric amounts of $Sm(NO_3)_3$, $Sr(NO_3)_2$, $Co(NO_3)_2 \cdot 6H_2O$ are mixed in a mixture of water and ethanol to form a 0.1 $mol \cdot l^{-1}$ solution, a stoichiometric amount of glycine was added as a complexing agent and 5 % wt polyvinyl pyrrolidone (PVP) is added as surfactant, 15 µl of the so-prepared solution is deposited on the surface of the porous cells. Three cycles are done, followed by a calcination step at 800 ºC for 2 h. The final amount of SSC infiltrated is determined to be ~ 25 % wt (calculated by weight difference). A basic scheme with the steps followed is shown in **Figure 2.9**. The morphology of the layers and the electrochemical characterization of the infiltrated mesoporous scaffolds as cathodes of IT-SOFCs are presented in **Chapter 5**.

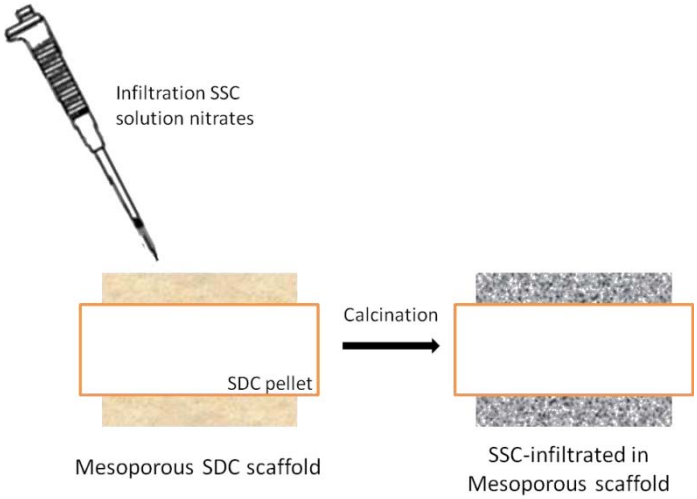

Figure 2.9. Basic scheme of the fabrication of MIEC infiltrated in mesoporous scaffolds symmetrical cells.

2.3.2.2. Fabrication of electrolyte-supported cells

The fabricated electrolyte-supported cells were based on a commercial electrolyte of 10Sc1CeSZ (10% mol Sc_2O_3, - 1% mol CeO_2 – ZrO_2) made by tape casting of 150 µm thickness (Kerafol). As explained the **section 2.3.1.1**, a dense diffusion barrier layer of

CGO of 1-2 µm was deposited by Pulse Laser Deposition (PLD), onto the cathode side of the tape casting. In order to improve the attachment of the electrodes firstly, a very thin layer of a diluted ink of CGO is airbrushed on both sides of the 10Sc1CeSZ tape casting.

Ethanol-based inks of the mesoporous/commercial powder used as electrodes were air-brushed onto the tape casting and sintered. Details of the composition, materials, sintering conditions and the chapter with the structural and the electrochemical characterization results are depicted in **Table 2.4**. A scheme of the electrolyte supported cells and typical images of the cells measured in this work are shown in **Figure 2.10**.

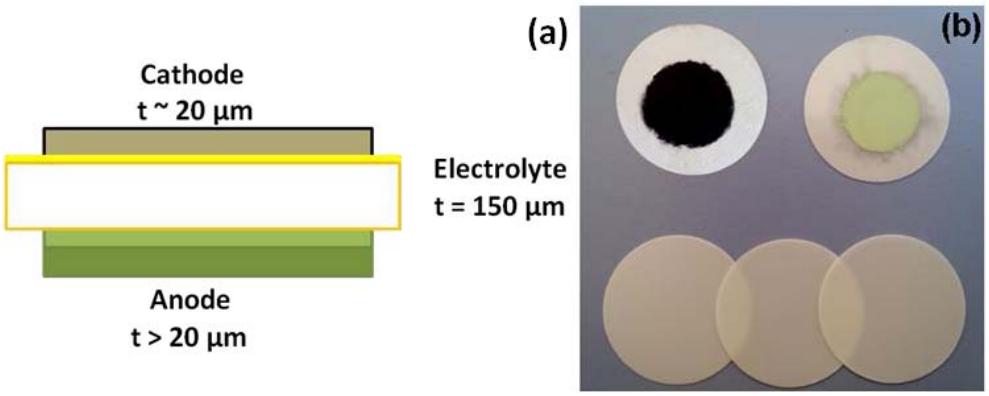

Figure 2.10. (a) Scheme of the different layers and thicknesses and (b) Typical images of electrolyte-supported cells fabricated in this thesis.

Table 2.4. Summary of the electrolyte-supported cells fabricated and characterized (in the denoted chapter).

Anode	% wt	T attachment	Cathode	T attachment	Chapter
Mesoporous Ni - CGO	50:50 65:35	1200 ºC, 3 h	$La_{0.6}Sr_{0.4}Co_{0.2}Fe_{0.8}O_3$ (LSCF)	1100 ºC, 3 h	**4**
Mesoporous Ni - SDC	50:50 65:35	1200 ºC, 3 h	Mesoporous SDC scaffold Infiltrated $Sm_{0.5}Sc_{0.5}CoO_{3-\delta}$ (SSC)	1000 ºC, 2 h 800 ºC, 2 h	**6**

2.3.2.3. Fabrication of anode-supported IT-SOFCs

Anode-supported cells based on tape casting of both mesoporous and commercial NiO-YSZ powders were fabricated as explained the **section 2.3.1.3.** Subsequently, a double electrolyte layer of SSZ-SDC ($(Sc_2O_3)_{0.10}(ZrO_2)_{0.90}$ - $Sm_{0.20}Ce_{0.80}O_{2-x}$) are deposited by drop coating (**section 2.3.1.4**), resulting a total thickness of ~ 10-15 µm. The anode and the electrolyte assembly are co-fired together at 1250 ºC. Finally, an ink of SSC-SDC powder is brushed onto the sintered electrolyte as cathode.

The fabrication of the cells was performed by following the standards of *Meilin Liu Group* (MSE, Georgia Institute of Technology). The conditions followed in each fabrication step are described in **Table 2.5,** as well as it is indicated the chapter were the cells are characterized. The **Figure 2.11** shows a scheme of the different layers and typical pictures of the anode-supported cells fabricated.

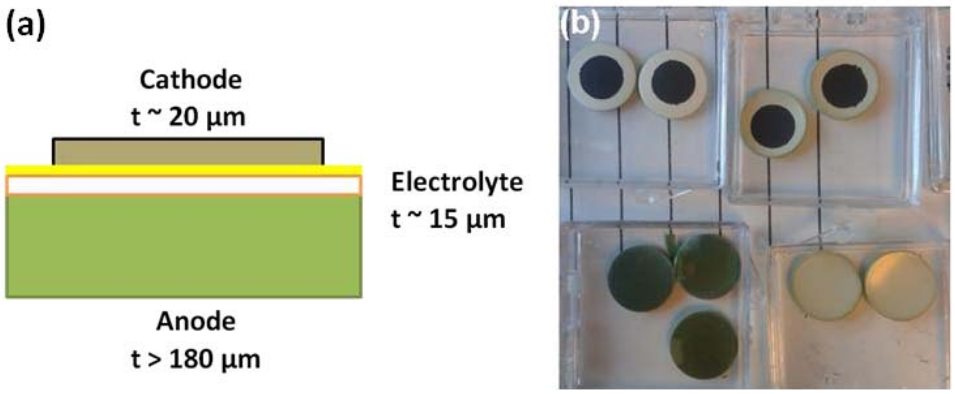

Figure 2.11. (a) Scheme of the different layers and thicknesses and (b) Typical images of anode-supported cells fabricated in this thesis.

In addition, efforts to reduce the co-sintering temperature of the anode/electrolyte assembly were done, in order to reduce the fabrication cost and minimize the inter-diffusion or reaction between the cell components, while maintaining the optimum electrode microstructure. The results were performed over standard cells from Meilin Liu's Group and are shown in **Appendix B**. Dense double SSZ-SDC electrolyte layers

were successfully fabricated at temperatures of 1200º C by engineering the particle size of the electrolyte precursors and by adding sintering aid.

Table 2.5. Summary of the anode-supported cells fabricated and characterized (in the denoted chapter).

Tape Casting	% wt	Pre-sintering step	Electrolyte	Co-firing T	Cathode	Sintering T	Chapter
Mesoporous Ni - YSZ	55:45	1100 °C, 2 h	SSZ- SDC	1250 ºC	SSC-SDC	950 ºC, 2 h	**4**
Commercial Ni – YSZ	55:45	850 ºC, 2 h	SSZ- SDC	1250 ºC	SSC-SDC	950 ºC, 2 h	**4**

2.3.3. Fabrication of humidity sensors

Sensors were fabricated from ethanol inks based on mesoporous powder (30 % wt). Inks of CGO were airbrushed on a commercial alumina substrate with interdigitated electrodes (Planar IDE Au, *Synkera*) and sintered at 900 ºC for 1 h, to ensure mechanical strength and thermal stability (**Figure 2.12**). The so-prepared mesoporous layer has dimensions of 6.35 mm length and two different thicknesses were tried 12-13 μm and 4 μm.

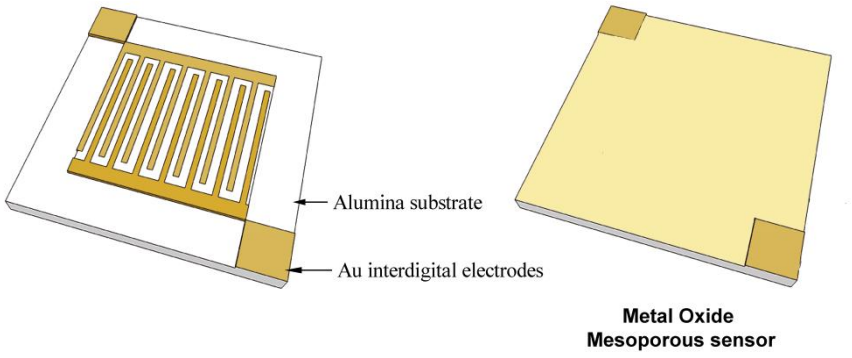

Figure 2.12. Scheme of the alumina substrate with interdigital electrodes (left) and the sensor after deposition of the ceramic oxide mesoporous layer (right).

2.4. Structural Characterization Techniques

2.4.1. X-Ray Diffraction (XRD)

X-ray diffraction is a non-destructive characterization technique in which the pattern collected is produced by exposition of a crystal to X-rays. If the wavelength of the X-rays launched is on the order of magnitude of the interatomic distances of the crystal, the X-rays will diffract with a specific direction and intensity and therefore, the so-generated diffraction pattern is specific of the atomic and molecular structure of the crystal under study. A qualitative and quantitative analysis of the patterns allows identifying the crystalline phase and determining the lattice parameter.

An analysis of the peak shape gives information about the crystallite size distribution, the micro-strain or the extended defect concentration. Williamson and Hall proposed a method for deconvoluting size and strain broadening by analysis of the peak width as function of 2θ [12]. According to the Scherrer and Wilson equation [13,14],

$$\beta \cos\theta = \frac{4K\lambda}{3D} + 4\varepsilon \sin\theta \qquad \textbf{(2.2)}$$

where,

β = integral breadth of a reflection (in radians)

K = Scherrer constant (equals 0.89 for spherical grains)

λ = X-ray wavelength

θ = diffraction angle

D = crystallite size

ε = microstrain

The plot $\beta cos\ \theta$ on the y-axis and $4sin\ \theta$ on the x-axis allows to linear fit the data and extract the crystallite size and the strain.

X-ray diffraction (XRD) was routinely used **in this thesis** to identify and further, corroborate the phase of all materials. The so-called Williamson-Hall methodology was employed to determine the crystallite size and micro-strain the samples in the **Chapter 3**. Different equipments were used, but generally the scans were performed at room temperature, using copper K_α radiation, in the 2θ range from 20 to 80°. Most of the XRD patterns were obtained from a Philips X'Pert Pro automated diffractometer equipped with an X'celerator detector (located in the Scientific-Technical Services, University of Barcelona) and a Bruker D8 automated diffractometer, with a nickel filter and Lynx Eye detector.

2.4.2. In-situ high temperature XRD

In-situ XRD is a powerful technique determining structural changes of the materials. In particular, in-situ high temperature XRD is a high throughput technique, being time saving compared to the measurement of several samples annealed individually.

Figure 2.13. X-ray diffraction with the heating stage accessory to perform in-situ measurements located at IREC.

In this thesis in-situ temperature XRD was used to study the crystallography changes of the synthesized mesoporous $Ce_{0.8}Gd_{0.2}O_{1.9}$ (**Chapter 3**) with both, temperature and time. The measurements were performed in the heating stage of an Anton Paar XRK 900 heating chamber coupled in the Bruker D8 equipment (**Figure 2.13**). The powder was loaded onto the alumina sample holder and heated at a rate of 12 ºC· min^{-1} up to the target temperature (800 and 900 ºC) and held for 24 h.

2.4.3. Small Angle X-ray Scattering (SAXS)

Small angle X-ray scattering (SAXS) or low angle X-ray diffraction is a non destructive technique, usually performed at angles between 0º and 10º. It follows the same principles of X-ray diffraction, in this case for investigating nanostructures from < 1 nm up to 200 nm in size. Therefore, the structure and space group symmetry of the ordered mesoporous materials are detected.

Generally **in this thesis**, the low angle X-ray spectra were collected in the same Bruker D8 automated equipment in a 2θ range from 0.5º to 3.5º to study the structural ordered mesoporous structure of the synthesized materials.

2.4.4. Nitrogen physisorption measurements (BET)

Fundamental parameters of the surface of the solids, such the specific surface area and porosity can be obtained from the nitrogen physisorption measurements.

The Brunauer-Emmet-Teller (BET) theory is widely used in surface science to determine the specific surface area of solid materials. It is an extension of the Langmuir theory, to the physical adsorption of gas molecules on multilayers. The total volume of pores was obtained from a single point adsorption method at $P/P_0 = 0.999$.

The pore size distribution was calculated by the Barrett-Joyner-Halenda (BJH) model, which uses a modified Kelvin equation and the statistical thickness equation (t-curve) to determine the pore size. The BJH can be generated from both the adsorption and the desorption branches of the isotherms.

In the present thesis, N_2-physisorption measurements were performed in a Micromeritics Tristar 3000 surface analyzer at the temperature of liquid nitrogen (77 K) to study the specific surface area, volume and distribution of pores of the mesoporous materials.

2.4.5. Scanning Electron Microscopy (SEM)

Scanning electron microscopy (SEM) utilizes a focus beam of high-energy electrons to generate a variety of signals at the surface of the solid sample, coming from the electron-sample interaction. The beam of electrons which typically have energy from ~ eV to keV is focused by a series of electromagnetic lenses to an spot size up to 1 nm.

The accelerated electrons impact with the sample and cause electrons to be scattered from the sample due to elastic or inelastic events. Low energy electrons resulting from inelastic scattering are secondary electrons and it is the most common imaging mode. Due to their low energy (< 50 eV) these electrons are generated few nanometers from the surface and contain information about the morphology and the topography of the sample. Backscattered electrons (BSE) are higher energy electrons produced by elastic scattering interactions. Since elements with different atomic number backscatter different, BSE is commonly used to illustrate contrast of samples with different chemical composition. Finally, X-rays are produced when the electron beam removes an inner shell electron of the sample, causing a higher energy electron to fill the shell and releasing energy. These characteristic X-rays are used to identify the composition and abundance of the elements of the sample.

In this work, SEM routinely used to investigate the morphology of the samples before and after the electrochemical tests, generally using a ZEISS AURIGA and a LEO 1550 scanning electron microscopes.

An estimation of the remaining silica content in the mesoporous oxide replicas was done by Energy Dispersive X-Ray Analysis (EDX) in a SEM Leica Stereoscan S-360 instrument (located in the Scientific-Technical Services, University of Barcelona) (**Chapter 3**). SEM-EDX line profile was performed to study possible ion diffusion

through the barrier layer of the IT-SOFC after a long-term degradation test (**Chapter 6**) (Zeiss Auriga – Inca).

2.4.6. Transmission Electron Microscopy (TEM) and Electron Energy Loss Spectroscopy (EELS)

Transmission electron microscopy (TEM) utilizes a beam of high-energy electrons accelerated with a higher voltage usually 200-300 kV. In this electronic microscope the image is generated from the beam of electrons that are transmitted through a sample, magnified and usually focused onto a fluorescent screen or detected by CCD camera detector.

Scanning Transmission Electron Microscopy (STEM) formed the image by collecting the transmitted electrons. If the apertures are placed to collect only the non scattered electrons the image technique is generally called bright field (circular detector). Transmitted electrons include not only bright field signals but also scattered electrons.

If the aperture is moved and only scattered electrons are collected (annular detector) the image technique is called dark field or high-angle annular dark field (HAADF). The dark field image is sensitive to variations in the atomic number. The annular dark field detector gives the advantage to allow the main beam to pass to an Electron Energy Loss Spectroscopy (EELS) detector, thus both measurements can be done simultaneously (**Figure 2.14**).

EELS in TEM is a very powerful and precise technique to analyze the elemental and chemical composition in the nano-scale. The signal collect the electrons that inelastic scattered after interact with the specimen, losing part of their energy. The amount of energy lost is measured with an electron spectrometer giving different information including inner shell ionizations, which are characteristic of any chemical element.

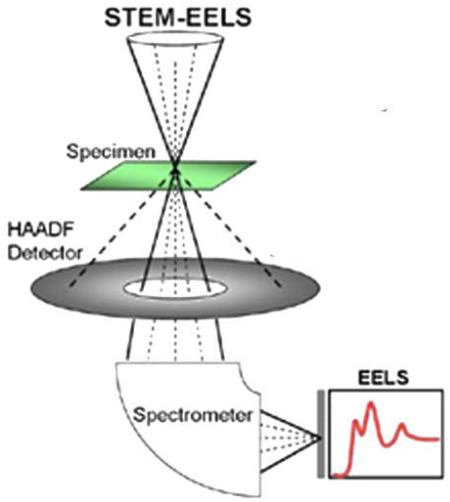

Figure 2.14. Diagram of the configuration of STEM using EELS and HAADF detectors.

In this work, TEM was fundamental to corroborate a proper impregnation of the precursors inside the template and study the structure of the synthesized mesoporous oxides. Routinely the formation of the mesoporous structure was examined using a TEM JEM 2100 (200 kV) (placed in the Scientific-Technical Services, University of Barcelona) and Zeiss Libra 120, placed in IREC.

Possible compositional deviations inside the nanostructures were determined using a Transmission Electron Microscope (TEM) operating at 300 kV and a FEI Titan Low Base coupled to a Tridiem Gatan Imaging Filter (GIF) instrument located in LMA (Laboratorio de Microscopias Avanzadas) and INA (Instituto de Nanociencia de Aragón) (**Chapter 3**).

To study in detail a proper infiltration of the ceria doped gadolinia nanoparticles into the NiO mesoporous matrix, STEM and EELS analysis was performed in the TEM microscope JEOL JEM 2010F (200 kV) placed in the Scientific-Technical Services, University of Barcelona (**Chapter 4**).

2.4.7. Temperature Programmed Reduction (TPR)

Temperature Programmed Reduction (TPR) is a very common tool in the field of catalysis to characterize solid materials. The technique uses a gas flow of a reducing element (usually hydrogen diluted in an inert gas such argon or nitrogen) through the

sample while the temperature increases linearly with the time. The consumption of hydrogen is detected through changes in the thermal conductivity detector. Thus, this technique determines the number of reducible species present on the surface of a material surface and reveals the temperature at which the reduction takes place.

In the present thesis, temperature-programmed reduction by hydrogen (H_2 - TPR) was performed to characterize the functionality of the thermally treated mesoporous ceria doped powder (**Chapter 3**), using a Micromeritics Autochem 2950 system equipped with a thermal conductivity detector (TCD).

2.4.8. Thermogravimetric Analysis (TGA) and Oxygen Storage Capacity Experiments (OSC)

Thermogravimetric analysis (TGA) is a method which measures changes in weight of a selected material, with an increase of the temperature and the time. If the measurements are carried out under cycles of oxidizing and reducing atmospheres, the oxygen storage capacity (OSC) of the materials can be determined. The oxygen storage measures the change in oxidation state associated with the reversible removal and addition of oxygen.

In this work, OSC experiments were carried out using a Setaram Sensys Evo Thermogravimetric Analyzer (TG-DSC) equipped with atmospheric control in order to study the redox properties of the thermal treated mesoporous ceria compounds (**Chapter 3**).

2.4.9. Inductively Coupled Plasma Optical Emission Spectroscopy (ICP-OES)

Inductively Coupled Plasma Optical Emission Spectroscopy (ICP-OES) is one of the most common precise analytical techniques to detect inorganic elements into aqueous solutions at very low levels (up to parts per billion). ICP-OES is a type of ICP-Mass Spectrometry which uses the electromagnetic emission from the atoms ionized by the plasma; the characteristic wavelength of the element of interest is collected.

In this thesis, ICP-OCP allows determining the amount of remaining silica in the samples after the removal of the template (**Chapter 3**). The solutions were prepared dissolving the mesoporous powder into a diluted hydrofluoric (HF) solution.

2.4.10. Raman spectroscopy

Raman spectroscopy is a spectroscopic technique based on the inelastic scattering of monochromatic radiation, usually from a laser source. The photons of the laser source interact with the sample resulting in a scattered laser light shifted up or down, giving information about the vibrational modes of the sample.

In this thesis, Raman spectroscopy was done to determine phase instabilities of the electrolyte in SOFCs after a long-term degradation test (**Chapter 6**). An excitation wavelength of 532.5 nm was used in the experiment.

2.5. Electrical Characterization Techniques

Apart from the structural characterization, it is important to measure the performance of the fabricated devices under operational conditions and understand the different electrochemical processes that take place. In order to have an accurate characterization of the electrochemical devices it is critical to control diverse parameters e.g. temperature, partial pressure of oxygen, humidity, etc.

In this section, the experimental setups used **in this thesis** to fully control and electrochemical characterized the devices (i) SOFCs and (ii) sensors are described. After that, a brief introduction to impedance spectroscopy and potentiostatic - galvanostatic measurements is shown.

2.5.1. Experimental setup SOFCs

The experimental setup to electrochemically characterize the SOFCs was composed by the following elements, shown in **Figure 2.15**:

- Cell sample holder
- Furnace and temperature control system
- Gas flow and humidifier
- Impedance analyzer
- Potentiostat/galvanostat

Different programs developed by Matlab at IREC were used to fully automate and control the measurements of the cells.

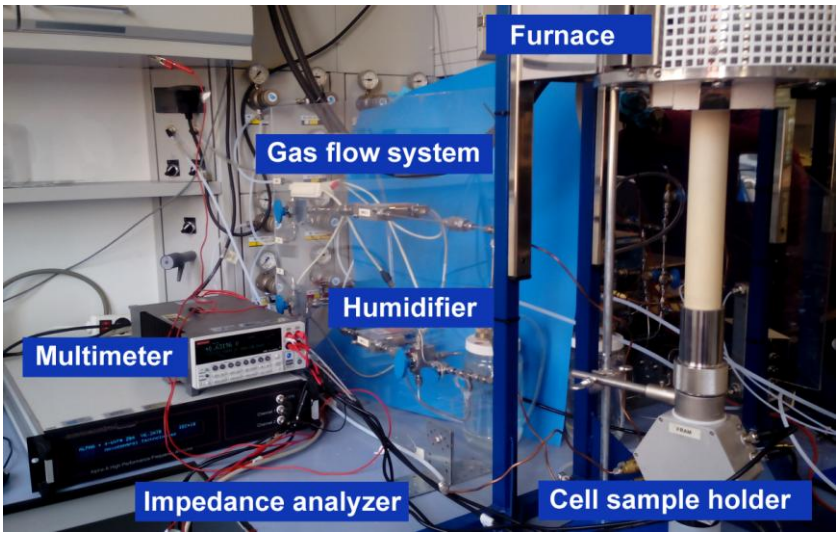

Figure 2.15. Image of one experimental setup used in this work to electrochemical characterize the Solid Oxide Fuel Cells (located in IREC).

One of the most critical parts of the experimental setup in SOFCs is to mount the cell. The cells were put on the top of an alumina tube, which formed part of the commercial ProboStat^{TM} NorECs AS system [15]. The high temperatures (T up to

850 ºC) used to characterized the cells, made the choice of alumina as the ideal ceramic component for tubes/holders, and platinum as wires/meshes for current collection. Controlled atmospheres and gas tightness are mandatory as explosive gases as pure hydrogen, is routinely used. For SOFCs characterization the sealing of the chamber of the anode compartment was generally done by a silver ring and *Ceramabond*™. A schematic diagram and a picture of the sample holder used in this work to characterize the SOFCs are depicted in **Figure 2.16**.

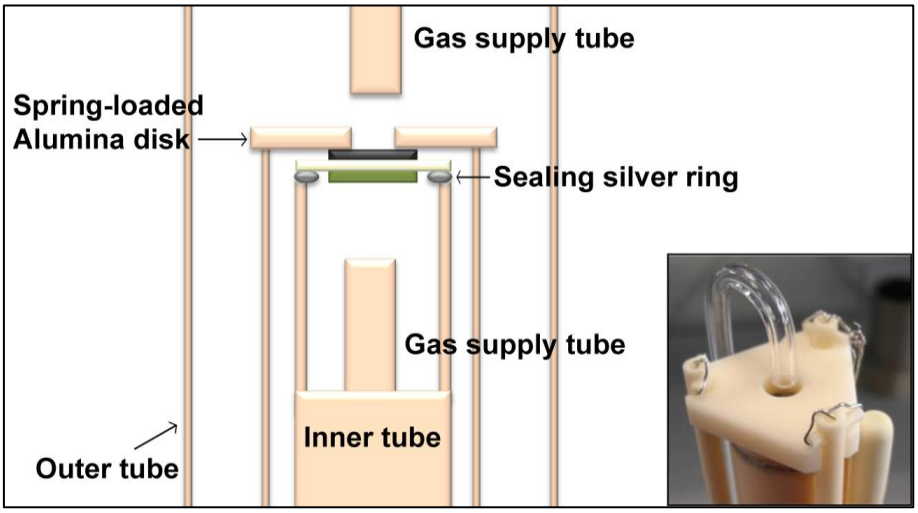

Figure 2.16. Scheme of the ProboStat™ NorECs AS sample holder. Inset image shows a detail of the top part view of a real mounted cell.

2.5.2. Experimental setup sensors

The experimental setup used to measure the sensor properties is shown in **Figure 2.17**. Sensors were placed in the Linkam chamber which allows controlling the temperature and the humidity level was fixed with the commercial humidification system (Bronkhorst) composed of a liquid flow controller (LFC) and a controlled evaporator mixer (CEM) from 0 to 3 ml/min H_2O. The sensors were electrically characterized using the gold contact pads (**Figure 2.12**) by impedance spectroscopy using a frequency response analyzer.

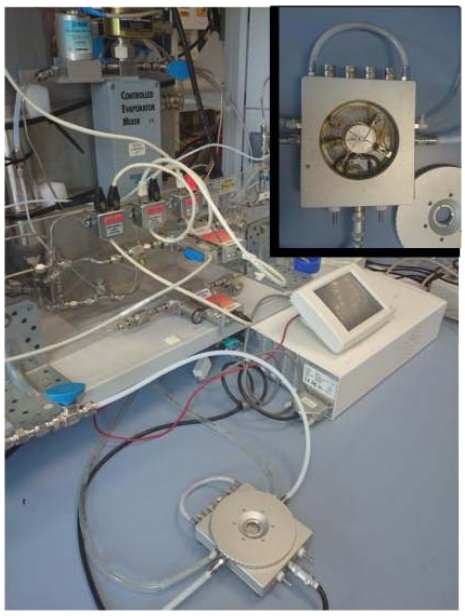

Figure 2.17. Image of the setup used to electrochemical characterize the humidity sensors (located in IREC).

2.5.3. Impedance spectroscopy measurements

The electrochemical impedance spectroscopy (EIS) is a powerful tool to study solid-state ionic devices (*e.g.* solid oxide cells (SOC), batteries and gas sensors) and electrochemical devices (*e.g.* gas separation, electro-synthesis), since the phenomena that take place in such complex systems can be separated into individual processes. Each process has associated a characteristic time and thus, EIS has the capability to separate the different impedance contributions ranging a frequency domain [16–18].

The technique is based on applying an AC small excitation signal and measure the response obtained through the device (**Figure 2.18a**). The impedance defined by the **equation (2.3)** can be expressed as a complex number in terms of real (Z´) and imaginary part (Z´´) as a function of the frequency (ω),

$$Z(\omega) = \frac{E e^{i\omega t}}{I e^{i(\omega t+\theta)}} e^{-i\theta} = \frac{E}{I} e^{-i\theta} = |Z| e^{-i\theta} = |Z| \cos\theta - i \sin\theta = Z' - iZ'' \quad \textbf{(2.3)}$$

Since the definition of impedance implies a linear dependence, a small AC voltage has to be applied to keep a linear regime in the electrochemical systems. One of the most common representations of the impedance spectra is the so-called Nyquist plot (- Z′′(ω) versus Z′(ω)), shown in **Figure 2.18b**.

The linear time-response of the electrochemical systems, is often modeled in terms of equivalent circuit (EC) elements, with resistance (R) representing charge transfer and capacitance (C_1, C_2) representing charge polarization (**Figure 2.18c**) [19]. This description is often extended to non-interfacial processes by introduction of additional empirically or theoretically derived circuit elements [20].

The simplest electrode-material system represented in the Nyquist plot by a semicircle, in terms of EC has a geometrical capacitance in parallel with a bulk resistance with an associated time constant defined by $\tau = 1/RC$. Bauerle [21] proposed a model based on a linear combination of RC circuits to fit a more complex system (*i.e.* electrode/electrolyte/electrode) extracting separated values of R, C and the time constant (τ) characteristic of each individual process. However, experimentally RC circuits do not fit well the impedance spectra as usually a depressed semicircle appears in the complex plane, related with a discrete distribution of relaxation times and the use of constant-phase elements (CPEs (Q,n)) is often required.

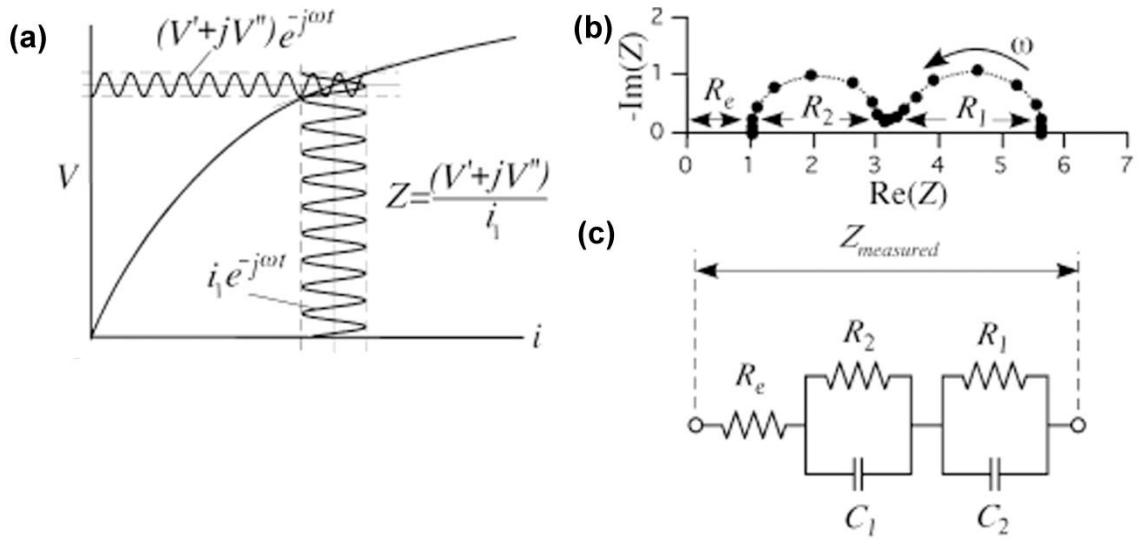

Figure 2.18. (a) Steady-periodic linear response of a cell to a sinusoidal current or voltage perturbation is measured and analyzed in terms of gain and phase shift as a function of frequency (ω). Results are usually expressed in terms of the impedance (Z), the complex ratio of voltage displacement to current displacement. (b) Nyquist plot of an impedance spectrum of a system with an electrolyte and two process electrodes (c) Equivalent electrical circuit associated to the measured impedance spectra (*taken from ref.* [20]).

A number of equivalent circuits could fit the same impedance spectra. As general criteria and in particular during this thesis, the simplest EC which permitted fitting the measured impedance spectra with high quality was chosen. Moreover, all the elements chosen in the fitting must have a physical meaning in terms of resistive processes in the material, charge transfer or mass transfer processes.

In this thesis EIS measurements of the electrochemical cells were carried out in different equipments: two frequency response analyzers *Solartron SI 1260* and *Novocontrol Alpha-A* and a potentiostat/galvanostat *Parstat 2273, PAR*. In general, a range of frequencies from 1 MHz to 0.05 Hz and an AC signal of 50 mV were used for the SOFCs and 300 mV for the sensors. All the generated impedance spectra were analyzed with *ZView* software [22].

2.5.4. Potentiostatic and galvanostatic measurements

Potentiostatic or galvanostatic measurements can be described by the injection of a constant voltage or current (DC signal) through the cell. The measured variable is the cell current or voltage, respectively.

More in detail, a potentiostat is an electronic instrument which controls the voltage difference between a working and a reference electrode. It implements this control by injecting a current into the cell through an auxiliary electrode. The potentiostat measures the current flow between the working and the auxiliary electrodes. It becomes galvanostat when the injection of the controlled variable is switched from cell voltage to cell current.

In this work two systems to monitor the potential-intensity of the electrochemical cells were used a potentiostat/galvanostat Parstat 2273, PAR and a multimeter Keithley Model 2400. This type of measurements allows obtaining the typical current density - voltage (iV) curves and the corresponding power cell density, characterizing the SOFC behavior.

References

[1] F. Kleitz, S.H. Choi, R. Ryoo, Chem. Commun. (Camb). (2003) 2136.

[2] E.P. Butler, J. Drennan, J. Am. Ceram. Soc. 65 (1982) 474.

[3] X. Guo, C.-Q. Tang, R.Z. Yuan, J. Eur. Ceram. Soc. 15 (1995) 25.

[4] T. Zhang, Z. Zeng, H. Huang, P. Hing, J. Kilner, Mater. Lett. 57 (2002) 124.

[5] T. Zhang, Solid State Ionics 167 (2004) 203.

[6] R.A. Terpstra, P.P.A.C. Pex, A.H. Vries, eds., Ceramic Processing, Springer Netherlands, Dordrecht, 1995.

[7] R.E. Mistler, E.R. Twiname, Mistler, Tape Casting: Theory and Practice, Wiley, 2000.

[8] W. Schafbauer, N.H. Menzler, H.P. Buchkremer, Int. J. Appl. Ceram. Technol. 11 (2014) 125.

[9] K. Chen, Z. Lü, N. Ai, X. Chen, X. Huang, W. Su, J. Power Sources 180 (2008) 301.

[10] M. Liu, J. Gao, D. Dong, X. Liu, G. Meng, Int. J. Hydrogen Energy 35 (2010) 10489.

[11] D. Ding, M. Liu, Z. Liu, X. Li, K. Blinn, X. Zhu, M. Liu, Adv. Energy Mater. 3 (2013) 1149.

[12] G. Williamson, W. Hall, Acta Metall. 1 (1953) 22.

[13] P. Scherrer, Nachrichten von Der Königlichen Gesellschaft Der Wiss. Zu Göttingen, Math. Klasse (1918) 1.

[14] A.J.C. Wilson, X-Ray Opt. (1949) 5.

[15] T. Norby, Solid State Ionics 28-30 (1988) 1586.

[16] J.R. MacDonald, Phys. Rev. 92 (1953) 4.

[17] E. Barsoukov, J.R. Macdonald, Impedance Spectroscopy: Theory, Experiment, and Applications, 2 Edition, 2005.

[18] S. Singhal, High-Temperature Solid Oxide Fuel Cells: Fundamentals, Design and Applications: Fundamentals, Design and Applications, Elsevier, 2003.

[19] J.E.B. Randles, Faraday 1 (1941) 11.

[20] S.B. Adler, Chem. Rev. 104 (2004) 4791.

[21] J.E. Bauerle, J. Phys. Chem. Solids 30 (1969) 2657.

[22] D. Johnson, Z-view. and Z-plot. a S.P. for I. Analysis, (2002).

3

Synthesis and thermal stabilization of mesoporous metal oxides. A case study on CGO

3. Synthesis and Thermal Stabilization of Mesoporous Metal Oxides. A Case Study on CGO

3.1. Interest of CGO for High Temperature Applications and Self-limited Grain Growth Regime 75

3.2. Synthesis and Characterization of the CGO Mesoporous Oxide 78

3.3. Thermal Treatment and Stability of the Ordered Mesoporous Structure .. 82

3.3.1. Structural evolution with temperature 82

3.3.2. Validity of the self-limited grain growth for nanocasting of mesoporous ... 87

3.4. Functionality of the Long-term Stable Mesoporous CGO 91

3.5. Conclusions 94

References 95

3. Synthesis and Thermal Stabilization of Mesoporous Metal Oxides. A Case Study on CGO

3.1. Interest of CGO for High Temperature Applications and Self-limited Grain Growth Regime

Ceria-based materials have the ability to store and release oxygen by changing the valence of the cerium cations between Ce^{3+}/Ce^{4+}. This oxygen storage capacity (OSC) feature gives ceria outstanding catalytic properties that make it very attractive for a wide range of applications such in automotive exhaust catalysis. Solid solutions of ceria and gadolinia (CGO) have been proposed for the steam reforming of natural gas since the addition of gadolinium [1,2]:

(i) Improves the dynamic OSC resulting in an enhanced resistance against carbon deposition.

(ii) Reduces the total OSC at the intended operating temperatures, ensuring a better stability against deactivation by metal decoration and a lower reactivity with sulfur.

The maximum benefit from the addition of Gd is obtained for high surface area materials. Nevertheless, ceria suffers from a lack of thermomechanical stability that reduces its active surface area at elevated temperatures by coarsening and sintering processes, *e.g.* Perrichon *et al.* reported a surface area drop from 115 to 5 m^2g^{-1} after 6 h at 850 ºC under air [3], which represents a severe limitation for its implementation in high-temperature devices.

This is a major drawback for energy applications since most of the uses in this field involve high temperature long-term operation (T ~ 800 ºC) and even higher temperature fabrication or activation steps (T ~ 1000 ºC), *e.g.* electrocatalysis in Solid Oxide

Fuel/Electrolysis Cells (SOFC/SOEC) [4,5], oxygen separation membrane [6] or high temperature catalysis for fuel conversion [7,8].

Some attempts to stabilize ceria-based mesoporous materials at intermediate temperatures (500-750 ºC) can be found in the literature. Different methods like soft template using Pluronic P123 [9], self-assembly of individual CeO_2 nanoparticles in a liquid crystal phase [10], evaporation-induced self-assembly (EISA) derived methods [11], neutral soft templating routes [12] or replica synthesis from originally prepared mesoporous hard templates [13–15] have been reported. However, it is still necessary to develop new strategies for keeping the ordered mesoporous structure leading to high specific surface area at temperatures high enough to cover the previously mentioned applications.

The thermal stability of mesostructures at high operation temperatures strongly depends on the atom diffusion processes across and along the grain boundaries, *i.e.* the grain growth kinetics.

The classical Burke's and Turnbull's formulation determines a parabolic grain growth behavior [16] and therefore, a continuous grain growth with time defined by the following equation,

$$G^2 - G_0^2 = k_2 t \qquad \textbf{(3.1)}$$

where $k_2 = 2M\gamma$ is a characteristic material constant (γ: grain boundary energy , M: grain boundary mobility).

However, this model has been proved to be insufficient to describe grain growth when the grain sizes are in the nanometric scale. Limited grain growth has been reported for nanocrystalline metals by solute drag [17] or by the presence of high concentrations of defects [18].

More interestingly, Rupp *et al.* [19–22] recently reported self-limited grain growth kinetics for biphasic amorphous-crystalline metal oxides in thin films. According to them, the driving force for grain growth in these biphasic materials is the reduction of free volume and the crystallization enthalpy during isothermal annealing. Once the

crystallization enthalpy equals zero, the self-limited growth regime becomes dominant and the grain growth stops in isothermal conditions, making the structure stable over time.

In agreement to this model, temperatures below 1100 ºC lead to this self-limited growth regime, in which the grain growth mostly stops after the first 5 - 10 h of isothermal treatment at T > 600 ºC for ceria. This regime can be described by the relaxation function:

$$G - G_0 = (G_L - G_0)\left(1 - \exp^{-t/\tau_1}\right) \quad \textbf{(3.2)}$$

where G is the average grain size, G_0 the initial grain size, G_L the limited grain size, τ_1 the relaxation time and t the time.

Rupp *et al.* indicate this self-limited growth regime is related to a decrease of the micro-strain after a certain relaxation time. This reduction of the micro-strain is explained by the process of crystallization of the amorphous-based oxide running in parallel to the grain growth. The decrease is defined by the exponential **equation (3.3)**,

$$\varepsilon = \varepsilon_L + \varepsilon_0 \ \exp^{-t/\tau_2} \quad \textbf{(3.3)}$$

where ε is the average micro-strain, ε_L is the constant value of residual microstrain, ε_0 is the initial micro-strain, τ_2 is the relaxation time and t the time.

The first (time-temperature-transformation) TTT diagram for a metal oxide thin film (CGO) was proposed based on these results, making possible to predict the kinetics and degree of crystallization of nano-grained films.

In this Chapter, a novel methodology is developed to stabilize open ordered mesoporous structures. Firstly, the synthesis and characterization of mesoporous gadolinium doped ceria ($Ce_{0.8}Gd_{0.2}O_{1.9}$) one of the most common materials for high energy temperatures is presented. The mesoporous CGO is synthesized from a silica template with KIT-6 structure.

In order to study the validity of the self-limited growth regime for the ceria-based mesoporous materials synthesized by a nanocasting method, a XRD study was performed studying the evolution of the crystallite size and the micro-strain at high temperatures over the time. The replicas maintained the mesoporosity after thermal stability tests at 800, 900 and 1000 ºC in air.

This stability is based on achieving the self-limited grain growth regime within the KIT-6 silica hard template. The extension of the self-limited grain growth regime to open 3D structures by the partial crystallization of the metal oxide inside the hard template is shown and the functionality, *i.e.* good catalytic activity, of the resulting stabilized materials is presented in the long term for the range of temperatures from 800 ºC to 1100 ºC.

3.2. Synthesis and Characterization of the CGO Mesoporous Oxide

Contrary to widely employed high temperature stabilization treatments inside the template, in this work gadolinium-doped-ceria ($Ce_{0.8}Gd_{0.2}O_{1.9}$) mesoporous powder was synthesized by using the nanocasting method based on KIT-6 template at 600 ºC for 5 h, in order to demonstrate the long term stability of the material achieved when reaching the self-limited grain growth regime, recently proved for thin films, to open three-dimensional structures. Thus, a counterintuitive and cost-effective thermal treatment at intermediate temperatures (600 ºC) is performed lower than the further operational temperatures (800 – 1000 ºC).

Details of the synthesis procedure can be found in the experimental part (see **Chapter 2.2.2, Table 2.2**). The synthesized mesoporous replica is denoted in this chapter as **CGO-600**.

Figure 3.1 presents the X-ray diffraction (XRD) patterns of the CGO mesoporous powders synthesized and calcined at T = 600 ºC after template removal. The indexed peaks correspond to a cubic fluorite structure of $Ce_{0.8}Gd_{0.2}O_{1.9}$ (s.g. *Fm3m*) with lattice parameter a = 5.423(2) Å (as determined by Le Bail fits). Pure CGO single phase was obtained as shown by XRD (JCPDS 75-0162).

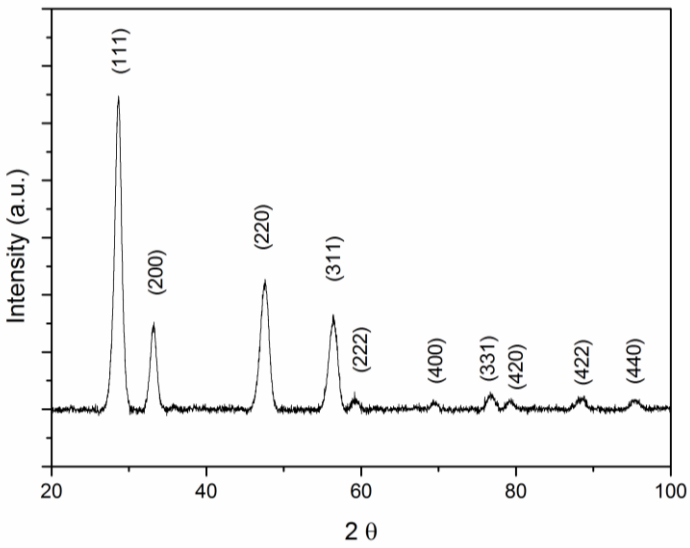

Figure 3.1. XRD pattern of CGO as synthesized at T = 600 ºC. Diffraction peaks corresponding to the cubic fluorite with space group *Fm3m* are labeled.

To corroborate the mesoporous structure of the as-synthesized CGO sample (CGO-600) low-angle XRD was carried out (**Figure 3.2**). Reflections corresponding to a three dimensional *Ia3d* symmetry are labeled in agreement with the ones for the KIT-6 mesoporous structure, confirming the mesoporous structure is transferred from the original matrix to the mesoporous replica. The pattern shows the typical reflections of a double gyroid structure consisting of a sharp peak at 0.94-0.98º indexed as (211) and a weak reflection at 1.08-1.1º corresponding to (220). The position of the (211) reflection of the mesoporous structure allows determining the periodicity of the ordered structure (**Table 3.1**). The calculated lattice constant (*b*) for the CGO-600 is 22.1 nm indicating a slight decrease of the long-range order of the replica in comparison to the original template KIT-6-90 (*b* = 22.7 nm).

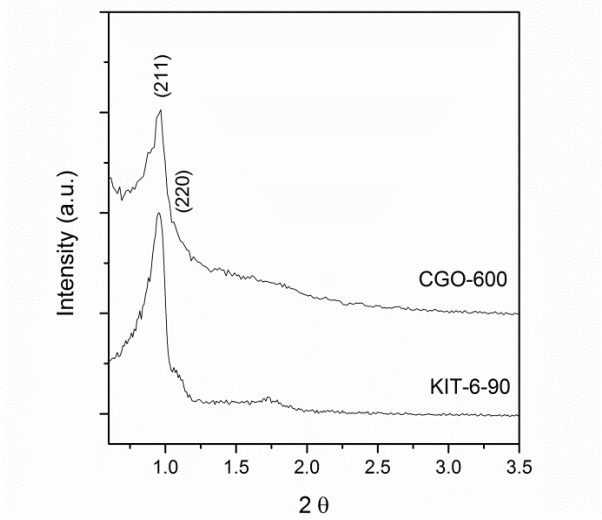

Figure 3.2. Low angle XRD of mesoporous CGO-600 and of the KIT-6-90 silica template.

Figure 3.3 shows the nitrogen adsorption-desorption isotherms for the CGO-600 mesoporous replica calcined at 600 ºC, after the template removal. Type IV isotherms with H1 hysteresis loops, are obtained as is typically reported for mesoporous metal oxides synthesized by the same hard template route [23–25]. A BET area of 115 m^2/g and pore volume of 0.275 cm^3/g was obtained (**Table 3.1**). The pore size distribution obtained using the BJH model from the desorption branch of the isotherm was 3.9 ± 0.7 nm.

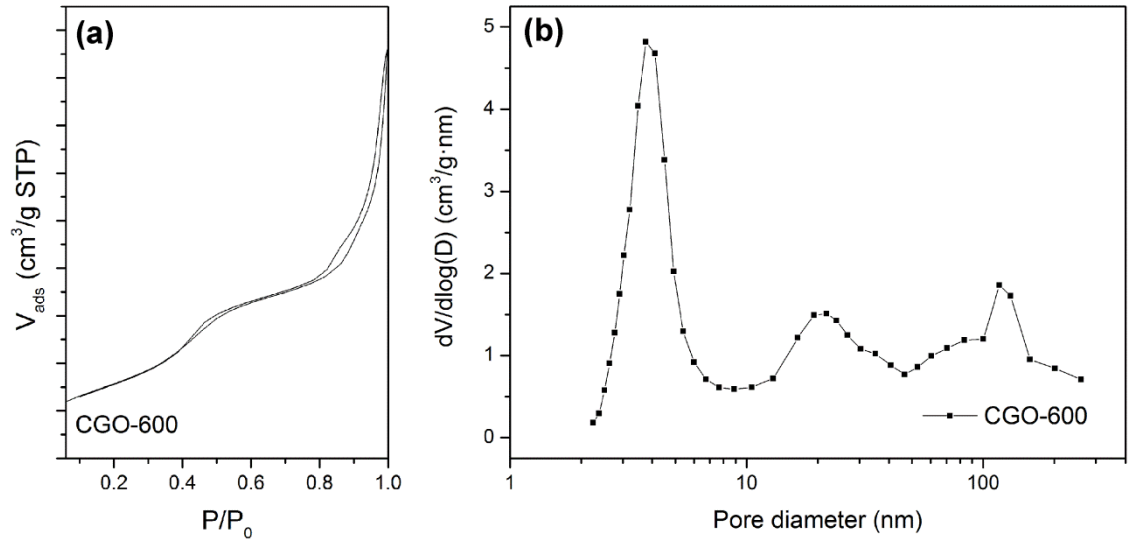

Figure 3.3. a) N_2 adsorption–desorption isotherms and b) Pore size distribution, of CGO-600 calcined at 600 ºC replica of the KIT-6-90.

To corroborate the meso-structure of the CGO-600 replica typical TEM images of are presented in **Figure 3.4**. As expected from XRD, highly ordered porous matrixes keeping ordered cubic symmetry, are observed for the mesoporous CGO-600 powder. Well-connected spherical mono-crystalline domains of *ca.* 8 nm in diameter can be observed consistent with the reported 3D process of nucleation and growth of the replica materials within the isotropic pore structure of the KIT-6-90 template. The inset figure, corresponds to a TEM image of a mesoporous CGO-600 particle recorded along the [111] direction. The image clearly shows the double gyroid with *Ia3d* symmetry, thus both interpenetrated channels were filled and the original structure of the template KIT-6-90 is completely transferred.

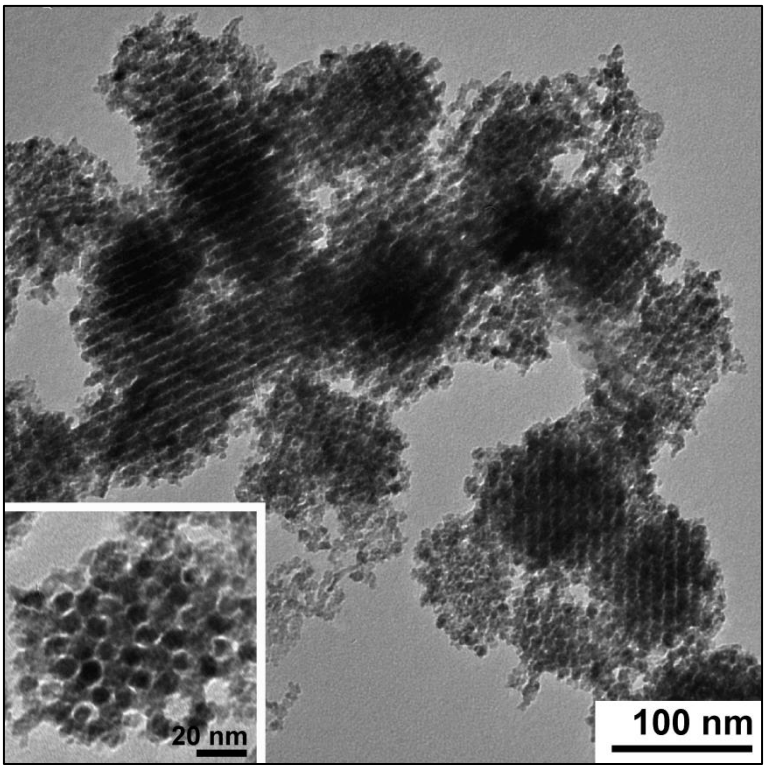

Figure 3.4. TEM images of particles of CGO-600 synthesized at 600 ºC where the mesoporous structure is clearly observed. The inset figure was acquired along the [111] direction, demonstrating the infiltration of both channels of the original structure of the template KIT-6-90.

3.3. Thermal Treatment and Stability of the Ordered Mesoporous Structure

To study the crystallite grain growth of the mesoporous powder and study the proposed self-limited growth regime at different temperatures, long-term thermal treatments of the sample CGO-600 were carried out at 800, 900, 1000 and 1100 ºC during 24 h inside furnaces with open atmosphere. These samples will be labeled **CGO-600-800, CGO-600-900, CGO-600-1000** and **CGO-600-1100** in the following.

3.3.1. Structural evolution with temperature

A set of diffraction patterns is presented in **Figure 3.5** corresponding to measurements of CGO-600 samples after a thermal treatment of 24 h at 800, 900, 1000 and 1100 ºC in air. All diffraction patterns, except that of the sample tested at 1100 ºC for 24 h, show reflections corresponding to the mesoporous structure suggesting that the ordered pattern is surprisingly maintained for the CGO replica after removal of the hard template and after the durability tests up to 1000 ºC.

Despite this, the patterns present lower scattering intensities for higher temperatures as shown by the peak broadening of the (211) reflection. This indicates a decrease of the long-range order of the replica in comparison to the original template. The periodicity of the ordered structure is shown in the first column of the **Table 3.1**. The reduction of the mesoporous lattice constant (*b*), when increasing the temperature of the durability test, is presumably related to the shrinkage of the whole system by sintering.

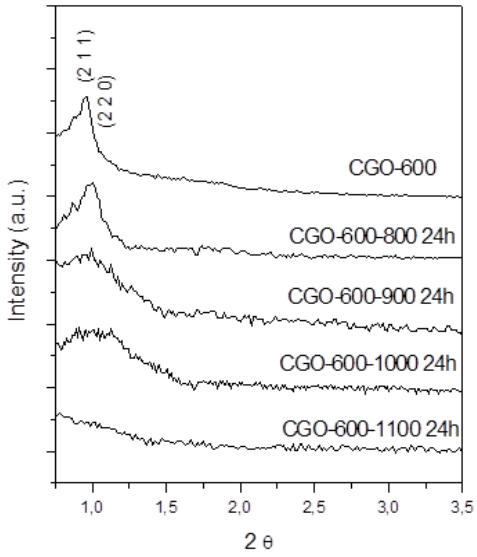

Figure 3.5. Low angle XRD of CGO as-synthesized (CGO-600) and after the isothermal stability tests at 800, 900, 1000, 1100 ºC for 24 h.

Table 3.1. Structural parameters obtained by analysis of XRD diffraction and nitrogen adsorption-desorption data

Sample	b (nm)	BET (m^2/g)	Pore volume (cm^3/g)	Micropore Area (m^2/g)
KIT-6	22.7(1)	786 (2)	0.829	256.78
CGO-600	22.1(1)	115 (1)	0.275	38.37
CGO-600-800	21.5(1)	78(1)	0.266	25.35
CGO-600-900	21.3(2)	44(1)	0.254	15.14
CGO-600-1000	21.0(5)	20(1)	0.171	5.63
CGO-600-1100	--	4(1)	0.018	0.19

To corroborate the mesoporous nature of CGO, TEM and SEM images of the as synthesized sample at 600 ºC and after the stability tests at 800 and 1000 ºC for 24 h are presented in **Figure 3.6** As already shown in the **previous section**, a highly ordered porous matrix keeping the parent KIT-6 structure are observed for the CGO as synthesized at 600 ºC (**Figure 3.6a**). Moreover, the samples isothermally treated for 24 h

at higher temperatures of 800 ºC and 1000 ºC (**Figure 3.6b and c**) also maintain the parent KIT-6 structure. After treatment at 1000 ºC the ordered mesoporosity is still observed, with similar microstructure.

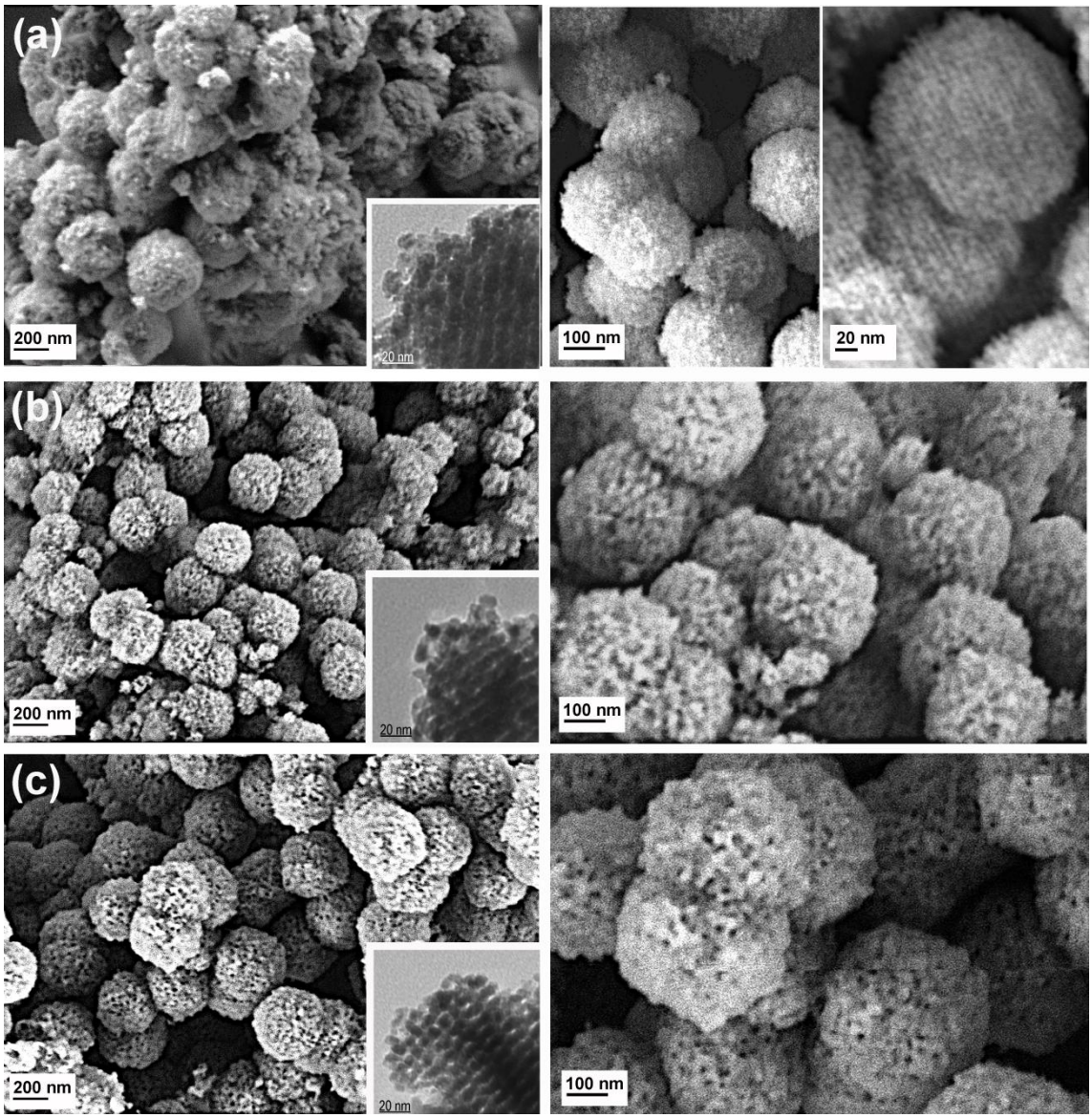

Figure 3.6. SEM images of the mesoporous CGO as (a) synthesized at 600 ºC. After the stability tests at (b) 800 ºC and (c) 1000 ºC under 24 hours in air. The insets show TEM images of the corresponding mesoporous particles.

A more detailed TEM study was carried out after the treatment at the expected operation temperature, *i.e.* 800 ºC, in order to determine possible compositional deviations inside the nanostructure. TEM and Electron Energy Loss Spectroscopy (EELS) mapping of CGO-600 after a thermal treatment of 24 h at 800 ºC in air (CGO-600-800) was performed. According to **Figure 3.7**, there is no significant dopant segregation to the surface or grain boundaries that could induce a reduction of the oxygen mobility by dopant-oxygen vacancy association [26,27].

Moreover, **Figure 3.6** clearly shows that no significant changes in the mesostructure take place during the self-limiting grain growth regime and therefore, no reduction of the bulk oxygen diffusion is expected. Well-connected spherical mono-crystalline domains of *ca.* 8-10 nm in diameter are observed consistent with the reported 3D process of nucleation and growth of the replica materials within the isotropic pore structure of the KIT-6 template [28].

This good connectivity of the replica is of the utmost importance since, for applications requiring good percolation paths through the material, represents a great advantage. This is the particular case of electrodes for SOFC or gas separation membranes where oxide ionic conduction is crucial for a good device performance.

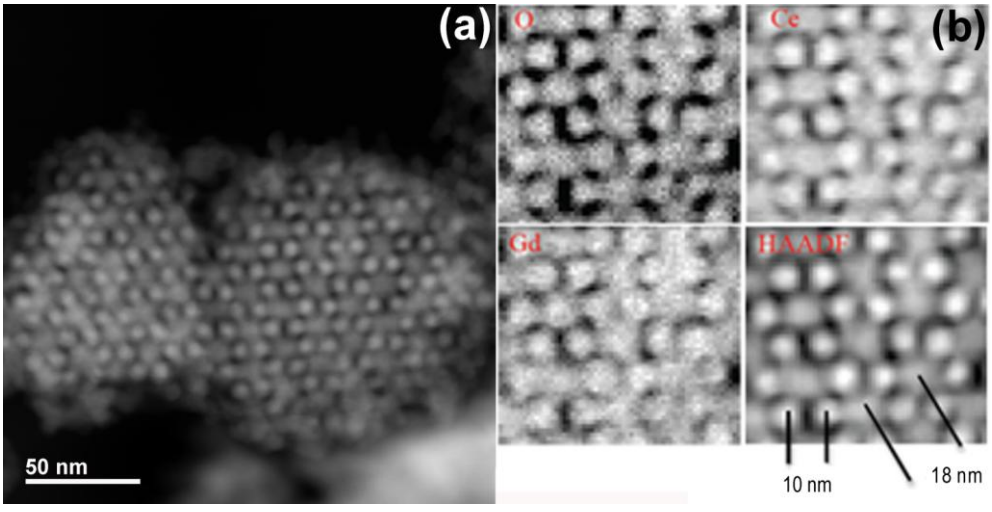

Figure 3.7. Structural and compositional characterization of CGO-600 after the stability test at 800 ºC for 24 h. (a) TEM image of CGO-600-800 particles. (b) EELS compositional map and HAADF of a CGO-600-800 particle.

A detailed structural characterization of the CGO mesoporous oxides after the stability tests are presented in **Figure 3.8**. **Figure 3.8a** presents XRD patterns of the thermal treated powder (CGO-600-800, -900, -1000 for 24 h). Single phase of pure CGO was obtained for all the samples under study.

The surface stability of the samples was studied by nitrogen adsorption-desorption measurements. **Figure 3.8b** shows the nitrogen adsorption-desorption isotherms of the mesoporous samples used to determine the BET, pore volume and micropore area parameters shown in **Table 3.1**.

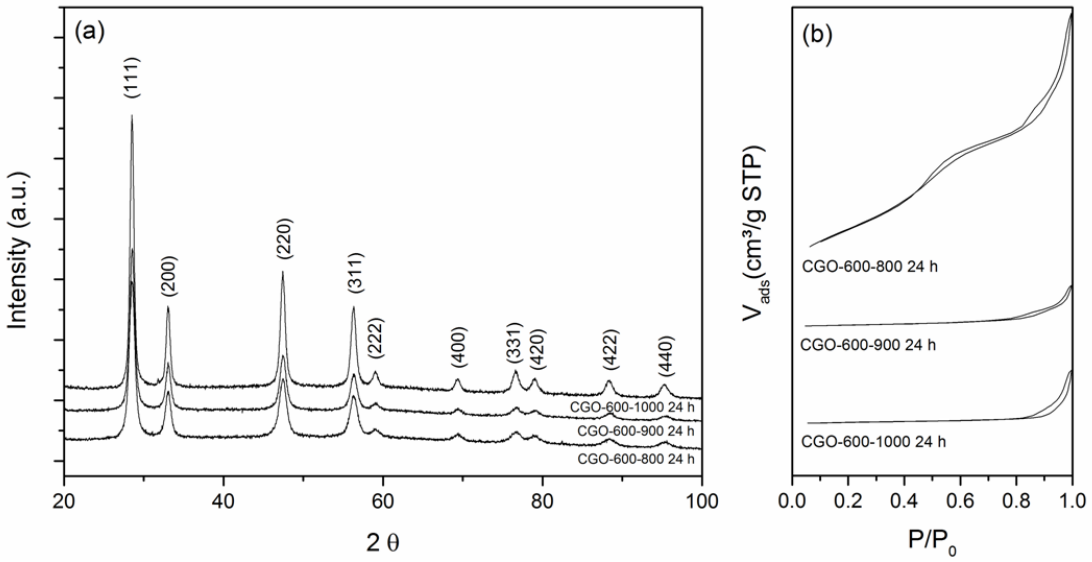

Figure 3.8. Structural characterization of 24 h thermal treated mesoporous CGO-600 at different temperatures (CGO-600, -800, -900, -1000 24 h): (a) XRD patterns, (b) Nitrogen adsorption- desorption isotherms.

A BET area of 786 m^2/g was obtained for pure KIT-6 while for the CGO replica calcined at 600 ºC and after the stability tests at 800, 900, 1000 and 1100 ºC was 115, 78, 44, 20 and 4 m^2/g, respectively. A progressive decrease of the specific surface area was clearly observed up to 1000 ºC probably due to a reduction of the pore size with temperature and the shrinkage of the whole structure.

On the other hand, the total pore volume of the samples that decreases slightly up to 900 ºC shows a drastic drop over 1000 ºC. This phenomenon can be explained by a major reduction of the surface roughness of the samples (microporosity) likely related to the promotion of the ion diffusion in the structure. **Figure 3.9**, shows the TEM images of the mesoporous CGO as synthesized at 600 ºC and after the stability test at 800 ºC after 24 hours in air. The inset figures show the surface flattening and the microporosity reduction taken place after increasing the temperature of the long stability measurements. From the previous results, the microstructural stability of the mesporous samples after long-term treatments at high temepratures is proved.

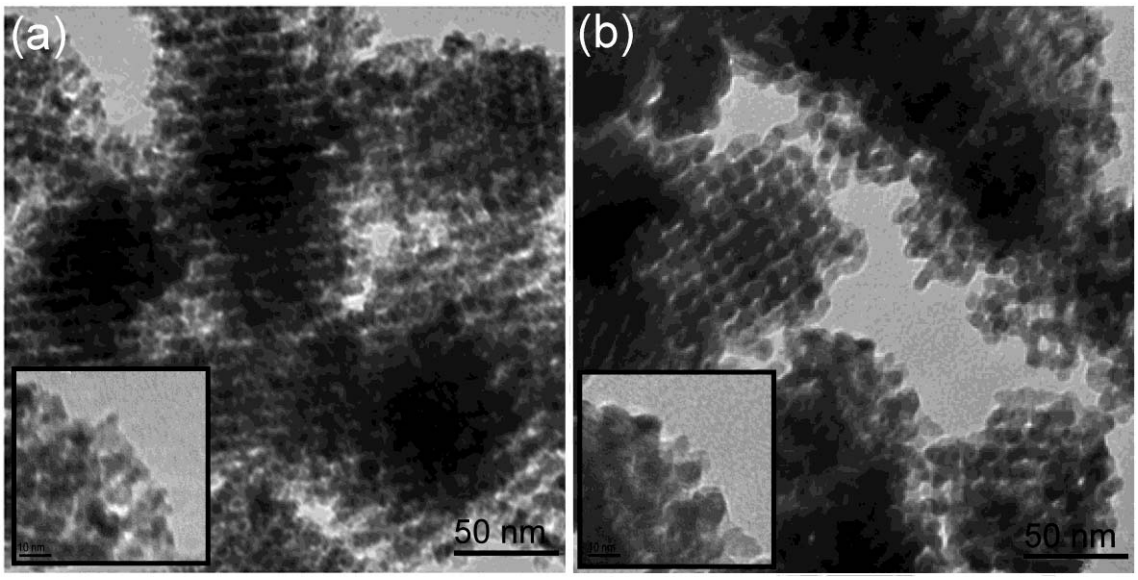

Figure 3.9. TEM images of the mesoporous CGO as (a) synthesized at 600 ºC. (b) After the stability test at 800 ºC after 24 hours in air. The insets show a detail of the mesoporous particles.

3.3.2. Validity of the self-limited grain growth for nanocasting of mesoporous

To understand the origin of this stability and, therefore, predict how long the mesostructure will remain stable over time, a XRD study with *in situ* temperature experiments of the evolution of grain size and micro-strain with time was performed (see details in **Chapter 2, section 2.4.1**).

The Williamson-Hall methodology [29], was employed to determine the average grain size and microstrain during stability tests above the annealing temperature (T = 600 ºC) carried out at 800, 900, 1000 and 1100 ºC for 24 h. According to the Scherrer and Wilson equation [30,31],

$$\beta \cos\theta = 4K\lambda/3D + 4\varepsilon \sin\theta \qquad \textbf{(3.4)}$$

where β is the integral breadth of a reflection (in radians), K is the Scherrer constant (equals 0.89 for spherical grains), λ denotes the X-ray wavelength, θ the diffraction angle, D the average grain size and ε the microstrain.

Figure 3.10 shows a typical Williamson-Hall plot obtained in this study, for the CGO replica stabilized at 600 ºC. By using **equation (3.4),** this plot was used to determine the average grain size and micro-strain of all the XRD spectra.

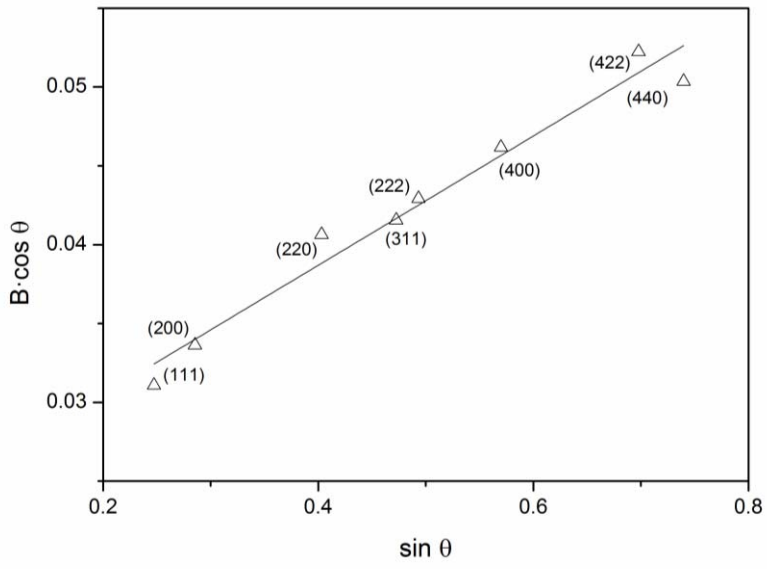

Figure 3.10. Williamson-Hall plots of CGO as synthesized at T = 600 ºC. The reflections used to determine each data point are labeled.

Figure 3.11 shows the variation of the average grain size during stability tests above the annealing temperature (T = 600 ºC), carried out at 800, 900, 1000 and 1100 ºC for 24 h. Two different regimes of grain growth are observed.

The CGO annealed at 600 ºC and stabilized at temperatures exceeding 1000 ºC involves larger grains and the classical parabolic grain growth according to the Burke's and Turnbull's formulation (**equation (3.1)**) (dashed line in the **Figure 3.11**).

On the other hand, when stabilized at 800, 900 and 1000 ºC the CGO shows an increase of its grain size only during the first 5 - 10 h. After this time, the average size stabilizes suggesting a new regime of growth.

This can be explained according to the self-limited grain growth proposed for two-dimensional structures by Rupp *et al.* (**equation (3.2)**) [19–22]. The good agreement between the experimental data of this work and the self-limited grain growth model (solid line in the **Figure 3.11**) suggests its validity for the nanocasting synthesis employed here where biphasic amorphous-crystalline CGO remains inside the template before full crystallization.

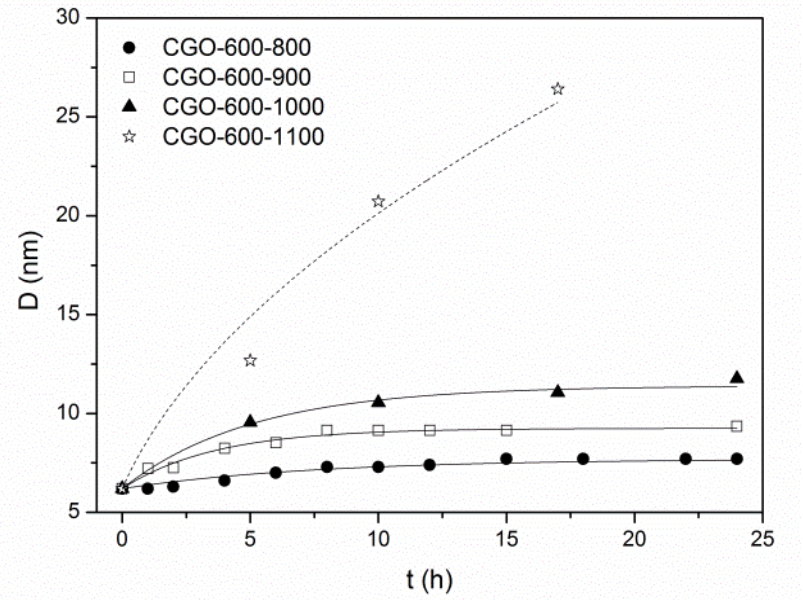

Figure 3.11. Average crystal size evolution with time of the CGO sample calcined at 600 ºC during isothermal stability tests at 800, 900, 1000, 1100 ºC.

Figure 3.12 shows the evolution of the microstrain with time during the stability tests for the whole set of samples. For the temperature of 1100 ºC the microstrain of the films tends to relax. However, for the samples stabilized at 800 and 900 ºC the microstrain decreases during the first 5 - 10 h, following the **equation (3.3)**.

The correlation between the microstrain and grain growth behavior reinforces the applicability of the self-limited grain growth model for explaining the resistance of the mesoporous structures towards thermally activated microstructural coarsening.

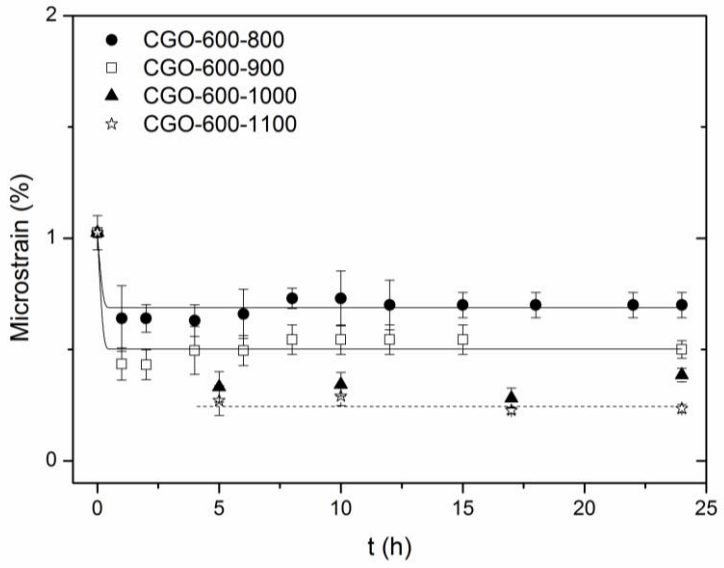

Figure 3.12. Microstrain evolution with time of the CGO sample calcined at 600 ºC during isothermal stability tests at 800, 900, 1000, 1100 ºC.

This agreement allows predicting extremely long-term stability of mesoporous CGO and therefore, the suitability of employing it in applications involving continuous operation at high temperature. Moreover, this novel methodology is a non-trivial and counterintuitive approach radically different to the widely employed idea of using hard templates just to support the stabilization of the grain size at temperatures above the application temperature. Finally, this low temperature method allows reducing the reactivity with the template and the diffusion of silicon before removing it.

3.4. Functionality of the Long-term Stable Mesoporous CGO

In this section the functionality of the long-term treated mesoporous CGO will be evaluated by temperature programmed reduction (TPR) and by means of oxidation/reduction cycles inside a TGA.

Considering that the redox ability of a material is closely related with its catalytic activity [32], TPR was performed on the thermally treated samples. **Figure 3.13** shows H_2 - TPR patterns for the as-synthesized (CGO-600) and isothermally treated powder (CGO-800, -900, -1000 and 1100 for 24 h). While a single high-temperature reduction peak is present at around 800 ºC for the sample treated at 1100 ºC, other peaks appear at lower temperatures for the rest of the samples.

The single high-temperature peak indicates a bulk-like behavior [33], whilst the presence of the low temperature peaks corroborates a dominating surface reduction typical of the nanostructures. Peaks around 450 and 650 ºC, measured for CGO-600, CGO-600-800 and CGO-600-900, are totally consistent with previous studies about the catalytic activity of mesoporous ceria [32,34].

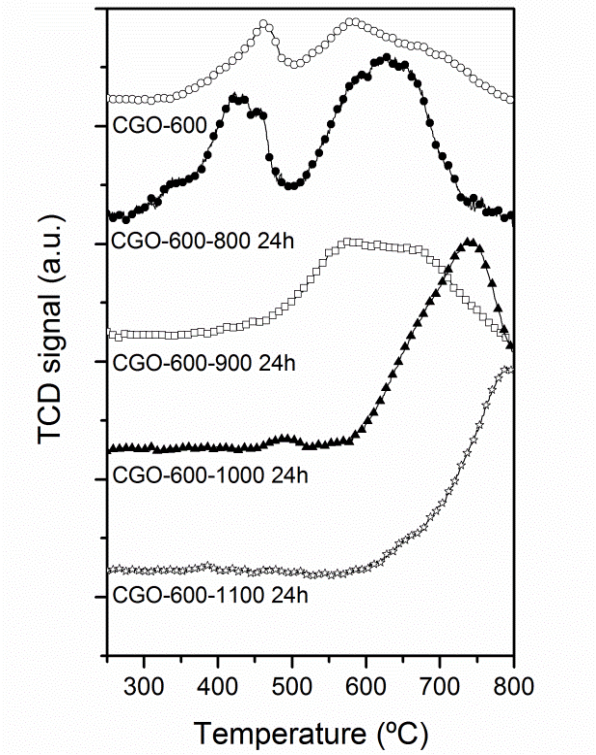

Figure 3.13. H_2 - TPR patterns of CGO as synthesized at 600 ºC and after the isothermal stability tests at 800, 900, 1000, 1100 ºC for 24 hours.

Increasing the temperature of the thermal treatment shifts the surface and bulk peaks for making them merge in a single broader one at intermediate temperature (T = 600 - 700 ºC). This accounts for a partial sintering of ceria reduced at temperatures above 900 ºC in agreement with the lower thermal stability of the mesoporous materials presented in **Figure 3.6** and **Table 3.1**. Despite this, it is clear that the total hydrogen uptake at a surface and bulk level, below the operation temperature, is still reasonable while keeping a high enough surface area.

The redox properties of the thermal treated materials were further studied at 800 ºC by means of oxidation/reduction cycles inside a TGA (**Figure 3.14**), which also allowed quantification of the degree of reduction of the CGO. The 800 ºC temperature was chosen because it is the preferred operating temperature for the targeted high-temperature applications, *e.g.* steam reforming of natural gas [1,2].

Figure 3.15 shows the total oxygen storage capacity, *i.e.* the maximum amount of oxygen extractable from the sample at the temperature of study. As expected, the total OSC do not show significant variation with time for the CGO-600-800 (after 24 h) neither the one post-treated at 1000 ºC for 5 h.

The value of OSC is ranged between 450 - 500 μmol O_2/g CGO while the ceria reduction percentage between 40 - 50 %. These excellent values are comparable to the ones previously reported by Hennings *et al.* ~300 μmol O_2/g and ~ 28 % Ce^{+3}/Ce^{+4} for CGO [1,2], confirming the qualitative observation in the TPR patterns for the temperature peak evolution.

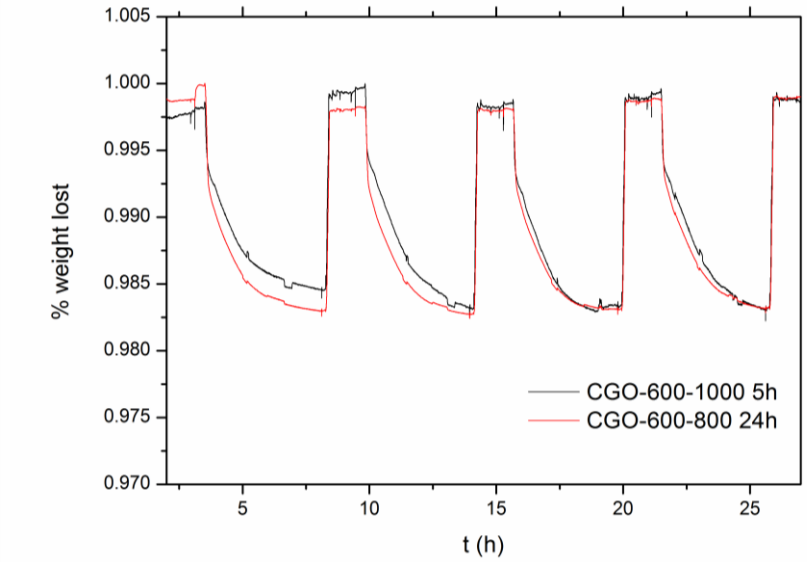

Figure 3.14. Oxidation/Reduction cycles of the CGO-600 after the isothermal stability tests at 800 ºC (CGO-600-800 24 h) during 24 h and of the sample CGO-600 after the isothermal stability tests at 1000 ºC during 5 h (CGO-600-1000 5 h).

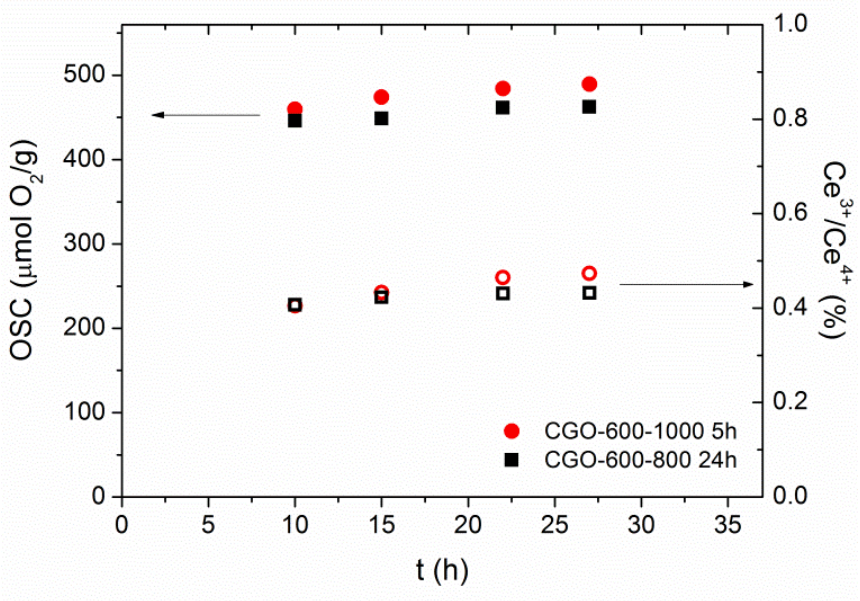

Figure 3.15. OSC of CGO-600 after the isothermal stability tests at 800 ºC for 24 h and 1000 ºC for 5 h.

From the TPR and OSC experiments, it is possible to conclude that the stabilized mesoporous materials are strongly resistant against one of the most critical factors that contribute to decrease the catalytic activity during aging for ceria supports, *i.e.* the sintering process [35] and therefore, are suitable for being used in continuous operation mode inside high temperature catalytic reactors.

3.5. Conclusions

Stabilization of mesostructures at temperatures significantly over the state-of-the-art for mesoporous materials were achieved by intermediate temperature calcinations before template removal, *i.e.* extending to 3D materials the self-limiting growth regime previously proved for thin films.

One of the most promising materials for high temperature applications involving natural gas, *i.e.* gadolinia doped ceria (CGO), was synthesized in mesoporous form with KIT-6 structure by filling both channels of the double gyroid with cubic symmetry corroborate after a calcination step at 600 ºC and the template removal.

Long-term stability in terms of microstructure and catalytic activity of the mesostructure was proved at temperatures as high as 1000 ºC. Since achieving the self-limited grain growth regime is only dependent on the simultaneous presence of amorphous and crystalline phases before the template removal, the present conclusions can be extrapolated to most of the oxides of interest making it a quasi universal method.

These high-surface area three-dimensional nanostructures could be employed in up-to-now forbidden applications such as solid oxide fuel/electrolysis cells, gas membrane separation or high temperature catalysis, as present the next sections of the thesis.

References

[1] U. Hennings, R. Reimert, Appl. Catal. A Gen. 325 (2007) 41.

[2] U. Hennings, R. Reimert, Appl. Catal. B Environ. 70 (2007) 498.

[3] V. Perrichon, A. Laachir, S. Abouarnadasse, O. Touret, G. Blanchard, Appl. Catal. A Gen. 129 (1995) 69.

[4] B. Steele, Solid State Ionics 134 (2000) 3.

[5] T. Zhang, J. Ma, L. Kong, P. Hing, Y. Leng, S. Chan, J. Kilner, J. Power Sources 124 (2003) 26.

[6] V. V. Kharton, A. V. Kovalevsky, A.P. Viskup, F.M. Figueiredo, A.A. Yaremchenko, E.N. Naumovich, F.M.B. Marques, J. Electrochem. Soc. 147 (2000) 2814.

[7] A. Trovalleri, Catal. Rev. 38 (1996) 439.

[8] O.A. Marina, M. Mogensen, Appl. Catal. A Gen. 189 (1999) 117.

[9] M. Lundberg, B. Skårman, F. Cesar, L. Reine Wallenberg, Microporous Mesoporous Mater. 54 (2002) 97.

[10] A. Corma, P. Atienzar, H. García, J.-Y. Chane-Ching, Nat. Mater. 3 (2004) 394.

[11] E.L. Crepaldi, G.J. de A A Soler-Illia, A. Bouchara, D. Grosso, D. Durand, C. Sanchez, Angew. Chem. Int. Ed. Engl. 42 (2003) 347.

[12] D.M. Lyons, K.M. Ryan, M.A. Morris, J. Mater. Chem. 12 (2002) 1207.

[13] S.C. Laha, R. Ryoo, Chem. Commun. (2003) 2138.

[14] J. Roggenbuck, H. Schäfer, T. Tsoncheva, C. Minchev, J. Hanss, M. Tiemann, Microporous Mesoporous Mater. 101 (2007) 335.

[15] W. Yue, W. Zhou, J. Mater. Chem. 17 (2007) 4947.

[16] J.E. Burke, D. Turnbull, Prog. Met. Phys. 3 (1952) 220.

[17] H. Natter, M. Schmelzer, M.-S. Löffler, C.E. Krill, A. Fitch, R. Hempelmann, J. Phys. Chem. B 104 (2000) 2467.

[18] N. Schell, T. Jensen, J.. Petersen, K.. Andreasen, J. Bøttiger, J. Chevallier, Thin Solid Films 441 (2003) 96.

[19] J.L.M. Rupp, A. Infortuna, L.J. Gauckler, Acta Mater. 54 (2006) 1721.

[20] J.L.M. Rupp, B. Scherrer, A.S. Harvey, L.J. Gauckler, Adv. Funct. Mater. 19 (2009) 2790.

[21] J.L.M. Rupp, B. Scherrer, L.J. Gauckler, Phys. Chem. Chem. Phys. 12 (2010) 11114.

[22] J.L.M. Rupp, B. Scherrer, N. Schäuble, L.J. Gauckler, Adv. Funct. Mater. 20 (2010) 2807.

[23] F. Jiao, A.H. Hill, A. Harrison, A. Berko, A. V Chadwick, P.G. Bruce, J. Am. Chem. Soc. 130 (2008) 5262.

[24] K. Jiao, B. Zhang, B. Yue, Y. Ren, S. Liu, S. Yan, C. Dickinson, W. Zhou, H. He, Chem. Commun. (2005) 5618.

[25] F. Jiao, P.G. Bruce, Adv. Mater. 19 (2007) 657.

[26] F. Ye, T. Mori, D.R. Ou, J. Zou, G. Auchterlonie, J. Drennan, Solid State Ionics 179 (2008) 827.

[27] Z.P. Li, T. Mori, G.J. Auchterlonie, J. Zou, J. Drennan, Mater. Res. Bull. 47 (2012) 763.

[28] F. Kleitz, S. Hei Choi, R. Ryoo, Chem. Commun. (2003) 2136.

[29] G. Williamson, W. Hall, Acta Metall. 1 (1953) 22.

[30] P. Scherrer, Nachrichten von Der Königlichen Gesellschaft Der Wiss. Zu Göttingen, Math. Klasse (1918) 1.

[31] A.J.C. Wilson, X-Ray Opt. (1949) 5.

[32] M. Jin, J.N. Park, J.K. Shon, Z. Li, M.Y. Yoon, H.J. Na, Y.K. Park, J.M. Kim, Res. Chem. Intermed. 37 (2011) 1181.

[33] H. Yao, J. Catal. 86 (1984) 254.

[34] S. Liang, E. Broitman, Y. Wang, A. Cao, G. Veser, J. Mater. Sci. 46 (2010) 2928.

[35] E. Rogemond, N. Essayem, R. Fréty, V. Perrichon, M. Primet, S. Salasc, M. Chevrier, C. Gauthier, F. Mathis, Catalysis and Automotive Pollution Control IV, Proceedings of the Fourth International Symposium (CAPoC4), Elsevier, 1998.

4

Ceramic-metal mesoporous composites as anode for SOFCs

4. Ceramic-Metal Mesoporous Composites as Anode for SOFCs

4.1. Anode Requirements for SOFC Applications 101

4.2. Structural Characterization of Powder of Mesoporous Composites of NiO-CGO 105

4.2.1. NiO matrix 105

4.2.2. CGO infiltrated matrix 108

4.3. Electrochemical Performance and Stability of Ni-CGO Mesoporous Anodes 113

4.3.1. Morphological characterization 113

4.3.2. Electrochemical performance 116

4.3.3. Stability 118

4.4. Fuel Cell Performance of Ni-CGO Mesoporous Anodes 119

4.4.1. Electrolyte supported cells 119

4.4.2. Anode supported cells 122

4.5. Conclusions 124

References 126

4. Ceramic-Metal Mesoporous Composites as Anode for SOFCs

4.1. Anode Requirements for SOFC Applications

The anode role in a Solid Oxide Fuel Cell (SOFC) is the electrochemical oxidation of the fuel. If hydrogen is used, the cell generates only water as sub-product and the reaction is,

$$H_2 + O^{2-} \rightarrow H_2O + 2e^- \quad \textbf{(4.1)}$$

Anode materials for SOFCs must meet a series of requirements, namely, sufficient electrical conductivity and catalytic activity, porous structure, high stability under reducing conditions and a thermal expansion coefficient (TEC) matching with the other components of the cells from ambient temperature to high temperatures (operating temperature or even higher temperatures during the cell fabrication) [1,2].

One common option to fabricate anodes is the use of ceramic-metal composites (cermets). The mentioned requirements limit the choice of the catalytic metal materials to basically noble metals (Pt, Ru) and nickel (Ni). In practice most of the SOFCs uses Ni due to its lower cost.

Porous Ni-YSZ cermets (YSZ: nickel stabilized zirconia) is currently the *state of art* anode material for high temperature SOFC applications. In order to maintain the required porous structure and avoid the agglomeration of Ni during long-term measurements, YSZ is added as structural matrix [3,4]. Moreover, its ionic conductivity extends the triple phase boundary (TPB) and the TEC perfectly matches with the most common electrolyte (YSZ) [5,6].

However, for intermediate temperatures (IT = 600 – 800 ºC) and particularly when using hydrocarbons fuels, Ni-YSZ is usually substituted by ceria-based materials [7]. Ceria and doped-ceria materials present higher ionic conductivity [8,9] and a better catalytic activity than YSZ for reforming and oxidization of hydrocarbons at lower

temperature [10,11], since they prevent the typical coke deposition that takes place in Ni–YSZ anodes [12,13]. This excellent catalytic performance together with good thermomechanical compatibility with a ceria-based electrolytes, makes ceria cermets the typical anode choice for IT-SOFCs [14].

Apart from material composition issues, the microstructure of the anodes, particularly if they are cermets, plays a key role in their performance [15,16]. Barnett *et al.* [17–19] have recently reported excellent visual representations of the importance of the anode microstructure for the global performance of the SOFCs. In particular, a well-defined ceramic scaffold is necessary to avoid the coarsening of the metallic part of the cermet anodes at the typical SOFC operation temperatures.

According to Barnett *et al.*, [19] it is also of major relevance to ensure a good connectivity along the metallic pathways of the cermet, since the metal is more prone to the generation of isolated, and therefore, electrochemically inactive areas than the ceramics (**Figure 4.1**). In addition to a good connectivity, low tortuosity and enough porosity, reducing the effective particle diameter to the nanoscale greatly increases the triple-phase-boundary (TPB) proportionally reducing the activation polarization [20].

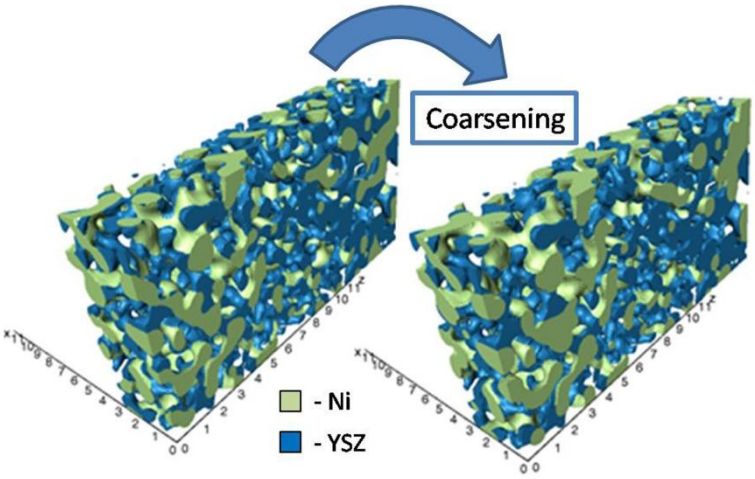

Figure 4.1. 3-D reconstruction of a Ni-Yttria Stabilized Zirconia (YSZ) anode functional layer microstructure in an SOFC. The figure on the left was experimentally found with FIB/SEM, while the figure on the right was obtained by simulating the coarsening of Ni particles by phase field methods (*taken from ref.* [18]).

The use of nanostructures in SOFC anodes is still limited due to a dramatic grain growth taking place at the high temperature required in some SOFC fabrication steps, *e.g.* the attachment of the anode to the electrolyte which takes place at temperatures over 1000 °C.

Despite this, some smart approaches have been already tried to implement nanostructured cermets in solid oxide cells [21]. Visco *et al.* [22], Gorte *et al*. [23] and Shao *et al.* [24] have recently reported uniform and continuous networks of metallic nanoparticulates incorporated by infiltration into temperature stable micrometer-sized electrolyte supporting backbones that clearly improve the SOFC performance.

A different approach has been presented by M. Mamak *et al*. [25,26] based on the decoration of mesoporous YSZ with uniformly dispersed nanoparticles of metals (Ni and Pt) (**Figure 4.2a**). Although Mamak *et al.* showed peak power densities lower than 150 mW cm^{-2} at 800 °C (**Figure 4.2b**), the mesoporous material can potentially increase the efficiency and reduce the operating temperatures below 700 °C.

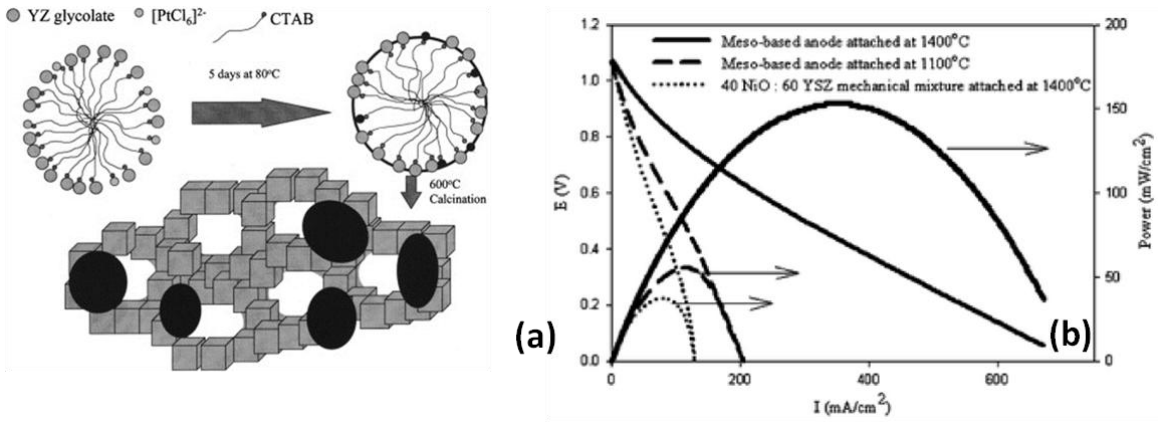

Figure 4.2. (a) Schematic of the formation mechanism of the mesoporous (metal)-YSZ following a soft template route. (b) I-V characteristics at 800 °C for cells made from mesoporous anodes attached at 1100 and 1400 °C, and mechanically mixed NiO/YSZ powders attached at 1400 °C (*taken from ref.* [25,26]).

The rich structural variation of mesoporous materials has not been fully exploited for practical applications [27]. Apart from their high surface area and pore uniformity, mesoporous materials have unique features that can be of major interest for electrodes in SOFCs.

In particular, the explained mesoporous structure of the KIT-6 (**Chapter 2.2.1**) consisting on a double gyroid geometry formed by two sets of interpenetrating mesoporous channels, perfectly matches with the cermet anode requirements of good ceramic and metal connectivity, homogeneity and large TPBs.

In the previous **Chapter 3**, a novel strategy to stabilize 3D open ordered mesoporous oxides was presented by reaching the self-limited grain growth regime inside the template and virtual non-degradation was presented up to temperatures of 1000 ºC.

In this chapter, mesoporous materials are thermally stabilized by another approach. In this case, a classical ceramic - metal (cermet) scaffolding method is used [28]. A compact close unit is fabricated by NiO and CGO mesoporous matrices, one of each formed by selectively filling the channels of the original KIT-6 template replica (see **Figure 4.3** for a sketch of the structure) as presented in **section 2.2.3 (Figure 2.4)**. By this technique the materials are intimate mixed in the nanoscale and keep the mesostructure stable in temperature up to 1200 ºC (T used in this work to attach the electrodes to the electrolyte). A detail structural characterization of the synthesized mesoporous nickel-gadolinium doped ceria (Ni-CGO) is presented (**section 4.2**).

Section 4.3 shows the operation of the mesoporous electrodes after implementation in electrochemical cells, in a symmetrical cell configuration under reducing atmosphere and high temperature (**Chapter 2.3.2, Figure 2.8**). Long-term stability tests under real operation conditions have been carried out and the evolution of the electrode microstructure with time has been evaluated.

Finally, the **section 4.4** is focused on the most common nickel based mesoporous cermets synthesized by this approach tested as whole SOFCs in different configurations. The mesoporous cermets are tested as anodes of electrolyte supported cells (**Chapter 2.3.2, Figure 2.10**). and as anode supports (tape casting) and anode functional layer in anode supported cells (**Chapter 2.3.2, Figure 2.11**).

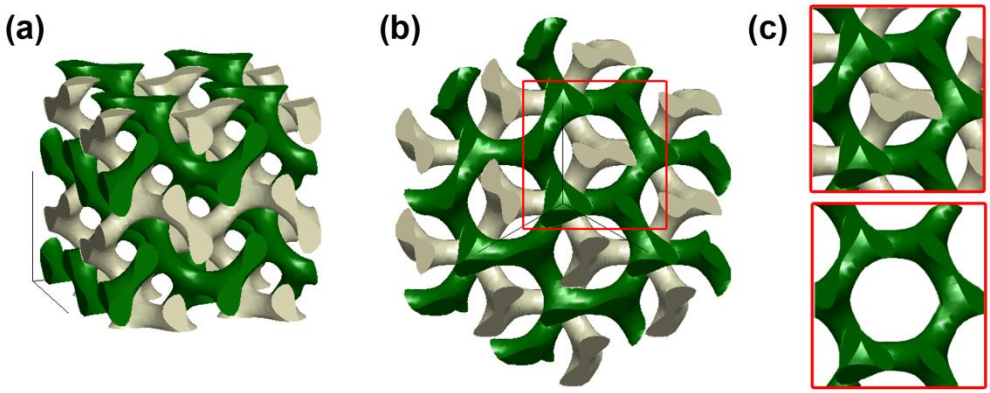

Figure 4.3. Sketch of the replica resulting from a double gyroid KIT-6 mesoporous template. (a) Two sets of interpenetrating mesoporous channels in the template; (b) [111] projection of the mesostructure and (c) bimodal pore size distribution obtained after filling one or two of the channels.

4.2. Structural Characterization of Powder of Mesoporous Composites of NiO-CGO

4.2.1. NiO matrix

Starting from silica powder with KIT-6-90 structure (see **2.2.1** for synthesis details), high-surface area NiO mesoporous replicas were synthesized by infiltration of nickel nitrate salts and calcination at 600 ºC (see details in the experimental **Chapter 2.2.2, Table 2.2**).

A typical TEM image of the as-synthesized mesoporous nickel oxide powder is presented in **Figure 4.4**. The picture clearly shows a highly ordered porous matrix with spherical NiO domains, consistent with the previously reported KIT-6 symmetry and the 3D process of nucleation and growth. The pore pattern observed in the figure corresponds to a typical bimodal pore size distribution generated by the infiltration of one or two of the interpenetrated channels originally present in the KIT-6 template structure. **Figure 4.5b** corroborates this local observation, by the pore size distribution calculated from the desorption branch of the isotherms using the BJH method.

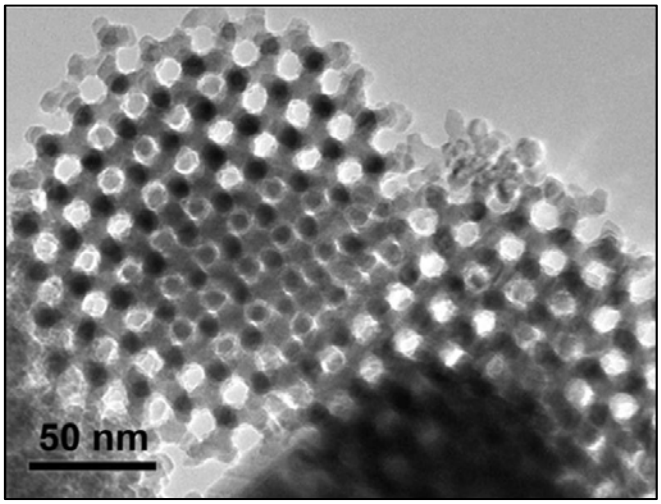

Figure 4.4. TEM image of the [111] projection of the mesoporous NiO replica after calcination at 600 ºC.

Nitrogen adsorption-desorption isotherms are shown in **Figure 4.5a** presenting a H1 hysteresis loop, yielded a BET surface area of 55 m^2/g after silica template removal similar to other oxides synthesized by the same hard template route [29]. Pore size distributions centered in 3 and 13 nm, corresponding to single- or double-filled channels, respectively, have been calculated for the NiO replica (**Figure 4.5b**). The ratio of the bimodal distribution is a key aspect for filling with a second material since narrower pores show problems with the employed infiltration method. In the present work, 3 nm pores represent less than 10 % of the total pore volume therefore expecting a good infiltration and interconnectivity for CGO on NiO.

The **Figure 4.6a** shows the powder X-ray diffraction pattern of the NiO. A single phase with cubic structure (*Fm-3m*) and lattice parameter a = 4.177 Å, is obtained after calcination (JCPDS 00-047-1049). **Figure 4.6b** shows the low-angle XRD pattern of the NiO mesoporous calcined at 600 ºC compared to the hard silica template KIT-6. Both diffraction patterns correspond to a three dimensional *Ia3d* symmetry, typically reported in the literature for KIT-6 mesoporous structures. The patterns show one sharp peak at 0.94-0.96º indexed as (211), at 1.08-1.1º the reflection (220) and another broad peak indexed as the (332) at 1.8-1.82º. The indexes indicate the reflections of the cubic cells with a lattice parameter of 22.7 nm for the KIT-6 and of 22.1 nm for the NiO replica. The

comparison of the NiO pattern with the original silica KIT-6 confirms that the mesostructure was transferred.

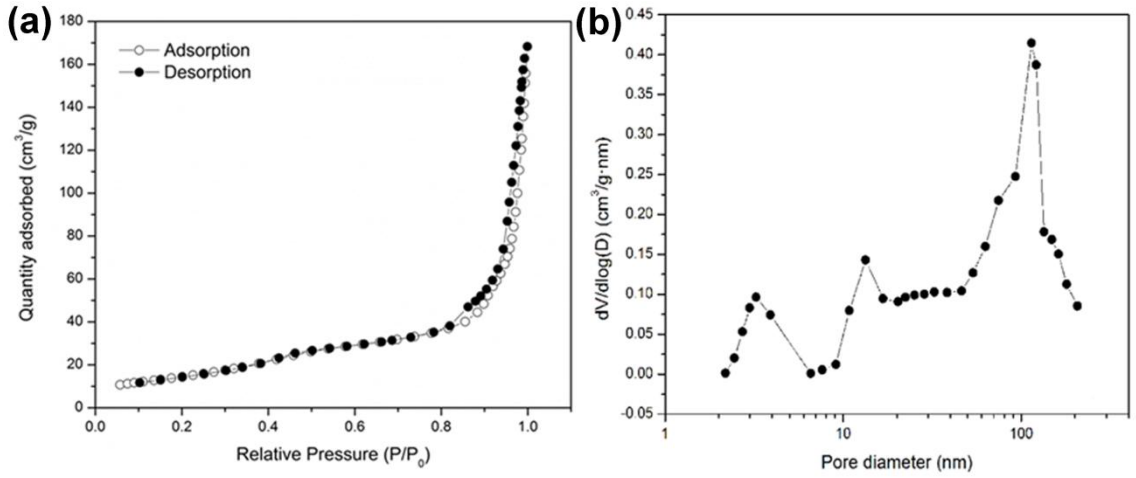

Figure 4.5. a) N_2 adsorption-desorption isotherms and b) pore size distribution calculated from the desorption branch using the BJH method, of the NiO mesoporous annealed at 600ºC.

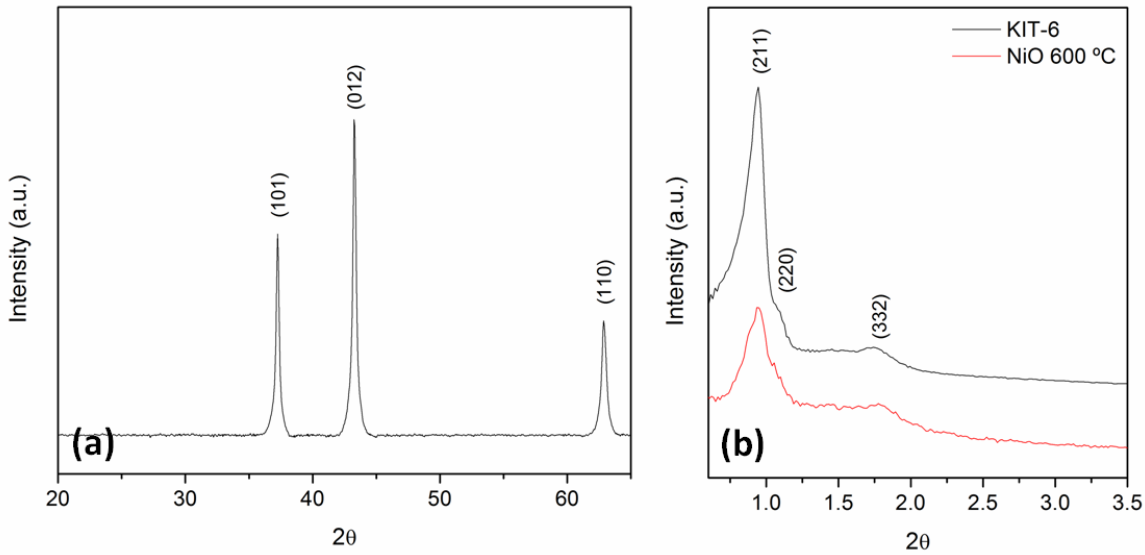

Figure 4.6. NiO mesoporous replica calcined at 600 ºC a) Powder XRD pattern; b) Low angle XRD (KIT-6 pattern is shown as comparison).

4.2.2. CGO infiltrated matrix

The CGO was impregnated in the NiO mesoporous matrix, from an stoichiometric solution of the nitrates salts and calcined at T = 1100 ºC for 3 h (details indicated in the experimental procedure of **Chapter 2.2.3, Table 2.3**). In order to corroborate the correct infiltration of the CGO within the pores of the mesoporous NiO replica, STEM-EELS was performed for the NiO-CGO samples stabilized at high temperature.

Figure 4.7a shows a bright field STEM image of a partially filled mesoporous particle of NiO (presented here opposite to a fully filled grain for clarity reasons). **Figure 4.7b** and **Figure 4.7c** show the EELS spectra for inside and outside of the filled pores, respectively (corresponding to the points indicated by the same color arrows). EELS analysis confirms that the mesoporous particles mainly contain Ni and O while inside the filled pores Ce, O and Gd are present. **Figure 4.8** shows additional typical images of NiO mesoporous particles fully filled with CGO.

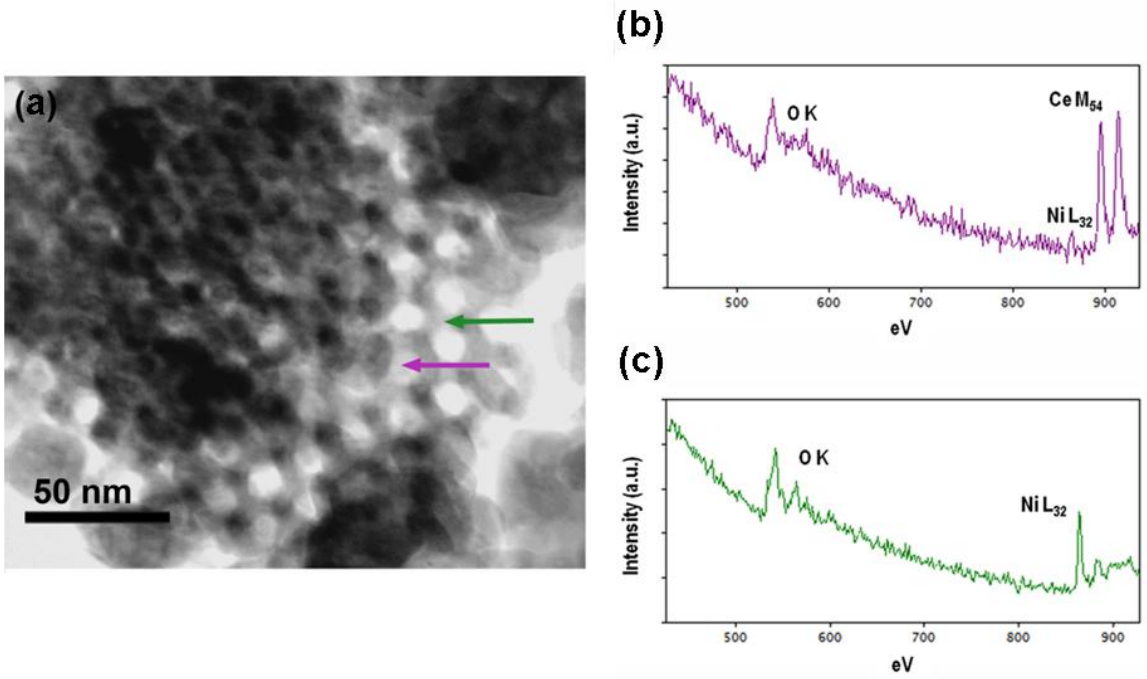

Figure 4.7. a) Bright field STEM image of the mesoporous NiO partially impregnated with CGO (50 % wt) and stabilized at high temperature; EELS spectra corresponding to the points indicated by the arrows: b) inside a NiO porous and c) in the wall of the mesoporous material.

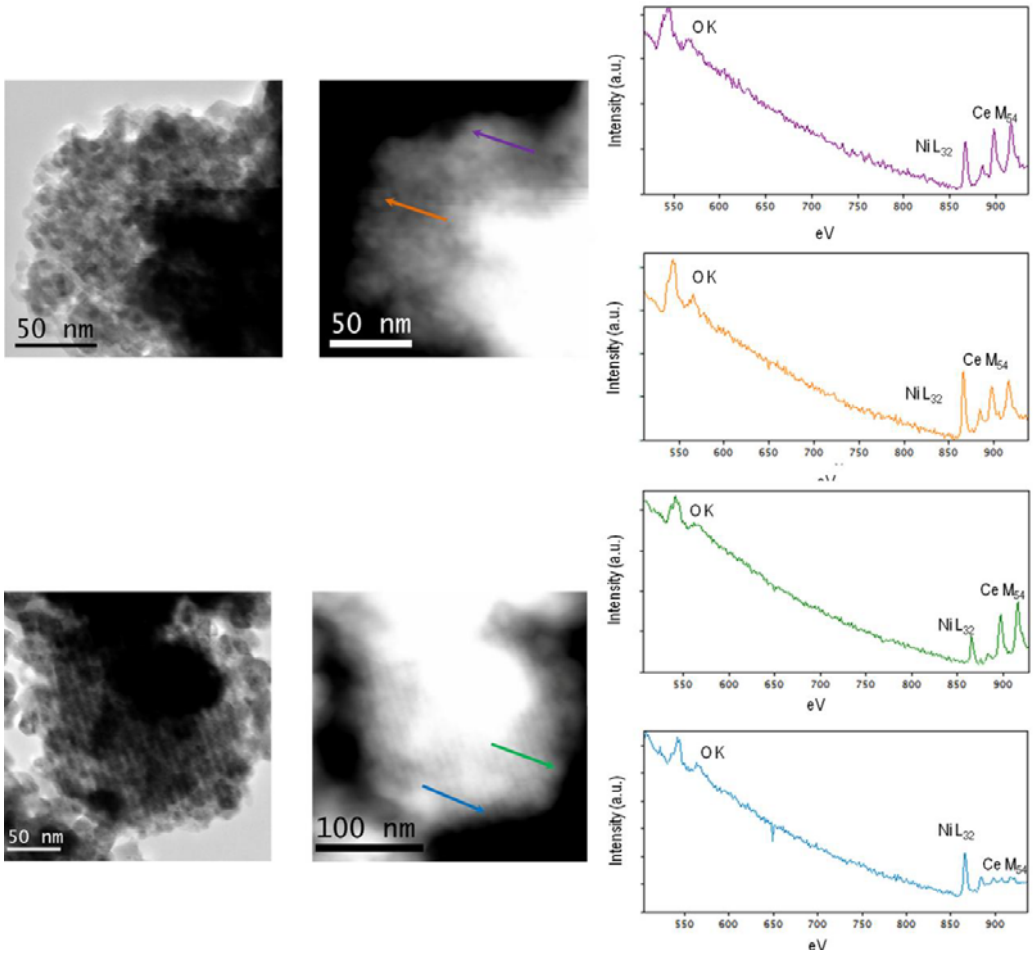

Figure 4.8. Bright field STEM images, HAADF STEM images and EELS spectra (corresponding to the points marked with the arrows) of two typical mesoporous particles of NiO-CGO.

It is worthy to mention that the energy window of the EEL detector is technically limited to 500 eV. Since the energy gap between the oxygen and Gd peaks is higher than 500 eV, they cannot be evaluated in a single spectrum at a time. Thus the **Figure 4.9** is presented, to confirm the presence of O and Ce and Gd inside the mesoporous structure.

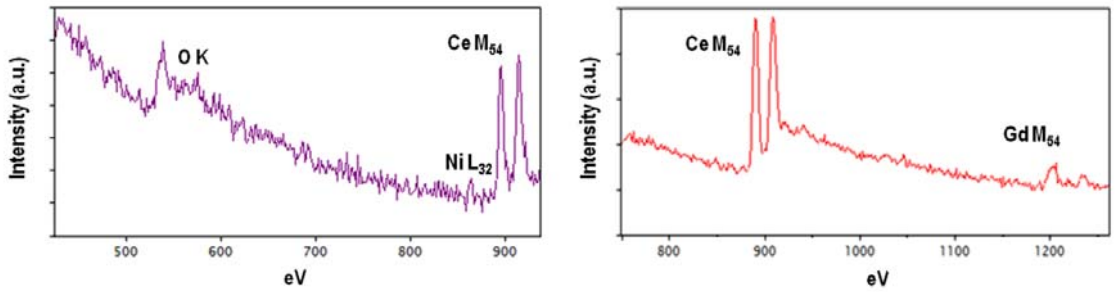

Figure 4.9. EELS spectra covering the electron energy loss of O, Ce and Gd inside a filled pore of the NiO nanoparticle shown in Figure 4.7a.

X-ray diffraction carried out on the NiO-CGO mesoporous composites confirmed the presence of two single phases: the cubic structure (s.g. *Fm-3m*) of NiO with lattice parameter a = 4.177 Å (JCPDS 47-1049) and a cubic fluorite structure (s.g. *Fm-3m*) of $Ce_{0.8}Gd_{0.2}O_{1.9}$ with lattice parameter a = 5.423 Å (JCPDS database 75-0162). No parasitic phases were observed in any of the spectra (**Figure 4.10**).

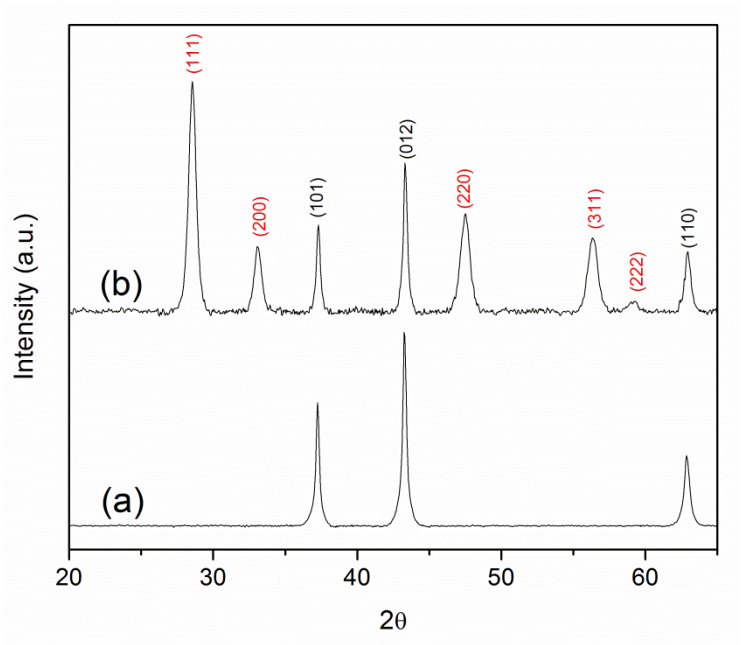

Figure 4.10. a) XRD pattern of NiO mesoporous calcined at 600 ºC; b) XRD pattern of the composite NiO-CGO sintered at high temperature. Diffraction peaks are labeled according to the reflections corresponding to each phase.

Figure 4.11 shows low-angle XRD patterns corresponding to samples extracted at the different fabrication and evaluation stages (original silica template powder is included for comparison). The diffraction peaks observed for all the patterns correspond to the reflections of a three dimensional *Ia3d* symmetry. Although a decrease of the long-range order of the mesoporosity is observed at each step, **Figure 4.11** confirms that the ordered mesoporous structure is transferred from the templates to the replica and most importantly, that the layer of Ni-CGO attached to the electrolyte at 1200 ºC also maintains the mesostructure after the NiO reduction and cell performance studies.

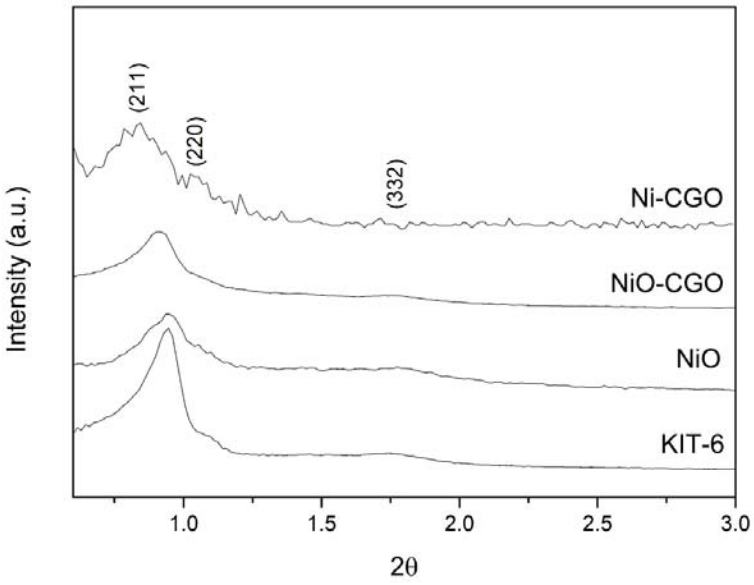

Figure 4.11. Low angle XRD of silica template with KIT-6 structure are compared to diffractograms from i) powder of the NiO mesoporous replica (calcined at 600 ºC); ii) powder of the NiO-CGO (65:35 % wt) obtained from the infiltration of CGO into the NiO replica and stabilization at 1100 ºC; iii) the layer of Ni-CGO attached to the electrolyte of CGO at 1200 ºC after the NiO reduction and cell performance studies.

The good connectivity of the CGO network created inside the mesoporous NiO was checked itself. In order to proved it the NiO backbone was reduced to metallic Ni and then removed by nitric acid leaching (HNO_3) 2 M at 60 ºC. Although the acid leaching etches both Ni and CGO, the CGO etch rate is lower. XRD confirmed there is no Ni present after the etching (only CGO). A TEM image of the Ni-CGO powder after being

subjected to the explained acid leaching process is presented in **Figure 4.12**, the following characteristics are observed,

- Good connectivity between the CGO particles
- Particle size of the order of magnitude of the porosity of the mesoporous NiO (the CGO penetrated inside the NiO)
- High porosity maintained (not perfectly ordered, attributed to the effects of the nitric acid etch on the CGO)

The results demonstrate that crystalline and well-connected NiO-CGO interpenetrated nanoparticles were successfully synthesized and stabilized at 1100 ºC.

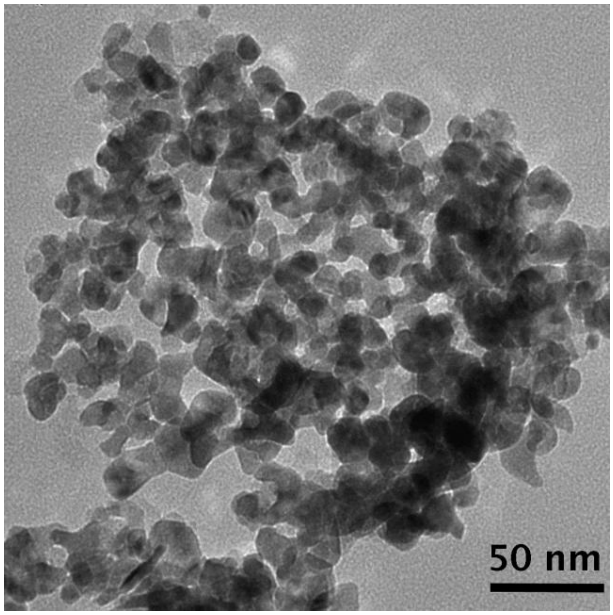

Figure 4.12. TEM image of a CGO particle after nitric acid leaching of a Ni-CGO mesoporous particle stabilized at high temperature.

4.3. Electrochemical Performance and Stability of Ni-CGO Mesoporous Anodes

4.3.1. Morphological characterization

Ceria based symmetrical cells with NiO-CGO mesoporous powder as electrodes were fabricated airbrushing ethanol inks based on the synthesized powder. A thin CGO layer is first applied onto the electrolyte, to improve the attachment of the electrodes. NiO-CGO is further deposited and the thermal treatment for the attachment to the electrolyte was fixed at T_{att} = 1200 ºC and 3 h (details indicated in **section 2.3.2.1**).

Cells with single and double layers were fabricated. The single layer electrode is composed by NiO:CGO with 65:35 % wt (from now on abbreviated as NiO-CGO(65)); while the double layer is composed of a functional layer of NiO-CGO with 50:50 % wt, (NiO-CGO(50)) located close to the electrolyte and a layer of NiO-CGO(65) close to the current collector (find an scheme of the cell in **Chapter 2, Figure 2.8**). A study performed to fabricate the cells with the optimum nickel concentration and composition of the layers (above described) is shown in **Appendix A**.

Figure 4.13 shows a set of SEM images of the electrolyte-anode interface of the fabricated Ni-CGO//CGO//Ni-CGO symmetrical cells after nickel oxide reduction in hydrogen. Since the images have been acquired with a backscattering detector, it is possible to observe the intimate interpenetration between phases (the Ni phase appears in a darker grey than the CGO). The anode bi-layer, from now on abbreviated as Ni-CGO(50-65) is homogeneous, continuous and well-formed (**Figure 4.13a**) with an extremely fine microstructure consisting of highly-interconnected networks of Ni, CGO and open porosity (**Figure 4.13b**). This ideal situation in which the two phases of nickel and CGO are intimately mixed will increase the length of the triple phase boundary, while the open porosity network will help for the required rapid gas diffusion [30].

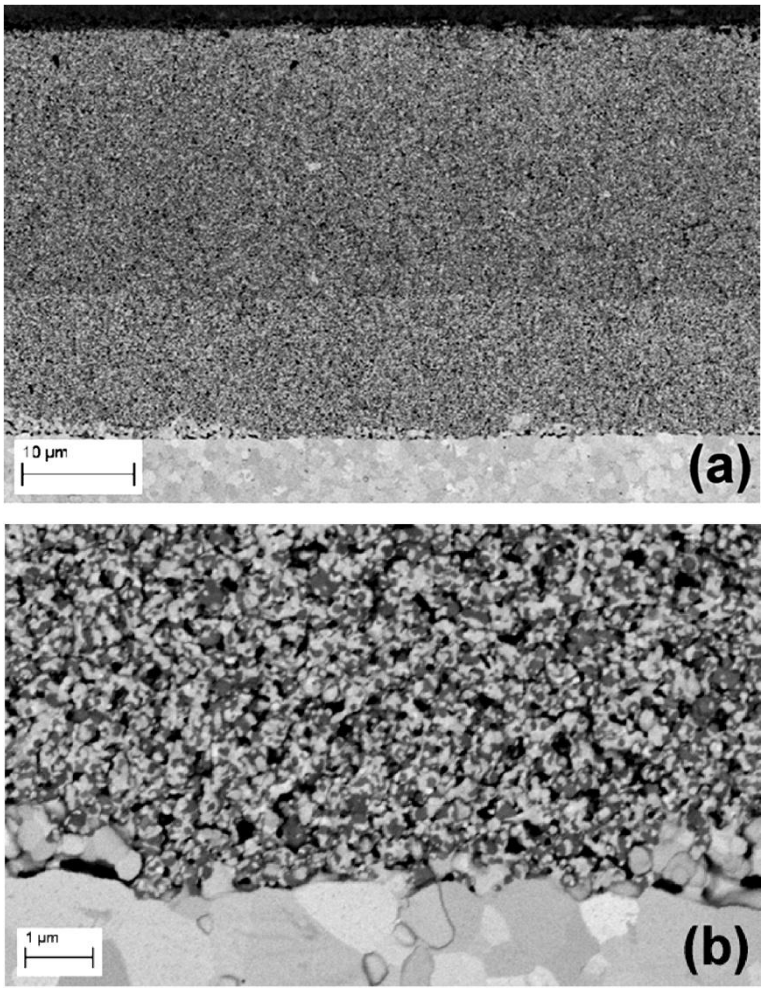

Figure 4.13. Backscatter SEM images of the Ni-CGO mesoporous composite attached to the CGO electrolyte after electrochemical measurements showing a) double layer with different Ni compositions, Ni-CGO(50-65); b) excellent homogeneity and highly interconnected metallic and ceramic networks. Compositional contrast obtained by backscattering SEM allows the identification of Ni (darker) and CGO (lighter) intermixed particles.

Figure 4.14 shows the rough layer of CGO attached at higher temperature to the CGO electrolyte (T = 1350 ºC). This rough layer enhances the continuity of the anode-electrolyte interface by increasing the surface area of the electrolyte [31].

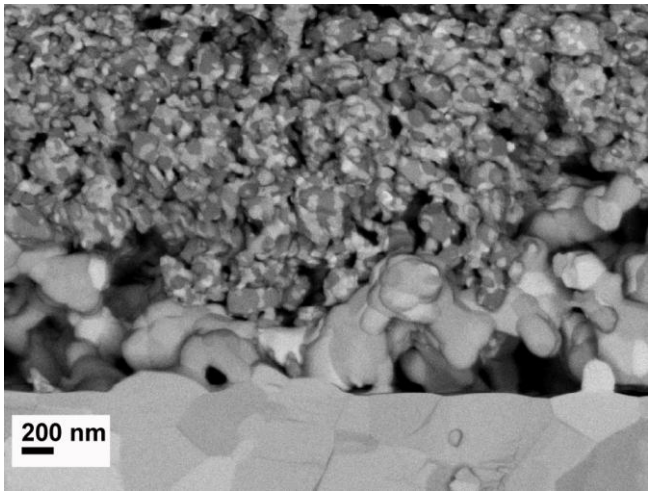

Figure 4.14. Backscatter SEM images of the rough layer of CGO attached to the electrolyte at a higher temperature, improving the interface electrode-electrolyte.

Figure 4.15 shows a direct comparison of the microstructure of the here-fabricated anode and a commercial cermet. As a result of using a mesoporous composite, a microstructure clearly in the nanoscale can be achieved and maintained at high temperatures (T = 1100 ºC) without significantly compromising the metallic and the ceramic continuity or the porosity of the electrode.

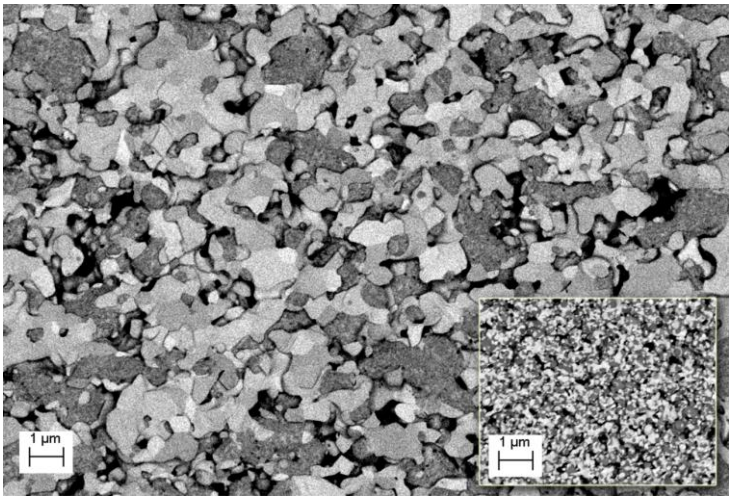

Figure 4.15. Backscatter SEM image of a cross-section of commercial Ni-CGO fabricated by tape casting (FAE S.A.) compared to mesoporous Ni-CGO fabricated for this work. Please notice that both images are presented in the same scale.

4.3.2. Electrochemical performance

The symmetrical cells were electrically characterized by impedance spectroscopy using the experimental setup described in the **Chapter 2.5.1** (**Figure 2.15**). The electrical measurements were carried out under a water vapor saturated 5 % Hydrogen in argon atmosphere in the temperature range between 600 ºC and 900 ºC.

Figure 4.16a depicts a typical Nyquist plot for the electrochemical response of the Ni-CGO//CGO//Ni-CGO symmetrical cells in wet 5 % H_2 at 650 ºC. All the spectra were fitted with an equivalent circuit (EC) formed by an inductance in series with a resistance (mainly attributed to the electrolyte contribution) and a Finite Gerischer Element, which is mathematically equivalent to the Adler-Lane-Steele (ALS) analytical model developed for porous Mixed Ionic-Electronic Conductors (MIECs) [32–34].

The continuous line represents the fitting of the proposed EC. The inductance contribution was subtracted in this figure for clarity reasons. The excellent agreement between model and experimental data suggests that the here-presented Ni-CGO cermet is formally analogous to the intrinsic MIEC materials due to the intimate connection between both the ionic conductor (CGO) and the electronic conductor (Ni) and the percolation pathways ensured for both components.

The main benefit of this MIEC behavior is the reduction of the charge transfer resistance by increasing the Triple Phase Boundary. Since the limiting phenomena are expected to be the non-charge transfer processes (solid-state diffusion, surface exchange and gas-phase diffusion) the properties of the electrolyte, in terms of oxygen diffusion and oxygen surface exchange, play a crucial role contrary to the structural function for traditional cermets [35]. Therefore, the approach used for this work, involving a totally reproducible continuous matrix, represents a powerful tool in the systematic study of engineered mixed conduction in electrodes for SOFCs.

Figure 4.16b shows the evolution with temperature of the anode/electrolyte interfacial area-specific resistance (ASR) in wet 5 % H_2 as calculated from the impedance spectra measurements. In terms of SOFC applications, this interface should not contribute more than 0.25 $\Omega \cdot cm^2$ to the total fuel cell area-specific resistance [36]. This target value is attained at 675 ºC for the Ni-CGO//CGO system ensuring a good performance of the anode within the intermediate range typical of IT-SOFC applications.

In comparison to recently reported nanostructured anodes prepared by infiltration [37], an excellent performance is confirmed. ASR values of 0.41 $\Omega \cdot cm^2$ and 0.24 $\Omega \cdot cm^2$ have been previously reported for pure Ni anodes and Ni-YSZ anodes both impregnated with doped ceria nanoparticles at 800 ºC in humidified pure hydrogen [38,39]. The anode presented here also compares well to highly optimized standard cells from Risø/Topsoe Fuel Cell (TOFC) based on Ni-YSZ anodes with ASRs = 0.24 $\Omega \cdot cm^2$ at 700 ºC in humidified pure H_2 [40,41] and commercial cells of Ni-CGO/YSZ/Ni-CGO characterized by Magnière *et al.* [42] that present ASR = 0.50 $\Omega \cdot cm^2$ at 820 ºC in Ar / 2 % H_2 / 2 % H_2O atmospheres.

According to **Figure 4.16b**, the conductivity dependence on temperature follows an Arrhenius-type law. A slight deviation can be observed at temperatures above 750 ºC likely due to the increase of electronic conductivity of the CGO electrolyte under reducing conditions, considering this fact the calculated activation energy is E_a = 1.4(1) eV (red line).

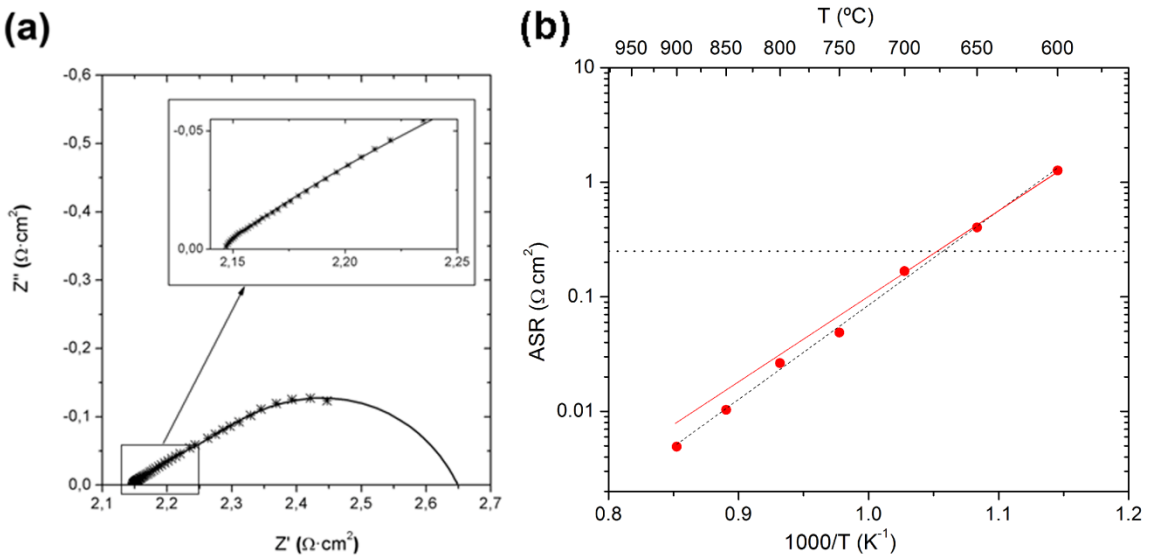

Figure 4.16. a) Nyquist plot obtained from an EIS measurement of Ni-CGO(50-65)//CGO//Ni-CGO(50-65) symmetrical cells at 650 ºC under wet 5 % H_2 atmosphere. The solid line shows the fit of the ALS model to the experimental data; b) Arrhenius plot of the electrode/electrolyte resistance of the same symmetrical cells measured in the temperature range from 600 to 900 ºC. Pointed line shows the targeted value of ASR = 0.25 Ω·cm^2.

4.3.3. Stability

In order to demonstrate the stability of the microstructure with time, a symmetrical cell of Ni-CGO(65)//CGO//Ni-CGO(65) was subjected to a long time impedance measurement at 800 ºC under wet 5 % H_2 (notice here that the layer with higher content on nickel was chosen for the stability evaluation since it is expected to be more prone to degrade through nickel agglomeration).

Figure 4.17 shows the ASR values obtained from impedance spectra recorded every 5 hours during more than 200 h. According to these results, the ASR of the electrode/electrolyte interface remains almost constant suggesting virtually no degradation of the electrode all across the experiment. In fact, an enhancement of the electrochemical performance is observed (67.8 μΩ·cm^2/h corresponding to an improvement of 32.4 %) probably due to an accommodation of the percolation pathways with time. Backscatter SEM images of the electrode microstructures at the beginning and

end of the measurements are inserted for comparison in **Figure 4.17**. No significant agglomeration can be appreciated with naked eye, demonstrating a long term stability of the nanostructure under a typical operational temperature and reducing atmosphere.

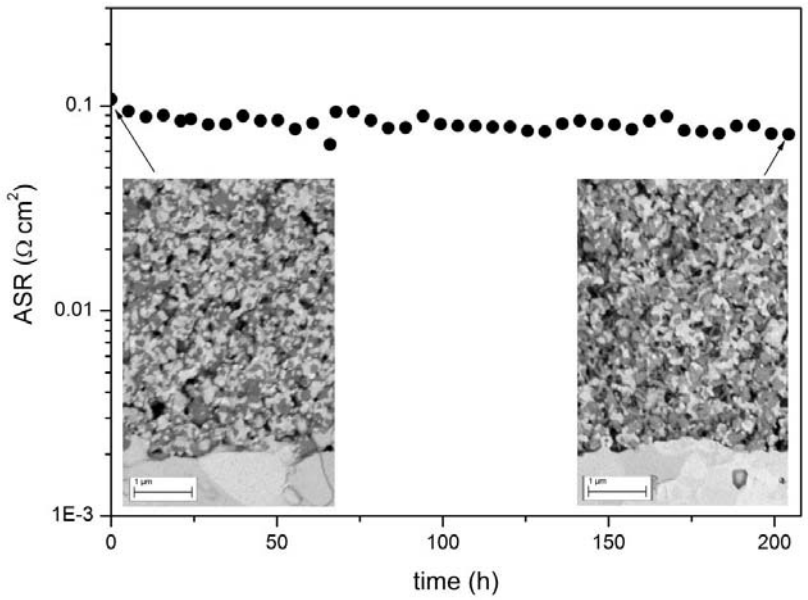

Figure 4.17. Evolution with time of the electrode/electrolyte resistance of a symmetrical cell of Ni-CGO(65)//CGO//Ni-CGO(65) at 800 ºC under water vapor saturated 5 % H_2 in Ar atmosphere. The two insets correspond to backscatter SEM images of the microstructure at the beginning and the end of the stabilization test.

4.4. Fuel Cell Performance of Ni-CGO Mesoporous Anodes

4.4.1. Electrolyte supported cells

The performance of the mesoporous Ni-CGO composites were also studied as anode in electrolyte supported IT-SOFCs, fabricated with commercial tape castings of 10Sc1CeSZ (150 μm thickness, Kerafol) and commercial $La_{0.6}Sr_{0.4}Co_{0.2}Fe_{0.8}O_3$ (LSCF, Kceracell) powder as cathode (fabrication cell details in **section 2.3.2.2, Table 2.4**). A dense PLD barrier layer of 2 μm of CGO was applied onto the cathode side of the tape casting to prevent the formation of secondary phases (see **Chapter 2, Figure 2.10**). Cells

were measured in the setup described in **Chapter 2.5.1** using pure humidified hydrogen as fuel and synthetic air as oxidant.

Figure 4.18 shows the current-voltage and power density curves for different temperatures (600 ºC - 850 ºC) using pure humidified H_2 as fuel and synthetic air as oxidant. Open circuit voltages (V_{oc}) of V_{oc} = 1.12 V at 600 ºC and V_{oc} = 1.05 V at 850 ºC have been measured. The maximum power density obtained for a single cell was 514 mW·cm^{-2} at 850 ºC. The values of power higher than 325 mW·cm^{-2} at 750 ºC demonstrate that the proposed mesoporous anode may render high performance within the intermediate range of temperatures.

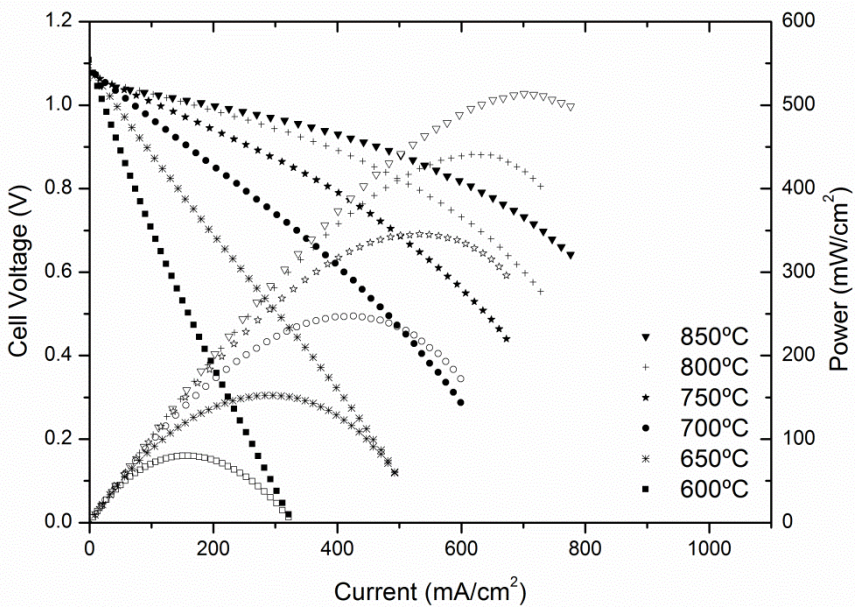

Figure 4.18. Cell voltage and power density as a function of the current density for a Ni-CGO//10Sc1CeSZ//LSCF fuel cell operating at different temperatures under pure humidified H_2 as fuel and synthetic air as oxidant.

A more detailed analysis of the different contributions to the total resistance was carried out by using impedance spectroscopy (EIS) at using a bias voltage of 0.7 V to simulate the operation conditions. **Figure 4.19** shows the Arrhenius plot of the ASR coming from both the series resistance, *i.e.* mainly the electrolyte contribution, and the

polarization resistance, *i.e.* mainly the electrode contribution. The electrodes showed an excellent performance in pure H_2, with values below the targeted 0.5 **Ω**·cm^2 at *ca.* 700 ºC.

Apart from these facts, it should be indicated that there is change of slope in the IV curves of **Figure 4.18** at high current densities attributed to slow mass diffusion or concentration polarization (**Chapter 1, section 1.4.1.2**), which may be due to the close micro-structure of the mesoporous cermets as anodes. Although this polarization diffusion cannot be observed in the EIS measurement performed under a bias voltage of 0.7 V (operational point), they would have observed if EIS measurements were performed under low bias.

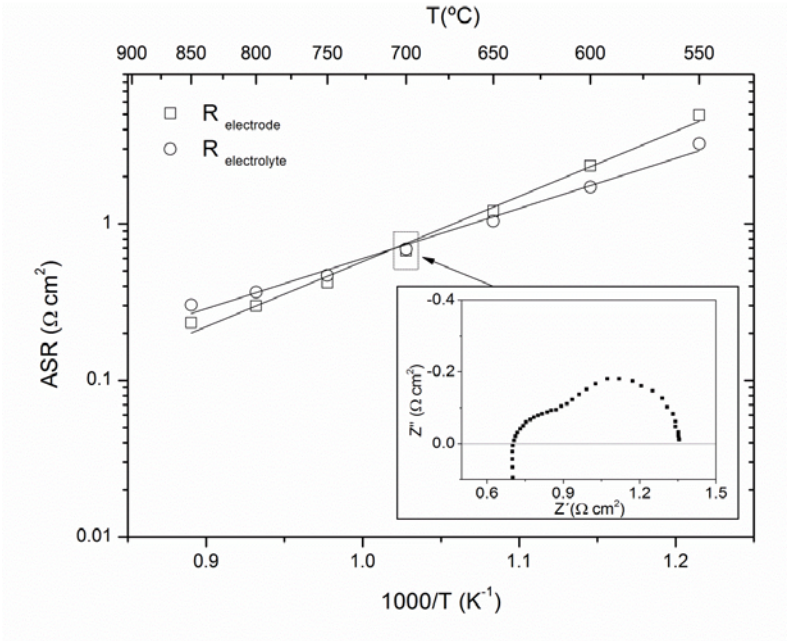

Figure 4.19. Arrhenius plot of the series ($R_{electrolyte}$) and polarization ($R_{electrode}$) resistances of the Ni-CGO//10Sc1CeSZ//LSCF cells characterized in fuel cell mode (bias 0.7 V). The inset shows a Nyquist plot of the device at 700 ºC.

4.4.2. Anode supported cells

In the previous sections, the feasibility of the so-fabricated mesoporous cermets as anodes for SOFCs has been proved. However, when lowering the operating temperature the most common electrolyte yttria-stabilized zirconia (YSZ), show low ionic conductivity. For conventional YSZ electrolyte supported cells (150 μm thickness) an operating temperature around 1000 ºC is required, to achieve the power density (500 $mW \cdot cm^{-2}$) called for SOFC applications. If the YSZ electrolyte thickness is reduced to 15 μm the same power output can be achieved at temperatures as low as 700 ºC [30]. Therefore, anode-supported cells with thin electrolytes are currently the preferred choice for intermediate temperature (IT) SOFCs. Anode supported cells based on the characterized mesoporous cermets were fabricated and electrochemically tested.

Tape casting of mesoporous NiO-YSZ was fabricated (as explained the experimental procedure of **Chapter 2.3.1.3**). A double layer of SSZ-SDC ($(Sc_2O_3)_{0.10}(ZrO_2)_{0.90}$ - $Sm_{0.20}Ce_{0.80}O_{1.9}$) was deposited by drop coating (**section 2.3.1.4**) on the top and sintered at 1250 ºC, conforming a dense electrolyte. Commercial SSC-SDC ($Sm_{0.5}Sr_{0.5}CoO_{3-\delta}$ - $Sm_{0.2}Ce_{0.8}O_{1.9}$) powder was used for preparing inks, that after deposition act as cathode (see **Table 2.5** for more details and **Figure 2.11** for a scheme of the anode supported cells).

Figure 4.20 shows a cross-sectional SEM image of the so-fabricated cells, the mesoporous anode showed a homogeneous and continuous structure. In this case, the microstructure of the mesoporous anode shows bigger pores, due to the addition of pore formers (starch and graphite) which were included during the fabrication of the *green tapes* to allow fast gas diffusion. The SSZ electrolyte layer is dense and had a thickness of ~ 8 μm, while the SDC layer show close porosity of ~ 3 μm in thickness, after being co-fired at 1250 ºC. The cells were tested under pure hydrogen as fuel and ambient air as oxidant at 650 ºC in the standard setup for measuring of the *Meilin Liu Group* (MSE, Georgia Institute of Technology).

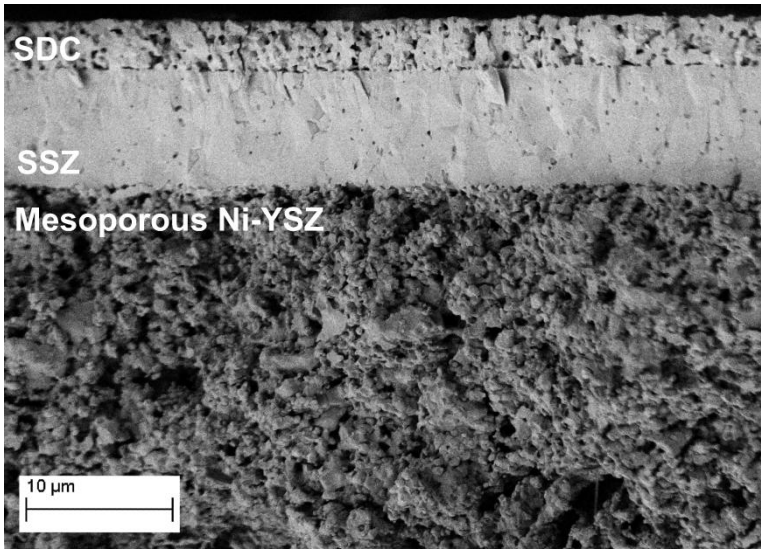

Figure 4.20. Cross-sectional SEM image of the anode supported cell made with Ni-YSZ mesoporous tape-casting.

Figure 4.21 shows the current-voltage and power density curves of the single cell at 650 ºC using pure humidified H_2 as fuel and ambient air. A maximum powder density of 690 mW/cm^2 was obtained. For comparison purposes an anode supported cell was fabricated in parallel, following the same procedure and materials with exception of the Ni-YSZ tape casting, which was made from a mechanical mixture of commercial nickel carbonate and YSZ powder. The obtained peak power density of this cell was 380 mW/cm^2.

Due to the explained differences between the cells, the dissimilar performance of the cells could be attributed to the microstructure of the anode supports. The better performance of the Ni-YSZ mesoporous cell in comparison with the Ni-YSZ commercial cell, can be explained by the unique nature of the mesoporous powder. In opposition to the classical mechanical mixture of commercial powder, the strategy followed to fabricate the cermet mesoporous materials consists in the interpenetration of the metallic and the ceramic part before the sintering of the anode.

Although a great improvement on the electrochemical performance was observed, these types of cells were not feasible to be measured for long-term stability tests due to a poor consistency (brittleness) after the nickel reduction. This was attributed to the joined

effects of the pore formers and the intrinsic high thermal stability of the mesoporous powder which leads to a low volume shrinkage of the anode support (studied in **Chapter 2, section 2.3.1.3.2**).

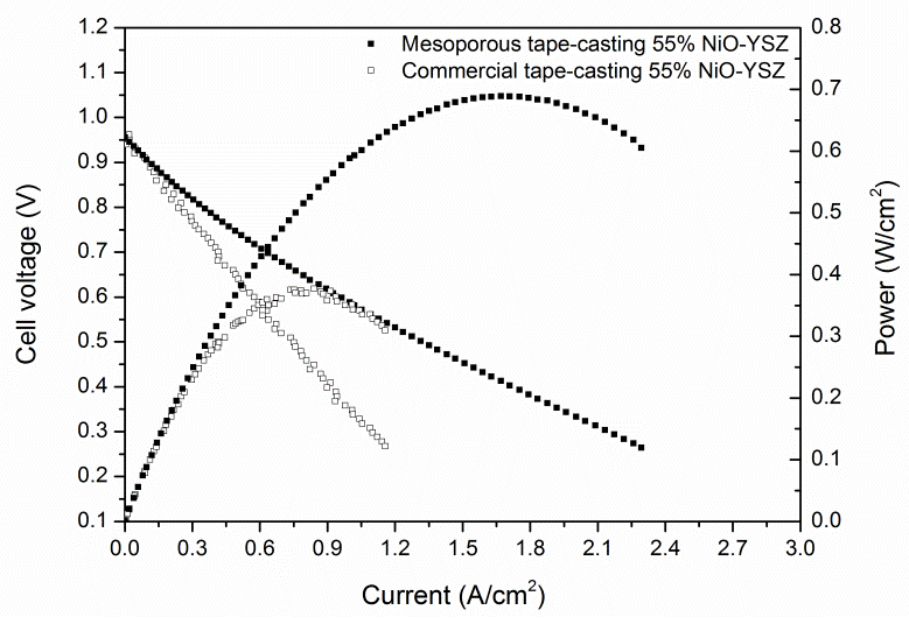

Figure 4.21. Cell voltage and power density as a function of the current density at 650 ºC under pure H_2 as fuel and ambient air as oxidant, for anode-supported IT-SOFCs fabricated with mesoporous versus commercial Ni-YSZ tape castings.

4.5. Conclusions

High temperature stable mesoporous cermets were successfully synthesized by a replication method starting from a hard silica template with KIT-6 structure. Mesoporous nickel oxide was first obtained from replication of the silica template and calcination at 600 ºC. After template removal a second infiltration step allowed the ceramic crystallization inside the NiO channels.

TEM-EELS analysis demonstrated an excellent impregnation of the CGO into NiO. Powder of NiO-CGO composite was stabilized at high temperatures (T_{sint}=1100 ºC) before implementation as anode material for SOFC hence maintaining the mesoporous microstructure after the attachment step. Electrochemical evaluation of the composites

working as anodes yielded an excellent performance with targeted values of area specific resistance obtained at temperatures below 700 ºC (ASR= 0.25 $\Omega \cdot cm^2$ for T=675 ºC).

According to the EIS measurements, the mesoporous cermet is formally analogous to a mixed ionic electronic conductor probably due to the high interpenetration of nickel and CGO structures that gives as a result a good electronic conductivity of the metallic part and a strong penetration of the active area in the electrode by increasing the TPB.

Long-term stability was also confirmed by operation during 200 h at 800 ºC in wet 5% H_2 atmosphere with an improvement of 32.4 % (67.8 $\mu\Omega \cdot cm^2/h$) of the electrochemical behavior and no significant microstructural variation. The well-connected ceramic and metallic networks should be the reason of the stability of the nanostructure.

A maximum power density of 514 mW/cm^2 at 850 ºC was measured in fuel cell mode for an electrolyte-supported SOFC based on the mesoporous Ni-CGO composite. Moreover, anode supported cells were fabricated using Ni-YSZ mesoporous tape castings giving a peak power density of 690 mW/cm^2 at 650 ºC.

In order to improve the mechanical consistency of the tape castings, taking advantage of the excellent electrochemical performance and stability of the mesoporous cermets, the addition of an optimize mesoporous functional layer (AFL) between the electrode and the electrolyte, seem to be a promising approach to be implemented in anode-supported schemes.

References

[1] A. Atkinson, S. Barnett, R.J. Gorte, J.T.S. Irvine, A.J. McEvoy, M. Mogensen, S.C. Singhal, J. Vohs, Nat. Mater. 3 (2004) 17.

[2] W. Zhu, S. Deevi, Mater. Sci. Eng. A 362 (2003) 228.

[3] S. Tao, J.T.S. Irvine, Nat. Mater. 2 (2003) 320.

[4] C. Sun, U. Stimming, J. Power Sources 171 (2007) 247.

[5] M. Brown, S. Primdahl, M. Mogensen, J. Electrochem. Soc. 147 (2000) 475.

[6] J. Lee, Solid State Ionics 148 (2002) 15.

[7] S.P. Jiang, S.H. Chan, J. Mater. Sci. 39 (2004) 4405.

[8] A. Tarancón, Energies 2 (2009) 1130.

[9] J.W. Fergus, Mater. Sci. Eng. A 397 (2005) 271.

[10] C. Xia, F. Chen, M. Liu, Electrochem. Solid-State Lett. 4 (2001) A52.

[11] C. Xia, Solid State Ionics 152-153 (2002) 423.

[12] C.A.-H. Chung, S.J.A. Livermore, R.M. Ormerod, Ionics 9 (2003) 342.

[13] N. Laosiripojana, W. Sutthisripok, S. Charojrochkul, S. Assabumrungrat, Fuel 90 (2011) 136.

[14] S. Zha, Solid State Ionics 166 (2004) 241.

[15] N.P. Brandon, D.J. Brett, Philos. Trans. A. Math. Phys. Eng. Sci. 364 (2006) 147.

[16] J.C. Ruiz-Morales, J. Canales-Vázquez, J. Peña-Martínez, D. Marrero-López, J.T.S. Irvine, P. Núñez, J. Mater. Chem. 16 (2006) 540.

[17] J.R. Wilson, W. Kobsiriphat, R. Mendoza, H.Y. Chen, J.M. Hiller, D.J. Miller, K. Thornton, P.W. Voorhees, S.B. Adler, S.A. Barnett, Nat. Mater. 5 (2006) 541.

[18] J.S. Cronin, J.R. Wilson, S.A. Barnett, J. Power Sources 196 (2011) 2640.

[19] J.R. Wilson, J.S. Cronin, S.A. Barnett, Scr. Mater. 65 (2011) 67.

[20] E.D. Wachsman, K.T. Lee, Science 334 (2011) 935.

[21] Z. Shao, W. Zhou, Z. Zhu, Prog. Mater. Sci. 57 (2012) 804.

[22] M.C. Tucker, G.Y. Lau, C.P. Jacobson, L.C. DeJonghe, S.J. Visco, J. Power Sources 171 (2007) 477.

[23] L. Adijanto, R. Küngas, J. Park, J.M. Vohs, R.J. Gorte, Int. J. Hydrogen Energy 36 (2011) 15722.

[24] Y. Lin, C. Su, C. Huang, J.S. Kim, C. Kwak, Z. Shao, J. Power Sources 197 (2012) 57.

[25] M. Mamak, N. Coombs, G. Ozin, J. Am. Chem. Soc. 122 (2000) 8932.

[26] M. Mamak, N. Coombs, G. a Ozin, Chem. Commun. (2002) 2300.

[27] Y. Han, D. Zhang, Curr. Opin. Chem. Eng. 1 (2012) 129.

[28] L. Almar, B. Colldeforns, L. Yedra, S. Estradé, F. Peiró, A. Morata, T. Andreu, A. Tarancón, J. Mater. Chem. A 1 (2013) 4531.

[29] F. Jiao, A.H. Hill, A. Harrison, A. Berko, A. V Chadwick, P.G. Bruce, J. Am. Chem. Soc. 130 (2008) 5262.

[30] N.P. Brandon, S. Skinner, B.C.H. Steele, Annu. Rev. Mater. Res. 33 (2003) 183.

[31] A. Tarancón, A. Morata, G. Dezanneau, S.J. Skinner, J.A. Kilner, S. Estradé, F. Hernández-Ramírez, F. Peiró, J.R. Morante, J. Power Sources 174 (2007) 255.

[32] S.B. Adler, J.A. Lane, S.B.C. H, J. Electrochem. Soc. 143 (1996) 3554.

[33] B.A. Boukamp, H.J.M. Bouwmeester, 157 (2003) 29.

[34] B. Boukamp, M. Verbraeken, D. Blank, P. Holtappels, Solid State Ionics 177 (2006) 2539.

[35] B. Rosch, Solid State Ionics 175 (2004) 113.

[36] N.P. Brandon, S. Skinner, B.C.H. Steele, Annu. Rev. Mater. Res. 33 (2003) 183.

[37] S.P. Jiang, Int. J. Hydrogen Energy 37 (2012) 449.

[38] R. Barfod, M. Mogensen, T. Klemenso, A. Hagen, Y.-L. Liu, P. Vang Hendriksen, J. Electrochem. Soc. 154 (2007) B371.

[39] R. Barfod, A. Hagen, S. Ramousse, P. V. Hendriksen, M. Mogensen, Fuel Cells 6 (2006) 141.

[40] W. Wang, S.P. Jiang, A.I.Y. Tok, L. Luo, J. Power Sources 159 (2006) 68.

[41] S.P. Jiang, Y.Y. Duan, J.G. Love, J. Electrochem. Soc. 149 (2002) A1175.

[42] C. Magnière, S. Di Iorio, B. Morel, ECS Trans., (2011), 1841–1849.

5

Infiltrated mesoporous composites as a cathode for IT-SOFCs

5. Infiltrated Mesoporous Composites as a Cathode for IT-SOFCs

5.1. Cathode Requirements and Advantages of Infiltrated Microstructures ...133

5.2. Structural Characterization of $Sm_{0.5}Sr_{0.5}CoO_{3-\delta}$ Infiltrated Mesoporous Scaffolds of $Ce_{0.8}Sm_{0.2}O_{1.9}$.....138

5.2.1. Mesoporous samarium-doped ceria (SDC) powder.....138

5.2.2. Mesoporous SDC ceramic scaffold infiltrated with SSC.....140

5.3. Electrochemical Performance and Stability of $Sm_{0.5}Sr_{0.5}CoO_{3-\delta}$ Infiltrated Mesoporous $Ce_{0.8}Sm_{0.2}O_{1.9}$ Cathodes.....144

5.3.1. Optimization of attachment temperature and electrochemical characterization of symmetrical cells.....144

5.3.2. Equivalent circuit for MIEC electrodes.....147

5.3.3. Long-term stability.....149

5.4. Conclusions 158

References 159

5. Infiltrated Mesoporous Composites as a Cathode for IT-SOFCs

5.1. Cathode Requirements and Advantages of Infiltrated Microstructures

The oxygen reduction reaction (ORR) in the cathode of a SOFC can be globally expressed as,

$$O_2 + 4e^- \rightarrow 2O^{2-} \quad \textbf{(5.1)}$$

Cathode materials for SOFCs must meet a series of requirements, namely, high electronic conductivity, thermomechanical and chemical compatibility matching the electrolyte and the interconnect materials, open and interconnected porosity to allow oxygen gas to diffuse to the cathode-electrolyte interface, stability under oxidizing conditions and high catalytic activity towards the ORR [1].

In the case of cathodes with pure electronic conductivity, the oxygen reduction process takes place at the interface between the electrode and the electrolyte and can be simply described by the following steps depicted in **Figure 5.1** and **Figure 5.2a** [2,3]:

1. Gas diffusion of oxygen through the electrode pores.
2. Oxygen adsorption, dissociation and ionization in the triple phase boundary (TPB).
3. Oxide ions diffusion through the electrolyte.

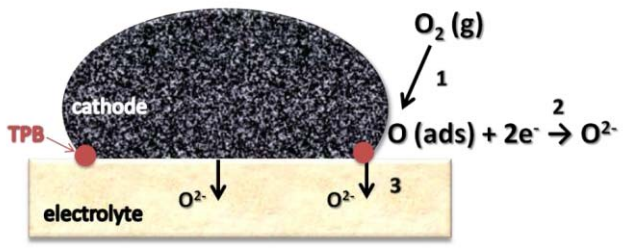

Figure 5.1. Different steps of the reduction reaction of oxygen for a pure electronic cathode.

$La_{1-x}Sr_xMnO_3$ perovskite (LSM) is the state-of-art choice for pure electronic cathode material in SOFCs working between 800 – 1000 ºC, due to its high thermal and chemical stability in this temperature range. However, when lowering the operating temperature the catalytic performance of LSM rapidly decreases [4].

One strategy to improve the electrochemical performance of a cathode is to fabricate a composite formed by a mechanical mixture of an electronic conductor and an ionic conductor material. By using this approach, the triple phase boundary (TPB) or the electrochemically active region greatly increases (see **Figure 5.2b**) due to the increase of active sites (encounter of electrons, oxide ions and gas). Another strategy, involves the use of mixed ionic-electronic conductors (MIEC) like cobaltite, ferrite or ferro-cobaltite perovskites [5–8]. The higher ionic conductivity and catalytic activity of these materials extends the TPB to the entire cathode surface and part of the bulk (**Figure 5.2c**).

In particular, mixed ionic-electronic conductors formed by Sr-doped $LaCoO_3$ (LSC) compositions have been widely studied, due to its high ionic conductivity and enough electronic conductivity. However, LSC reacts at fabrication temperatures with the typical YSZ electrolyte forming the insulating secondary phase $La_2Zr_2O_7$, therefore increasing the polarization resistance [9]. Moreover, the presence of strontium (Sr) can produce other secondary phases, like $SrZrO_3$ [10]. Trying to improve the stability of the cobaltites under reducing conditions, lanthanum (La) was substitute for other elements like gadolinium (Gd) or samarium (Sm) [11]. Systems like $Sm_{1-x}Sr_xCoO_{3-\delta}$ have shown lower reactivity with YSZ to the formation of $SrZrO_3$ [12].

The rate determining step for the $Sm_{0.5}Sr_{0.5}CoO_{3-\delta}$ (SSC) and LSC cathodes is the adsorption-desorption at the surface of the electrodes, although the rate constants of the SSC were shown to be one order of magnitude higher [13]. Adding ceria to SSC was observed to enhance the electrochemical performance, as the ceria helped to avoid the agglomeration of the SSC and the TEC of the electrode became closer to the one of the electrolyte [13,14].

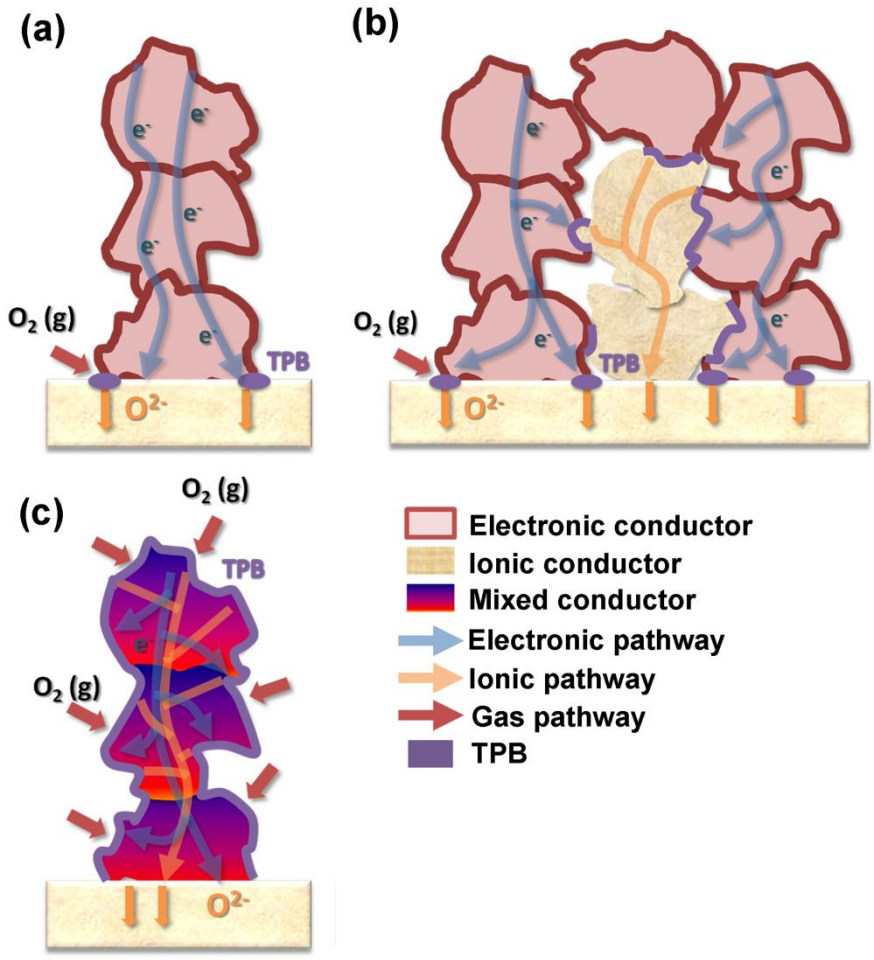

Figure 5.2. Scheme of the triple phase boundary (TPB) in: (a) a pure electronic conductor (b) a composite mixing an ionic and an electronic conductor (c) a mixed conductor; as cathode materials for SOFC.

Higher activation energies are associated for cathodes compared to the other SOFC components, leading to the highest resistance contribution in the total fuel cell performance [1,15,16], especially when lowering the operating temperature to the intermediate range (IT = 600-800 ºC). Infiltration methods have been recently proposed to develop SOFC cathodes, their advantages over more conventional methods are listed as below [17–21]:

i) The thermal expansion (TEC) mismatch between the electrode and the electrolyte decreases if the scaffold is formed by a ceramic oxide ion conductor, minimizing delamination of the cathodes upon thermal cycles.

ii) A little amount of catalyst is needed to infiltrate as the ionic scaffold formed in a previous sintering step is already percolating.

iii) The ionic scaffold and the electro-catalyst layers are formed sequentially, allowing multilayer catalyst systems.

iv) The sintering of the scaffold at higher temperatures will give more mechanical strength and thermal stability, while the particle size of the infiltrated catalyst can be controlled and optimized apart.

However, retaining the high surface area of the ionic scaffold at the higher temperatures requires the difficult task to fabricate stable ionic conductor backbones (T > 1100 ºC). A highly porous and connected network is desirable, in order to form a percolating electronic/catalytic structure that increases the number of catalytic active sites and improves the overall performance of the cells.

A gradual loss of the high surface area and thus, of the catalytic activity over time (due to unstable morphology and agglomeration of the nanoparticles) is the primary issue of nanostructured electrodes [18,22–25].

In the **Chapter 3** of this thesis, a counterintuitive and cost effective strategy for stabilizing open ordered mesoporous metal oxides themselves was presented (below T ~ 1100 ºC), by forcing a self-limited grain growth regime by the partial crystallization of the metal oxide inside the template [26]. This structure presents excellent properties for being used as a backbone for infiltration.

Many efforts have been dedicated to investigate the wetting properties of the catalyst materials by different infiltration techniques. **Figure 5.3** shows the typical solution infiltration process into a fired backbone. Either discrete nanoparticles or thin film coating are the typical morphologies observed after the calcination of the infiltrated material [17].

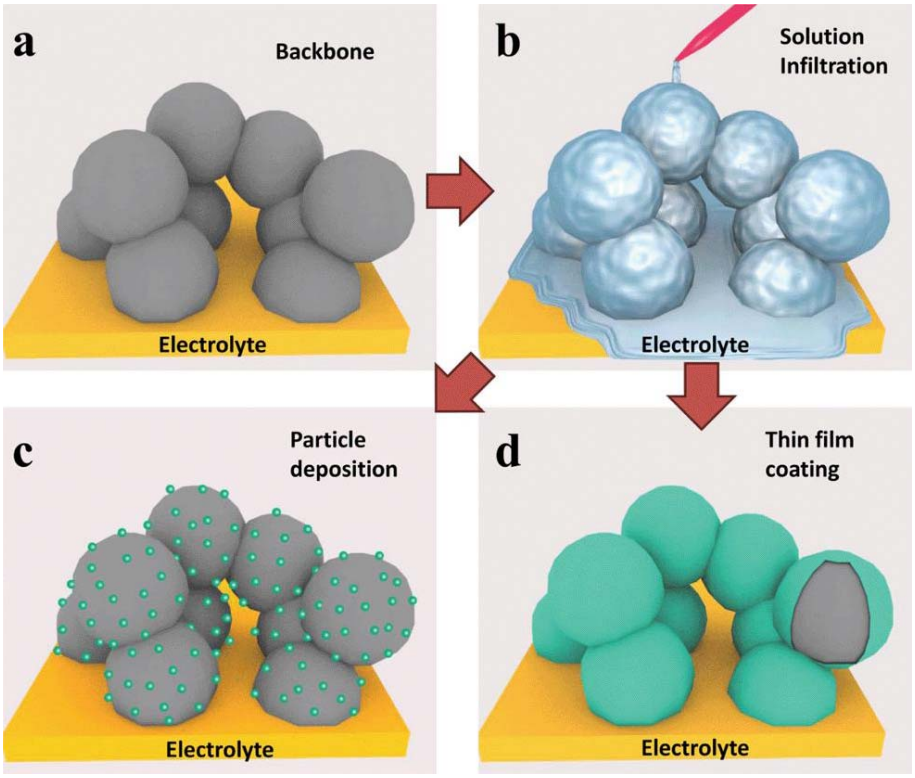

Figure 5.3. Typical procedure for infiltration (a) as-sintered electrode scaffold, (b) solution infiltration into the pores of the scaffold. Typical morphologies of the infiltrated electrode after calcination (c) discrete nanoparticles, (d) thin film coating (*taken from ref* [17]).

However, few works have been published studying the long-term stability and the degradation mechanisms of these infiltrated cathodes, being equally important for determining their feasibility for use as electrodes in real devices [27–32]. It is clear that a well-defined ceramic scaffold is the first goal to avoid the agglomeration of the infiltrated particles [33].

In this chapter, thermally stable mesoporous samarium-doped ceria (SDC) ceramic oxide is fabricated and characterized as ionic conductor scaffold for cathodes in IT-SOFCs [34,35]. The attachment temperature is optimized, keeping the self-limited grain growth regime and therefore, maintaining the high surface area and the functionality during continuous operation conditions **(section 5.2.1)**. The perovskite-type $Sm_{0.5}Sr_{0.5}CoO_{3-\delta}$ (SSC) is chosen as a catalyst for infiltration **(section 5.2.2)** [30,36,37]. An electrochemical characterization based on EIS on symmetrical cells has been carried

out **(section 5.3.1)**. The impedance spectra are further analyzed, in order to understand the mechanisms and changes taking place and an equivalent circuit based on transmission lines is proposed to fit the impedance spectra [38]. Moreover, the analogy between the proposed circuit and the Adler-Lane-Steele (ALS) model [39] developed for mixed ionic electronic conductors (MIEC) is complete and therefore, the obtained parameters fitted by the equivalent circuit permit understanding the physical phenomena involved and their evolution with time **(section 5.3.2)**. The model proposed and applied forms part of the work presented in A. Tarancón's PhD thesis, here presented in **Appendix C** [40]. The optimized symmetrical cell was further subjected to a long-term stability test for 230 hours **(section 5.3.3)**.

5.2. Structural Characterization of $Sm_{0.5}Sr_{0.5}CoO_{3-\delta}$ Infiltrated Mesoporous Scaffolds of $Ce_{0.8}Sm_{0.2}O_{1.9}$

5.2.1. Mesoporous samarium-doped ceria (SDC) powder

Samarium-doped ceria ($Ce_{0.8}Sm_{0.2}O_{1.9}$) mesoporous powder was synthesized as a replica of the as-prepared hard template of silica KIT-6-36, by a single impregnation approach and calcined at 600 ºC for 5 h (see details of the experimental procedure in **Chapter 2.2.2, Table 2.2**). The as-calcined SDC will be denoted as **SDC-600-36** in the next.

Figure 5.4a shows the nitrogen adsorption-desorption isotherms of the SDC-600-36. They can be classified as type IV, the typical type of mesoporous materials which show pore condensation and a H1 hysteresis loop characteristic of channel pores with narrow size. Typical values of a BET area of 121 m^2/g and pore volume of 0.290 cm^3/g were obtained from the measurement [41].

The mean pore size obtained using the BJH model at the desorption branch of the isotherm was 11.3 ± 4 nm (**Figure 5.4b**). In agreement with Doi *et al.* [42], the use of different hydrothermal temperature during the synthesis of the KIT-6 silica template allows to selectively depositing into both pores or one single pore of the *Ia3d* bi-

continuous structure, leading to small pores of ~ 4 nm (shown in **Chapter 3.2**, CGO-600 synthesized from KIT-6 hydrothermal treated at 90 ºC) or larger pores over 10 nm (the here-characterized, named SDC-600-36 synthesized from KIT-6 hydrothermal treated at 36 ºC).

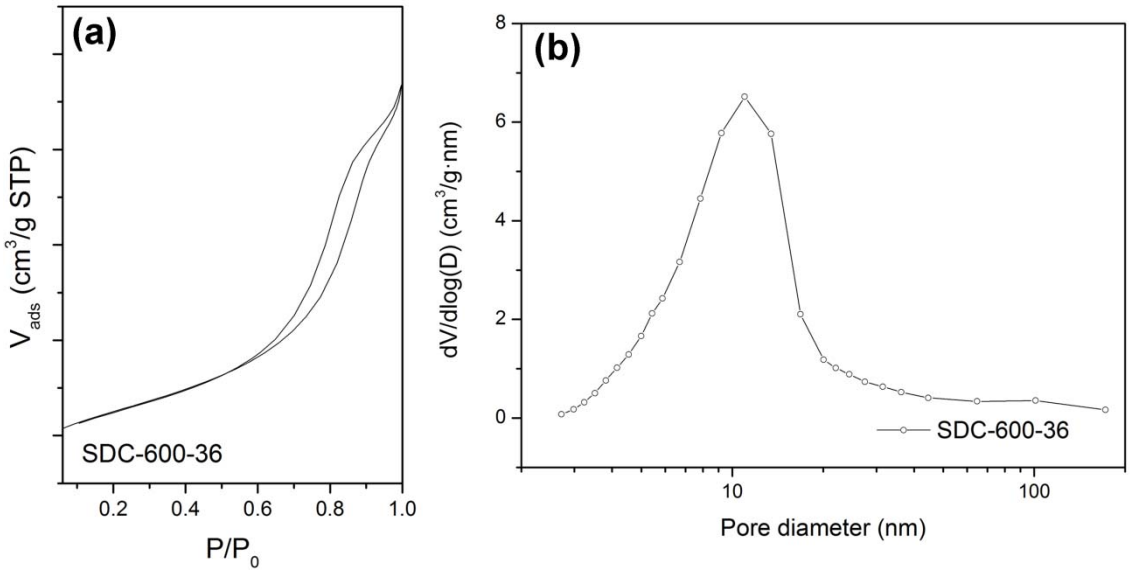

Figure 5.4. a) N_2 adsorption–desorption isotherms and b) Pore size distribution from the desorption branch using the BJH method of SDC-600-36 calcined at 600 ºC (replica of the KIT-6-36).

Figure 5.5 shows a SEM image of mesoporous SDC-600-36 particles as synthesized at 600 ºC. The inset shows the TEM image of a typical single particle. The image presents a particle oriented in the [111] direction in order to easily measure the pore size. The pore sizes observed in both images corroborates the results obtained in the N_2 physisorption measurements. The pore pattern observed in the figures correspond to filling one of the two interpenetrated channels in the original KIT-6 template structure, as expected from the low hydrothermal temperature (36 ºC) used during the template synthesis. It is demonstrated that the control of the synthesis parameters allows obtaining mesoporous oxides replicas with larger pore sizes, which further facilitates a uniform infiltration of the catalyst.

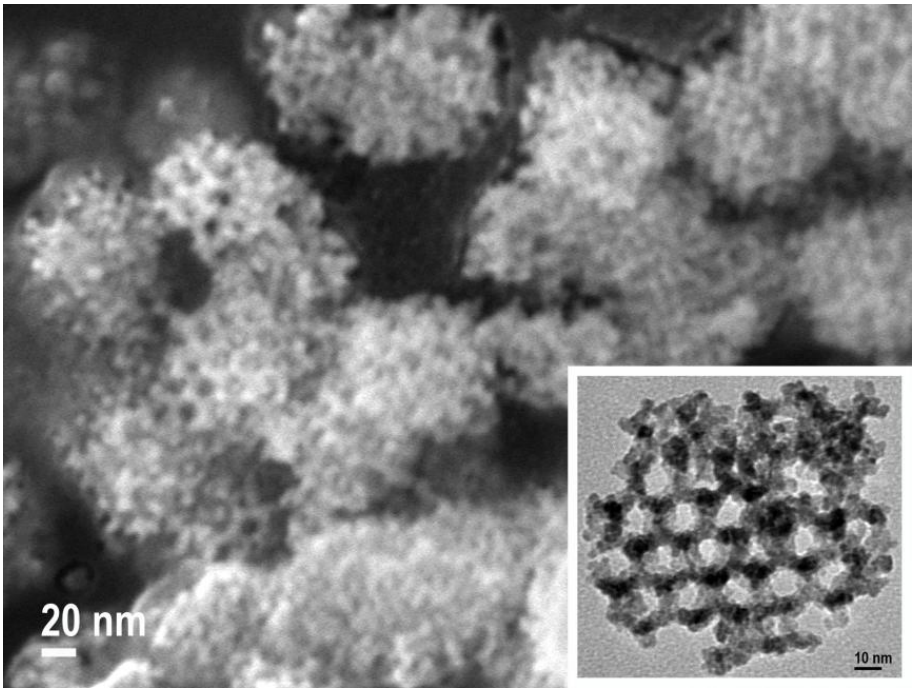

Figure 5.5. SEM image of the mesoporous SDC-600-36 powder as synthesized at 600 ºC. The inset shows a TEM image of a single SDC-600- 36 particle oriented in the [111] direction.

5.2.2. Mesoporous SDC ceramic scaffold infiltrated with SSC

In the **Chapter 3**, a route for keeping the meso-structure and functionality under operational conditions up to temperatures below 1100 ºC was studied for mesoporous ceria-based compounds [26]. This novel property is further demonstrated in this work, where the mesoporous SDC-600-36 is used to fabricate ceramic scaffolds as IT-SOFC cathodes. According to the results of Chapter 3 an attachment temperature of the SDC-600-36 ceramic scaffold to the electrolyte below 1100 ºC is expected to keep the meso-structure.

SSC-infiltrated mesoporous SDC symmetrical cells were fabricated as schematically depicted in **Figure 5.6** (details of the experimental procedure in **Chapter 2.3.2.1**). Briefly, ethanol inks of the mesoporous SDC-600-36 were deposited onto ceria based pellets and attached at different temperatures (T_{att} = 1000, 1050 and 1100 ºC). The catalyst ($Sm_{0.5}Sr_{0.5}CoO_{3-\delta}$) was infiltrated into the fabricated mesoporous

ceramic backbone with a solution formed by the stoichiometric precursors and calcined after three impregnation cycles at 800 ºC.

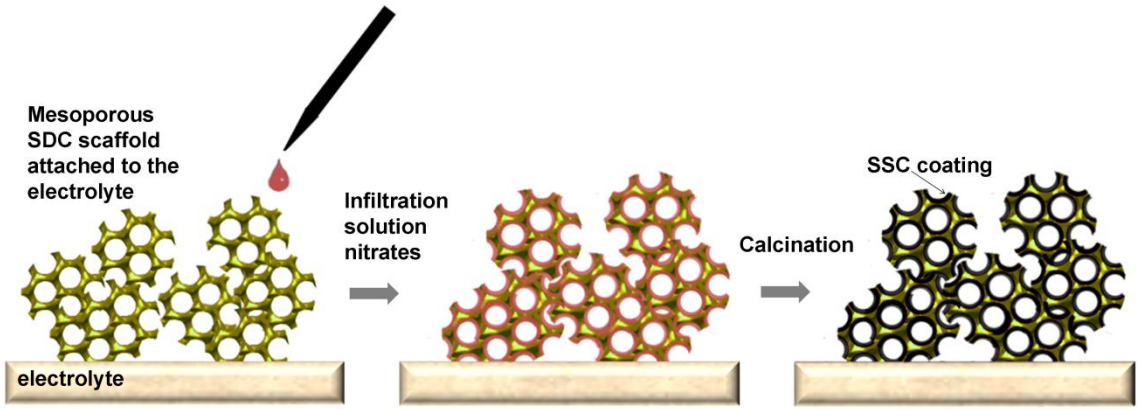

Figure 5.6. Schematic diagram of the procedure followed to fabricate a mesoporous SDC ceramic scaffold infiltrated with SSC.

Figure 5.7 shows the XRD pattern of the infiltrated-SSC on mesoporous SDC electrodes of one symmetrical cell. The mesoporous SDC ceramic scaffold shows the corresponding cubic structure with s.g. *Fm3m* and cell parameter 5.4330 Å (JCPDS database 75-0158). The formation of the perovskite phase of the $Sm_{0.5}Sr_{0.5}CoO_{3-\delta}$ (SSC) with space group *Pnma* and orthorhombic lattice a = 5.4048 Å, b = 7.5791 Å, c = 5.3604 a/b = 0.7131 and c/b = 0.7073 (JCPDS database 53-0112) after calcination at 800 ºC is in agreement with a previous study, where addition of glycine as complexing agent (**section 2.3.2.1.2**) leads to the perovskite phase [30]. The non-indexed peak at 36.92º could be related to the presence of a certain amount of the hexagonal perovskite phase of the SSC which was not detect to affect the electronic or the oxygen ion-conductivity [30,31].

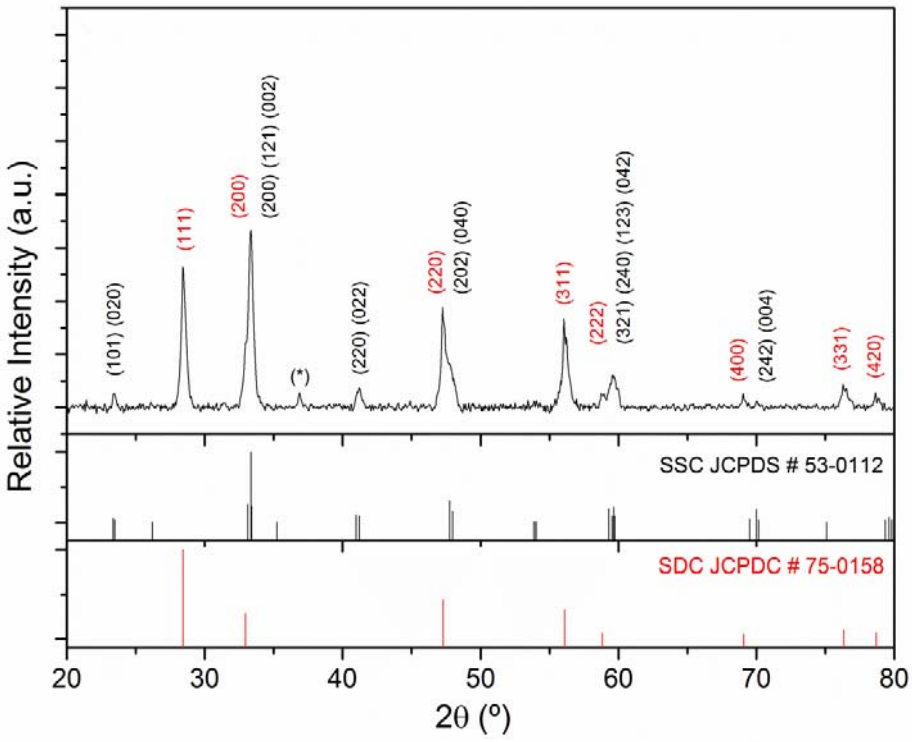

Figure 5.7. XRD pattern of SSC-infiltrated mesoporous SDC (T_{att} = 1000 ºC) after calcination at 800 ºC.

Figure 5.8 (a,c) shows SEM images of the fabricated mesoporous SDC scaffolds after attachment to the electrolyte at T_{att} = 1000 ºC. As expected from results of **Chapter 3**, the SDC scaffolds kept the mesoporosity after a heat treatment at temperatures of 1000 ºC [26]. In **Figure 5.8 (b,d)** typical SEM images of the SDC mesoporous scaffolds (T_{att} = 1000 ºC) infiltrated with SSC after calcination at 800 ºC are shown. Melted nanoparticles of SSC uniformly covering the SDC scaffold can be observed and the porosity of the thin coating layer seems to be high, which is attributed to the wetting agent capability of the PVP, added to the precursor solution (**section 2.3.2.1.2**). The highly interconnected network together with the high surface area, yield to the desired properties for high performance and stable electrodes for SOFCs.

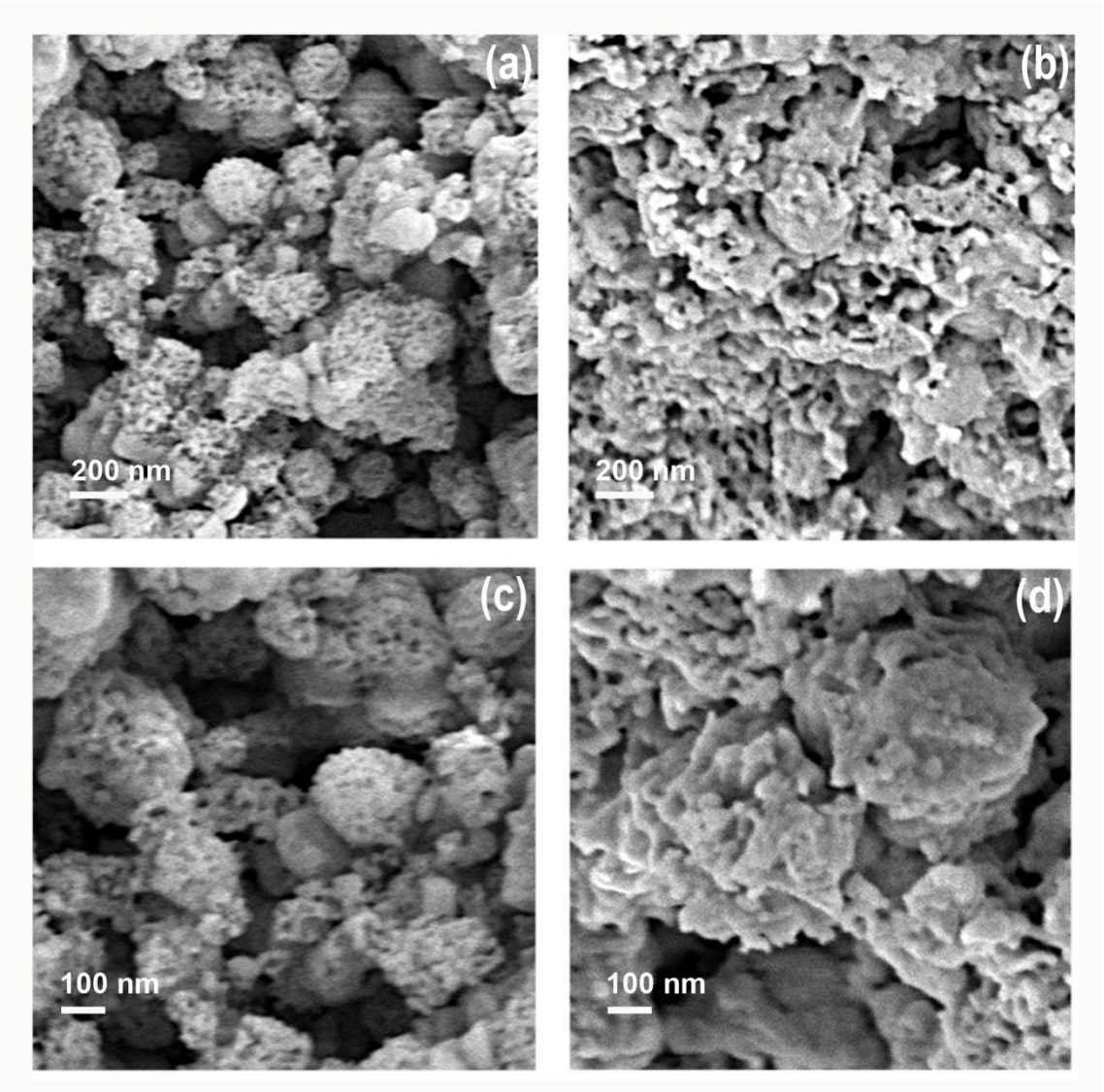

Figure 5.8. SEM micrographs of (a,c) mesoporous SDC scaffold after attachment to the electrolyte at 1000 ºC, (b,d) SSC-infiltrated SDC mesoporous electrodes (T_{att} = 1000 ºC) after calcination at 800 ºC.

5.3. Electrochemical Performance and Stability of $Sm_{0.5}Sr_{0.5}CoO_{3-\delta}$ Infiltrated Mesoporous $Ce_{0.8}Sm_{0.2}O_{1.9}$ Cathodes

5.3.1. Optimization of attachment temperature and electrochemical characterization of symmetrical cells

The symmetrical cells formed with SSC-infiltrated mesoporous SDC cathodes were electrically characterized by impedance spectroscopy using the setup described in **Chapter 2.5.3**, under ambient air in a temperature range between 500 - 750 ºC. A layer of $Sm_{0.5}Sr_{0.5}CoO_{3-\delta}$ (SSC) commercial powder (*Kceracell*) was airbrushed onto the infiltrated electrodes and sintered at 800 ºC for 2 h, as current collector.

The morphology of the SSC-infiltrated mesoporous SDC electrodes was studied by SEM. **Figure 5.9** shows a set of images of the electrolyte/electrode interface of the symmetrical cells SSC-SDC/SDC/SDC-SSC, with the SDC scaffold attached at different temperatures (T_{att} = 1000, 1050 and 1100 ºC). A similar morphology of the cathodes with uniform and well-formed interface is observed for all the cells. In order to determine the best attachment, electrochemical measurements are required.

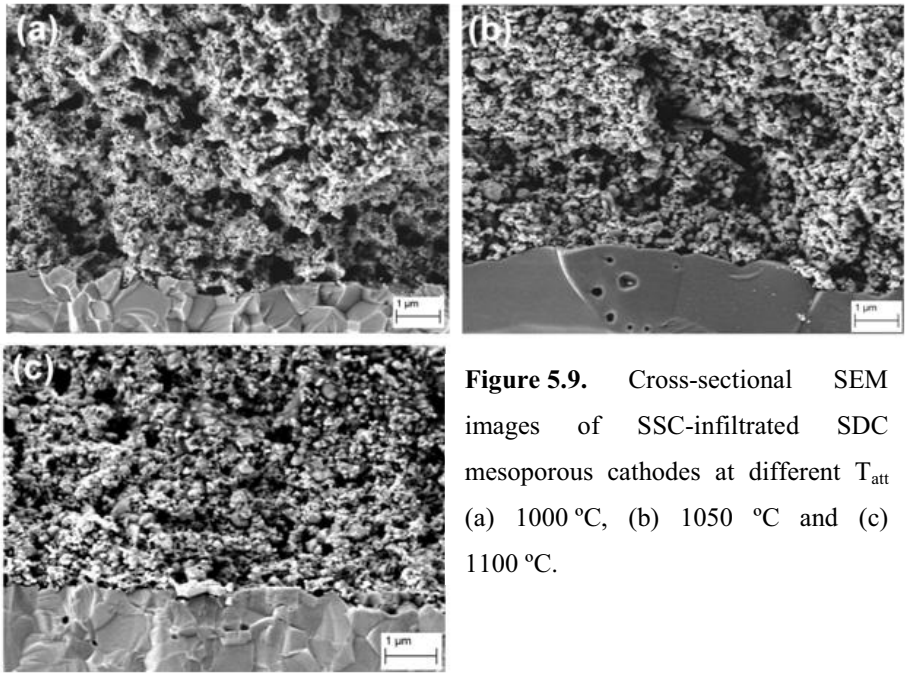

Figure 5.9. Cross-sectional SEM images of SSC-infiltrated SDC mesoporous cathodes at different T_{att} (a) 1000 ºC, (b) 1050 ºC and (c) 1100 ºC.

Figure 5.10a shows the Nyquist plot of the symmetrical cells at 700 ºC, fabricated by infiltrated-SSC on SDC mesoporous scaffolds attached at 1000, 1050 and 1100 ºC. An equivalent circuit formed by a series of an inductance (L), a resistance (R_s), a transmission line analogous to the Adler-Lane-Steele model (explained in detail in **next section** and in **Appendix C**) and a ZARC element representing the gas diffusion $(RC)_{dif}$, was used to fit all the impedance spectra. The solid lines observed in the figure are the result of the fitting.

Figure 5.10b shows the area specific resistance (ASR) of the cathode-electrolyte interface of the same symmetrical cells between 500 - 750 ºC. The ASR is calculated as the sum of the chemical resistance (R_{chem}) defined in the **equation C.9** of **Appendix C** and the R_{dif}. All the cells follow an Arrhenius-type law, with activation energies (E_a) of 1.3(1), 1.4(1) and 1.2(1) eV for the cells attached at 1000, 1050 and 1100 ºC, respectively. The best performance was observed for the cells fabricated with SDC mesoporous scaffolds attached at 1000 and 1050 ºC. This electrode-electrolyte interface should not contribute more than 0.25 $\Omega \cdot cm^2$ to the total cell resistance in order to obtain a typical target value of power density for SOFC applications [43]. This ASR value was attained in this work for a temperature of *ca.* 660 ºC for the cells attached at 1000 and 1050 ºC, demonstrating the suitability of the fabricated electrodes for IT-SOFC applications.

The observed electrochemical behavior is in agreement with the novel property of the mesoporous materials to keep their mesoporous structure to temperatures below 1100 ºC (**Chapter 3**) when the materials loss their mesoporosity and their microstructure collapses. In contrast to the usual strategy of sintering ceramic scaffolds at very high temperatures (T_{att} > 1100 ºC), this property of the mesoporous materials allows fabricating thermal stable and high-surface-area electrodes at a lower attachment temperature, while obtaining the required electrochemical performance in the IT range.

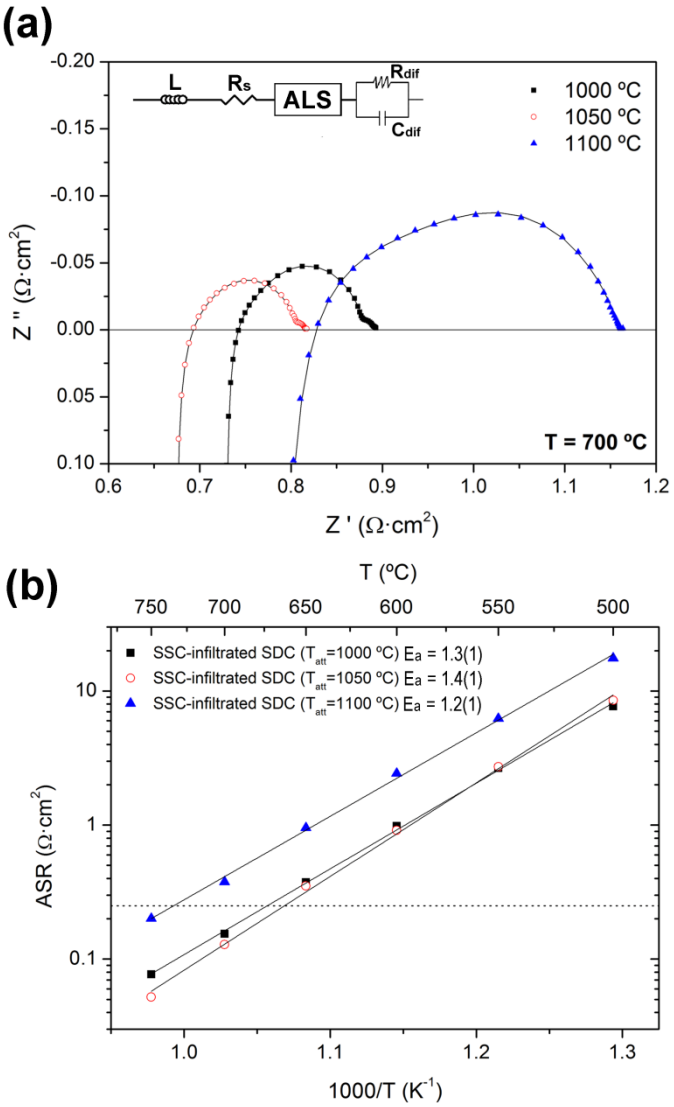

Figure 5.10. a) Nyquist plot obtained from EIS measurements of SSC-SDC//SDC//SDC-SSC symmetrical cells, with mesoporous SDC attached at different temperatures to the electrolyte (T_{att} = 1000, 1050 and 1100 ºC) at 700 ºC under ambient air. The solid line shows the fit of the model depicted in the *inset* to the experimental data. b) Arrhenius plot of the electrode/electrolyte resistance of the same cells measured in the temperature range from 500 to 750 ºC. The dashed line shows the targeted value of ASR of 0.25 Ω·cm^2.

5.3.2. Equivalent circuit for MIEC electrodes

A sketch of the half cell Electrolyte - Mixed Ionic Electronic Conductor (MIEC) - Current Collector (≡ SDC - SSC infiltrated SDC - SSC) measured is shown in **Figure 5.11a.** The global reaction of the reduction of oxygen in the cathode, as well as the main physical phenomena involved, are represented in the figure by different numbers and described below:

1) Oxygen gas phase at the surface of the MIEC
2) Oxygen exchange at the gas - MIEC interface
3) Oxide ions pathway to the electrolyte
4) Electrons pathway from the current collector

The analogy described in the **Appendix C** between the equivalent circuit based on transmission lines and the analytical Adler-Lane-Steele (ALS) model, permit to understand the measured system (Electrolyte – MIEC – Air) as two coupled transmission lines as shows the **Figure 5.11b** [38,40]. On one hand, we can consider one transmission line for the ionic pathway of the oxide ions produced after reduction of the oxygen gas in the MIEC, presenting a resistance (R_1). On the other hand, the other transmission line can be considered the electronic pathway for the electrons from the current collector to the MIEC, presenting a resistance (R_e). The resistance of the electronic pathway (R_e) is considered negligible compared to the resistance of the ionic pathway (R_1), as good electronic conductivity is considered for MIEC materials.

The coupling elements connecting the ionic and electronic channels elements represent the oxygen exchange reaction at different points of the surface of the MIEC. In this case, these processes are defined by a parallel RQ circuit $(RQ)_3$. The use of a constant phase element (CPE (Q,n)) with capacitance (Q) and frequency dispersion (n) allows introducing in-homogeneities in the behavior, which would be very difficult to introduce in a continuum analytical model. The oxygen exchange reaction can take place along the

entire surface of the MIEC and therefore, the use of a transmission line to define the ionic pathway is required.

The complete analogy between the equivalent circuit and the analytical ALS model gives thus, a physical meaning to all the fitted parameters. The resistance of the ionic pathway (R_1) refers the vacancy diffusion of the oxygen vacancies in the MIEC (*Adler et al.* named it Z_0), while the resistance R_3 is associated to the exchange reaction of oxygen across the MIEC-gas interface (*Adler et al.* named it Z_S) [39].

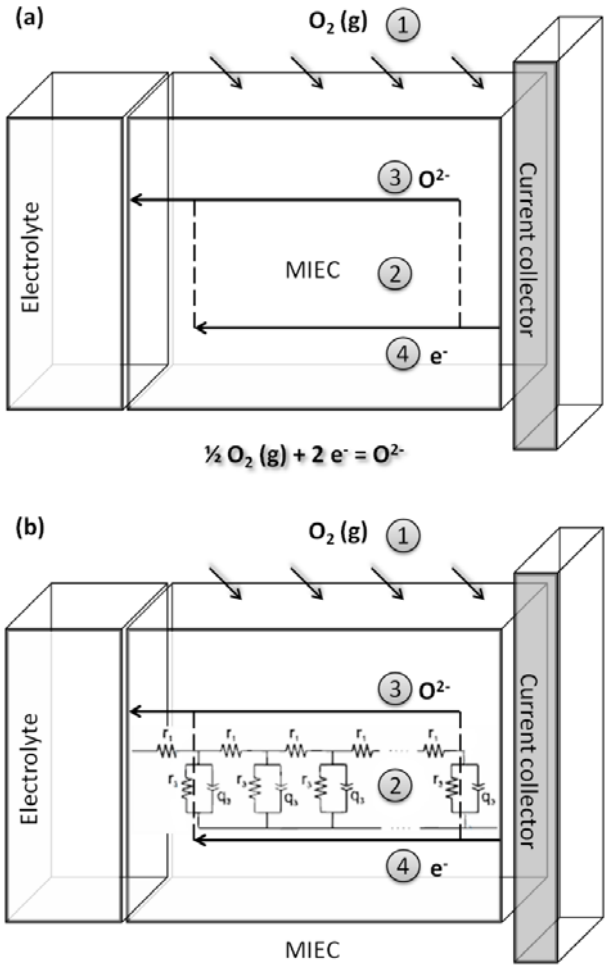

Figure 5.11. (a) Sketch of the system electrolyte – MIEC – current collector, equivalent to the half cell (SDC – SSC infiltrated SDC – SSC) measured. (b) Equivalent circuit based on transmission lines added to the sketch of the half-cell.

5.3.3. Long-term stability

To demonstrate the long-term stability of the mesoporous structures under continuous operation conditions the optimized symmetrical cell with SSC-infiltrated mesoporous SDC (T_{att} = 1000 ºC) was subjected to impedance measurements, recorded every 5 hours, at 700 ºC under ambient air for 230 hours.

Figure 5.12a shows the Nyquist plots at the beginning of the test and after 230 hours of test and corresponding fitted spectra, obtained by applying the equivalent circuit depicted in the inset figure. The proposed equivalent circuit shown in the inset is formed by and inductance (L) in series with a series resistance (R_s) (associated to electrolyte and current collection losses) and the transmission line accounting for the MIEC. Finally, a ZARC element is used for representing the gas diffusion $(RC)_{dif}$.

The equivalent circuit proposed perfectly fits all the data, i.e. perfectly matches the evolution of the impedance spectra with time for the whole experiment, as shown the solid lines of **Figure 5.12a**.

For clarity reasons, **Figure 5.12b** shows the fitted impedance spectra at the beginning of the test and after 230 hours when the calculated series R_s and L contributions are subtracted from the spectra (the resulting equivalent circuit is shown as inset figure for clarification). The half-tear-drop shape characteristic of mixed conducting (MIEC) behavior is clearly observed after subtraction.

The transmission line used is analogous to the ALS model as explained in the previous section, allowing obtaining expressions to associate the electrical elements of our circuit with physical parameters. **Table 5.1** shows the evolution of the different parameters obtained in the fitting (notice that C_3 corresponds to the true capacitance associated to Q_3 and calculated by $C = (Q \cdot R)^{1/n}/R$).

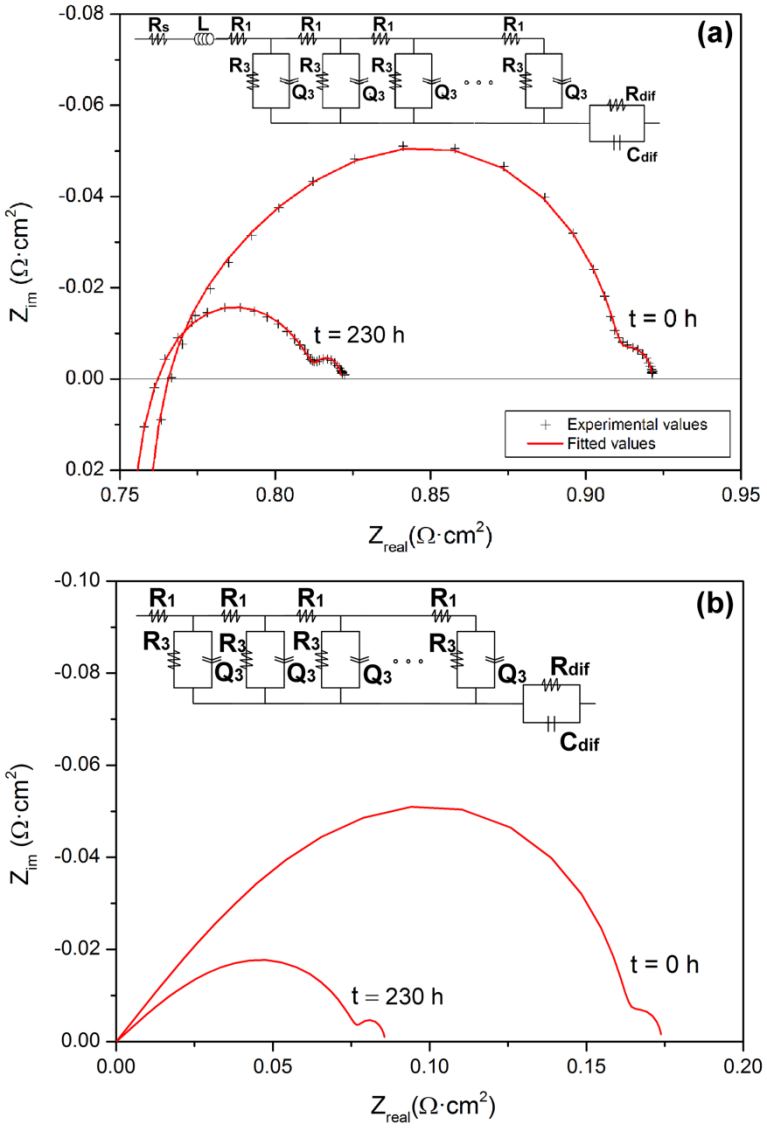

Figure 5.12. Nyquist plots for the symmetrical cell SSC-SDC/SDC/SDC-SSC (T_{att} = 1000 ºC) subjected to a long- term stability test at 700 ºC. The spectra shown were recorded at the beginning of the test and after 230 hours. (a) Experimental (crosses) and fitted values (solid line); (b) Fitted values obtained after subtracting R_s and L contributions are shown. The inset figures show the equivalent circuit model used to fit the corresponding EIS spectra.

Table 5.1. Parameters obtained from fitting the equivalent circuit to the experimental impedance data, for the SSC-infiltrated SDC symmetrical cell during the long-term stability test at 700 ºC.

Test time (h)	R_s (Ωcm^2)	R_1 (Ωcm^2)	R_3 (Ωcm^2)	C_3 (Fcm^{-2})	n_3	R_{dif} (Ωcm^2)	C_{dif} (Fcm^{-2})
0	1.49	1.83	0.015	0.0406	0.90	0.0097	4.58
70	1.49	0.53	0.016	0.0099	0.81	0.0082	4.39
140	1.47	0.27	0.022	0.0046	0.75	0.0083	4.14
230	1.47	0.24	0.025	0.0039	0.70	0.0079	4.49

Figure 5.13 shows the evolution of the so-called resistance 1 (R_1) and resistance 3 (R_3) versus the test time. The resistance R_1 shows a higher value than R_3 for all the spectra analyzed. According to the model, the resistance associated to the ionic pathway (R_1) decreases during the long-term stability test, while the resistance associated to the reaction of oxygen along the gas-MIEC interface (R_3) increases. R_1 is dominant and decreases during the stability test probably due to the accommodation of the microstructure of the electrode improving the oxide-ion percolation with the temperature and time, while the increase tendency of R_3 may be related to an increase difficulty for the oxygen molecules to reach the place where the oxygen exchange reaction takes place (due to formation of inhomogenities).

Two different regimes can be considered for each of the resistances: during the first ~ 125 hours, the resistance R_1 decreases with a rate of 6500 $\mu\Omega \cdot cm^2 \cdot h^{-1}$ (85.2 %) and R_3 increases with a rate of 1500 $\mu\Omega \cdot cm^2 \cdot h^{-1}$ (46.7 %). In the second regime (t > 125 h) the decrease rate of R_1 became 700 $\mu\Omega \cdot cm^2 \cdot h^{-1}$ (~ 13 %), the same increase rate of R_3.

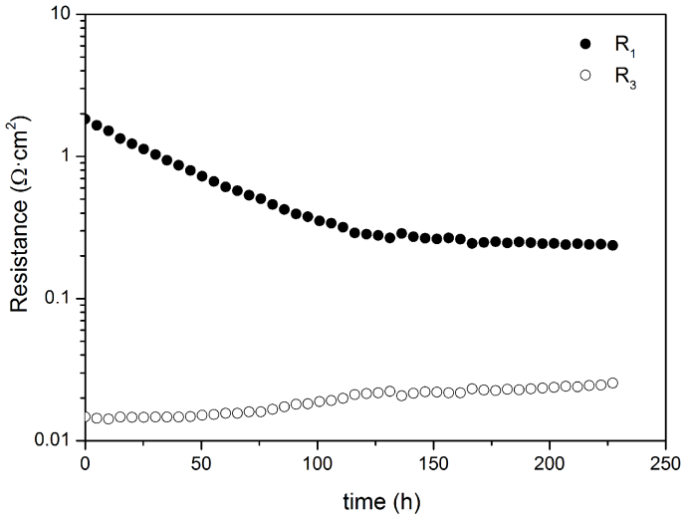

Figure 5.13. Evolution of the resistances R_1 and R_3 parameters of the model during the long-term stability test at 700 ºC.

Figure 5.15 summarizes the evolution of the ohmic resistance (R_s), the chemical resistance ($R_{chem} = (R_1 \cdot R_3)^{1/2}$) and the diffusion resistance (R_{dif}), associated to the different processes that take place in the system. The ohmic resistance (R_s) is mainly associated to the resistance of the electrolyte and it shows a constant value during the entire thermal stability test. The high value 1.5 $\Omega \cdot cm^2$ is due to the thickness of the SDC pellet (~ 0.6 mm) fabricated by dry pressing as electrolyte.

The so-called diffusion resistance (R_{dif}) is associated to a limitation in the diffusion of the oxygen gas phase, as this type of contributions appears in this low frequency range and the ALS model does not include them in the continuum model [39]. The R_{dif} shows a constant value and very low compared to the other resistance contributions during the stability test (indicating an enough open porosity under operational conditions).

Finally, the chemical resistance (R_{chem}) calculated from the analogy of the ALS model and the equivalent circuit under the particular limiting situation ($R_1 > R_3$, **expression C.8** of **Appendix C**), is associated to non-charge transfer processes (*i.e.* solid-state diffusion and surface exchange). It decreases during the first ~ 100 hours, due to the dominant contribution of R_1 over R_3 (attributed to the accommodation of the microstructure). After 100 hours, the chemical resistance shows a constant value,

explained by the same reduction rate of R_1 and increased rate of R_3. The convolution of these two parameters leads to a constant value of the resistance associated to non-charge transfer processes over the time.

Taking into account the **Chapter 3,** where a self-limited-grain growth regime is attained for mesoporous ceria up to temperatures below 1100 ºC, and the SEM images of the microstructure of the cells before and after the long term stability test (**Figures 5.14 a and b**) which confirmed that the microstructure of the SDC scaffold does not show big changes or agglomeration of the particles; the decrease of R_{chem} during the first 100 hours is thus mainly attributed to the infiltrated catalyst SSC, which tends to move penetrating inside the meso-pores of the scaffold. After 100 hours the microstructure kept stable with the temperature and time.

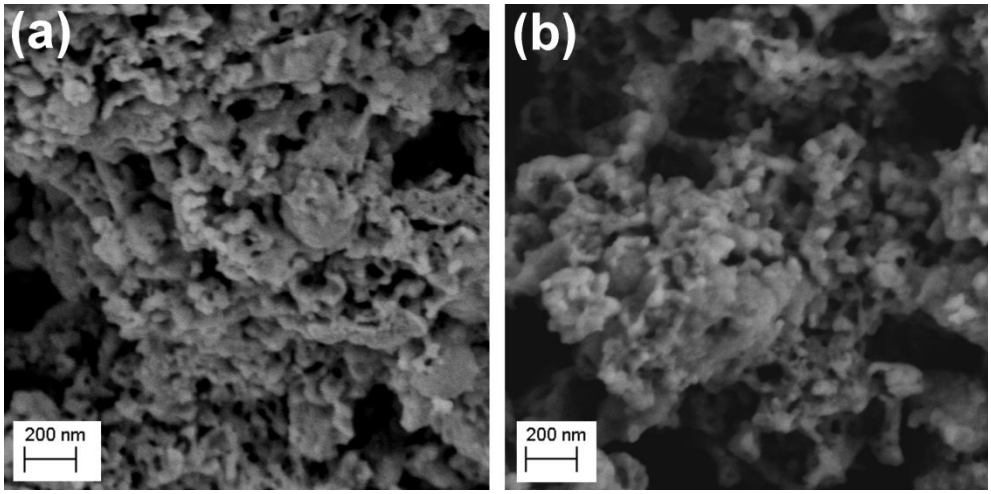

Figure 5.14. Cross-sectional SEM images of SSC-infiltrated SDC mesoporous cathodes (a) before and (b) after the stability tests at 700 ºC for ~ 230 h.

Moreover, it agrees with the observed better initial performance for the SDC scaffold attached at 1000 ºC than for the scaffolds attached at 1050 and 1100 ºC and the improvement of performance during the long-term experiment.

On the other hand, the RC_{dif} arc attributed to a limitation in the diffusion of the gas phase along the surface of the MIEC may be related with the difficulty of the oxygen molecules to reach the SSC which is covering and filling the meso-pores of the SDC

scaffold. Further modification of the microstructure of the electrodes incorporating pore formers (*i.e.* starch, graphite, PMMA) could be done in order to study these phenomena.

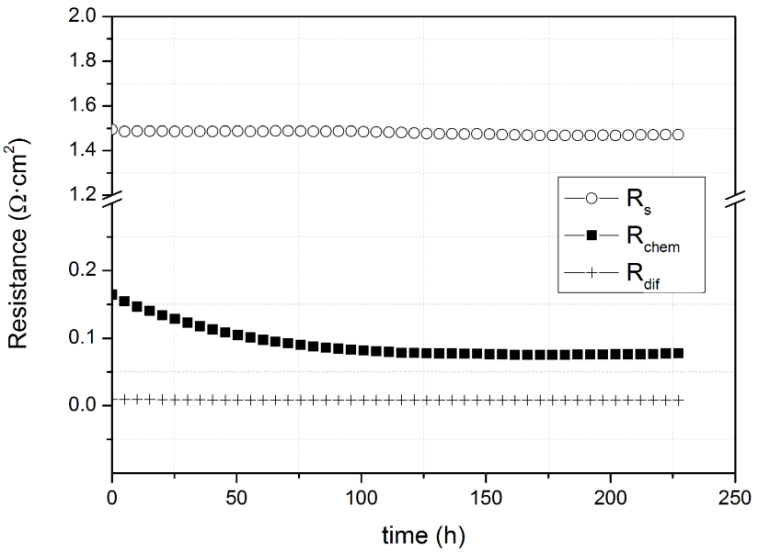

Figure 5.15. Evolution of the ohmic resistance (R_s), the chemical resistance (R_{chem}) and the so-called diffusion resistance (R_{dif}) during the long-term thermal stability test performed at 700 ºC.

Figure 5.16 shows the evolution of the true capacitance (C_3) associated to the constant phase element 3 (CPE 3: $(Q, n)_3$) associated to gas-phase diffusion polarization (*Adler et al.* named it C_{gas}) and the capacitance C_{dif} associated to the gas-phase diffusion limitation. The decrease observed for the n-parameter (n_3) (**Figure 5.16b**) which started with a value close to one i.e. perfect capacitance, may be associated with inhomogeneities of the active surface appearing during the accommodation time.

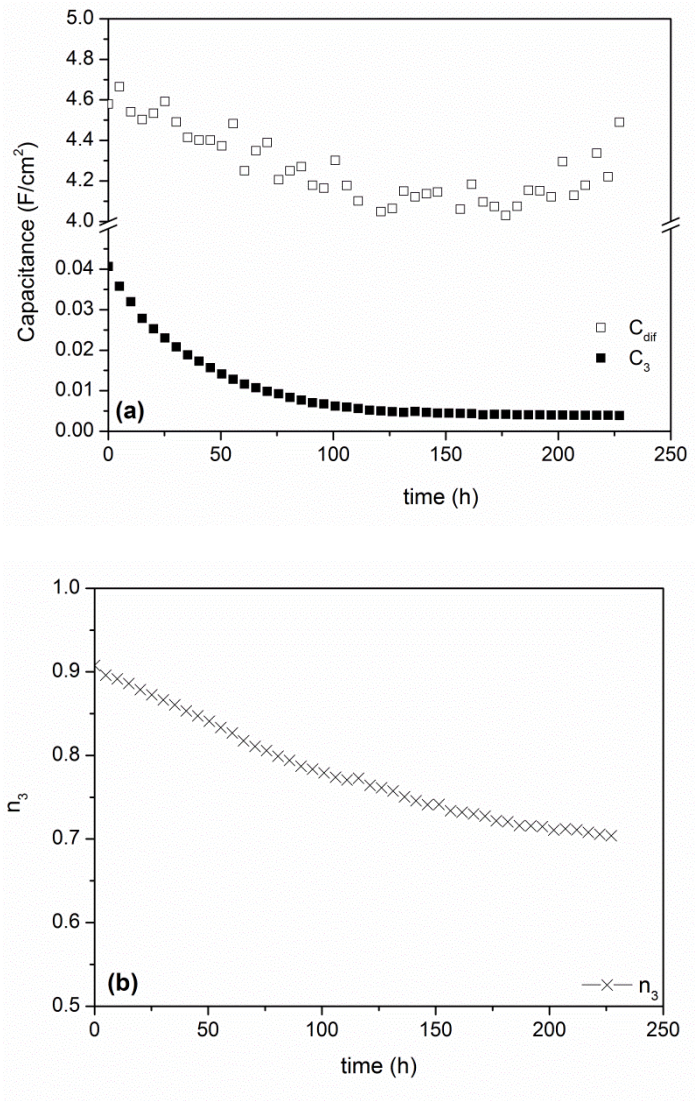

Figure 5.16. Evolution of the (a) True capacitance C_3 **(**associated to the constant phase element CPE 3) and C_{dif}; (b) Frequency dispersion n_3 (associated to CPE 3); values obtained from fitting the impedance spectra to the equivalent shown in Figure 5.12 during the long-term stability test of the optimized SSC-infiltrated SDC cell at 700 ºC.

The evolution of the chemical capacitance (C_{chem}) calculated from the analogy, by the **expression C.10, Appendix C.** is observed in the **Figure 5.17**. This chemical capacitance is associated to changes of the active area of the MIEC (electrode). The C_{chem} increases with the test time, physically meaning that more area of the MIEC electrode became active with the time. Values of C_{chem} are higher than the values of the typical

capacitances associated to charge transfer phenomena (10^{-6} F·cm^{-2}) because of the bigger active area of the MIEC. On the other hand, the high value of C_{dif} is explained by the high characteristic time (low frequencies) associated.

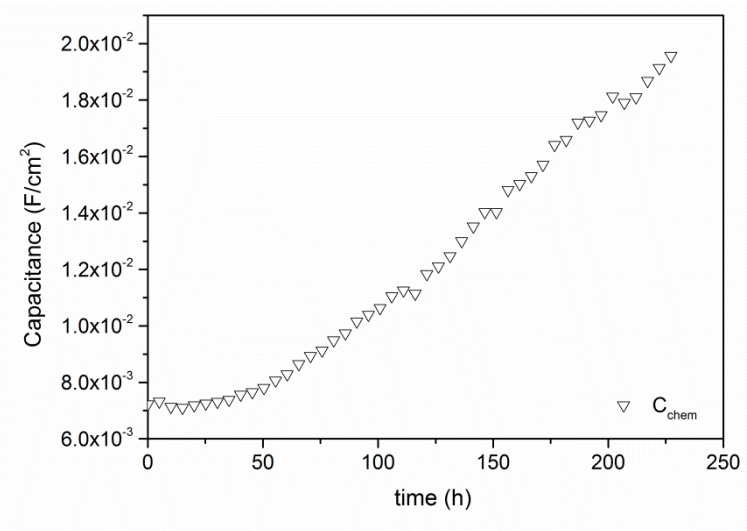

Figure 5.17. Evolution with the test time of the chemical capacitance (C_{chem}) associated to the ALS model for the optimized SSC-infiltrated SDC cell during the long-term stability test at 700 ºC.

Figure 5.18 shows the total electrode-electrolyte interface resistance (ASR = R_{chem} + R_{dif}) values with the time of the SSC-SDC/SDC/SSC-SDC optimized symmetrical cell subjected to long-term stability test.

As mentioned for the R_{chem} in **Figure 5.15**, an enhanced performance in the first stage of the degradation test was observed for all the measured cells. The here-fabricated cathodes showed a different mechanism compared to previously reported infiltrated cathodes, which usually showed degradation of the ASR with the time [27–29,44].

In particular, a stable electrolyte-electrode interface resistance of 0.08 Ω·cm^2 is obtained for the optimized SDC/SDC/SSC-SDC symmetrical cell (T_{att} = 1000 ºC) after 230 hours. The ASR value achieved compares excellently to recently reported values for infiltrated-SSC composite electrodes: *C. Lu et al.* ASR = 8.5 Ω·cm^2 @ 600 ºC [45], *H. Zhang et al.* ASR = 0.13 Ω·cm^2@ 700ºC [37] and *F. Wang et al.* ASR = 0.14 Ω·cm^2 @ 700ºC [30] and to other SSC + SDC composite electrodes prepared by co-firing of pre-

mixed powders or other conventional solution-infiltrated composite electrodes [18–20,28,46].

After the initial degradation period, the cell showed a decrease of ASR of 799 $\mu\Omega\cdot cm^2/h$ during the first 100 hours (representing 48.5 % of improvement) and a decrease of ASR of 29.5 $\mu\Omega\cdot cm^2/h$ between 100 and 230 hours (representing 4.7 % of improvement). The expected high thermal stability of this kind of mesoporous based-electrodes formed by thermally stable open 3D nano-structures, was here-demonstrated under real operational conditions.

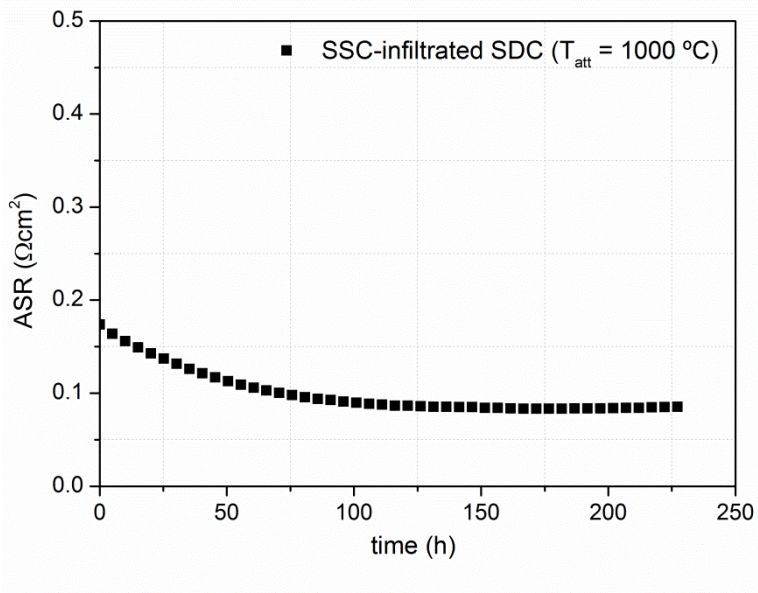

Figure 5.18. Long term stability tests of the symmetrical SSC-infiltrated mesoporous SDC cells (T_{att} = 1000 ºC) at 700 ºC under ambient air. The electrode/electrolyte resistance was calculated from the impedance spectra recorded every 5 hours. The ASR corresponds to the R_{chem} of the ALS model and the R_{dif}.

5.4. Conclusions

Mesoporous SDC was successfully synthesized and used as ionic ceramic scaffold for cathodes in IT-SOFCs. By filling one of the two interpenetrated channels of the structure of the KIT-6 silica template a pore size over ~ 10 nm and a more open structure was obtained. The bigger pore size allows infiltrating the SSC used as a catalyst, within the mesopores of the SDC backbone.

Electrochemical evaluation of the infiltrated cells working as cathodes, allowed optimizing the attachment temperature of the SDC scaffold to 1000 ºC where the mesoporous structure was demonstrated to be thermally stable (by reaching the self-limited grain growth regime). The target ASR value (0.25 $\Omega \cdot cm^2$) was obtained at 660 ºC for this symmetrical cell.

Long-term stability was confirmed for 230 hours for the optimized cell. The initial 100 hours resulted in a performance improvement of 48.5 %, yielding to a stable and excellent performance with area specific resistance of 0.08 $\Omega \cdot cm^2$ at 700 ºC under ambient air.

Moreover, the impedance spectra recorded during the stability test were analyzed by an equivalent circuit based on transmission lines formally analogous to the ALS model developed for MIEC. This allows calculating and correlating the different parameters with a complete physical meaning. From that study, it can be extracted that the accommodation of the infiltrated SSC inside the pores of the SDC and the improvement of the ionic conduction pathway probably by increasing the SDC and SSC interconnectivity, are the main contribution to the observed decrease of chemical resistance during the activation period (first 100 hours) to the stable regime.

This chapter demonstrates the possibility to implement thermal stable 3D-open nanostructures into electrochemical cells being long-term thermally stable while presenting a novel guidance to engineer high efficient and stable electrodes for IT-SOFCs.

References

[1] C. Sun, R. Hui, J. Roller, J. Solid State Electrochem. 14 (2009) 1125.

[2] M. Kleitz, F. Petitbon, Solid State Ionics 92 (1996) 65.

[3] J. Ruiz Morales, J. Canales Vázquez, D. Marrero López, J. Peña Martínez, D. Pérez Coll, P. Núñez, C. Savaniu, C. Rodríguez Placeres, V. Dorta Martín, B. Ballesteros, Pilas de Combustible de Óxido Sólido, Centro de la cultura popular canaria, (2008).

[4] S. Singhal, Solid State Ionics 135 (2000) 305.

[5] W. Wang, M. Mogensen, Solid State Ionics 176 (2005) 457.

[6] B. Steele, Solid State Ionics 86-88 (1996) 1223.

[7] S. Carter, A. Selcuk, J. Charter, J. Kajda, J. Kilner, S. B.C.H, Solid State Ionics 53-56 (1992) 597.

[8] Y. Takeda, R. Kanno, M. Noda, Y. Tomida, O. Yamamoto, J. Electrochem. Soc. 134 (1987) 2656.

[9] S. Charojrochkul, K. Choy, B. Steele, Solid State Ionics 121 (1999) 107.

[10] S.P. Simner, M.D. Anderson, M.H. Engelhard, J.W. Stevenson, Electrochem. Solid-State Lett. 9 (2006) A478.

[11] S.J. Skinner, Fuel Cells Bull. 4 (2001) 6.

[12] T. Hibino, A. Hashimoto, I. Takao, T. Jun-ichi, S. Yoshida, M. Sano, Science 288 (2000) 2031.

[13] C. Xia, W. Rauch, F. Chen, M. Liu, Solid State Ionics 149 (2002) 11.

[14] X. Zhang, M. Robertson, S. Yick, C. Deĉes-Petit, E. Styles, W. Qu, Y. Xie, R. Hui, J. Roller, O. Kesler, R. Maric, D. Ghosh, J. Power Sources 160 (2006) 1211.

[15] J. Fleig, Annu. Rev. Mater. Res. 33 (2003) 361.

[16] S.B. Adler, Chem. Rev. 104 (2004) 4791.

[17] D. Ding, X. Li, S.Y. Lai, K. Gerdes, M. Liu, Energy Environ. Sci. 7 (2014) 552.

[18] J.M. Vohs, R.J. Gorte, Adv. Mater. 21 (2009) 943.

[19] T.Z. Sholklapper, H. Kurokawa, C.P. Jacobson, S.J. Visco, L.C. De Jonghe, Nano Lett. 7 (2007) 2136.

[20] S.P. Jiang, Int. J. Hydrogen Energy 37 (2012) 449.

[21] A.J. Samson, M. Søgaard, P. Hjalmarsson, J. Hjelm, N. Bonanos, S.P. V. Foghmoes, T. Ramos, Fuel Cells 13 (2013) 511.

[22] S. Lee, N. Miller, K. Gerdes, J. Electrochem. Soc. 159 (2012) F301.

[23] M.C. Tucker, G.Y. Lau, C.P. Jacobson, L.C. De Jonghe, S.J. Visco, J. Power Sources 171 (2007) 477.

[24] T. Klemensø, K. Thydén, M. Chen, H.J. Wang, J. Power Sources 195 (2010) 7295.

[25] J.S. Kim, N.L. Wieder, A.J. Abraham, M. Cargnello, P. Fornasiero, R.J. Gorte, J.M. Vohs, J. Electrochem. Soc. 158 (2011) B596.

[26] L. Almar, T. Andreu, A. Morata, M. Torrell, L. Yedra, S. Estradé, F. Peiró, A. Tarancón, J. Mater. Chem. A 2 (2014) 3134.

[27] W. Wang, M.D. Gross, J.M. Vohs, R.J. Gorte, J. Electrochem. Soc. 154 (2007) B439.

[28] M. Shah, P.W. Voorhees, S.A. Barnett, Solid State Ionics 187 (2011) 64.

[29] Y. Liu, F. Wang, B. Chi, J. Pu, L. Jian, S.P. Jiang, J. Alloys Compd. 578 (2013) 37.

[30] F. Wang, D. Chen, Z. Shao, J. Power Sources 216 (2012) 208.

[31] D. Chen, G. Yang, F. Ciucci, M.O. Tadéc, Z. Shao, J. Mater. Chem. A (2013).

[32] Y. Gong, D. Palacio, X. Song, R.L. Patel, X. Liang, X. Zhao, J.B. Goodenough, K. Huang, Nano Lett. 13 (2013) 4340.

[33] L. Almar, B. Colldeforns, L. Yedra, S. Estradé, F. Peiró, A. Morata, T. Andreu, A. Tarancón, J. Mater. Chem. A 1 (2013) 4531.

[34] Z. Liu, D. Ding, M. Liu, X. Ding, D. Chen, X. Li, C. Xia, M. Liu, J. Power Sources 241 (2013) 454.

[35] Z. Liu, D. Ding, M. Liu, X. Li, W. Sun, C. Xia, M. Liu, J. Power Sources 229 (2013) 277.

[36] C. Xia, W. Rauch, F. Chen, M. Liu, Solid State Ionics 149 (2002) 11.

[37] H. Zhang, F. Zhao, F. Chen, C. Xia, Solid State Ionics 192 (2011) 591.

[38] J. Bisquert, Phys. Chem. Chem. Phys. 2 (2000) 4185.

[39] S.B. Adler, J.A. Lane, S.B.C. H, J. Electrochem. Soc. 143 (1996) 3554.

[40] A. Tarancón, PhD Thesis. Strategies for Lowering Solid Oxide Fuel Cells Operating Temperature, University of Barcelona, (2007).

[41] F. Kleitz, S.H. Choi, R. Ryoo, Chem. Commun. (2003) 2136.

[42] Y. Doi, A. Takai, Y. Sakamoto, O. Terasaki, Y. Yamauchi, K. Kuroda, Chem. Commun. 46 (2010) 6365.

[43] N.P. Brandon, S. Skinner, B.C.H. Steele, Annu. Rev. Mater. Res. 33 (2003) 183.

[44] S. Lee, H.S. Song, S.H. Hyun, J. Kim, J. Moon, J. Power Sources 195 (2010) 118.

[45] C. Lu, T.Z. Sholklapper, C.P. Jacobson, S.J. Visco, L.C. De Jonghe, J. Electrochem. Soc. 153 (2006) A1115.

[46] Z. Jiang, C. Xia, F. Chen, Electrochim. Acta 55 (2010) 3595.

6

Performance and stability of fully mesoporous electrodes fuel cells

6. Performance and Stability of Fully Mesoporous Electrodes Fuel Cells

6.1. Nano-structured Electrodes for IT-SOFCs. Performance and Stability Concerns.....165

6.2. Fabrication and Structural Characterization of a SOFC with Fully Mesoporous Electrodes 167

6.3. Fuel Cell Performance 170

6.4. Long-term Stability Test.....172

6.5. Post-Test Cell Characterization 177

6.6. Conclusions 181

References 183

6. Performance and Stability of Fully Mesoporous Electrodes Fuel Cells

6.1. Nano-structured Electrodes for IT-SOFCs. Performance and Stability Concerns.

The capital cost of the power supplies will determine whether a system will succeed or not in the market. Increasing the lifetime of the devices clearly implies a step further towards the commercialization; hence, in 2007 the US Department of Energy's Solid State Energy Conversion Alliance (SECA) began a focused effort to improve the stability of Solid Oxide Fuel Cells.

The objective values include efficiencies greater than 60 %, with a stack cost of 175 $/kW and a lifetime performance degradation of less than 0.2 % per 1000 hours over 40000 hours lifetime [1]. One of the primary challenges is to achieve long-term stability of the electrodes by unraveling the degradation mechanism that take place under realistic operating conditions. Diminishing the stability issues by engineering new materials and electrode structures will help to meet the cost and performance goals [2].

The use of nanostructured materials in Solid Oxide Fuel Cells has received special interest during the last years. In particular, infiltration techniques become popular due to the reported increase of performance. Different groups successfully implemented this approach decreasing the polarization resistance of the cells compared to their baseline (standard) cells. Excellent reviews have been recently published gathering the different approaches, materials and electrochemical results reported [3–5].

However, only few works have been devoted to study the long-term stability of nanostructured electrodes under realistic SOFC operating conditions. Moreover due to the lack of degradation standards procedures, the methods to measure the degradation vary from group to group. Fixing a constant voltage (potentiostatic) or a constant current (galvanostatic) are the most common degradation tests. Galvanostatic experiments seem to be more appropriate to measure the degradation as it keeps constant the thermodynamic conditions, fixing the reactants utilization and avoid introducing secondary sources of degradation (as occurs in voltage constant experiments) [6].

Up to our knowledge, few groups have performed long-term galvanostatic experiments of whole fuel cells with nanostructured anode and cathode. Lee et al. reported the performance of commercial cells with a composite cathode modified by infiltration, for 1500 hours at 750 ºC under a current density of 0.5 A/cm^2. The infiltration approach used by Lee increased the performance from their baseline cells by 20-35 %. The polarization resistance of both cells follows a parabolic power law (**Figure 6.1**), showing 65 % of the total increase in the initial 150 hours [7].

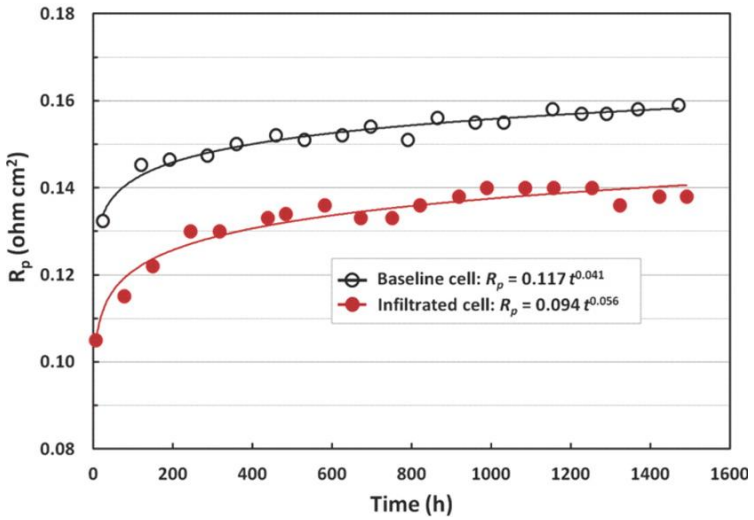

Figure 6.1. Variation of the polarization resistance under DC bias current of 0.5 A/cm^{2}of a baseline cell and an infiltrated cell for ~1500 hours. Fitting data are shown as solid lines and fitting equations are presented (*taken from ref.* [7]).

Samson et al. reported no measureable degradation for 1500 hours for anode supported cells with an infiltrated cathode at 700 ºC under a current density of 0.5 A/cm^2. Post analysis revealed no significant micro-structural changes to the nominally identical untested counterpart [8,9].

These works encourage the use of infiltrated electrodes although the evolution of the nanostructure electrodes under a constant high current density (the realistic operational conditions) requires better understanding. The microstructural evolution and the different degradation mechanisms involved have to be clearly determined in order to

tune the performance and durability. The development of new strategies to fabricate materials with stable microstructures with the time contributes to achieve this goal.

In this chapter of the thesis, a SOFC with scandia-doped ceria (10Sc1CeSZ) electrolyte and fully mesoporous electrodes has been structurally (**section 6.2**) and electrochemically characterized (**section 6.3**). A mesoporous cermet based on a nickel closed structure (Ni-$Ce_{0.8}Sm_{0.2}O_{1.9}$) methodology described in **Chapter 4,** was used as an anode, while a mesoporous ($Ce_{0.8}Sm_{0.2}O_{1.9}$) ceramic scaffold infiltrated with a MIEC catalyst ($Sm_{0.5}Sr_{0.5}CoO_{3-\delta}$), described in **Chapter 5,** was used as a cathode. Moreover, the cell was subjected to a long-term stability test under real operation conditions, namely at 750 ºC under a constant current density of 635 A/cm^2 for 1000 hours (**section 6.4**). The evolution of the different resistance (ohmic and polarization) contributions was analyzed. Finally, structural characterization of the cell after the long-term stability test illustrates the more likely degradation mechanisms (**section 6.5**).

6.2. Fabrication and Structural Characterization of a SOFC with Fully Mesoporous Electrodes

Table 6.1 summarizes the main characteristics of the different components of the fabricated SOFC with scandia-doped ceria (10Sc1CeSZ) electrolyte and fully mesoporous electrodes such as the materials, the fabrication or deposition techniques, the attachment temperature and the thickness measured by SEM. The material 10Sc1CeSZ was employed instead of the more stable YSZ to cover the IT-range. Details about the experimental procedure followed are found in **Chapter 2, Table 2.4.**

Table 6.1. Materials and relevant fabrication details used for the fabrication of IT-SOFCs with fully mesoporous electrodes.

	Material	Acronym	Fabrication Technique	T	Thickness	Chapter	Sketch
Current Collector (Anode)	Pt mesh + Ni	Ni	Painting	T_{curing} 750 ºC (in-situ)	~ 5 µm	commercial	
Anode	Ni-$Ce_{0.8}Sm_{0.2}O_{1.9}$	Ni-SDC	Multistep nanocasting Air-spraying	$T_{attachment}$ 1200 ºC	~ 35 µm	**2, 4**	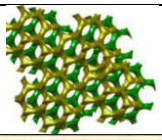
Electrolyte	$(ZrO_2)_{0.89}(Sc_2O_3)_{0.1}(CeO_2)_{0.01}$	10Sc1CeSZ	Tape Casting	--	150 µm	commercial	
Barrier Layer	$Ce_{0.8}Gd_{0.2}O_{1.9}$	CGO	PLD	$T_{deposition}$ 100 ºC	1.2-1.9 µm	**2**	
Cathode	$Ce_{0.8}Sm_{0.2}O_{1.9}$ - $Sm_{0.5}Sr_{0.5}CoO_{3-\delta}$	SSC-SDC	Nanocasting SDC + SSC Infiltration Air-spraying	1000 ºC ($T_{attachment}$ SDC) 800 ºC ($T_{sintering}$ SSC)	~ 10 µm	**2, 3, 5**	
Current Collector (Cathode)	$Sm_{0.5}Sr_{0.5}CoO_{3-\delta}$ + Pt mesh	SSC	Air-spraying	T_{curing} 800 ºC	~ 20 µm	commercial	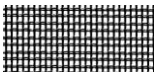

Figure 6.2 shows SEM cross-sectional images of the electrolyte-anode interface, formed with mesoporous Ni-SDC powder as an anode and 10Sc1CeSZ as an electrolyte as deposited after the attachment at 1200 ºC, before the electrochemical experiment. The continuous layer shows a thickness of ~ 35 µm and a fine and homogenous morphology (in agreement with the morphology observed in **Chapter 4 (section 4.3.1),** fabricated with the same kind of mesoporous powder). The CGO rough layer deposited by airspraying and attached in a single step together with the anode, to enhance the continuity of the interface is observed in **Figure 6.2b**.

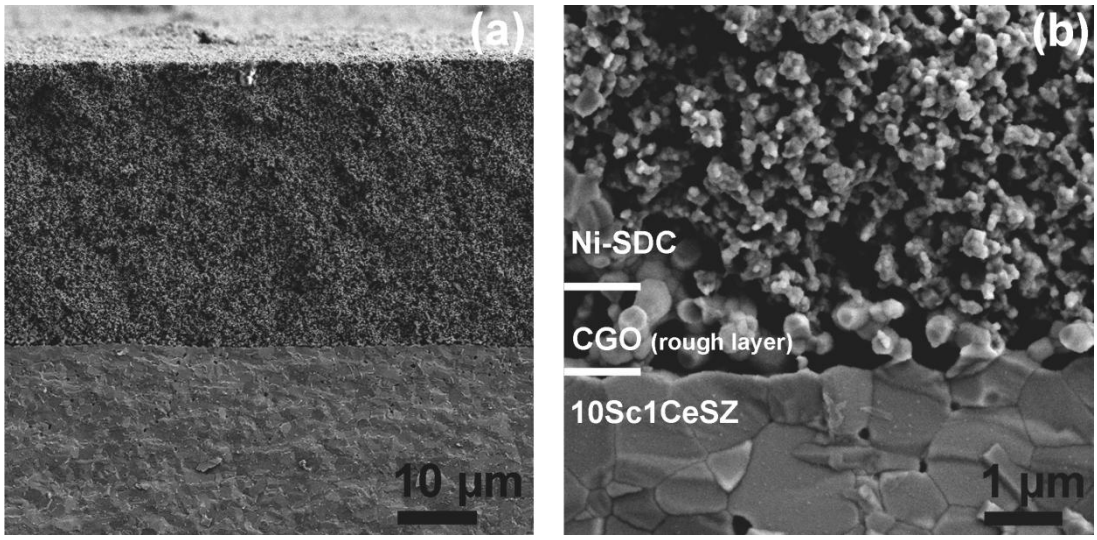

Figure 6.2. SEM cross-sectional images of the anode-electrolyte interface formed by mesoporous Ni-SDC cermet as anode and 10Sc1CeSZ tape casting as electrolyte.

In the intermediate range of temperatures usually Sr-doped lanthanide cobalt oxides (LSC) are commonly used as cathode material, although this material placed together with the conventional YSZ electrolyte lowers the performance and stability of the SOFCs, due to the Sr migration from the cathode to the electrolyte and the formation of secondary insulating phases ($La_2Zr_2O_7$). Therefore, a common approach to avoid the formation of the zirconates is the deposition of dense CGO barrier layers [10–12]. The reported solid solutions between the CGO and the YSZ which starts to be formed from 1200 ºC [13], can be diminished by using PLD. A low temperature of 100 ºC is used during the deposition and the formed layer by impacted ionized particles, subsequently permits the attachment of the CGO grown layer onto the tape casting, in the same step with the anode sintering at a temperature of 1200 ºC for 3 h (more details about fabrication conditions and the PLD technique are explained in **Chapter 2, section 2.3.1.1**).

Figure 6.3 shows the cross-sectional image of the electrolyte-cathode part. The CGO diffusion barrier layer deposited by PLD is fully dense after the sintering step at 1200 ºC, with an average thickness of 1.5 µm along the electrolyte-cathode interface. The SSC-infiltrated into mesoporous SDC showed the expected uniform and nanostructured microstructure as described the previous **Chapter 5, section 5.2.**

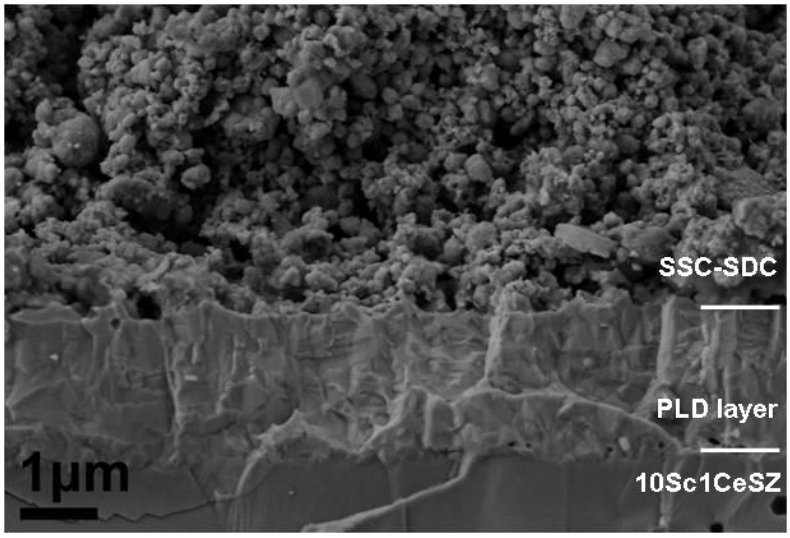

Figure 6.3. SEM cross-sectional images of the cathode-electrolyte interface, formed by a 10Sc1CeSZ tape casting as electrolyte, a CGO diffusion barrier layer (deposited by PLD) and a SSC-infiltrated into a mesoporous SDC ceramic scaffold as cathode.

6.3. Fuel Cell Performance

The cells fabricated with fully mesoporous electrodes were electrically characterized in the experimental setup described in the **section 2.5.1** of **Chapter 2**, under pure humidified hydrogen as fuel and synthetic air as oxidant at 750 ºC.

Figure 6.4 shows the current-voltage and power density curves. The single cell showed an open circuit voltage of 1.10 V indicative of a dense electrolyte and good sealing and a maximum power density of 565 mW/cm^2. Our baseline electrolyte supported SOFC fabricated with commercial $La_{0.6}Sr_{0.4}Co_{0.2}Fe_{0.8}O_3$ (LSCF) powder (measured in the previous **Chapter 4, section 4.4.1)** [2], showed a peak power density of 325 mW/cm^2 at the same temperature. Therefore, demonstrating the here-employed infiltration method over a mesoporous ceramic scaffold increases 74 % the performance.

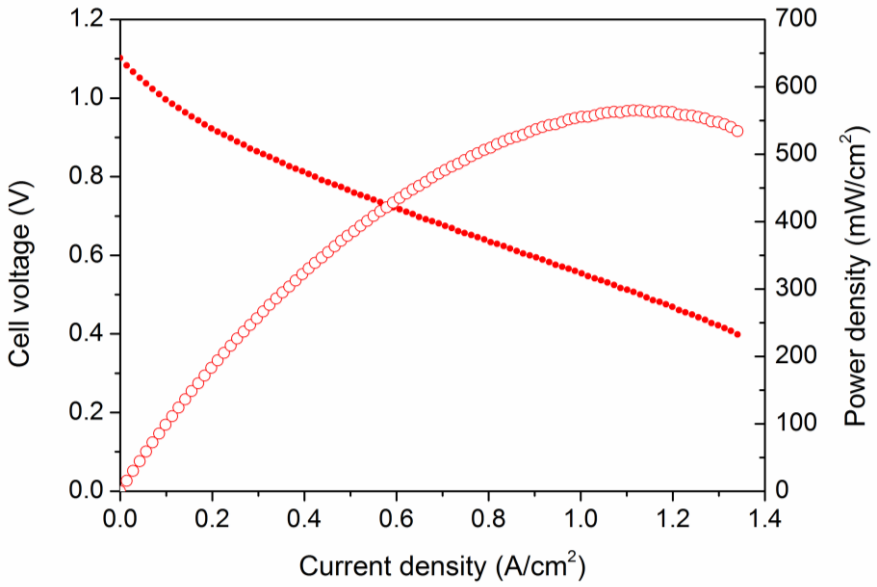

Figure 6.4. Cell voltage and power density as a function of the power density for a cell with fully-mesoporous electrodes operating at 750 ºC under pure humidified H_2 and synthetic air.

Figure 6.5 shows the Nyquist plot of the impedance measurement performed to analyze the different resistance contributions under open circuit voltage (OCV). The inset of the figure shows the equivalent circuit used to fit the obtained spectra $LR_s(RQ)_{HF}(RQ)_{LF}$ where L is an inductance, R a resistance and Q a constant phase element, the subscripts HF and LF indicate the high and low frequency contributions. A series resistance (R_s) of 0.277 $\Omega \cdot cm^2$ and a polarization resistance ($R_p = R_{HF} + R_{LF}$) of 0.945 $\Omega \cdot cm^2$ were obtained under OCV conditions. The contribution of the different resistances allow obtaining a maximum peak power density above the required for SOFC applications (P = 500 mW/cm^2).

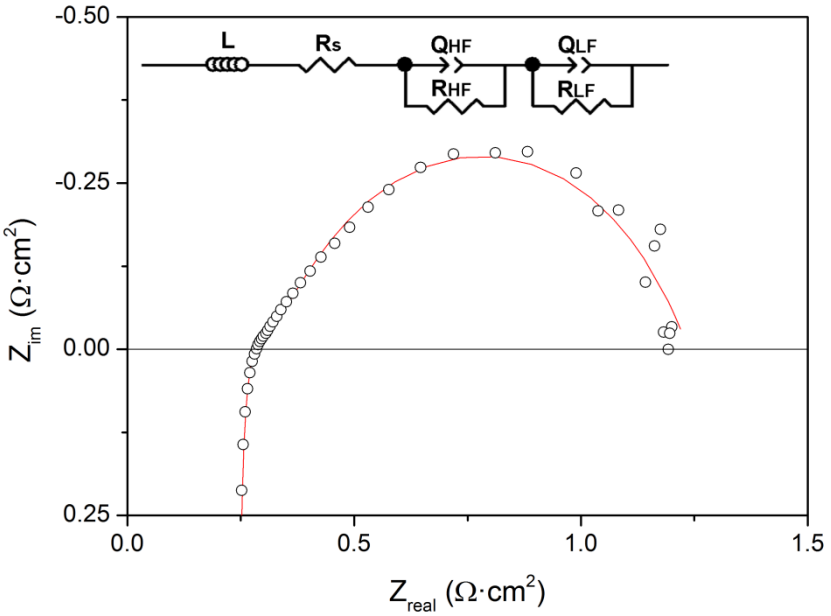

Figure 6.5. Nyquist plot of the IT-SOFC with fully-mesoporous electrodes at 750 ºC under OCV.

6.4. Long-term Stability Test

Apart from the performance characterization, the fabricated fully mesoporous fuel cell was subjected to a long-term degradation test under a constant current density of 635 mA/cm^2 at 750 ºC for 1000 hours. Impedance spectra were recorded every ~ 50 hours under OCV conditions.

Figure 6.6a shows the Nyquist plots obtained at the beginning (t = 0 h), after 500 and 1000 hours of the experiment. It is observed that the series resistance (R_s), mainly attributed to the electrolyte and current collection, increases from 0.277 Ω·cm^2 to 0.331 Ω·cm^2 after 1000 hours, while the polarization resistance (R_p), mainly attributed to the electrodes contribution surprisingly decreases, from 0.945 Ω·cm^2 to 0.740 Ω·cm^2 after 1000 h of the degradation test.

Figure 6.6b shows the evolution of R_s and R_p calculated from the EIS measurements under OCV with the time (some representative values of R_s and R_p, are shown in **Table 6.2**, columns R_s and R_p (OCV)). The degradation rate of the cell was calculated dividing the test time in two regions. In the initial region between 0 to 200 h (Region 1), after an initial stabilization period of ~ 24 h, the value of R_s increases with an

average rate of 85 $\mu\Omega\cdot cm^2/h$ (6 %) and the R_p decreases, with an overall rate of -303 $\mu\Omega\cdot cm^2/h$ (6 %). In the second region, from 200 to 1000 h (Region 2), the R_s increases with a rate of 65 $\mu\Omega\cdot cm^2/h$ (21 %), while the R_p decreases with a rate of -227 $\mu\Omega\cdot cm^2/h$ (20 %). Therefore, the route presented in this chapter to fabricate cells with fully mesoporous electrodes seem to be promising for developing high-performance and long-term stable IT-SOFCs.

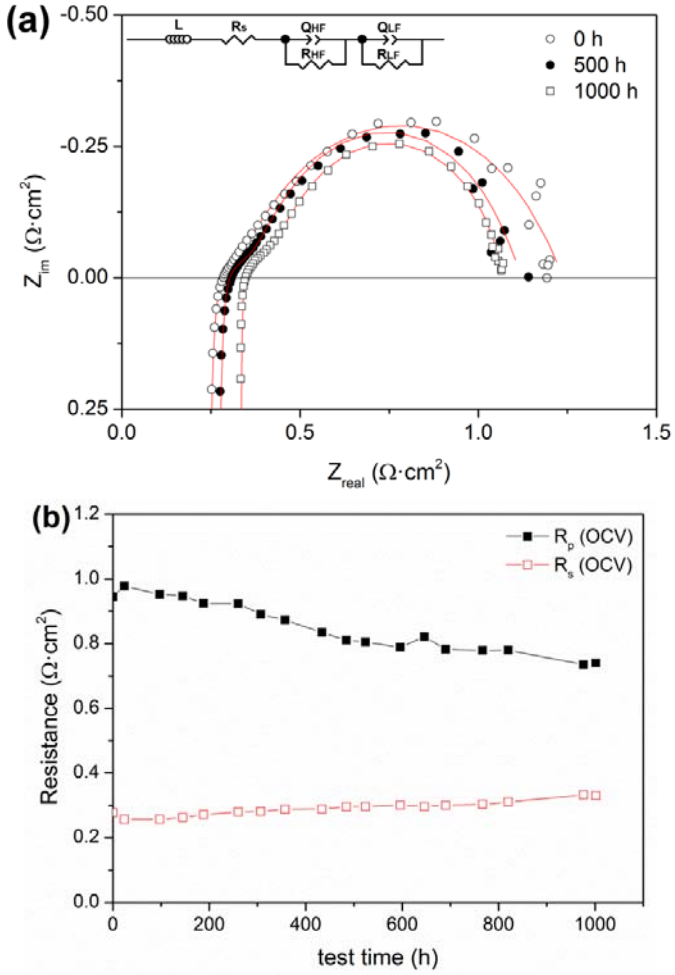

Figure 6.6. EIS measurements of the IT-SOFC with fully-mesoporous electrodes performed under OCV obtained during the long-term stability test. (a) Nyquist plots recorded at the beginning, after 500 h and 1000 h, (b) Evolution of series resistance (R_s) and polarization resistance (R_p) under OCV with the test time.

Figure 6.7a shows the cell voltage (V_{cell}) with the test time recorded during the long-term stability test under a current density of 635 mA/cm^2 at 750 ºC for 1000 hours. The voltage of the cell decreases due to different voltage losses. The main voltage losses are the ohmic or series resistance and the polarization resistance (i.e. electrochemical reactions and gas diffusion through the electrodes) and can be expressed by the following equation:

$$V_{cell} = OCV - i \cdot ASR = OCV - i(R_s - R_p) \quad \textbf{(6.1)}$$

where V_{cell} is the recorded cell voltage, OCV is the open circuit voltage, ASR is the total cell area specific resistance, R_s is the series or ohmic resistance and R_p is the polarization resistance.

After 1000 hours, the cell voltage decreases from a value of 0.7 V to 0.6 V and the total ASR increases from 0.62 Ω·cm^2 to 0.79 Ω·cm^2 (**Table 6.2**). A more detail study of the overpotentials or voltage losses is detailed in **Figure 6.7b**. On the other hand, impedance spectra under a bias DC voltage of 0.7 V were measured at 976 and 1001.5 hours (two last filled points $i \cdot R_s$ and $i \cdot R_p$ of **Figure 6.7**). These measurements confirmed that the series resistance is the same under OCV or under bias and allow calculating the polarization resistance during the test time (R_p = ASR – R_s). The calculated overpotentials help to understand better the degradation mechanisms.

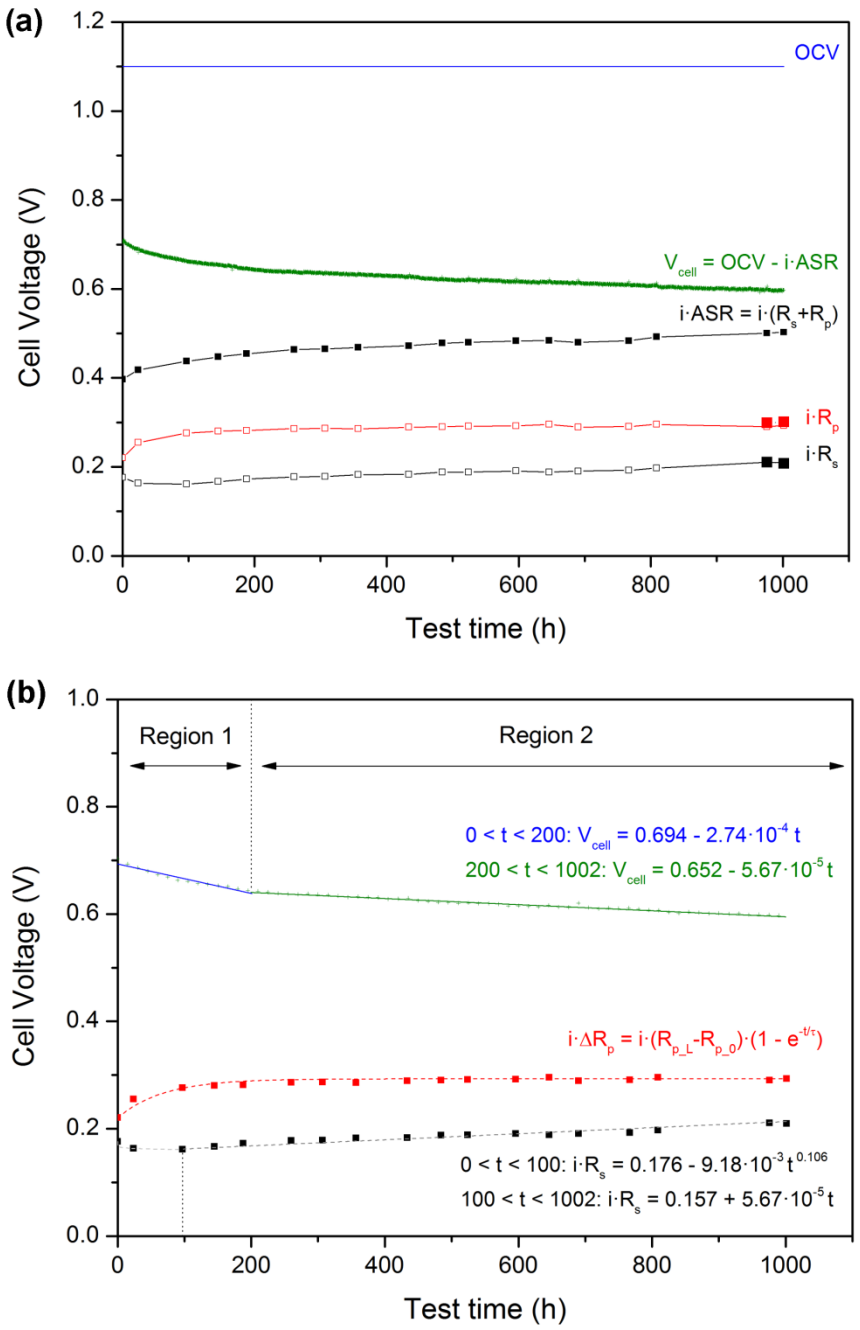

Figure 6.7. Evolution of the cell voltage (V_{cell}) with the test time under a current density of 635 mA/cm^2 at 750 ºC for 1000 hours, **(a)** V_{cell}, the total overpotential (i·ASR) and its different contributions, series (i·R_s) and polarization (i·R_p) overpotentials, are shown. Last two filled square points of i·R_s and i·R_p were obtained from EIS measurements under a DC bias voltage of 0.7 V, i.e. operation voltage. **(b)** Fitting data and equations of the V_{cell} (solid lines) and the corresponding overpotentials i·R_s and i·R_p (dash lines).

Table 6.2. Representative resistance values obtained during the long-term stability test performed under 635 mA/cm^2 at 750 ºC for 1000 hours.

Test time (h)	ASR ($\Omega \cdot cm^2$)	R_s ($\Omega \cdot cm^2$)	R_p ($\Omega \cdot cm^2$) (OCV)	R_p ($\Omega \cdot cm^2$) (0.7 V)
0	0.624	0.277	0.945	0.347
24	0.657	0.256	0.977	0.401
97	0.688	0.257	0.952	0.431
188	0.714	0.271	0.924	0.443
357	0.736	0.287	0.873	0.449
596	0.760	0.300	0.788	0.459
767	0.760	0.303	0.779	0.457
976	0.787	0.331	0.735	0.456
1002	0.791	0.331	0.740	0.460

Figure 6.7b shows the fitting data for the variation of the cell voltage (V_{cell}), the series overpotential ($i \cdot R_s$) and the polarization overpotential ($i \cdot R_p$) during the long-term stability test. The cell voltage versus time decays with two different rates, which were fitted by the linear equations shown. In the Region 1, from 0 to 200 h, the decay obtained was 274 µV/h (9 %) and in the Region 2, from 200 to 1002 h, was 57 µV/h (7 %). It is noteworthy, that 57.5 % of the cell drop occurred within the first 200 hours.

The polarization overpotential can be fitted by the following equation which defines an asymptotic behavior of the polarization resistance versus the time,

$$i \cdot \Delta R_p = i \cdot \left(R_{p_L} - R_{p_0}\right) \cdot (1 - \exp^{-t/\tau}) \qquad \textbf{(6.2)}$$

where R_{p_0} is the initial polarization resistance, R_{p_L} is the limited polarization resistance, τ is the time constant and t is the test time.

Values of R_{p_L} of 0.46 $\Omega \cdot cm^2$ ($i \cdot R_{p_L} = 0.29$ V) and τ of 68.3 hours were obtained from the fitting, indicating that degradation of the electrodes mainly occurred during the first ~ 70 hours of the test. The fitted degradation rate decreases from 31 % during the first 200 hours, to 1 % from 200-500 hours, to 0.016 % from 500-1000 hours. This fact is attributed to the accommodation of the microstructure and is probably more pronounce than shown in Chapter 4 and 5 due to the high constant current.

In any case, after the initial degradation, a stable polarization resistance was achieved, implying that high stable electrode structures were obtained under the realistic and severe conditions imposed during more than 1000 hours.

The asymptotic behavior of R_p clearly differs from the previously reported by Lee parabolic plot (**Figure 6.1**) [7]. This promising trend to a fully stable system could be attributed to the demonstrated high thermal stability of the mesoporous materials as independent electrodes, anode (see **Chapter 4**) and cathode (see **Chapter 3 and 5**). In fact extrapolating the last stabilize degradation rate, a value of 0.032 % per 1000 hours would be achieved, which is below the objective imposed for the US Department of Energy's Solid State Energy Conversion Alliance (SECA) of 0.2 % per 1000 hours [1].

After an initial decrease of the series overpotential during ~ 97 hours, the data can fit a linear equation with a slope of 57 μV/h (30 %) which corresponds to the decay rate of the cell voltage in the region 2.

Further microstructural analysis is necessary to explain the sources of degradation (grain coarsening, cation interdiffusion, electrode delamination, phase transformation or formation of secondary phases) and will be presented in the next section.

6.5. Post-Test Cell Characterization

Figures 6.8a and b show the cross-sectional SEM image of the anode-electrolyte interface after 1000 hours of degradation test under a constant current density of 635 mA/cm^2 at 750 ºC. Open porosity and intimate adhesion of the anode to the electrolyte is observed. In **Figure 6.8d** the BSE mode allows identifying Ni and SDC phases. The nickel (darker grey) keeps the grain size in the nano-scale, although evolution

from the initial micro-structure (see **Figure 6.8c**) is observed. Evolution and accommodation of the microstructure is mainly occurring during the first ~ 70 hours of the degradation test.

It should be pointed out that the rough CGO layer deposited to improve the attachment densified during the long-term stability test. A denser layer of ~ 0.5-0.7 μm was observed along the anode-electrolyte interface and it could be one explanation of the increase in the ohmic resistance (indicated in **Figure 6.8b**).

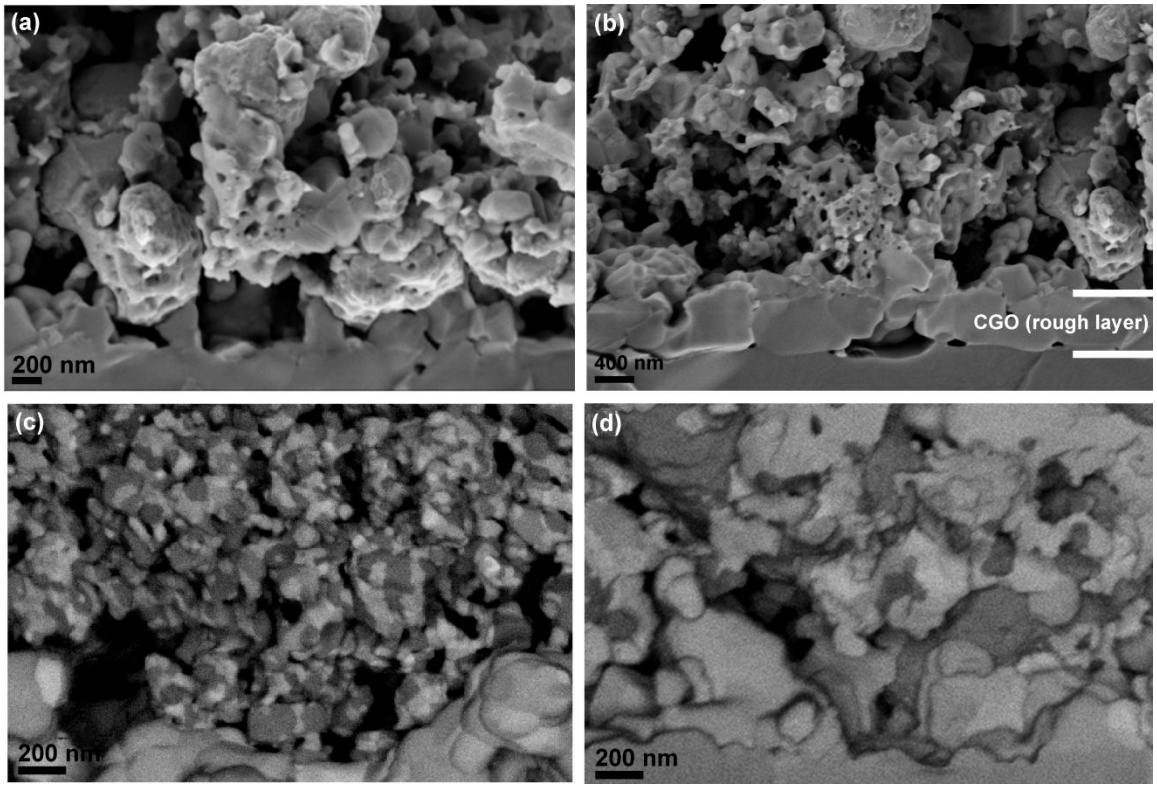

Figure 6.8. (a, b) SEM images of the interface of the mesoporous Ni-SDC anode and the electrolyte of the fully mesoporous cell, after the degradation test performed for 1000 hours under a current density of 635 mA/cm^2 at 750 ºC. (c,d) Backscatter images of the interface before and after the degradation test, respectively.

However, the most suitable hypothesis of the R_s evolution is related to some phase instabilities (from cubic to rhombohedral phase) previously reported for scandia-doped zirconia (10Sc1CeSZ) based electrolytes, working in electrolysis mode under high operating voltages for long times. This change of the crystal structure would cause ionic

conductivity degradation [14]. To confirm this micro-Raman spectroscopy was performed before and after the degradation test.

In this work since the electrolyte is under reducing conditions at the anode side and under oxidizing conditions at the cathode side a gradient and degradation across the tape is also expected. Moreover, the anode side (fuel electrode) present an orange coloured characteristic of the presence of the Ce^{+3} ion [15].

Figure 6.9 shows the Raman spectra of an original tape casting of 10Sc1CeSZ and the same tape on the anode side after the long-term degradation measurement. The original tape shows the cubic phase of the zirconia with peaks in 620, 480, 370 and 150 cm^{-1}. The other non-indexed peaks suggest that a certain amount of tetragonal phase also exists [16]. Nevertheless for the tape after the degradation test, the most intense peak of the cubic mode around 620 cm^{-1} shifted to lower wavenumbers around 590 cm^{-1} indicating the presence of the β-rhombohedral phase [14,17].

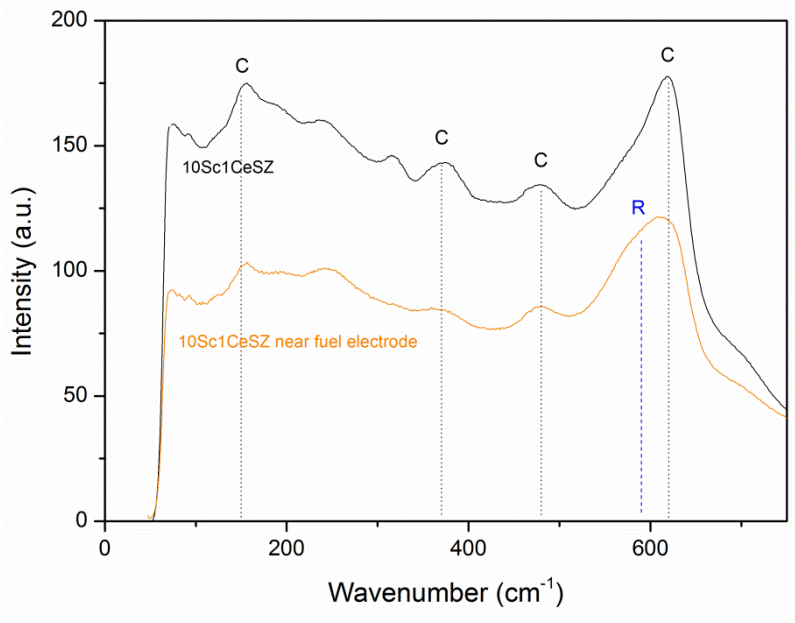

Figure 6.9. Raman spectra of the 10Sc1CeSZ electrolyte original (black) and the same tape after the long-term degradation test in the anode side (orange coloured). Cubic (C) and most intense rhombohedral (R) peaks of zirconia are labeled.

Another source of degradation could be the evolution of the CGO PLD diffusion barrier layer with the time. As explained in the **section 6.2 of this Chapter**, Sr ion diffusion is one typical degradation mechanism that occurs between the cathode and the electrolyte. In order to study the ion diffusion of the cell with fully mesoporous electrodes after the long-term stability test, SEM Energy Dispersive X-Ray (EDX) compositional profile was performed in the interface between the cathode the CGO barrier layer and the electrolyte, along the line shown in **Figure 6.10a**. Although the resolution of the technique together with the length of the line profile selected are not adequate to quantify the stoichiometry of each part of the sample (due to a 1 µm integration of the X-ray), the presence of Sr in the electrolyte was not detected, demonstrating the CGO diffusion barrier layer made by PLD was dense and thick enough to prevent the Sr migration from the cathode to the electrolyte.

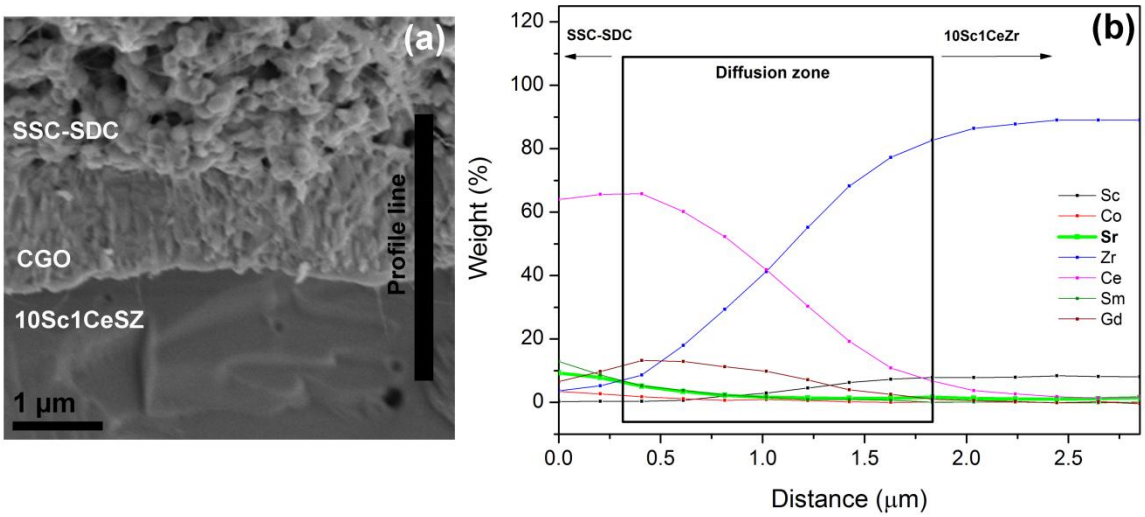

Figure 6.10. SEM-EDX line concentration profiles of the mesoporous SSC-SDC cathode/CGO diffusion barrier layer/10ScCeSZ electrolyte after the galvanostatic long-term degradation test at 750 ºC for 1000 hours.

Finally, **Figure 6.11** shows the SEM image of the interface between the cathode and the CGO diffusion barrier layer after the long-term stability test (1000 hours). The fabricated cathode, SSC infiltrated into the mesoporous SDC ceramic scaffold, keep the

meso-porosity even after 1000 hours under the severe realistic operating conditions, confirming again the route stability shown in **Chapter 3**.

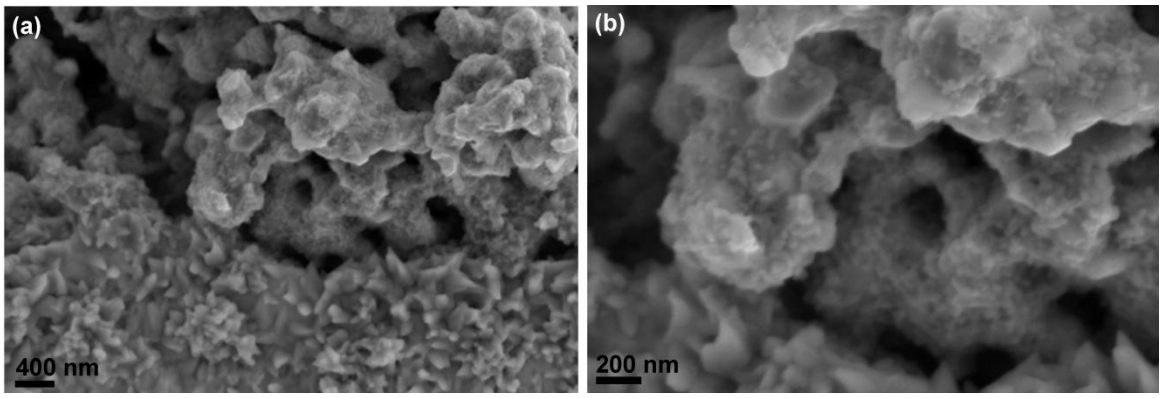

Figure 6.11. SEM cross-sectional images of the interface of the cathode of SSC-infiltrated in the mesoporous SDC ceramic scaffold and the CGO diffusion barrier layer, after the degradation test performed for 1000 hours under a current density of 635 mA/cm^2 at 750 ºC.

6.6. Conclusions

An IT-SOFC with fully mesoporous electrodes were fabricated and characterized for the first time. Mesoporous Ni-SDC was used as anode and SSC-SDC as cathode. Structural and electrochemical characterization of these electrodes independently were described in detail in the previous chapters of this thesis. For the whole cell, a maximum power density of 565 mW/cm^2 at 750 ºC was obtained, implying an improvement of 74 % compared to our baseline cells based on commercial cathode powders.

This cell was subjected to a long-term stability test under real operational conditions (750 ºC under a constant current density of 635 A/cm^2) for 1000 hours showing two different regions of degradation with linear decay. The first region from 0 to 200 h showed a degradation rate of 274 μV/h (9 %) and the second region of 57 μV/h (7 %). The 57.5 % of the cell drop occurred within the first 200 hours. The impedance analysis performed under OCV conditions showed an increase of the ohmic series resistance (R_s) in the region 1 of 85 μΩ·cm^2/h (6 %) and in the region 2 of 65 μΩ·cm^2/h (21 %) and a surprising decrease of the polarization resistance (R_p) in the region 1 of -303 μΩ·cm^2/h (6 %) and in the region 2 of -227 μΩ·cm^2/h (20 %).

The continuous improvement of the performance of the electrodes shows under a bias voltage of ~ 0.7 V and after the stabilization period an asymptotic behavior. The limited polarization resistance growth is attributed to the astonishing stability of these electrodes presented in previous chapters (with an accommodation period of 70 hours). In fact, the polarization overpotential showed a degradation of 0.032 % per 1000 hours after stabilization, which is below the objective of 0.2 % degradation per 1000 hours imposed by the SECA.

The evolution of the series overpotential can be explained by several facts: an observed densification of the CGO rough layer (deposited to improved the attachment) in the anode side, the possibility of part of loss of contact of the current collectors non-optimized for stability purposes and the change of phase from cubic to β-rhombohedral of the scandia-doped zirconia electrolyte support in the anode (fuel) side.

Structural analysis of the cell after the degradation test, further confirmed the electrodes kept their nano-structure after more than 1000 hours. Moreover, SEM EDX-spectroscopy confirmed Sr did not diffused from the cathode due to the well-formed CGO barrier layer deposited by PLD.

Overall, the aim of the present chapter is accomplished as the long-term stability of the fully mesoporous electrodes was demonstrated, for more than 1000 hours under realistic and severe operational conditions.

References

[1] Office of Fossil Energy Fuel Cell Program Portfolio. Solid State Energy Conversion Alliance (SECA), 2013.

[2] Recent Solid Oxide Fuel Cell Cathode Studies. Tools, Results, and Novel Concepts for Making Better Cells. National Energy Technology Laboratory (NETL), 2013.

[3] D. Ding, X. Li, S.Y. Lai, K. Gerdes, M. Liu, Energy Environ. Sci. 7 (2014) 552.

[4] Z. Liu, B. Liu, D. Ding, M. Liu, F. Chen, C. Xia, J. Power Sources 237 (2013) 243.

[5] S.P. Jiang, Int. J. Hydrogen Energy 37 (2012) 449.

[6] R.S. Gemmen, M.C. Williams, K. Gerdes, J. Power Sources 184 (2008) 251.

[7] S. Lee, N. Miller, K. Gerdes, J. Electrochem. Soc. 159 (2012) F301.

[8] A.J. Samson, P. Hjalmarsson, M. Søgaard, J. Hjelm, N. Bonanos, J. Power Sources 216 (2012) 124.

[9] A.J. Samson, M. Søgaard, P. Hjalmarsson, J. Hjelm, N. Bonanos, S.P. V. Foghmoes, T. Ramos, Fuel Cells 13 (2013) 511.

[10] R. Knibbe, J. Hjelm, M. Menon, N. Pryds, M. Søgaard, H.J. Wang, K. Neufeld, J. Am. Ceram. Soc. 93 (2010) 2877.

[11] S. Uhlenbruck, N. Jordan, D. Sebold, H.P. Buchkremer, V. a. C. Haanappel, D. Stöver, Thin Solid Films 515 (2007) 4053.

[12] T. Klemensø, J. Nielsen, P. Blennow, Å.H. Persson, T. Stegk, B.H. Christensen, S. Sønderby, J. Power Sources 196 (2011) 9459.

[13] J. Peña-Martínez, D. Marrero-López, C. Sánchez-Bautista, A.J. Dos Santos-García, J.C. Ruiz-Morales, J. Canales-Vázquez, P. Núñez, Bol. Soc. Esp. Ceram. 49 (2010) 15.

[14] M.A. Laguna-Bercero, V.M. Orera, Int. J. Hydrogen Energy 36 (2011) 13051.

[15] V. Orera, R. Merino, F. Peña, Solid State Ionics 72 (1994) 224.

[16] Z. Wang, M. Cheng, Z. Bi, Y. Dong, H. Zhang, J. Zhang, Z. Feng, C. Li, Materials Letters 59 (2005) 2579.

[17] F. Tietz, W. Fischer, T. Hauber, G. Mariotto, Solid State Ionics 100 (1997) 289.

7

Mesoporous ceramic oxides for humidity sensors

7. Mesoporous Ceramic Oxides for Humidity Sensors

7.1. Requirements of Humidity Sensors and Advantages of using Ceramic Mesoporous Materials 189

7.2. Characterization of CGO Mesoporous Humidity Sensors 190

7.2.1. Structural characterization 190

7.2.2. Humidity sensing capabilities of a mesoporous CGO film 191

7.2.3. Mechanism of humidity sensing 195

7.2.4. Effect of temperature 198

7.2.5. Effect of the thickness of the sensing layer 200

7.2.6. Effect of the pore size 201

7.3. Conclusions 202

References 204

7. Mesoporous Ceramic Oxides for Humidity Sensors

7.1. Requirements of Humidity Sensors and Advantages of using Ceramic Mesoporous Materials

The humidity control is of utmost importance as it affects both living organisms and materials. Therefore, humidity sensors are currently used in many fields such as manufacturing processes, environmental and health monitoring or in domestic applications [1].

In general homogeneity and controllability of porous structures are important properties in sensor applications (**Chapter 1.4.3**). Mesoporous materials provide high area structures with a very precise shape, which make them perfect candidates for sensing applications [2–4]. In this respect, many studies have reported high sensitivity in silica based mesoporous humidity sensors [5–8]. However, during the fabrication of the sensor the mesoporous powder is usually attached to the electrodes at very low temperatures in order to preserve the nanostructure. This limitation makes these devices mechanically unstable and affects reproducibility, limiting their viability for commercial applications.

Moreover a heat treatment at temperatures over 400 ºC is normally used in commercial ceramic humidity sensors to recover the initial state. However, if this heat treatment process is performed, the sensing properties of the silica based mesoporous sensors became poor [9,10], due to either loss of the mesoporosity originated by the thermal stability lack of this type of mesoporous materials at high temperatures or the poor attachment of the sensing layer to the substrate. Mesoporous metal oxides with higher thermal stabilities would be ideal candidates, if they can keep their microstructure and thus their sensing properties.

In **Chapter 3**, the authors developed a novel strategy to stabilize mesoporous ceramic oxides up to high temperatures [11]. Contrary to widely employed high temperature stabilization treatments inside the mesoporous template, resistance to thermal processes is achieved by getting the simultaneous presence of amorphous and crystalline phases before the template removal, forcing the so called self-limited grain growth

regime. Using this strategy stabilization of mesoporous structures is achieved up to temperatures as high as 1000 ºC.

Among the ionic type of ceramic sensors, nanostructured CeO_2 has shown high sensitivity and fast response [12]. Moreover, it has been reported that metal doping changes the charge density surface of the ceramic oxide, the strong electric field generated around the surface of the material is expected to increase the ionization of the water molecules [13–15].

In **the present chapter**, gadolinium-doped ceria (CGO) mesoporous humidity sensors were fabricated and tested under different (i.e. humidity and temperature) conditions. The sensitivity, response and recovery times and the sensing mechanisms based on the analysis of the impedance spectra are presented and discussed.

7.2. Characterization of CGO Mesoporous Humidity Sensors

7.2.1. Structural characterization

A complete micro-structural characterization of mesoporous gadolinium doped ceria (CGO) powder obtained as replica of the KIT-6 silica template and calcined at 600 ºC was presented in **Chapter 3** (CGO-600) [11]. The same powder was airbrushed (ethanol based ink) on an alumina substrate with gold interdigitated planar contacts. After a sintering process at 900 ºC the layers are homogeneous and firmly stuck, details of the fabrication procedure can be found in **Chapter 2.3.3**.

The SEM images of **Figure 7.1a and c** show a continuous crack-free layer of the sensing material forming a network with thickness of ~ 12-13 μm, highly desirable to facilitate the conduction of the water molecules along the surface, increasing the sensitivity. A very fine microstructure with porous in the nanometric range and ordered structure can be observed in the high magnification SEM image (**Figure 7.1b**). As expected from the previous studies, the thermally stabilized mesoporous CGO oxides keep the microstructure after the attachment to the alumina substrate at high temperatures [11].

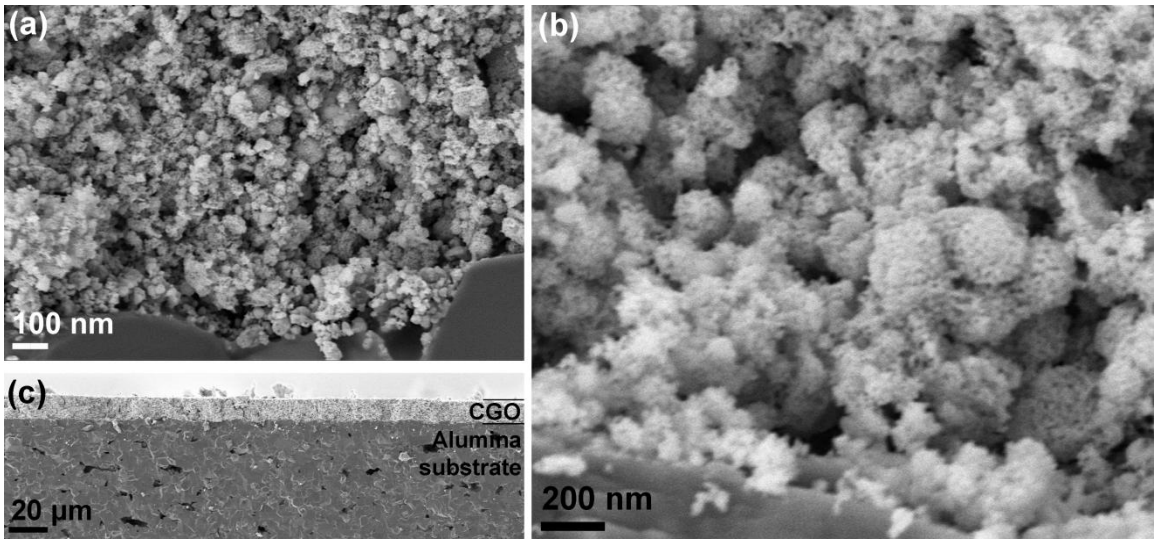

Figure 7.1. Cross-sectional SEM images of the CGO mesoporous humidity sensor (after electrochemical measurements).

7.2.2. Humidity sensing capabilities of a mesoporous CGO film

The response to humidity of the fabricated films is evaluated. Sinusoidal excitation signals of different frequencies are imposed and the resistance is measured. **Figure 7.2** shows the tendency of the resistance at different frequencies for several humidity levels at a controllable fixed room temperature (T = 30 ºC).

In the low frequency region (f = 1-10 Hz) the device presents the highest sensitivity, 10 Hz is a good trade-off between measurement velocity and selectivity, and will be the frequency used in the following. A detailed analysis of the impedance response of the sensors is presented in the **section 7.2.3**. There, the choice of the low frequency range for on line monitoring of the sensor response is justified.

The impedance does not change at higher frequencies (f = 10^4–10^5 Hz) where the response of the sensor becomes independent of the humidity. This indicates that in this higher range of frequencies, the change of direction of the electrical field is too fast compared to the characteristic time of the Grotthuss transport phenomenon.

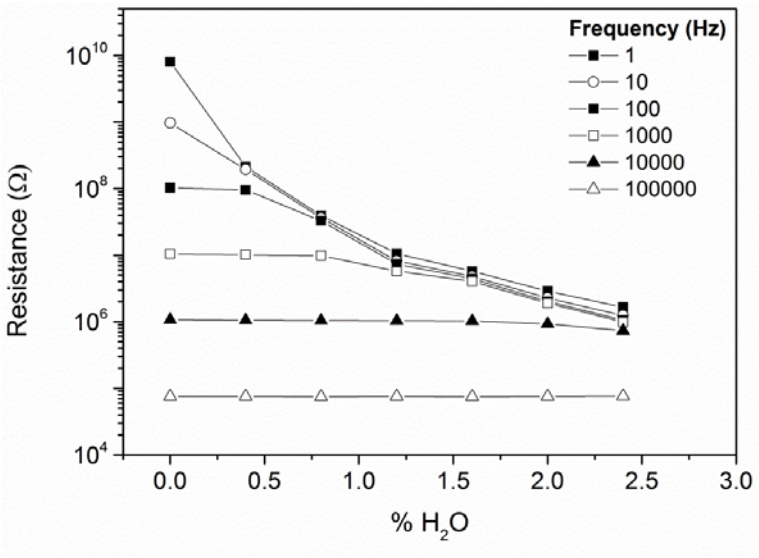

Figure 7.2. Resistance versus % H_2O curves of the CGO humidity sensor at different frequencies (T = 30 ºC).

The relative resistance (R_0/R_{RH}) versus the relative humidity (RH) is presented in **Figure 7.3,** for the here-fabricated mesoporous CGO humidity sensor and compared to different cerium oxides based humidity sensors extracted from the literature [12–14]. In this figure, R_0 indicates the resistance of the sensors at 25 % RH and R(RH) the resistance values at the corresponding humidity level.

Dense bulk cerium oxides show almost no change in resistance on the whole range of relative humidities, while for nanostructured materials sensitivity starts to become significant. The here-proposed CGO mesoporous material sensor shows an exponential decrease of the resistance with the increase of humidity. This behavior has been reported as arising from an ionic type humidity sensing mechanism [16–18]. Only complex nanostructured configurations like CeO_2 nanowires present a sensitivity comparable to the here presented material.

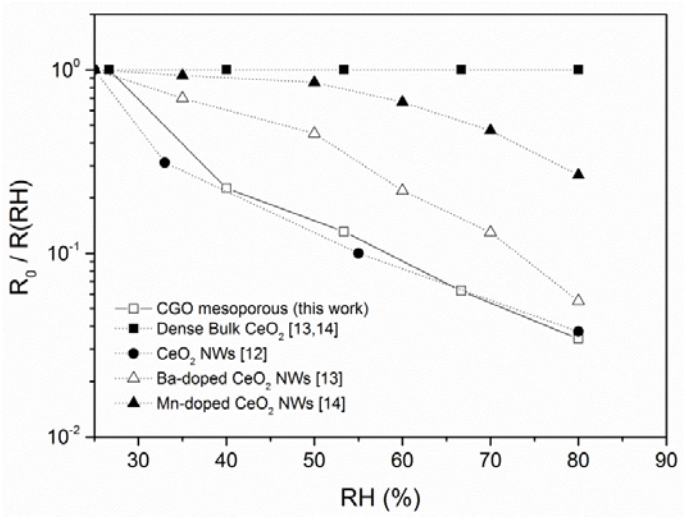

Figure 7.3. Relative resistance (R_0/R_{RH}) vs relative humidity for different ceria based humidity sensors.

In order to be reliable, a sensor must present low hysteresis. It is a measure of the capability of the system for measuring the same signal when exposed to the same conditions, independently of past inputs. **Figure 7.4** presents the resistance of the layer when changing the humidity levels from dry to humid (3 % H_2O) and then measuring back to the initial dry level. The adsorption and desorption curves practically overlap showing a maximum small hysteresis of ~ 0.1 % H_2O, thus making remarkable the reliability and the highly reversible characteristics of this type of mesoporous ceramic sensors.

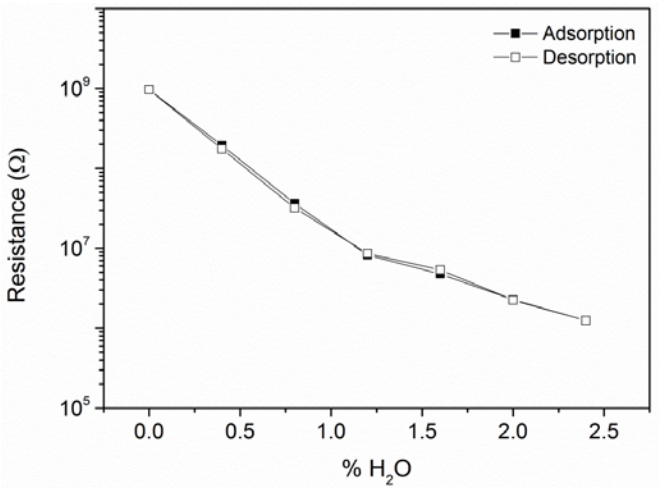

Figure 7.4. Hysteresis of mesoporous CGO humidity sensor at 10 Hz (T = 30 ºC).

The response and recovery of the CGO mesoporous humidity sensors at a frequency of 10 Hz (T = 30 ºC) is shown in **Figure 7.5a**. The changes of resistance with the humidity level were measured in cycles of 90 seconds from dry to 2.5 % H_2O. The sensitivity of a sensor is defined as the time taken by the sensor to reach the 90 % of the total impedance change ($S = R_0/R_{90\%}$) and is calculated to be 280 for the tested material. The response and recovery time constants calculated as the time that a sensor consumes to reach 63.2 % value of the steady state value are 19.1 and 1.3 seconds respectively, indicating quick response-recovery characteristics to humidity changes, compared to the generally reported times of several tens of seconds.

For instance, Pokhrel *et al*. showed a Cr_2O_3-WO_3 composite sensor with a response and recovery of 25 min and 7 min, respectively [19]. Rezlescu *et al*. made a Sn^{4+} and/or Mo^{6+} substituted Mg ferrites sensors with a response time between 3 to 5 min [20]. Z. Zhang *et al*. presented a Ba-doped CeO_2 NWs sensor with a response and recovery time of 3 min [13]. C. H. Hu *et al*. showed a sensor of Mn-doped CeO_2 nanorods with a response of 2 min and a recovery of 3 min [14]. Y. W. Hao *et al*. presented a CGO nano-sized based sensor with a response of 40 s and a recovery of 210 s [15]. The most comparable result was reported by Fu *et al*. who fabricated a fast CeO_2 sensor based on nanowires (NWs) with a response and recovery both about 3 s [12] (**Figure 7.5b**). Apart from the quick response and recovery, no drift in the dynamic response was detected during a test performed for 50 minutes (13 cycles).

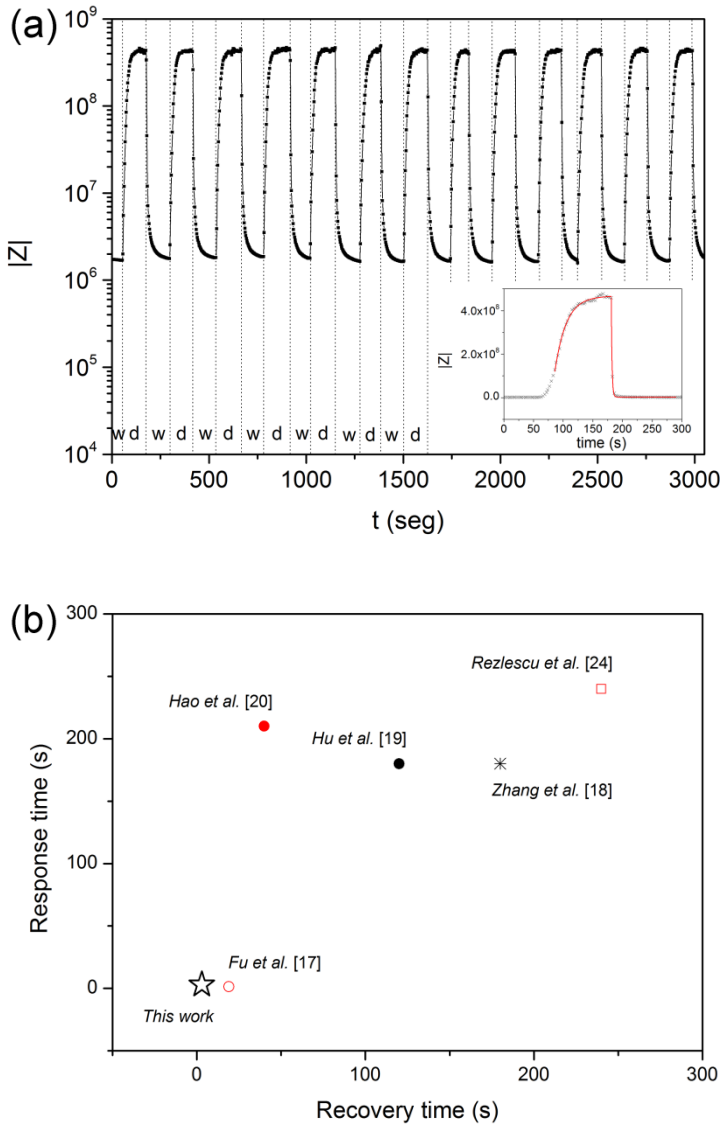

Figure 7.5. (a) Dynamic response of the mesoporous CGO humidity sensor during at 10 Hz (T = 30 ºC). The inset figure shows one cycle of response and recovery where the red line corresponds to the exponential fitting. (b) Response and recovery times of several humidity sensors.

7.2.3. Mechanism of humidity sensing

Different conduction mechanisms have been indentified analyzing the impedance spectra of porous ceramic humidity sensors. The mechanism of conduction is widely reported to change from low water concentrations to high water concentrations, where the

corresponding impedance spectra changes from a line usually fitted as an equivalent circuit formed by a constant phase element, to a semicircle (fitted by a resistance and capacitance in parallel) and a Warburg line at lower frequencies. The impedance spectra in those works are usually collected in a frequency range from ~ 50 Hz to 100 kHz and applying an AC voltage of 1 V. The humidity sensing mechanism has been extensively studied and even though the equivalent circuits used may differ from one author to another, the explained conduction mechanism is the same [4,5,8,21].

In the present work, impedance spectroscopy measurements were performed in a wide frequency range (1 MHz to 0.1 Hz) and an AC signal of 300 mV. **Figure 7.6** shows the experimental data (cross points) obtained from the impedance measurements for 0.08, 1.2 and 2.4 % of H_2O (T = 30 ºC). In all the samples, the impedance spectra was fitted with an equivalent electrical circuit formed by a resistance (R_{film}) in parallel with a capacitance (C) and a constant phase element (CPE (Q, n)) in series (**Figure 7.6a**). The curves arising from the fitted equivalent circuit are represented as a solid red line in the figure. R_{film} represents the protonic conduction on the CGO surface while C is the capacitance of the dielectric CGO material (electrical insulator). Therefore, the decrease of the semicircle's values with the increase of humidity reflects the decrease of the module of the impedance due to proton conduction. At lower frequencies, diffusion processes appeared to be dominant. When humidity is introduced in the atmosphere, a Warburg line (fitted in the circuit as a CPE with a fixed exponent n = 0.5) appears representing the migration of electro-active species in the adsorbed layer towards the electrode (mass-transfer process).

The inset of the **Figure 7.6b** shows the impedance spectra in the commonly collected frequency range from 10 Hz to 100 kHz, usually fitted by one element a constant phase element (infinite resistance) for dry atmospheres. Nevertheless, when extending the frequency range it results in a typical RC arc.

Now the use of 10 Hz frequency in the dynamic tests is further justified at the light of the impedance arcs. As it is observed in the figures the module of the impedance at this frequency is changing significantly, while this is not the case at higher frequencies.

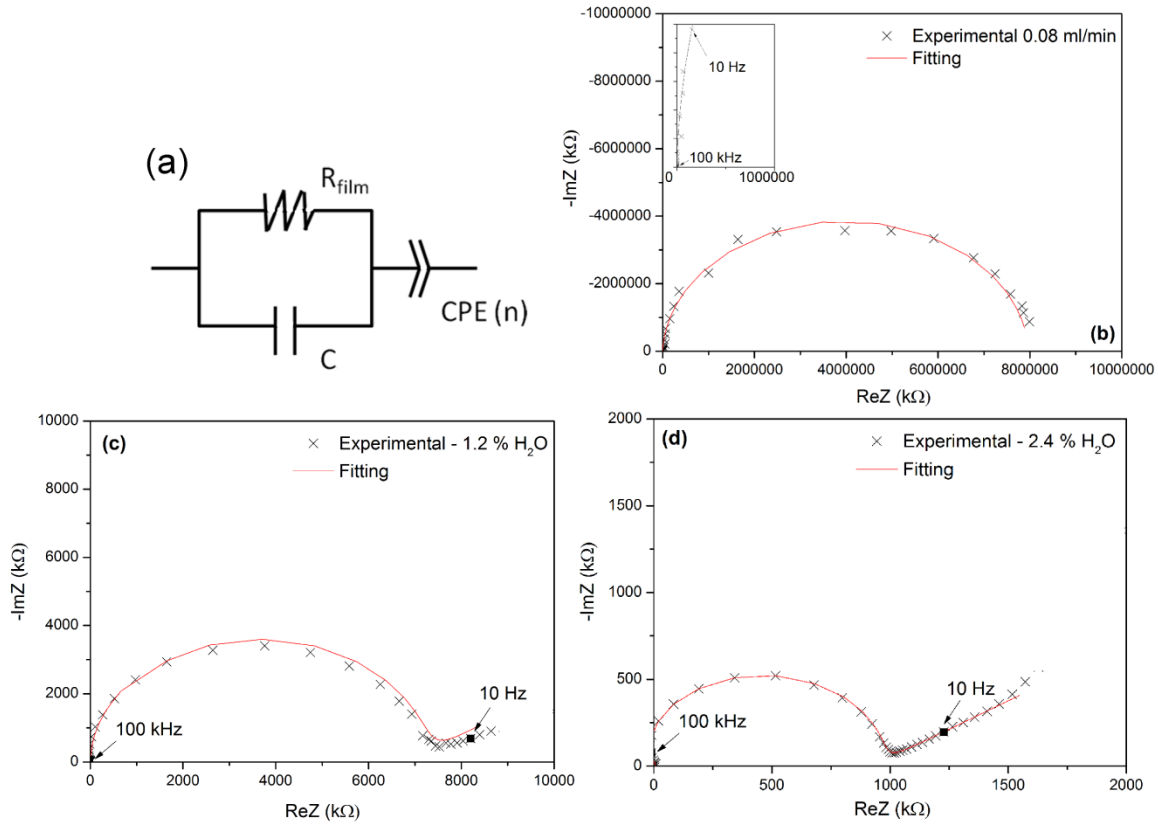

Figure 7.6. (a) Electrical equivalent circuit used to fit the impedance spectra. Impedance spectra of the CGO mesoporous sensor at 30 ºC for (b) 0.08 (d) 1.2 and (d) 2.4 % H_2O. The cross points indicate the experimental collected data and the line the corresponding fitted curve.

Figure 7.7 shows the evolution with humidity of the parameters obtained from the fitting of the equivalent circuit to the impedance spectra. The resistance of the film decreases around four orders of magnitude as the humidity increases, following an exponential behavior. The CGO capacitance is constant being intrinsic to the material.

The results are consistent with the Grotthuss conduction mechanism [1], the resistance of the film changes exponentially as water molecules are adsorbed gradually, from the very first monolayer to the physical adsorption of water molecules. Even at low humidity levels, it is possible to observe the hopping of protons in the chemisorbed monolayer of water. As the humidity increases, the continuous adsorption of water molecules (physisorbed) likely formed multilayers showing a liquid-like behavior (Grotthuss mechanism).

The cerium ions lead to a strong electric field around the surface increasing the ionization of the water molecules and affecting the deeper physisorbed water. Moreover, the large surface to volume ratio characteristic of the mesoporous materials plays a key role in the conduction [12]. The interconnected network with double gyroid structure make the water molecules pass easily through the regular pores. This also contributes to the previously reported quick response and extremely fast recovery.

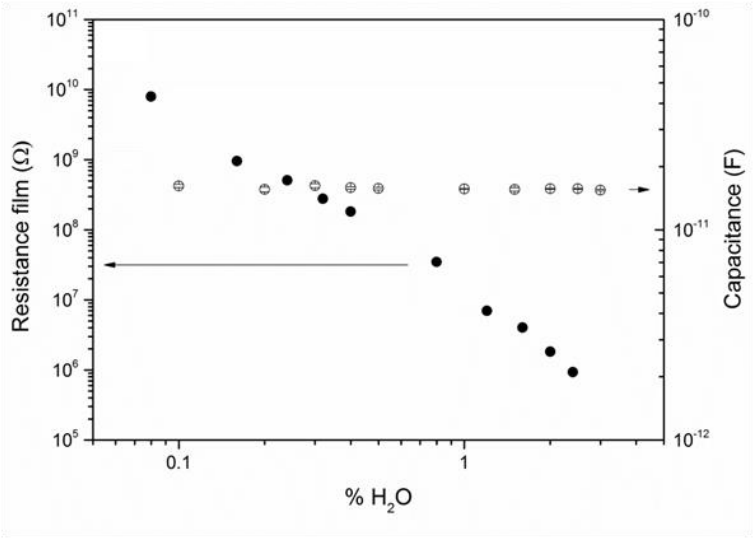

Figure 7.7. Fitted parameters: resistance and capacitance of the CGO film, obtained from the impedance spectra analysis of the humidity sensor at 10 Hz and different humidity levels (T = 30 ºC).

7.2.4. Effect of temperature

The response and recovery curves were measured at different temperatures (T = 60, 70, 80 and 90 ºC) once again fixing the frequency at 10 Hz. The results are shown in **Figure 7.8a and b**. The amplitude of the response (ΔR) decreases when operation temperature increases. This effect is consistent with the above explained Grotthuss mechanism, as the adsorbed layer becomes thinner when water molecules hold higher kinetic energy (at higher temperature). This would also explain the faster response and

lower recovery time, as the mobility of the ions is higher. The increase mobility promotes a higher adsorption-desorption exchange what also explains the observed slower recovery rate.

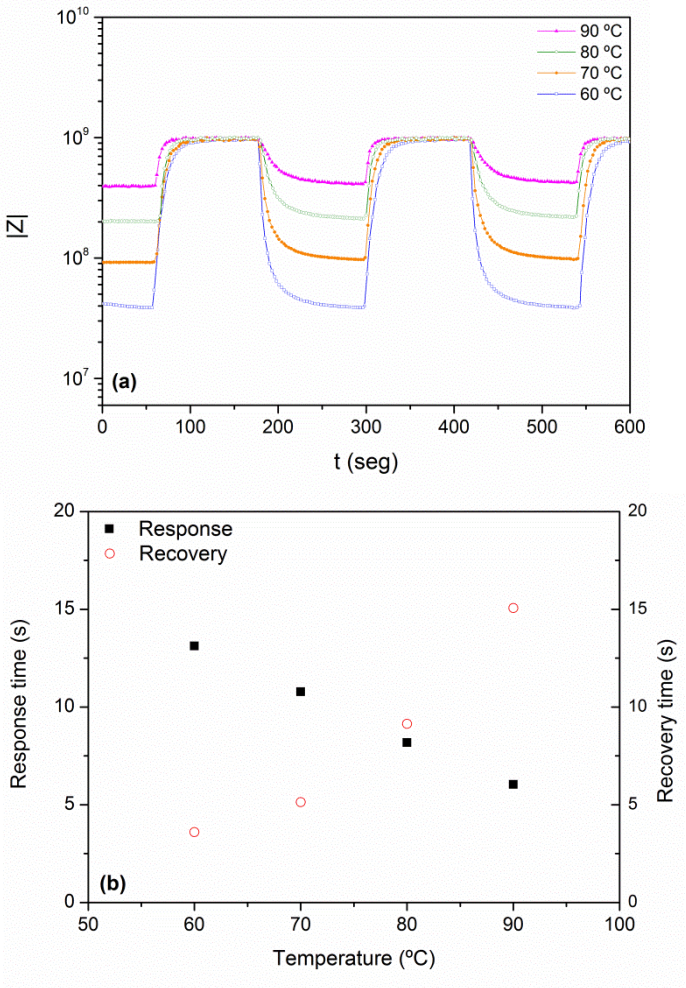

Figure 7.8. Response and recovery of the mesoporous CGO humidity sensor at 10 Hz and at different temperatures (T = 60, 70, 80 and 90ºC).

7.2.5. Effect of the thickness of the sensing layer

The influence of the thickness of the sensing layer was also investigated, with this purpose a thinner CGO mesoporous layer (thickness of ~ 4 μm) was deposited and measured, denoted as CGO-F (CGO-Fine layer). **Figure 7.9** shows a comparison of the response and the recovery time of the above presented CGO (layer thickness ~ 12-13 μm) and the CGO-F (layer thickness ~ 4 μm) mesoporous humidity sensors.

The thickness of the mesoporous layer has influence in both the sensitivity and the response/recovery. The explanation of the different sensitivity is also consistent according to the conduction mechanism and the number of adsorption sites in each sample. The higher resistance of CGO-F under dry conditions is explained by the different thicknesses of the films, the sensing layer of CGO-F is around three times thinner than the layer of the CGO sensor and therefore, the obtained resistance value (the measured resistance follows the equation $R = \rho \cdot l/A$, ($A = t \cdot H$) being ρ the resistivity of the material, l the length between contact electrodes, A the cross-sectional area, t the thickness and H the length of the of the sensing film).

On the other hand, higher thickness indicates more available adsorption sites and therefore, the amplitude of the response (ΔR) for the thicker layer sensor CGO is higher. Moreover, the measured resistance values are in agreement with the work presented by Shirpour et al. about the proton conductivity of pure and gadolinium doped nanocrystalline CeO_2 [22].

The time constants of CGO-F mesoporous sensor are calculated to be 5.6 and 3.2 seconds, compared to the values of 19.1 and 1.3 seconds of the thicker layer sensor. The quicker response for the thinner film and the quicker recovery for the thicker film is in agreement with previously reported results [9]. The thinner film presents a higher response rate, related with the shorter path that the H_3O^+ ions have to travel across the film and therefore, is more adequate for detecting humidity at low levels. On the other hand, the thicker film shows a lower recovery time related with the larger amount of

pores (higher number of adsorption places). Therefore, thicker films are more suitable for detecting high humidity concentrations.

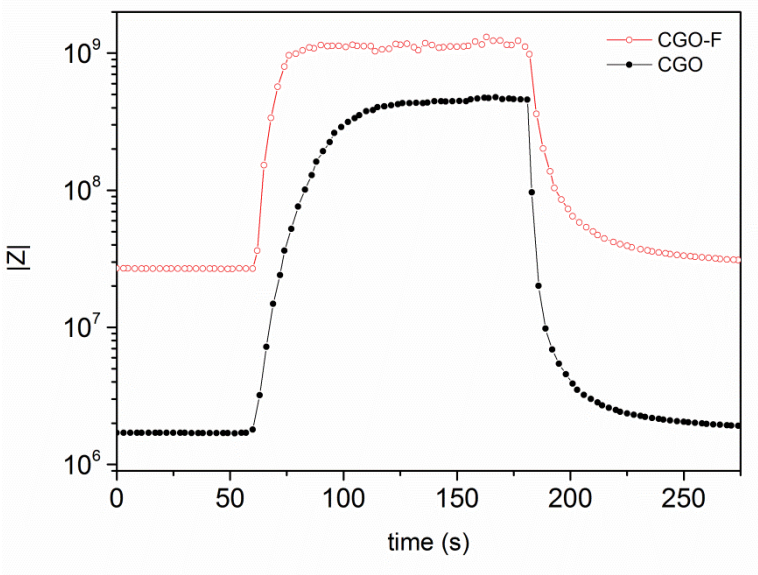

Figure 7.9. Response and recovery of the CGO and CGO-F humidity sensors at 10 Hz and T = 30 ºC.

7.2.6. Effect of the pore size

A big advantage of mesoporous materials is the possibility of tuning their pore size by modifying synthesis parameters. As explained in the experimental procedure of **Chapter 2** the pore size of the replicas of the KIT-6 silica template can be modified, by changing the hydrothermal temperature of the silica template and filling one (KIT-6-36) or two (KIT-6-90) of the interpenetrated channels.

To study the influence of the pore size in the humidity sensing properties, mesoporous CGO was also synthesized from KIT-6-36 (filling only one of the two sets of interpenetrated channels) and the fabricated sensor is denoted as CGO-D. A complete micro-structural characterization of a ceramic oxide synthesized by the same route (as replica of KIT-6-36) was presented in the **Chapter 5**.

The **Figure 7.10** shows a comparison of the response and recovery time between the CGO and CGO-D mesoporous humidity sensors. The time constants of the CGO-D

mesoporous sensor were calculated to be 15.5 and 0.98 seconds. Both response and recovery times are faster compared with the CGO sensor. The bigger pore size (over ~ 10 nm) of the CGO-D seems to have a positive influence in the dynamic response of the humidity sensors. The smaller pores of the sensor CGO (~ 3 nm) can limit the diffusion of the water molecules, reducing the rates of the adsorption-desorption processes. Differences shown in the resistance under dry conditions could be explained by the non-normalized thicknesses of both sensing layer. However the amplitude of the response (ΔR) is very similar for both sensors attributed to the similar surface area (BET) and therefore, similar number of adsorption sites of both sensors.

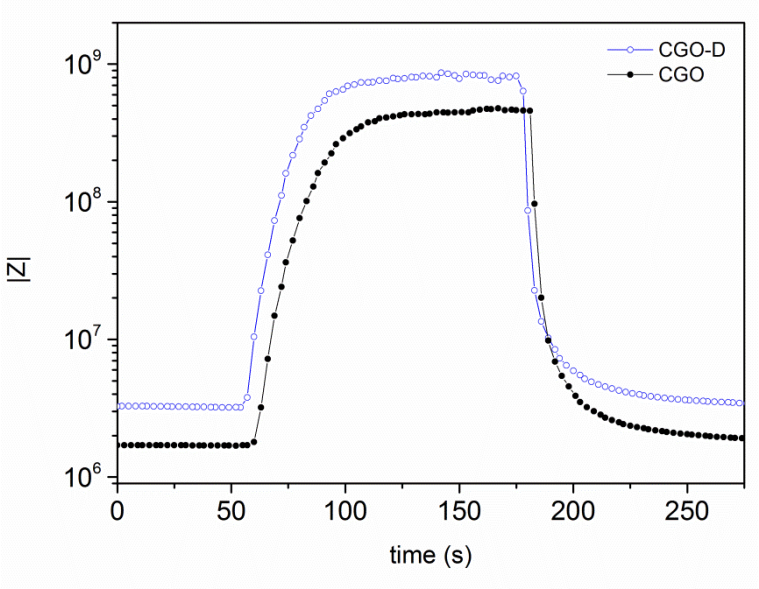

Figure 7.10. Response and recovery of the CGO and CGO-D mesoporous humidity sensors at f = 10 Hz and T = 30 ºC.

7.3. Conclusions

Mechanically robust mesoporous gadolinium-doped ceria (CGO) humidity sensors were fabricated by the attachment of the sensing layer at high temperatures (900 ºC) keeping the microstructure intact. The layers are stable to temperature cycles, the self-cleaning required in commercial ceramic sensors at high temperature could be performed

if required without detriment of the sensing properties. The resistance of the sensing film changes around four orders of magnitude within the measured humidity levels (0 - 2.4 % H_2O) at the selected optimum frequency (10 Hz) and the response and recovery times were 19.1 and 1.3 seconds, respectively. No drift was measurable during the 14 cycles of the dynamic response experiment performed. Maximum hysteresis was only ~ 0.1 % indicating very high reliability. Impedance spectra were analyzed and the parameters obtained from the fitting of the equivalent circuits verified an ionic type of conduction mechanism.

Moreover, the influence of temperature, thickness of the sensing layer and pore size were studied in order to check the consistency of the sensing mechanism and explore the possibility of adjusting sensing parameters to different applications. Higher temperatures imply higher mobility of ions and therefore, higher response and lower sensitivity and recovery. The thinner film sensor studied presents a higher response rate, although lower sensitivity, being suitable for measuring at low humidity levels, while the thicker film holds a higher recovery rate but also a higher sensitivity, being suitable for use at high humidity levels. Pore sizes over ~ 10 nm showed a faster response and recovery, while pore sizes over ~ 3 nm seem to limit the diffusion of the water molecules.

The CGO mesoporous sensors fulfilled all the required characteristics of high performance humidity sensors. Moreover, the synthesis route can be extrapolated to fabricate any other metal oxide.

References

[1] G. Korotcenkov, Handbook of Gas Sensor Materials, 1 (2013), Chapter 18, 389-404.

[2] B.J. Melde, B.J. Johnson, P.T. Charles, Sensors 8 (2008) 5202.

[3] A. Bearzotti, J.M. Bertolo, P. Innocenzi, P. Falcaro, E. Traversa, J. Eur. Ceram. Soc. 24 (2004) 1969.

[4] X. Liu, R. Wang, T. Zhang, Y. He, J. Tu, X. Li, Sensors Actuators B Chem. 150 (2010) 442.

[5] W. Zhang, R. Wang, Q. Zhang, J. Li, J. Phys. Chem. Solids 73 (2012) 517.

[6] W. Geng, R. Wang, X. Li, Y. Zou, T. Zhang, J. Tu, Y. He, N. Li, Sensors Actuators B Chem. 127 (2007) 323.

[7] W.C. Geng, L.B. Duan, Q.Y. Zhang, Appl. Mech. Mater. 249-250 (2012) 992.

[8] W. Geng, Q. Yuan, X. Jiang, J. Tu, L. Duan, J. Gu, Q. Zhang, Sensors Actuators B Chem. 174 (2012) 513.

[9] C.T. Wang, C.L. Wu, Thin Solid Films 496 (2006) 658.

[10] Q. Yuan, W. Geng, N. Li, J. Tu, R. Wang, T. Zhang, X. Li, Appl. Surf. Sci. 256 (2009) 280.

[11] L. Almar, T. Andreu, A. Morata, M. Torrell, L. Yedra, S. Estradé, F. Peiró, A. Tarancón, J. Mater. Chem. A 2 (2014) 3134.

[12] X.Q. Fu, C. Wang, H.C. Yu, Y.G. Wang, T.H. Wang, Nanotechnology 18 (2007) 145503.

[13] Z. Zhang, C. Hu, Y. Xiong, R. Yang, Z.L. Wang, Nanotechnology 18 (2007) 465504.

[14] C.H. Hu, C.H. Xia, F. Wang, M. Zhou, P.F. Yin, X.Y. Han, 34 (2011) 1033.

[15] Y.W. Hao, J. Wang, Z.Y. Chen, J. Mater. Sci. 45 (2009) 1361.

[16] E. Traversa, Sensors Actuators B Chem. 23 (1995) 135.

[17] T. Nenov, S. Yordanov, Sensors Actuators B Chem. 8 (1992) 117.

[18] B.M. Kulwicki, J. Phys. Chem. Solids 45 (1984) 1015.

[19] S. Pokhrel, K.S. Nagaraja, Sensors Actuators B Chem. 92 (2003) 144.

[20] N. Rezlescu, C. Doroftei, E. Rezlescu, P.D. Popa, Sensors Actuators B Chem. 115 (2006) 589.

[21] Z. Wang, L. Shi, F. Wu, S. Yuan, Y. Zhao, M. Zhang, Nanotechnology 22 (2011) 275502.

[22] M. Shirpour, G. Gregori, R. Merkle, J. Maier, Phys. Chem. Chem. Phys. 13 (2011) 937.

8
Conclusions

Imagination is more important than knowledge.
For knowledge is limited to all we know and understand,
while imagination embraces the entire world,
and all there ever will be to know and understand

- Albert Einstein

8. Conclusions

The work developed in this thesis was devoted to explore different strategies for stabilizing ordered mesoporous metal oxides and their implementation and evaluation in solid state devices, mainly Solid Oxide Fuel Cells (SOFCs) and gas sensors. Experimental, technological and theoretical aspects were covered to attain this purpose. The most relevant achievements are listed below,

Novel quasi-universal methods for the **thermal stabilization** of **ordered mesoporous metal oxides,**

- **Open 3-D nano-structures** were thermally stabilized up to temperatures of 1100 ºC which is significantly over the state-of-art of mesoporous materials (T ~ 500 - 750 ºC). Long term-stability was proved by reaching the self-limited grain growth regime, i.e. by the partial crystallization of the mesoporous oxide after a calcination step before the removal of the template. The catalytic activity and functionality of the ceria-based synthesized material was successfully demonstrated at these high temperatures over the time.
- **Compact 3D nano-structures** were thermally stabilized by a classical cermet approach up to temperatures of 1100 ºC, due to the excellent connectivity achieved by selectively filling both interpenetrated channels of the original silica template structure.

Suitability of mesoporous materials as **electrodes** for **Intermediate Temperature Solid Oxide Fuel Cells (IT-SOFCs),**

- Nickel based mesoporous cermets were implemented and tested as **anode for IT-SOFCs**. The optimized cells showed a target area specific resistance (ASR = 0.25 $\Omega \cdot cm^2$) required for electrodes in SOFC applications in the IT range at 675 ºC. Long-term stability was proved during 200 hours under humidified 5 % H_2 at 800 ºC, showing an improvement of 67.8 $\mu\Omega \cdot cm^2/h$, 32.4 % in the electrochemical performance and no micro-structural degradation.

- Mesoporous samaria-doped ceria (SDC) was synthesized and attached to the electrolyte below 1100 ºC, i.e. within the self-limited grain growth regime. The so-fabricated stable mesoporous ceramic scaffold was further infiltrated with a good catalyst with composition $Sm_{0.5}Sr_{0.5}CoO_{3-\delta}$ (SSC). The infiltrated composite was tested as cathode and the target ASR of 0.25 $\Omega \cdot cm^2$ was obtained at a temperature of 660 ºC for the optimized cell (T_{att} = 1000 ºC). A long-time impedance measurement performed at 700 ºC under ambient air for 230 hours, showed a performance improvement of 48.5 % to a stable and low value of 0.08 $\Omega \cdot cm^2$. Moreover, an equivalent circuit based on transmission lines was used to fit all the impedance spectra and their analogy with the Adler-Lane-Steele model developed for MIECs allowed understanding the different contributions and phenomena involved.

Fabrication and evaluation of **SOFCs** with **mesoporous electrodes** (under pure H_2 as fuel and synthetic air as oxidant),

- **SOFCs with mesoporous anodes,**
  - **Electrolyte supported fuel cells** with **mesoporous Ni-CGO** as anodes were measured as a proof-of-concept. A maximum power density of 514 mW/cm^2 at 850 ºC and 325 mW/cm^2 at 750 ºC was obtained.
  - **Anode supported fuel cells** (ideal configuration in the IT range) were fabricated using a developed **mesoporous Ni-YSZ** tape casting. A maximum power density of 690 mW/cm^2 at 650 ºC was attained, demonstrating the feasibility of using this type of mesoporous structures as high performance electrodes in the intermediate temperature range.
- **SOFCs with fully mesoporous electrodes** were fabricated as a combination of the above contributions. Mesoporous Ni-SDC as anode and SSC-infiltrated mesoporous SDC as cathode were fabricated and characterized for the first time. An electrolyte supported fuel cell configuration was chosen as it was supposed to be more stable and the aim was to study the evolution of the electrodes under real operational conditions. A maximum power density of 565 mW/cm^2 at

750 ºC was obtained, demonstrating an improvement of 74 % of our baseline cells. A long-term degradation experiment for more than 1000 hours under a constant current density of 635 $A \cdot cm^{-2}$ was successfully performed. The region 1 from 0 to 200 h, showed a degradation rate of 274 μV/h (9 %) and the second region of 57 μV/h (7 %). Impedance analysis performed under OCV conditions showed an increase of the ohmic series resistance (R_s) in the region 1 of 85 $\mu\Omega \cdot cm^2/h$ (6 %) and in the region 2 of 65 $\mu\Omega \cdot cm^2/h$ (21 %) and a surprising decrease of the polarization resistance (R_p) in the region 1 of -303 $\mu\Omega \cdot cm^2/h$ (6 %) and in the region 2 of -227 $\mu\Omega \cdot cm^2/h$ (20 %). The polarization overpotential followed an asymptotic growth and main changes occurred only during the first 70 hours, in contrast to the typically reported parabolic growth. The degradation rate due to the R_p after the stabilization period was calculated to be 0.032 % per 1000 hours, which is below the target proposed by the US Department of Energy's Solid State Energy Conversion Alliance (0.2 % per 1000 hours).

Finally, the **implementation and evaluation** of the synthesized ceramic oxides mesoporous materials as **humidity sensors** was presented.

- Mechanically robust **mesoporous CGO sensors** were fabricated due to the possibility of attachment at high temperatures, while keeping the micro-structure. The resistance of the sensing film changed four orders of magnitude with the humidity range. A quick response of 19.1 and recovery of 1.3 seconds no drift and no hysteresis were measured, fulfilling the required characteristics of high performance humidity sensors. Moreover, a strategy to optimize the thickness or the pore size was defined and quantified depending on the desired sensing properties, based on the different experiments performed.

Appendixes

The most exciting phrase to hear in science,
the one that heralds the most discoveries
is not Eureka! (I found it!) but That's funny…

- Isaac Asimov

Appendix A

Compositional optimization of mesoporous nickel based cermets for SOFCs

A. Compositional Optimization of Mesoporous Nickel based Cermets for SOFCs

A.1. Structural characterization of symmetrical cells of Ni-CGO mesoporous cermets with different nickel content 217

A.2. Electrochemical performance of Ni-CGO mesoporous anodes 219

References 221

A. Compositional Optimization of Mesoporous Nickel based Cermets for SOFCs

A.1. Structural characterization of symmetrical cells of Ni-CGO mesoporous cermets with different nickel content

Porous nickel based cermets are the state-of-art anode material for SOFCs. The percolation threshold for the electronic conductivity of the cermets is around 30 % volume of nickel, above this value the conductivity of the cermets increases around three orders of magnitude, while below it shows a predominant ionic conductivity [1].

However, the percolation threshold is influenced by multiple factors e.g. porosity, sintering temperature, particle size and size distribution of the raw powders. Optimizing the composition of the mixture (metal and ceramic) has been proved as an effective way to minimize both activation and concentration polarizations [2,3].

In this appendix, a study devoted to lower the polarization resistance by compositional optimization of the fabricated mesoporous cermets characterized in **Chapter 4** is presented. **Figure A.1** shows a basic scheme of the three symmetrical cells (Ni-CGO/CGO/Ni-CGO) fabricated by air brushing following the procedure described in **section 2.3.2**. Cells with mesoporous NiO-CGO ratios of: 50 wt % (Ni-CGO(50)), 65-35 wt % (Ni-CGO(65)) and a dual electrode layer composed with 50 wt % close to the electrolyte (catalytic active layer) and 65-35 wt % close to the current collector (Ni-CGO(50-65)) were fabricated and electrochemically tested.

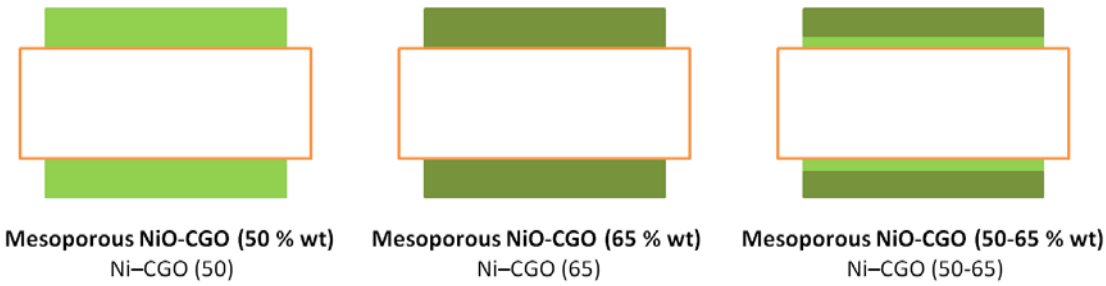

Figure A.1. Scheme of the symmetrical cells fabricated and electrochemical tested, namely: Ni-CGO(50), Ni-CGO(65) and Ni-CGO(50-65).

Figure A.2 shows the anode/electrolyte cross section of the three different symmetrical cells after the nickel reduction. The backscatter images (BSE) **Figure A.2 a, b** and **c**) allows identifying the regions where either the concentration of nickel (darker) or CGO (lighter) is higher. All symmetrical cells show a fine structure and homogeneous structure with Ni and CGO phases intimately mixed and no coarse grains. More in detail, **Figure A.2c** and **d** show the cell with double layer electrode Ni-CGO(50-65), in the BSE image the two layers can thus be distinguished. The catalytic active layer NiO-CGO (50 % wt) has a thickness of ~10 μm and the current collector layer NiO-CGO (65 % wt) of ~ 20μm.

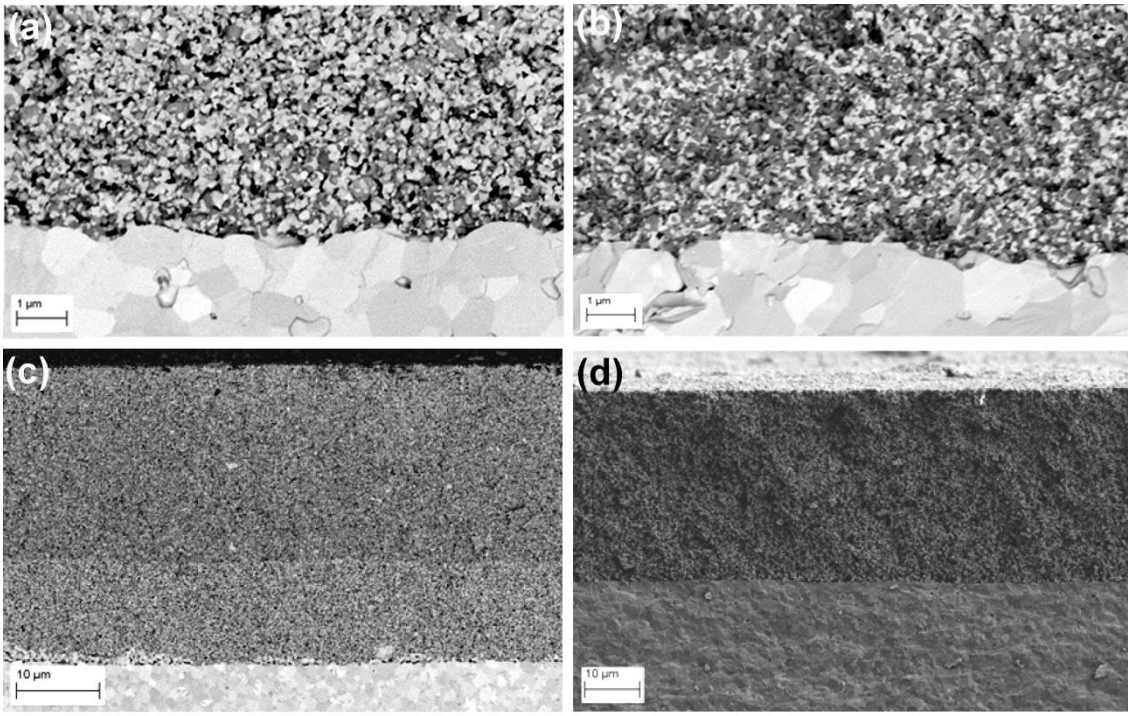

Figure A.2. Cross-sectional view of mesoporous Ni-CGO anodes. (a) BSE image of Ni-CGO(50), (b) BSE image of Ni-CGO(65), (c) BSE image of Ni-CGO(50-65) and (d) SE image of Ni-CGO(50-65).

A.2. Electrochemical performance of Ni-CGO mesoporous anodes

Figure A.3a shows the equivalent circuit used to fit the spectra obtained from the impedance measurements. The symmetrical cells with different nickel content were tested under wet 5 % H_2 in the temperature range (600 - 900 ºC).

In this section, the EIS spectra were analyzed by the same equivalent circuit $LR_s(RQ)_{HF}(RQ)_{LF}$ for all the temperature range, where L is an inductance, R is a resistance and Q a constant phase element. The subscripts HF and LF stand for the high and low frequency contributions. The resistance in series (R_s) is related to the electrolyte and current collection while R_{HF} and R_{LF} are due to the electrode polarization.

An analysis of the exponents of the constant phase elements (Q) is required to identify the different phenomena occurring in the electrodes. The arc at high frequencies is likely associated to charge transfer phenomena since the order of magnitude of the exponent of these constant phases is 10^{-5}-10^{-6} F/cm^2.

On the other hand, the low frequency arc shows orders of magnitude of the exponent of its constant phases around 10^{-2}-10^{-3} F/cm^2. This value suggests that non-charge transfer processes are dominating the electrochemical behavior in this range of frequencies. Non-charge transfer involves processes like gas diffusion across the electrodes or oxygen surface exchange processes. The Nyquist plot at 650 ºC of two symmetrical cells tested as anodes Ni-CGO(65) and Ni-CGO(50-65) are shown in **Figure A.3b** and **Figure A.3c**, respectively.

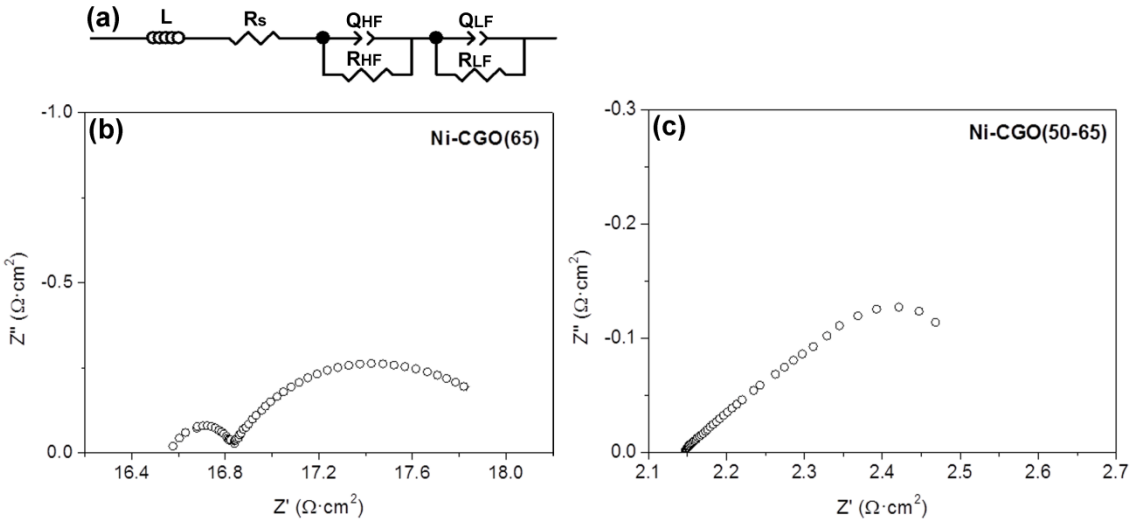

Figure A.3. (a) Equivalent circuit used to analyze all the impedance spectra generated. (b,c) Nyquist plots of the electrode contribution to the impedance spectra of the symmetrical cells Ni-CGO(65) and Ni-CGO(50-65), respectively measured at 650 ºC under water vapor saturated 5 % H_2.

Figure A.4 shows the evolution of the total anode/electrolyte interfacial area-specific resistance (ASR = R_{HF} + R_{LF}) for the three symmetrical cells tested the Ni-CGO(50), Ni-CGO(65) and Ni-CGO(50-65) in the 600-900 ºC temperature range. The activation energy obtained from the Arrhenius equation is presented in the legend of the figure. The calculated activation energies are similar E_a = 2.0(1) eV for the Ni-CGO(50), E_a = 1.5(1) eV for Ni-CGO(65) and E_a = 1.6(1) eV for Ni-CGO(50-65) cells.

As mentioned other sections of the thesis, in terms of SOFC applications the electrode/electrolyte interface should not contribute more than 0.25 Ω·cm^2 to the total fuel cell area-specific resistance [4]. This target value is obtained at ca. 822 ºC for Ni-CGO(50), 752 ºC for Ni-CGO(65) and 672 ºC for Ni-CGO(50-65). According to the figure, the cell showing the lowest polarization resistance and therefore the **optimum compositional mixture** is the cell with **mesoporous dual layer Ni(50-65)**.

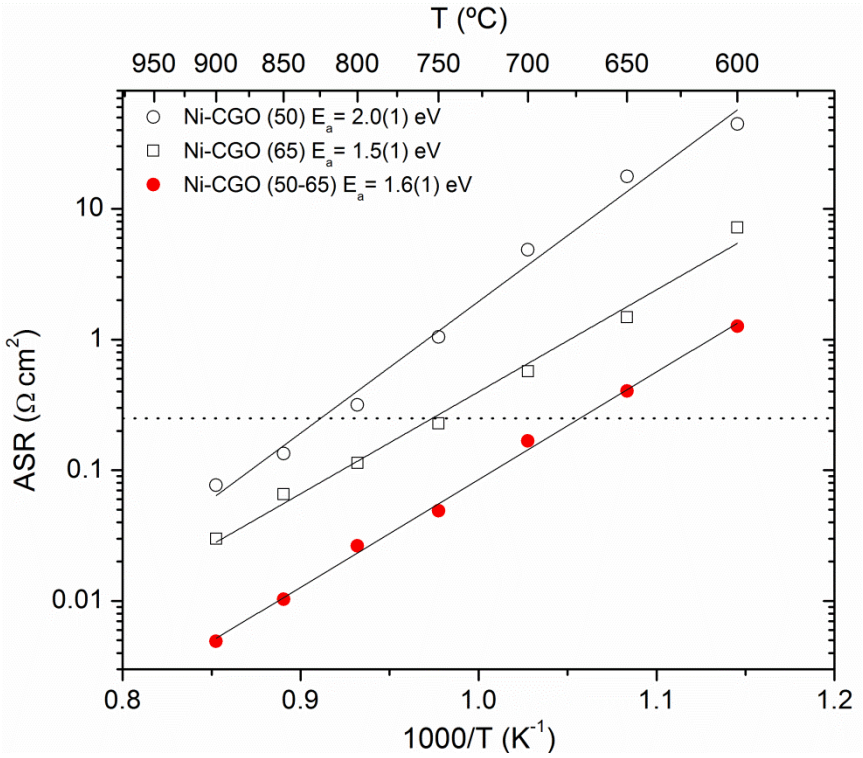

Figure A.4. Arrhenius plot of the anode/electrolyte total interfacial resistance of the symmetrical cells (Ni-CGO(50) (black circles), Ni-CGO(65) (black squares) and Ni-CGO(50-65) (red circles)) measured under wet 5 % H_2 between 900-600 ºC.

References

[1] D.W. Dees, T.D. Claar, D.C. Fee, J. Electrochem. Soc. 134 (1987) 2141.

[2] W.Z. Zhu, S.C. Deevi, Mater. Sci. Eng. A 362 (2003) 228.

[3] A. Virkar, Solid State Ionics 131 (2000) 189.

[4] N.P. Brandon, S. Skinner, B.C.H. Steele, Annu. Rev. Mater. Res. 33 (2003) 183.

Appendix A.

Appendix B

Lowering the sintering temperature of bi-layer electrolytes for anode-supported IT-SOFCs

B. Lowering the Sintering Temperature of Bi-layer Electrolytes for Anode-supported IT-SOFCs

B.1. Requirements and fabrication concerns of anode-supported cells 227

B.2. Fabrication and structural characterization of bi-layer electrolytes for anode-supported IT-SOFCs 228

B.2.1. Particle size distribution 228

B.2.2. Sintering aid 229

B.3. Fuel cells performance 233

B.4. Conclusions 234

References 235

B. Lowering the Sintering Temperature of Bi-layer Electrolytes for Anode-supported IT-SOFCs

B.1. Requirements and fabrication concerns of anode-supported cells

The Solid Oxide Fuel Cells field is not limited to the research of a new class of high performance materials at the laboratory scale. In fact for the industry, the assembly of the different components of a SOFC is a critical step and its standardization and optimization gives enormous advantages in terms of performance.

The fabrication of thinner electrolytes is one of the most employed approaches to decrease the operation temperature of the SOFCs [1,2]. However the thinner is the electrolyte, the lower is the mechanical resistance of the fabricated cells. The first SOFC designs were based in electrolyte supported cells, although as the efforts to lower the operational temperature increased, anode supported cell configuration became more and more popular. A summary of the most relevant advantages / disadvantages of the electrolyte *vs* anode supported cell configuration are presented in **Table B.1**,

Table B.1. Pros and cons of the most common SOFC configurations.

Configuration	Pros & Cons
Electrolyte-supported cell	✓ Mechanical strength of the structure ✓ Less susceptible to anode re-oxidation ✘ High resistance associated to lower conductivity of the electrolyte ✘ High temperatures required (due to high ohmic resistance)
Anode-supported cell	✓ Highly conductive anode ✓ Lower operation temperature (thinner electrolyte) ✘ Possible anode re-oxidation and thus cracks in the microstructure ✘ Limited mass transport (thicker anode)

The next-generation of SOFCs (T < 600 ºC) are expected to broad the commercialization applications, still have to deal with a lot of challenges i.e. avoid materials reaction and interdiffusion, keeping the microstructure with the time while minimizing costs and complex fabrication processes, etc.

Ceria is the usual choice as electrolyte when lowering the operating temperature although it usually gives lower open circuit voltage (OCV) due to its partial reduction upon exposure to a reducing atmosphere (anode side). If a thin layer of zirconia is applied, the usually required high sintering temperature to densify the ceria (T ~ 1400 ºC) leads to a high ohmic resistance, because of the formation of an interdifussed layer between the zirconia and the ceria with lower conductivity [3].

Another approach consists in fabricating a double layer electrolyte or a ceria based diffusion barrier layer. Albeit the success reached with ceria diffusion barriers, this implies an additional sintering step and often involves a quite expensive deposition technique to obtain good results e.g. physical vapor deposition or pulsed laser deposition.

In this appendix, a bi-layer zirconia/ceria electrolyte is fabricated by employing a single co-sintering step at 1200 ºC. The main challenge is to densify the ceria based layer (SDC) at this lower temperature, thus different methods were attempted and discussed (i) engineering the precursor particle size with combination of different raw powders and (ii) addition of transition metal oxides as sintering aids.

B.2. Fabrication and structural characterization of bi-layer electrolytes for anode-supported IT-SOFCs

B.2.1. Particle size distribution

Standard and optimized anode-supported cells from *Meilin Liu's Group* (MSE, Georgia Institute of Technology) were used in the present chapter. Cells were based on Ni-YSZ (55-45 % wt) tape casting supports, a Ni-YSZ (1:1 % wt) anode functional layer (AFL) applied by drop coating to match adjust the shrinkage between the

anode-electrolyte, the bi-layer SSZ-SDC ($(Sc_2O_3)_{0.10}(ZrO_2)_{0.90}$ - $Sm_{0.20}Ce_{0.80}O_{2-x}$) electrolyte and a brushed SDC-SSC cathode.

The SSZ-SDC bi-layer electrolyte was drop coated on the top of the anode functional layer and sintered in a single step at 1200 ºC for 5 h. The volume of the colloidal suspensions was adjusted in order to have a target SSZ/SDC electrolyte thickness of ~ 2 / 4-5 μm (estimated by cross-sectional SEM analysis). As explained above in order to densify the electrolyte layer at this low temperature, different kinds of SDC powders were evaluated. **Table B.2** shows the different fabricated cell batches, relevant characteristics about pre-/co- sintering conditions, thickness ratio of SSZ/SDC, description of SDC powder sources and acronyms further used.

As shown in **Table B.2** apart from SDC commercial powders (i.e. Standard, Middle (Mid) Grad and Nanopowder (Nextech)) $Sm_{0.2}Ce_{0.8}O_{1.9}$ (SDC) was synthesized via glycine–nitrate process (GNP). GNP SDC demonstrated high sinterability in a previous group's work which best suits for the preparation of dense, thin film electrolytes [4]. Briefly, stoichiometric amounts of the precursors were dissolved in distilled water until forming a clear solution, in which glycine was added as complexing agent, with glycine : nitrate ratio ~ 1.9. The stirred solution was heated on a hotplate till the self-sustaining combustion. The resulted ashes were calcined at 600 ºC for 2 h to form the crystalline SDC phase.

B.2.2. Sintering aid

Another approach was followed by the addition of metal oxides as sintering aids. Cobalt oxide was our first choice, since previous studies have shown that they can effectively reduce the densification temperature without affecting the ionic conductivity [5,6]. For Co - Std SDC the Co nitrate was directly ball-milled with the commercial standard powder, to obtain 2 mol % of Co after drop coating and sintering at 1200 ºC. An alternative approach was to introduce the cobalt into pre-calcined GNP SDC at 300 ºC via a wet impregnation process and further calcined together at 600 ºC [7].

Table B.2. Cells fabrication parameters and description of SDC powder sources.

Cell Batch #	Pre-/co-sintering conditions	Thickness ratio SSZ/SDC	Acronym	SDC powder mixture composition			
				Low A_{spec} / Source	High A_{spec} / Source	wt % ratio	Sintering Aid
1	850 ºC for 2 h /1200 ºC for 5 h	8 µm / 8-9 µm	**Std SDC**	10 m^2/g / Standard Grad (Nextech)	---	---	---
2		4-5 µm / 8-9 µm	**Mid SDC**		40 m^2/g / Mid Grad (Nextech)	75 / 25	---
3		3 µm / 4-5 µm	**Nano SDC**		220 m^2/g / Nanopowder (Nextech)		---
4		~ 2 µm / 4-5 µm	**GNP SDC**		GNP SDC		---
5		~ 1.5 µm / 4-5 µm	**Co - Std SDC**		---	---	2 % mol Co
6		2 µm / 4-5 µm	**Co - GNP SDC**	GNP SDC	---	---	2 % mol Co

Figure B.1 shows the cross-section image of the double layer electrolyte SSZ-SDC of different cells namely (1) Std SDC, (2) Mid SDC, (3) Nano SDC, (4) GNP SDC (5) Co - Std SDC and (6) Co - GNP SDC. The SSZ (bottom) layer is denser than the SDC layer for all the fabricated cells. In order to densify the SDC layer, the addition of powder with more specific surface area (A_{spec}) was used as first attempt, although it was not enough to promote substantial densification and porosity reduction (**Figure B.1b**).

On the other hand, addition of powder with nanometer size improves the sinterability, due to a larger driving force of densification at lower co-firing temperatures and by filling the pores between the bigger grains of the standard powder (**Figure B.1c**). This effect can explain the morphology observed with compact microstructure but not well-connected particles, it should be mentioned that EDX showed no evidence of impurities or phase segregation, as only stoichiometric SDC was found.

The use of GNP SDC powder as sintering agent (**Figure B.1c**), showed no advantage as a porous SDC microstructure was obtained, the low apparent density characteristic of this type powder joined to the absence of high compaction pressure may be the reason of the differences in morphology and porosity, as compared to the previous group's work [8].

Adding a sintering aid in a limited amount (1-2 % mol) promotes the grain growth of doped ceria at initial stages of sintering [9]. **Figure B.1e** shows the first attempt, adding the sintering aid (Co) in form of nitrates to commercial standard SDC powder and directly ball-milling. Even though the sintered SDC layer is less porous compared to the one without sintering aid, it still showed some porosity. It should be noticed here that the slurry of this cell was inhomogeneous and therefore, the density of the SDC layer.

Figure B.1f shows cross-section of the bi-layer fabricated by adding the precursor of the sintering aid added in a previous calcination step in order to improve the homogeneity and dispersivity. With this optimized approach, a rather uniform and dense SDC layer with ~ 4 μm thickness was obtained due to the faster shrinkage rate introduced by homogeneously dispersed fine Co_2O_3 particle in the GNP SDC powder (XRD analysis confirmed the pure single cubic phase of the SDC, not presented here).

Appendix B.

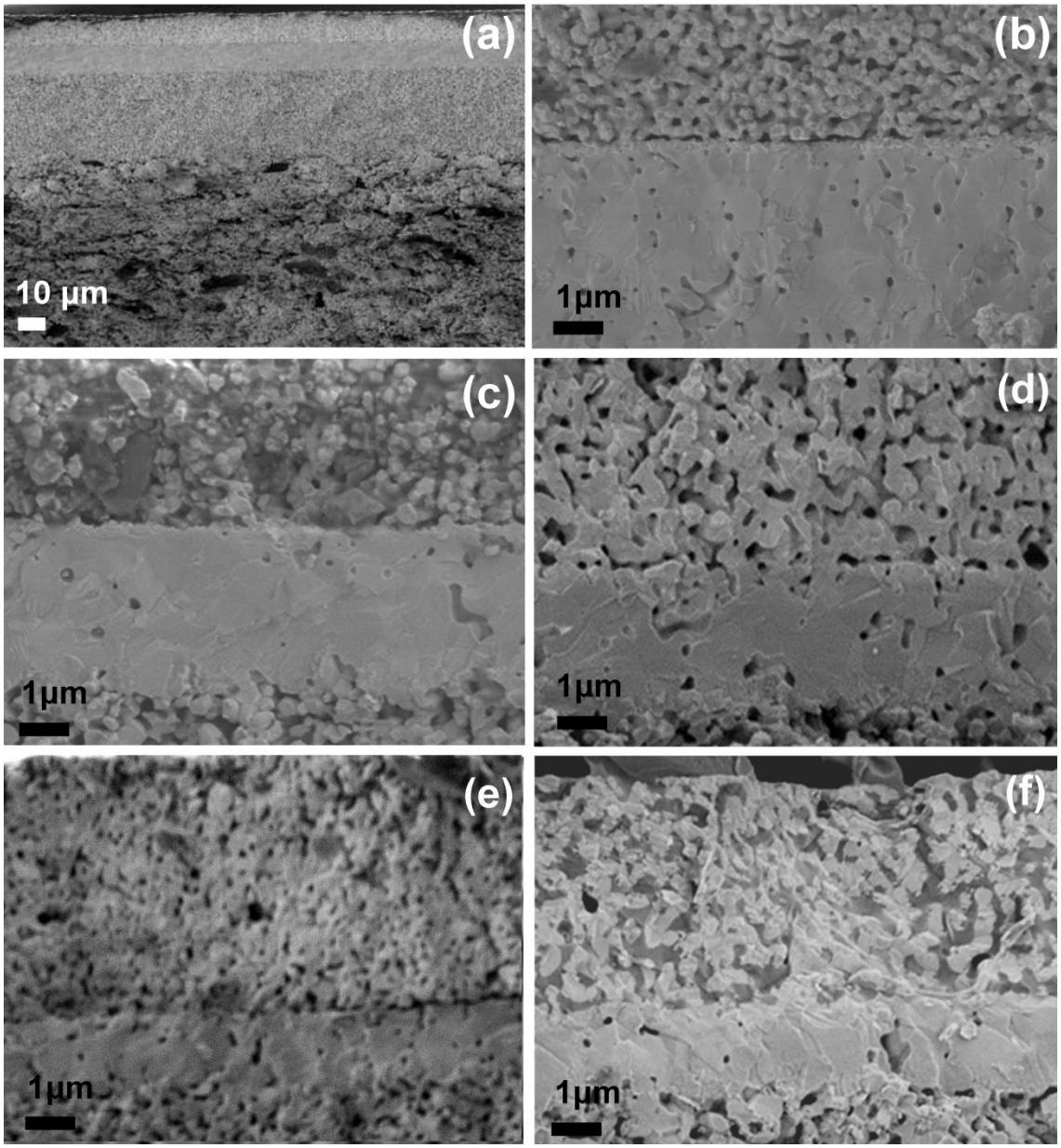

Figure B.1. Cross-sectional image of the SSZ-SDC double layer electrolyte made with different SDC powders (upper layer) after a single step sintering at 1200 ºC (a) Std SDC, (b) Mid SDC, (c) Nano SDC, (d) GNP SDC (e) Co - Std SDC and (e) Co - GNP SDC.

B.3. Fuel cells performance

The electrochemical performance of the cells 1-4 and cell 6 was tested at 650 ºC under hydrogen as fuel and ambient air as oxidant (**Figure B.2**). The cell 5 (Co - Std SDC) could not be tested due to the presence of several cracks (leaks) attributed to the above explained bad dispersivity of the cobalt nitrate in the colloidal slurry.

Regarding the other cells a maximum power density of: 210 mW/cm^2 for the Std SDC, 495 mW/cm^2 for Mid SDC, 600 mW/cm^2 GNP SDC, 685 mW/cm^2 Co-GNP SDC and 730 mW/cm^2 for Nano-SDC was obtained. The cell performance is in agreement with the densification and porosity of the SDC analyzed in the cross-sectional SEM study.

On the other hand, the lowest performance of the cells Std SDC and Mid SDC is more likely explained by the thicker SSZ layer (8 μm and 4-5 μm, respectively), before the optimization of the layer thickness, explaining also the highest OCV obtained for the Std SDC cell (1.04 V) which drops to 1.00 V with the decrease of the SSZ thickness, due to the electron blocking effect of the zirconia layer. Further decrease to 2-3 μm does not lead to apparent change of the OCV value.

Nano-SDC and Co-doped SDC cells lead to a considerable higher performance, attributed to the beneficial effects of adding nanopowder or well-dispersed sintering aid on improving the sinterability of the SDC electrolyte.

Albeit the best performance obtained for the cell made by adding nano-powder, a drop of the maximum power density was observed for further cells obtained with the same SDC slurry with the time i.e. from the initial 730 mW/cm^2, to 640 mW/cm^2 after one month and 350 mW/cm^2 after two months (IV-curves not presented here). This result is attributed to a worse dispersivity or deposition of the nanopowder in the slurry with the time.

Very recently Barnett et al. have been published a work on the reduced-temperature firing of SOFCs with zirconia-ceria layers [10]. They proved the densification of the electrolyte bi-layer, co-fired in a single step at 1250 ºC by the addition of Fe_2O_3 as sintering aid. The fabrication of the cells were performed by the same techniques by

depositing the layers from a colloidal solution and a maximum power density of ~ 480 mW/cm^2 at 650 ºC was measured. The comparisons with our results further confirm the high performance of the here-fabricated cells at even lower co-firing temperatures.

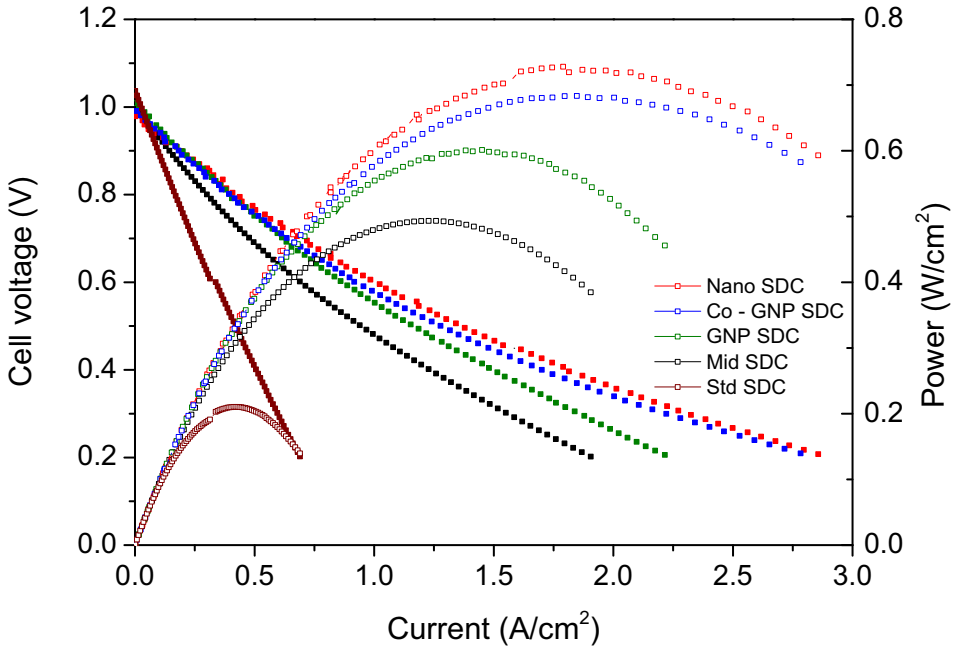

Figure B.2. Cell voltage and power density as a function of the current density for anode supported cells fabricated using different strategies to densify the SDC layer electrolyte at 650 ºC under pure hydrogen as fuel and ambient air as oxidant.

B.4. Conclusions

This appendix shows the successful fabrication of high performance IT-SOFCs by a single sintering step of the electrolyte at 1200 ºC, which is 200 ºC lower than the typical sintering temperature. Addition of nanometer size powder and doping with Co_2O_3 are efficient approaches for improving the sinterability of the SDC layer at this lower co-firing temperature. However, the colloidal suspension of Co-doped SDC is noticed to be much more stable and can be stored for extended fabrication.

The fabricated cells present other advantages since the reduced sintering temperature avoids the interdiffusion between ceria-zirconia yielding high fuel cell performance and the dense SDC layer acts as a barrier layer preventing Sr-diffusion from the cathode. Moreover, the fabrication of these high performance cells only involves inexpensive and reproducible deposition techniques.

References

[1] A. Tarancón, Energies 2 (2009) 1130.

[2] E.D. Wachsman, K.T. Lee, Science 334 (2011) 935.

[3] J. Peña-Martínez, D. Marrero-López, C. Sánchez-Bautista, A.J. Dos Santos-García, J.C. Ruiz-Morales, J. Canales-Vázquez, P. Núñez, Bol. Soc. Esp. Ceram. 49 (2010) 15.

[4] Z. Liu, D. Ding, M. Liu, X. Ding, D. Chen, X. Li, C. Xia, M. Liu, J. Power Sources 241 (2013) 454.

[5] G.S. Lewis, A. Atkinson, B.C.H. Steele, J. Mater. Sci. Lett. 20 (2001) 1155.

[6] D.P. Fagg, J.C. Abrantes, D. Pérez-Coll, P. Núñez, V.V. Kharton, J.R. Frade, Electrochim. Acta 48 (2003) 1023.

[7] D. Perez-Coll, P. Nuñez, J. Abrantes, D. Fagg, V. Kharton, J. Frade, Solid State Ionics 176 (2005) 2799.

[8] Z. Liu, D. Ding, M. Liu, X. Li, W. Sun, C. Xia, M. Liu, J. Power Sources 229 (2013) 277.

[9] X. Zhang, C. Decès-Petit, S. Yick, M. Robertson, O. Kesler, R. Maric, D. Ghosh, J. Power Sources 162 (2006) 480.

[10] Z. Gao, D. Kennouche, S. a. Barnett, J. Power Sources 260 (2014) 259.

Appendix B.

Appendix C

Transmission lines based equivalent circuit analogous to Adler-Lane-Steele model for MIECs

C. Transmission Lines based Equivalent Circuit Analogous to Adler-Lane-Steele Model for MIECs

The present study describes an equivalent circuit model based on transmission lines applied by Bisquert et al. in liquid electrochemistry [1] and the complete analogy between it and the analytical Adler-Lane-Steele (ALS) model [2]. The present Appendix C forms part of the derived equivalent circuit developed for non-charge transfer processes presented in the thesis of Dr. Albert Tarancón [3].

For cathodes and in particular for mixed ionic electronic conductors (MIEC) the Adler-Lane-Steele (ALS) model is commonly used [2]. *Adler et al*. defined a simple expression to quantify the impedance associated to the non-charge transfer processes (*i.e.* solid-state diffusion, surface exchange and gas-phase diffusion). Traditionally, these effects have been incorporated to the classical circuits in the form of modified charge-transfer processes or series or parallel combination of them, however, this model shows that the contribution to the total impedance of the non-charge-transfer processes take place in a convoluted manner. The expression for the non-charge transfer contribution (Z_{chem}) in the limit of a semi-infinite electrode, with no gas-phase diffusion limitations, is defined as follows:

$$Z_{nct} = \frac{R_{chem}}{\sqrt{1 + j\omega t_{chem}}} \qquad \textbf{(C.1)}$$

where R_{chem} and t_{chem} are the characteristic chemical resistance and the time constant of the chemical process, respectively. Both parameters are related to fundamental parameters as follows,

$$R_{chem} = \frac{RT}{2F^2}\sqrt{\frac{\tau}{a(1-\varepsilon)}\frac{1}{C_v D_v}\frac{1}{r_0(\alpha_f + \alpha_b)}} \qquad \textbf{(C.2)}$$

$$t_{chem} = \frac{(1-\varepsilon)}{a}\frac{C_v}{A}\frac{1}{r_0(\alpha_f + \alpha_b)} \qquad \textbf{(C.3)}$$

All the nomenclature and the associated physical magnitudes for the symbols used in the previous expressions are listed below (*taken from Adler et al.* [2]),

τ	tortuosity of the solid phase	
ε	porosity	
C_v	vacancy concentration	
D_v	vacancy diffusion coefficient	
a	surface area	
A	thermodynamic factor	$A = -\frac{1}{2}\,\partial\ln(pO_2)\partial\ln(C_v)$
T	temperature	
r_0	exchange neutral flux density	
α_f,α_b	constants-exchange reaction mechanism	
R	gas law constant	
F	Faraday constant	

Therefore, being possible to define the chemical capacitance (C_{chem}) associated to changes of oxygen stoichiometry in the MIEC. Moreover, it should be pointed out that since MIEC electrodes are not confined to an interface, the values of C_{chem} can be much larger than the typical interfacial capacitances [2],

$$C_{chem} \equiv \frac{t_{chem}}{R_{chem}} = \frac{2F^2}{RT}\frac{C_v}{A}(1-\varepsilon)\delta = \frac{2F^2}{RT}\frac{C_v}{A}(1-\varepsilon)\sqrt{\frac{1-\varepsilon}{a}\frac{C_v D_v}{r_0(\alpha_f+\alpha_b)\tau}} \qquad \textbf{(C.4)}$$

The equivalent circuit based in transmission lines [1], is formed by a single resistance in one of the channels and a parallel *RQ* (*Q*: constant phase element (CPE)) circuit at the crosswise element. The transmission line circuit is depicted in **Figure C.1,** showing impedance given by:

$$Z_{TL} = \frac{\sqrt{R_1 R_3}}{\sqrt{1+j\frac{\omega}{\omega_3}}}\coth\left[\left(\frac{\omega_3}{\omega_L}\right)^{1/2}\left(1+j\frac{\omega}{\omega_3}\right)^{1/2}\right] \qquad \textbf{(C.5)}$$

where,

$$\omega_3 = \frac{1}{R_3 C_3} \qquad \textbf{(C.6)}$$

$$\omega_L = \frac{1}{R_1 C_3} \qquad \textbf{(C.7)}$$

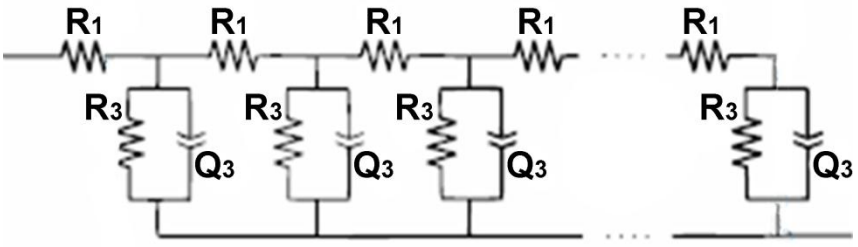

Figure C.1. Equivalent circuit based on transmission lines used to fit the impedance spectra in Chapter 5.

For the particular limiting situation when $R_1 > R_3$, the **expression (C.5)** is simplified to the following equation:

$$Z(R_1 > R_3) = \frac{\sqrt{R_1 R_3}}{\sqrt{1 + j\frac{\omega}{\omega_3}}} \quad \textbf{(C.8)}$$

Comparing the ALS analytical **expression (C.1)** defined for non-charge transfer process contributions and the **expression (C.8)** which defined the impedance of the transmission line for our particular situation, it is straightforward to obtain the formal equivalence between the ALS model and the here employed equivalent circuit based on transmission lines as follows:

$$R_{chem} = \sqrt{R_1 R_3} \quad \textbf{(C.9)}$$

$$C_{chem} = C_3 \sqrt{\frac{R_3}{R_1}} \quad \textbf{(C.10)}$$

Thus, for the particular situation when R_1 is higher than R_3, the here-proposed equivalent circuit is completely analogous to the ALS-model developed for MIEC electrodes.

References

[1] J. Bisquert, Phys. Chem. Chem. Phys. 2 (2000) 4185.

[2] S.B. Adler, J.A. Lane, S.B.C. H, J. Electrochem. Soc. 143 (1996) 3554.

[3] A. Tarancón, PhD Thesis. Strategies for Lowering Solid Oxide Fuel Cells Operating Temperature, University of Barcelona, 2007.

[4] B.A. Boukamp, H.J.M. Bouwmeester, 157 (2003) 29.

[5] B. Boukamp, M. Verbraeken, D. Blank, P. Holtappels, Solid State Ionics 177 (2006) 2539.

Appendix C.

Scientific Contributions

Publications

1. *High-surface-area ordered mesoporous oxides for continuous operation in high temperature energy applications*; L. Almar, T. Andreu, A. Morata, M. Torrell, L. Yedra, S. Estradé, F. Peiró and A. Tarancón, Journal of Materials Chemistry A 2 (2014) 3134-3141. Impact Factor J. Materials Chemistry (1991-2012) 6.101.

2. *High-temperature long-term stable ordered mesoporous Ni–CGO as an anode for solid oxide fuel cells*; L. Almar, B. Colldeforns, L. Yedra, S. Estradé, F. Peiró, A. Morata, T. Andreu and A. Tarancón, Journal of Materials Chemistry A 1 (2013) 4531-4538. Impact Factor J. Materials Chemistry (1991-2012) 6.101.

3. *$La_{2-x}Sr_xCoO_{4-d}$ (x = 0.9, 1.0, 1.1) Ruddlesden-Popper-type layered cobaltites as cathode materials for IT-SOFC application*; Y. Hu, Y. Bouffanais, L. Almar, A. Morata, A. Tarancon, G. Dezanneau, International journal of hydrogen energy 38 (2013) 3064-3072. Impact Factor 3.548.

Ongoing publications

1. *Mesoporous Ceramic Oxides as Humidity Sensors: a Case Study for Gadolinium doped ceria*; L. Almar, A. Morata, T. Andreu, M. Torrell, Y. Hu, G. Dezanneau and A. Tarancón.

2. *Infiltrated Mesoporous Composites as a Cathode for IT-SOFCs;* L. Almar, M. Gong, D. Ding, T. Andreu, M. Liu, A. Tarancón.

3. *Performance and Stability of Fully Mesoporous Electrodes Fuel Cells.* L. Almar, A. Morata, T. Andreu, A. Tarancón.

Conference proceedings

1. *Novel Ordered Mesoporous Architectures for Highly Stable Electrodes in Solid Oxide Cells.* L. Almar, T. Andreu, A. Morata, M. Torrell, R. Campana and A. Tarancón. Accepted for publication in Proceedings of the 11th European SOFC and SOEC Forum (July 2014).

2. *Catalytic hydrogen micro-combustor for SOFC Portable Applications.* D. Pla, L. Almar, G. Gadea, A. Morata and A. Tarancón. Accepted for publication in Proceedings of the 11th European SOFC and SOEC Forum (July 2014).

3. *High Temperature Long-Term stable ordered mesoporous electrodes for IT-SOFC*; L. Almar, M. Torrell, A. Morata, L. Yedra, S. Estradé, F. Peiró, T. Andreu and A. Tarancón, accepted for publication in Proceedings of the 38th Int'l Conf & Expo on Advanced Ceramics & Composites (ICACC 2014).

4. *High Electrochemical Performance of Mesoporous NiO-CGO as Anodes for IT-SOFC.* L. Almar, B. Colldeforns, L. Yedra, S. Estradé, F. Peiró, T. Andreu, A. Morata and A. Tarancón. Proceedings of the 10th European SOFC and SOEC Forum 13, B04 (2012) 195-203.

5. *High Electrochemical Performance of Mesoporous NiO-CGO as Anodes for IT-SOFC*; L. Almar, T. Andreu, A. Morata and A. Tarancón, ECS Transactions 35(1) (2011) 1647-1654.

Conferences

1. *Ordered Mesoporous cermets as anodes for intermediate temperatures Solid Oxide Fuel Cells*. L. Almar, M. Torrell, A. Morata, L. Yedra, S. Estradé, B. Colldeforns, F. Peiró, T. Andreu, and A. Tarancón; ICACC'14 (38th International Conference and Expo on Advanced Ceramics and Composites), Daytona Beach (Florida, USA). January 2014. Oral presentation (invited).

2. *Integration of nanoionics into functional (micro)systems.* A. Tarancón, I. Garbayo, D. Pla, A. M. Saranya, L. Almar, T. Andreu, M. Salleras, N. Sabaté, A. Morata; 7th International Discussion Meeting on Relaxation in Complex Systems, Barcelona (Spain). July 2013. Oral presentation (invited).

3. *Thermal Stabilization of Ordered Mesoporous Metal Oxides: A Case Study as Anodes for Solid Oxide Fuel Cells.* L. Almar, T. Andreu, A. Morata, B. Colldeforns, L. Yedra, S. Estradé, F. Peiró, and A. Tarancón. MRS Spring Meeting (Materials Research Society). San Francisco (California, USA). April 2013. Oral presentation.

4. *High Electrochemical Performance of Mesoporous NiO-CGO as Anodes for IT-SOFC.* L. Almar, B. Colldeforns, L. Yedra, S. Estradé, F. Peiró, T. Andreu, A. Morata and A. Tarancón. High Electrochemical Performance of Mesoporous NiO-CGO as Anodes for IT-SOFC. 10th European Solid Oxide Fuel Cell Forum. Lucerne (Switzerland). June 2012. Poster presentation.

5. *Etude de $LaSrCoO_{4\pm\delta}$ comme cathode pour l'application de IT-SOFC.* Y. Hu, Y. Bouffanais, L. Almar, A. Tarancón, G. Dezanneau. GDR - Piles à Combustible et systèmes. Belfort (France). June 2012. Oral presentation.

6. *Nanoionics for advance fuel cells. Solid Oxide Electrolyzers for Energy Applications.* A. Morata, L. Almar, B. Colldeforns, T. Andreu and A. Tarancón, VII Conferences Barcelona Global Energy Challenges. Barcelona (Spain). June 2012. Poster presentation.

7. *Mesoporous Cermets as High Surface Area Anodes for IT-SOFC.* L. Almar, T. Andreu, A. Morata and A. Tarancón. XXVII Trobades científiques de la mediterrània. Maó (Spain), 2011. Oral presentation.

8. *SOFCs for auxiliary power units.* A. Tarancón, I. Garbayo, D. Pla, A. M. Saranya, L. Almar, B. Colldeforns, T. Andreu, A. Morata. VI Conferences Barcelona Global Energy Challenges. Barcelona (Spain). June 2011. Poster presentation.

9. *Mesoporous Nickel-Yttria Stabilized Zirconia obtained by Hard Template as a High Surface Area Anode for IT-SOFC.* L. Almar, T. Andreu, A. Morata and A. Tarancón. E-MRS (European Materials Research Society) Spring & Bilateral. Nice (France) 2011. Poster Presentation.

10. *Mesoporous NiO-CGO obtained by Hard Template as a High Surface Area Anode for IT-SOFC.* L. Almar, T. Andreu, A. Morata and A. Tarancón. The Electro Chemical Society (ECS) Conference. Montreal (Canada) 2011. Poster Presentation.

Nanomaterials have received increasing attention during the last decades in the solid state field since they play a major role as catalyst and catalyst supports for many applications including fuel cells or gas sensors. The interest is mainly due to their high specific surface area, which leads to an increase of performance and a cost-effective solution for expensive or rare materials.

However, many studies have reported the collapse of nanostructures at high temperature as one of the main drawbacks for their implementation in real devices and therefore, routes to thermally stabilize these materials must be explored.

In this thesis, the unique features of ordered mesoporous materials fabricated by nanocasting are exploited to create quasi-universal thermal stabilization methodologies, allowing implementing and evaluating them in high temperature energy applications .

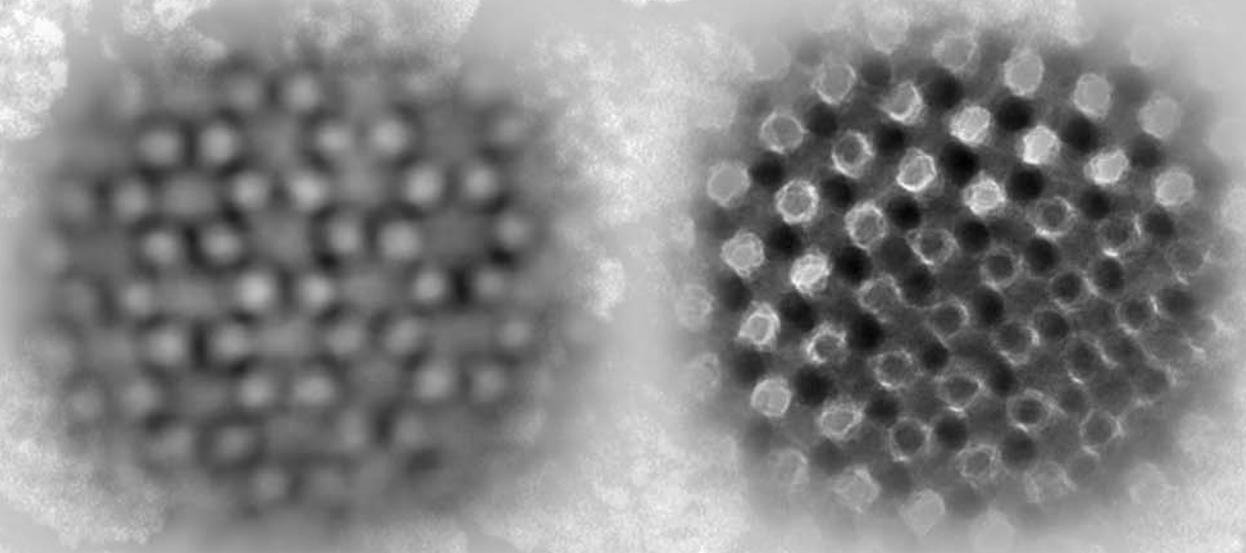

Universitat de Barcelona

Institut de Recerca en Energia de Catalunya
Catalonia Institute for Energy Research